University of California
Santa Barbara

Direct Numerical Simulations of Multiphase, Stratified, Environmental Fluid Flows

A dissertation submitted in partial satisfaction
of the requirements for the degree

Doctor of Philosophy
in
Mechanical Engineering

by

Raphael Ouillon

Committee in charge:

Professor Eckart H. Meiburg, Chair
Professor Pascale Garaud
Professor Frédéric Gibou
Professor Jeffrey R. Koseff
Professor Paolo Luzzatto-Fegiz
Professor Sally MacIntyre

December 2019

The Dissertation of Raphael Ouillon is approved.

Professor Pascale Garaud

Professor Frédéric Gibou

Professor Jeffrey R. Koseff

Professor Paolo Luzzatto-Fegiz

Professor Sally MacIntyre

Professor Eckart H. Meiburg, Committee Chair

December 2019

Direct Numerical Simulations of Multiphase, Stratified, Environmental Fluid Flows

by

Raphael Ouillon

To Sam and Dean

Acknowledgements

I decided to apply to the PhD program at UCSB after I joined Eckart's lab for a six-month research project. Even then, I did not know just how much I would be able to rely on Eckart's support, mentorship, endorsement and encouragement. Eckart has given me countless opportunities to present my work at conferences and seminars, to interact with collaborators and peers on many different projects, to be independent and creative in my work, and to thrive not only in my professional, but also private life outside of work. Eckart created the best conditions I could have hoped for as a PhD student, and set the benchmark of excellence for the role of PhD advisor I hope to one day fulfill.

I would also like to thank my coworkers with whom I shared my days in the lab over the years. I joined a lab in which a spirit of camaraderie and collectiveness thrived, and it contributed tremendously to my PhD experience. I particularly want to thank Edward Biegert, who until his graduation contributed more than anyone I have met to his lab. Ed was a true team-player in every aspect of academic life, who systematically took time out of his day to advise, support and mentor anyone who would ask him for help. Ed also organized the group hikes, the game nights, the Friday group lunches. Without that, my time at UCSB would have been very different, and far more challenging.

I also want to thank Thomas Köllner for his friendship and workplace mentorship. I learned a lot from his rigor and work ethic, and I hope to be a better researcher thanks to him. Perhaps more importantly, I have to thank Thomas for introducing me to rock climbing in the Santa Barbara mountains, and igniting a new passion !

I want to thank everyone I have had the privilege of working and collaborating with, and without whom this thesis would not have been possible. I first want to thank Prof. Pascale Garaud for all the time she took to discuss, improve and expand my research, for supporting me in my career choices, and for being a great mentor. I also want to give

many thanks to Prof. Jeffrey Koseff, Prof. Nicolas Ouellette, Prof. John Dabiri, Dr. Isabel Houghton, Dr. Nadav Lensky, Prof. Sally MacIntyre, Prof. Bruce Sutherland and Prof. Ben Kneller.

I would like to thank my dissertation committee members, who provided valuable feedback during my candidacy exam and who I enjoyed having the occasional spontaneous conversation with in the hallway.

Computational resources for this work used the Extreme Science and Engineering Discovery Environment (XSEDE), supported by the National Science Foundation, USA, Grant No. TG-CTS150053.

Curriculum Vitæ
Raphael Ouillon

Education

2019	Ph.D. in Mechanical Engineering (Expected), University of California, Santa Barbara.
2014	M.A. in Mechanical Engineering, Ecole Polytechnique Fédérale de Lausanne, Lausanne, Suisse.
2012	B.A. in Mechanical Engineering, Ecole Polytechnique Fédérale de Lausanne, Lausanne, Suisse.

Publications

1. R. Ouillon, E. Meiburg, N. T. Ouellette, and J. R. Koseff. Interaction of a downslope gravity current with an internal wave. *Journal of Fluid Mechanics*, 2019, `https://doi.org/10.1017/jfm.2019.414`
2. R. Ouillon, N. G. Lensky, V. Lyakhovsky, A. Arnon, and E. Meiburg. Halite precipitation from double-diffusive salt fingers in the dead sea: Numerical simulations. *Water Resources Research*, 2019, `https://doi.org/10.1029/2019WR024818`
3. R. Ouillon, E. Meiburg, and B. R. Sutherland. Turbidity currents propagating down a slope into a stratified saline ambient fluid. *Environmental Fluid Mechanics*, 2019, `https://doi.org/10.1007/s10652-019-09675-z`
4. R. Ouillon, I. A. Houghton, J. O. Dabiri, and E. Meiburg. Interactions between active particles and stratified fluids during collective vertical migration. *Journal of Fluid Mechanics*, submitted
5. P. Edel, R. Ouillon, P. Garaud, and E. Meiburg. Settling-driven large-scale instabilities in double-diffusive convection. *Journal of Fluid Mechanics*, in preparation
6. L. Zhao, R. Ouillon, B. Vowinckel, E. Meiburg, B. Kneller, and Z. He. Transition of a hyperpycnal flow into a saline turbidity current due to differential diffusivities. *Geophysical Research Letters*, 2018, `https://doi.org/10.1029/2018GL080150`
7. E. Biegert, B. Vowinckel, R. Ouillon, and E. Meiburg. High-resolution simulations of turbidity currents. *Progress in Earth and Planetary Science*, 2017, `https://doi.org/10.1186/s40645-017-0147-4`
8. B. Kneller, Y. Zhang, R. Ouillon, Z. Liu, E. Meiburg, and V. Birman. Strong versus weak marine hyper-pycnal flows: Detrainment of freshwater, heat and sediment, in preparation

Abstract

Direct Numerical Simulations of Multiphase, Stratified, Environmental Fluid Flows

by

Raphael Ouillon

Many fundamental processes in oceanic transport and limnology occur in geophysical flows that are both local in space and transient in time, and that require equally space and time-resolved methods of analysis. The importance of providing physics-based, quantitative modeling of such flows has driven the development of numerical methods for geophysical fluid dynamics for over three decades. Here, we use direct numerical simulations to investigate a range of stratified, particle-laden flows that are accurately described by the three-dimensional Navier-Stokes equations for an incompressible flow in the Boussinesq limit. We firstly investigate the propagation, transport and mixing dynamics of density-driven gravity currents moving in stratified environments. We propose new models for the intrusion of a turbidity current into a linearly stratified ambient based on three-dimensional simulations. We then describe the interaction between a gravity-current and an internal wave and characterize a phenomenological change in the long-term effect of the interaction at a critical wave height. We then quantify the role of double-diffusive processes in the Dead Sea in Summer and their role in the seasonality of salt crystallization and deposition. We also describe large-scale double-diffusive instabilities that arise in high-Prandtl sedimentary double-diffusive systems such as linearly stratified particle-laden salt water. Finally, we quantify mixing induced by a swarm of small-scale self-propelled organisms migrating in a stratified ambient fluid. We compare the relative contribution to mixing by individual swimmers within the swarm to that of the large-scale motion produced by the collective motion of the swarm.

Contents

Part I

Introduction

Chapter 1

Thesis motivation

1.1 A geophysical fluid dynamics context

Geophysical fluid dynamics (GFD) generally refers to the study of fluid motion at the Earth's surface. While the prefix 'geo' suggests that GFD considers the motion of fluids *within* the Earth, and not only at its surface, the study of the outer core and solid mantle is generally the subject of geodynamics. What differentiates geophysical fluid dynamics from classical fluid dynamics is thus the particular attention paid to naturally occurring flows on our planet's surface, most of which occur in the atmosphere, in bodies of water such as lakes, oceans and rivers, but also in lava flows, mud flows or avalanches. Because of the nature of the flows considered, two key principles permeate the field of geophysical fluid dynamics: Rotation, and stratification. Rotation is important because the effect of Coriolis forces cannot be neglected at the spatial scale of many flows of interest to the field of GFD. Stratification, i.e. the superposition of layers of varying density, is also crucial to GFD. Many of the flows that are considered in GFD are stratified in density, and their motion itself is driven by density differences. The dynamics of fluid transport, scalar transport, mixing, energy transfers are thus intimately tied to the fluid's density

and its spatial and temporal variations. In this work, we consider flows on the smaller end of GFD's spatial scales. We focus on problems that can be fully resolved down to the smallest scales through direct numerical simulations (more on that later) and thus restrict our analysis to lab-scale flows, or spatially localized flows in natural environments. This brings us to the topic of this thesis: Stratified, particle-laden flows.

Temperature is the most ubiquitous and dominant contributor to stratification and density variations in the world's water bodies. In the ocean for instance, away from the poles, the pycnocline - this region of rapidly increasing density with depth down to about 1km - is mostly the consequence of a negative temperature gradient (thermocline) from the surface down. This sharp temperature gradient, also present in lakes, is mainly due to the absorption of radiative heating from the sun in the well-mixed upper layer (epilimnion) of the water body. This results in a stable stratification, i.e. a water column in which energy needs to be spent to transport fluid vertically. The consequences of this stable stratification on mixing and thus on the biosphere are immense. The pycnocline acts as a natural barrier for vertical water circulation: Below a certain threshold, it inhibits shear-induced turbulence and above that threshold, damps the dyapycnal fluxes by requiring the conversion of kinetic energy into potential energy through mixing [47, 75, 46]. It becomes an accumulation region for the dense phytodetritus produced during phytoplankton bloom, allowing bacteria to bloom in turn, forming oxygen minimum layers [177, 12]. It also constitutes a natural barrier for the Diel migration of phytoplankton and reduces nutrient transport [178, 66].

Salinity also plays a central role in the ocean's stratification, although its variation with depth is usually not significant enough to take over the stable thermocline. The presence of a salinity gradient (halocline) at the thermocline might however have deeply

impactful consequences of vertical mixing and even large scale circulation in the ocean [123]. The mechanism by which the relatively weak contribution of salinity to density could be significant to the dynamics of the water column is known as double-diffusion, and is at the core of chapters 6 and 7. The third usual suspect to density variations is perhaps not as obvious role, but critically important. The transport of sediments - a solid material broken down and transported by fluid processes - is the focus of a considerable number of studies in the field of geophysical fluid dynamics. Numerous industrial applications, environmental challenges and answers to geological, biological and even societal [42, 117, 99] questions rely on our ability to understand, describe, and predict the motion of sediments. A dramatic example (and perhaps anecdotal) is found in the emergence of human civilizations, which all shared the progressive transition from nomadic to sedentary communities centered around fertile lands. These fertile lands were first and foremost the consequence of progressive deposition of nutrient rich sediments in river deltas, from the Tigris and Euphrates in Mesopotamia, the Ganges and the Yamuna in ancient India, the Yangtze and Yellow river in Ancient China, to the Fortaleza in Ancient Peru. The density of sediment particles differs from that of the carrying fluid, typically fresh water. The particles interact with the fluid phase and with each other hydrodynamically, and settle under the effect of gravity. In many geophysical applications, the volume fraction of particles is small, and the particle size is small, such that the effect of the particles on the inertia of the fluid mixture can be neglected. In this framework, the particles can be understood as a scalar concentration and contribute to the density in the same way that temperature and salinity would. Some of the implications of this are discussed in chapters 4, 7 and to a lesser extent 6.

Density variations, whether caused by temperature, salinity, particle loading or else, lead to hydrodynamic instabilities. When denser fluid is allowed to exchange momentum

with lighter fluid, the dense fluid forms a current. When the dense fluid is juxtaposed to the lighter fluid and the resulting motion is mostly horizontal, the flow is referred to as a gravity current. When the increase in density of the dense fluid is due to particle-loading, then the current is referred to as a turbidity current. Turbidity currents play a major role in sediment transport across the world's water bodies [99]. When the dense fluid overlays the lighter fluid, the Rayleigh-Taylor instability leads to the formation of plumes of lighter and denser fluid moving vertically in opposing directions. In the case where the bottom of the fluid column is heated and natural convection arises, the instability is best described by Rayleigh-Bénard convection. These instabilities transport energy by directly converting potential energy into kinetic energy. Internal waves, on the other end, transport energy from a trigger in the direction normal to a stable density gradient. Internal waves can occur in any stratified fluid, but internal waves propagating at a pycnocline, i.e. a sharp interface between a dense and lighter layers, are called interfacial internal waves. Due to the small density variations typically encountered along the water column in the ocean and in lakes, the amplitude and frequency of internal waves are typically much larger than that of surface waves, up to kilometres and hours respectively. These internal waves are typically triggered by tidal flow over submarine ridges and other forms of ocean floor topography, but can be the result of other types of perturbations, such as wind, or even rockslides along the coastline. Internal waves make a brief apparition in this thesis, in chapter 5. There exist in addition an abundance of hydrodynamic instabilities that are commonly observed in stratified geophysical flows, such as the Kelvin-Helmoltz instability in shear flows, the Holmboe instability in stratified shear flows, and the salt-fingering instability in double-diffusive convection. The latter has the particularity of allowing for the release of potential energy from a gravitationally stable stratified water column (see section III).

The flows resulting from all these hydrodynamic instabilities either generated or influenced by the presence of stratification lead to transport, mixing, and energy transfers. The importance of the transport of fluid in geophysical flows is evident. One might measure the velocity of the fluid flow, the existence of a steady or quasi-steady state, the flow rate across a certain plane, the average fluxes of a scalar field etc. Mixing is a metric that is particularly central to geophysical fluid dynamics. It is the result of the combined action of stirring and of molecular diffusion at gradients of concentration of a diffusing species. Stirring represents the deformation through advection by the velocity field of the diffusing scalar field. In a fluid domain with pre-existing variations in concentration of a scalar (say for instance a layer of fresh water overlying a layer of salt water with a sharp continuous transition in between), stirring results in the formation of elongated surfaces along which diffusion can occur. The vigor by which the flow is stirred and the diffusivity of the scalar field determine how much mixing occurs. The relationship between mixing, molecular diffusion and stirring is however not straightforward and one that we will encounter in most of this work.

In the following chapters, we will investigate the properties of strongly idealized physical systems in highly specific contexts. Each chapter corresponds to a stand-alone project, most often driven by observations from laboratory experiments or field studies conducted by our collaborators. While the projects are related in context, scope and methods, they differ sufficiently to be individually introduced at the beginning of each chapter. In the next section, we therefore simply motivate the projects and discuss their scope and aims.

1.2 Projects and objectives

Vertical momentum, mass transport, and transport of other scalar properties in the ocean and water bodies depend strongly on local, transient turbulent flow dynamics [65, 165, 63]. For instance, the breaking of internal waves generated by currents or tides, of surface waves generated by shear, or other types of wind-driven instabilities are commonly described as the main contributors to turbulence [120]. These events are intrinsically transient and local, and therefore require equally transient and spatially resolved methods of analysis. In addition, mixing layers, or thermohaline staircases, are observed in the world's ocean [133] to contribute locally to mixing [122], and are formed as a result of double-diffusive instabilities [147, 100, 122]. More recently, substantial interest in biogenic mixing, or animal-driven turbulent transport, has added to the complexity of vertical transport in the ocean [70, 36, 31]. Coastal event such as turbidity currents contribute greatly to the local transport of momentum, and of particular importance for biological and geological environments, to the transport of sediment [99]. The importance of improving quantification, modeling and predictability of these dynamical processes in stratified flows has opened the door to numerical methods of analysis for well over three decades, yet a lot remains to be done to fully understand local mixing events in the world's bodies of water, and eventually relate them to larger scale circulation. The content of this thesis is focused on better understanding parts of these broader topics, through the use of numerical simulations, scaling arguments, linear stability analysis and modeling.

Chapter 4 builds on the experimental work of Snow and Sutherland [142], studying the intrusion of a downslope turbidity current moving into a linearly stratified saline ambient fluid. The flow dynamics are explored as a function of settling speed of the sus-

pended particles and stratification of the ambient fluid. From the numerical results, new models to predict intrusion depth are proposed that account for settling, stratification and entrainment. The role of settling in the dynamics of the current is further explored by computing the energy budget of the flow.

In chapter 5, we consider the interaction between an internal wave propagating at a two-layer density interface and a downslope gravity current. Based on the experiments of [62], the numerical simulations aim at exploring the dynamics of the interaction for increasingly large waves and for various density configurations of the ambient and current. In particular, the study aims at understanding under which condition the internal wave permanently disrupts the propagation of the gravity current, and what the implications can be for gravity current discharge in coastal environments. To do so, we quantify the mixing and energy budget of the gravity current and describe a phenomenological transition at a certain wave height for which the wave-current interaction has a long-lasting impact on the mixing and transport of the current fluid.

In chapter 6, two-dimensional simulations are employed in order to describe the dynamics of the two-layer stratification in the Dead Sea in Summer. The goal of the study is to numerically confirm that double-diffusive convection allows for substantial transport of salt from the warm, salty top layer of the stratified water column into the lower layer. The water column in the Dead Sea in Summer is close to saturation of halite, and the simulations show that halite precipitation occurs in the double-diffusive fingers as they propagate in the colder, fresher lower layer, thus becoming supersaturated. Halite, or crystallized salt, is modeled as a continuous scalar field that settles at a constant Stokes velocity, allowing for the influence of the settling speed to be analyzed. These numerical observations of halite precipitation in Summer have direct implications for the formation

of salt layers in the geological record, in particular for how seasonality of the saturation profile allows for the formation of deep, spatially localized salt layers.

Chapter 7 addresses theoretical questions regarding double-diffusive convection, and particularly large-scale instabilities arising from the fingering regime, in high-Prandtl sedimentary systems. Motivated by experiments involving salt and particles as the fast and slow diffuser [26], we introduce a generalized mean-field theory following the procedure of Traxler et al. [156] to include settling. Using small-scale, two-dimensional direct numerical simulations, we show that high-Prandtl systems can be stable to the collective instability but unstable to the γ-instability. We then show with large-scale simulations that, in the presence of the γ-instability, layering can occur in such high-Prandtl systems despite the absence of collective modes, which was until now an open question [123]. We then further explore the dynamics of high-Prandtl sedimentary systems using the newly developed generalized mean-field theory.

Finally, chapter 8 describes a joint experimental study of mixing induced by diurnal migration of swarms of small-scale, inertial swimmers, based on the experimental setup of Houghton et al. [67], Houghton and Dabiri [66]. The study aims at better quantifying the effect of animal number density (or volume fraction of swimmers in the numerical model) on the amount of irreversible mixing produced by the swarm. The numerical simulations are additionally used to quantify the velocity of the coherent jet produced by the swarm, and to propose a simple model to predict jet velocity as a function of animal number density. The study further aims at differentiating mixing induced by the swarm at the scale of individual swimmers from mixing induced by the coherent jet at the swarm-scale. This disambiguation is particularly important as it shows that it is the coherent jet produced by the diurnal migration of many animals that generate the most

mixing, not the local stirring induced by the hydrodynamical interaction between the wakes of the individual swimmers.

Chapter 2

Physical modeling and governing equations

2.1 Fluid motion and transport

2.1.1 Incompressible Navier-Stokes equations

The fluid of interest in the geophysical and environmental applications considered in this work is water. Water behaves as a Newtonian fluid, i.e. the local shear stress experienced by a parcel of fluid is directly proportional to the shear rate through a constant viscosity coefficient. The bulk modulus of water is additionally extremely large, and water flows are thus often considered as incompressible. While this might not hold true under certain extreme circumstances, it certainly is true that compressibility effects can be neglected in most if not all naturally occurring water flows on Earth. Thus, the fluid motion of the problems of interest is well described by the three-dimensional Navier-Stokes equations for an incompressible flow of a Newtonian fluid. The momentum

conservation equations are written as

$$\rho_f \left[\frac{\partial \mathbf{u}}{\partial t} + (\mathbf{u} \cdot \nabla)\, \mathbf{u} \right] = -\nabla p + \mu \Delta \mathbf{u} + \mathbf{f}, \tag{2.1}$$

and the continuity equation is written as

$$\rho_f + \mathbf{u} \cdot \nabla \rho_f = 0, \tag{2.2}$$

which reduces to

$$\nabla \cdot \mathbf{u} = 0 \tag{2.3}$$

under the incompressibility condition on the material derivative $\frac{D\rho_f}{Dt} = 0$. Here, $\mathbf{u}$ is the fluid velocity, decomposed in Cartesian coordinates as $\mathbf{u} = u\mathbf{e}_x + v\mathbf{e}_y + w\mathbf{e}_z$, p is the pressure, ρ_f is the fluid density which is assumed constant in the momentum equation, μ is the dynamic viscosity and $\mathbf{f}$ is the sum of all external forces acting on the fluid. In the present work, the external force will be comprised of a gravitational term, representing the effect of small changes in density on the motion of the fluid, as well as a forcing term representing the effect of solid particles onto the fluid. This forcing term will have the objective of imposing the appropriate boundary condition at the surface of the spherical particles, i.e.

$$\mathbf{u} = \mathbf{u}_p + \omega_p \times \mathbf{r} \text{ on } \Gamma_p, \tag{2.4}$$

where $\mathbf{u}_p$ and ω_p are the translational and rotational velocities of particle p and $\mathbf{r}$ is the position vector from the center of mass of the particle to a point on the surface Γ_p of the particle.

2.1.2 Transport of scalar fields

Temperature, salinity and many other quantities of great importance to geophysical and environmental processes can be described in an Eulerian framework as a continuous scalar field. These quantities are transported mainly through two mechanisms in a fluid: Advection, i.e. the transport of the scalar field by the motion of its fluid parcel, or diffusion, i.e. the motion of the scalar quantity itself from regions of high concentration to regions of low concentration. Diffusion of a molecular or atomic quantity, say for instance salt ions in water, occurs due to the random motion of the molecules or atoms, self-propelled by their thermal energy. This thermal agitation itself diffuses through molecular collisions. Fick's law of diffusion states that the unit area diffusion flux J of a quantity ψ in direction x is given by $J = -\kappa\frac{\partial\psi}{\partial x}$, where κ is the diffusivity coefficient, or diffusivity. The transport of a diffusing scalar quantity ψ in the framework of an incompressible fluid is thus controlled by an advection-diffusion equation

$$\frac{\partial\psi}{\partial t} + \mathbf{u}\cdot\nabla\psi = \nabla\cdot(\kappa\nabla\psi) + \mathcal{S} \tag{2.5}$$

where $\mathcal{S}$ is a source term.

2.1.3 Density variations and the Boussinesq approximation

The density of water is mainly controlled by its temperature in fresh-water bodies, and its temperature and salinity in salt-water bodies. The density of a material fluid parcel in an incompressible flow cannot change, i.e. its material derivative is $\frac{D\rho_f}{Dt} = 0$. The existence of a unique solution to the variable density incompressible Navier-Stokes equations is a mathematical question of great complexity [94]. Numerical solutions involving a similar projection-correction step the one used for the constant density of the

Navier-Stokes equations exist and are readily available, but proving their stability remains a challenge [53, 121]. Often however, the density variations that are considered in the problem of interest are small, in that they do not significantly affect the inertia of the fluid. They can however generate appreciably strong variations in the specific weight, and thus are included in the momentum equations as a gravity-driven external force. Given that the gravitational force is often expressed as a hydrostatic term in the pressure, it is common to denote the gravity term of the Boussinesq approximation as $\mathbf{g}\,(\rho - \rho_0)$ where ρ now describes the local density of the fluid, ρ_0 is a constant reference density, and $\mathbf{g}$ is the gravitational acceleration vector. Under the Boussinesq approximation, the momentum equations can be further simplified as

$$\frac{\partial \mathbf{u}}{\partial t} + (\mathbf{u} \cdot \nabla)\,\mathbf{u} = -\frac{1}{\rho_0}\nabla p + \nu \Delta \mathbf{u} + \frac{\rho - \rho_0}{\rho_0}\mathbf{g} + \frac{1}{\rho_0}\mathbf{f}, \tag{2.6}$$

which is a valid simplification of the general equations (8.5) under the condition of validity of the Boussinesq approximation, i.e. $\frac{\rho(t,\mathbf{x})-\rho_0}{\rho_0} \ll 1$. The constant density, incompressible Navier Stokes equations under the Boussinesq approximation are more easily solved numerically, and present the additional advantage that the source of momentum due to gravity can be directly related to the presence of density-contributing scalar fields in the fluid. For instance, it is common to describe the density as a linear function of temperature and salinity. This writes as $\rho = \rho_0(1 + \alpha(T - T_0) + \beta(S - S_0)$, where T, S are the temperature and salinity respectively, T_0, S_0 are the reference values for which $\rho = \rho_0$, and α and β are referred to as expansion coefficients. In the following, we will assume a linear equation of state for the density such that for all density-contributing scalar fields c_j $j = 1, ..., J$, the density writes as

$$\rho = \rho_o \left(1 + \sum_j^J \beta_j c_j\right). \tag{2.7}$$

2.2 Particle motion and transport

2.2.1 Rigid, spherical particles

We firstly consider the case of passive, spherical, rigid particles in a fluid. Their motion is governed by the conservation of linear momentum,

$$m_p \frac{d\mathbf{u}_p}{dt} = \underbrace{\int_{\Gamma_p} \sigma \cdot \mathbf{n} dA}_{\mathbf{F}_{h,p}} + \underbrace{V_p \left(\rho_p - \rho_0\right) \mathbf{g}}_{\mathbf{F}_{g,p}} + \mathbf{F}_{c,p}, \tag{2.8}$$

and angular momentum

$$I_p \frac{d\omega_p}{dt} = \underbrace{\int_{\Gamma_p} \mathbf{r} \times (\sigma \cdot \mathbf{n}) dA}_{\mathbf{T}_{h,p}} + \mathbf{T}_{c,p}, \tag{2.9}$$

where m_p, I_p are the mass and moment of inertia of the particles, V_p and ρ_p are the volume and density of the particles respectively. Ω_p, Γ_p and $\mathbf{n}$ denote the volume domain of the particle, the surface domain of the particle, and the outward facing normal vector to the surface respectively. The force $\mathbf{F}_{h,p}$ and torque $\mathbf{T}_{h,p}$ result from the hydrodynamic stresses exerted on the particles by the fluid, where the hydrodynamic stress tensor σ is given by

$$\sigma = -p\mathbf{I} + \mu \left[\nabla \mathbf{u} + (\nabla \mathbf{u})^T\right]. \tag{2.10}$$

$\mathbf{F}_{g,p}$ is the buoyancy force, and $\mathbf{F}_{c,p}$ and $\mathbf{T}_{c,p}$ are the collision forces and torques that arise when particles collide with walls or other particles. A variety of collision models exist for rigid particles and we refer the reader to [15] for a detailed discussion of the models implemented in the code described in section 3.

2.2.2 Eulerian approach to particle transport

Numerical simulation of particle-laden flows in which the flow field around each individual particles is resolved requires the use of an interface-resolving method. Numerous such methods have been developed with various levels of complexity in the treatment of particle-particle and particle-fluid interactions [154, 48, 162, 78, 15]. When many particles are present and interact closely with each other, it is clear that particle-particle interactions need to be resolved. Even in more disperse suspensions, particles are expected to impact the fluid flow due to their intrinsic inertia and buoyancy. For instance, particles in turbulent flows can suppress the turbulence at low particle Reynolds numbers, and enhance turbulence at higher particle Reynolds numbers [58]. There exist however a range of flow parameters for which the influence of particles on the local dynamics of the fluid flow can be neglected. Very small particles, i.e. smaller than the smallest flow scales, in dilute suspensions, i.e. sufficiently far away from each other for any potential collision to influence the flow field, can be considered as passive and do not impact the momentum balance of the flow. These particles are considered non-inertial, i.e. their stopping time is much shorter than the typical time scale associated with the smallest fluid motion. Under these conditions, it is possible to treat the particle motion implicitly in a Eulerian framework instead of one, two, or four-way coupled Lagrangian approaches [50]. In this framework, a scalar particle concentration field emulates the presence of particles. Free of inertia, the particle concentration is transported through advection and diffusion much like temperature or salinity. Particles of a different density than the carrying fluid as subjected to gravitational forces and thus settle within the carrying fluid. Under the assumption of non-inertial particles much smaller than the smallest flow scale, the settling velocity of the particles in the reference frame of the carrying parcel of fluid is controlled by Stoke's law and takes the constant value $v_s = \frac{d_p(\rho_p - \rho_0)g}{18\rho_0\nu}$, where d_p is

the fictitious[1] particle diameter, and where ρ_p and ρ_0 are the particle and fluid densities respectively. Thus, the particle concentration c is advected at a velocity $\mathbf{u}_c = \mathbf{u} + v_s\mathbf{e}_g$, where $\mathbf{e}_g = \mathbf{g}/\|\mathbf{g}\|$. Similarly to equation 2.5, the transport equation for the particle concentration thus becomes

$$\frac{\partial c}{\partial t} + (\mathbf{u} + v_s\mathbf{e}_g) \cdot \nabla c = \nabla \cdot (\kappa \nabla c). \tag{2.11}$$

Particular attention must be given to the effective particle diffusivity κ. While the particles considered in the model are small, they are not required to be sufficiently small to experience Brownian motion and thus to diffuse as one would expect from Fick's law. In the case of non-Brownian particles, diffusion of the particle concentration field is thus to be understood as a simplistic effort to model the unresolved long-range hydrodynamic interactions between particles. The value of κ is not expected to play an important role in the dynamic of the flow, as long as the flow is sufficiently turbulent and that $\kappa \leq \nu$ [52, 108, 109].

[1] It is not always straightforward to discuss the Eulerian approach to particle transport, as particles do not exist explicitly in the model.

Chapter 3

Numerical methods

The numerical results presented in this text were obtained using two distinct codes, both developed in lab by former and current students. The first code, PARTIES (PARTicle-laden flows via immersed boundarIES), is a three-dimensional finite-difference Navier-Stokes solver coupled to an interface-resolving Immersed Boundary Method (IBM) for fully resolved particle-fluid simulations [14]. The second code is a two-dimensional pseudo-spectral Navier-Stokes solver designed for high accuracy simulations of density stratified flows, with emphasis on the investigation of double-diffusive convection [82]. PARTIES (chapters 4, 5 and 8) was developed in lab and is written in C. It uses the FFTW and HDF5 libraries, as well as MPI for parallelism. The Navier-Stokes solver implemented in PARTIES is based on TURBINS [106], also developed in lab. PARTIES in its present form and the particle-resolving features are the result of the PhD thesis work of Dr. Edward Biegert, with the help of Dr. Bernhard Vowinckel. Additional features of PARTIES used in the present work are the result of the work of Dr. Thomas Köllner (Volume of Fluid method and scalar transport solver) and myself (active particles, triple-periodicity and periodic stratified shear). The two-dimensional pseudo-spectral solver (chapters 6 and 7) was developed in lab and is written in C with C++

features. It uses the FFTW library and MPI for parallelism. The code was written by Dr. Nathan Konopliv. Additional features allowing for the crystallization and dissolution of salt (chapter 6) were implemented by myself. The numerical methods and recent developments are summarized in the following.

3.1 PARTIES

PARTIES uses a staggered uniform grid in Cartesian coordinates. A second-order finite difference scheme is used to discretize the Navier-Stokes equations in all three directions, and a low-storage third order Runge-Kutta (RK) method is used to integrate the discretized equations in time. A pressure-projection method is used to calculate the pressure and correct the velocity field to satisfy continuity. The implementation of the IBM allows for the simulation of polydisperse spherical particles. In recent developments, a Volume of Fluid (VoF) approach was implemented in PARTIES to allow for the transport of scalar fields in the presence of particles. This allows for the diffusivity of scalar properties to change from the fluid phase to the solid phase, and can for instance be used in conjunction with the IBM to impose a no flux condition at the surface of the particles. In its current form, PARTIES can simulate a wide variety of problems relevant to geophysical and environmental flows. For instance, gravity currents are turbulent, transient and intrinsically three-dimensional flows and similar numerical methods have been successfully employed to investigate their properties [108, 109, 114, 14, 107]. Recently, PARTIES was employed to study problems as varied as the properties of sediment beds [15], the hydrodynamic interaction between cohesive sediments [168], mixing induced by inertial swimmers (in review), and fully resolved simulations of gravity currents over particle beds (in preparation).

3.1.1 Immersed Boundary Method

The implementation of the IBM follows the work of Kempe and Fröhlich [78] and Uhlmann [162]. An IBM force $\mathbf{f}_{IBM}$ is added to the momentum equations in order to satisfy the boundary conditions of equation 2.4. In the IBM, the equation for conservation of momentum hold in the entire numerical domain Ω_0 which is comprised of a fluid region Ω_f and an immersed particle region $\Omega_p = \cup\Omega_p^i$ where Ω_p^i is the particle region of the i^{th} particle. In this formalism, the momentum equations become

$$\frac{\partial \mathbf{u}}{\partial t} + (\mathbf{u} \cdot \nabla)\,\mathbf{u} = -\frac{1}{\rho_0}\nabla p + \nu\Delta\mathbf{u} + \sum_j^J c_j\beta_j\mathbf{g}\delta_f + \mathbf{f} + \mathbf{f}_{IBM}, \tag{3.1}$$

where

$$\delta_f(\mathbf{x}) = \begin{cases} 1 \text{ if } \mathbf{x} \in \Omega_f \\ 0 \text{ if } \mathbf{x} \in \Omega_p \end{cases}, \tag{3.2}$$

and c_j is the concentration of the j^{th} density-contributing scalar field such that

$$\rho = \rho_0(1 + \sum_j^J c_j\beta_j). \tag{3.3}$$

By integrating the fluid momentum equations following the procedure of Tschisgale et al. [157] as described in Biegert et al. [15], we express the stress exerted onto the particles as a function of the fluid velocity and IBM forcing such that equations 2.8 and 2.9 become

$$m_p\frac{d\mathbf{u}_p}{dt} = \frac{d}{dt}\int_{\Omega_p}\rho_0\mathbf{u}dV - \int_{L_p}\mathbf{f}_{IBM}dV + V_p\left(\rho_p - \rho_0\right)\mathbf{g} + \mathbf{F}_{c,p}, \tag{3.4}$$

$$I_p\frac{d\omega_p}{dt} = \frac{d}{dt}\int_{\Omega_p}\rho_0\mathbf{r}\times\mathbf{u}dV - \int_{L_p}\mathbf{r}\times\mathbf{f}_{IBM} + V_p\left(\rho_p - \rho_0\right)\mathbf{g} + \mathbf{T}_{c,p}. \tag{3.5}$$

Here L_p is the shell volume surrounding the particle surface [15]. The surface of the particles is discretized with evenly distributed Lagrangian marker points. The no-slip condition is enforced at each marker points by calculating a required forcing $\mathbf{F}_l$ and spreading it onto the Eulerian grid to obtain $\mathbf{f}_{IBM}$. In order to compute the required forcing that imposes the no-slip condition at the surface of the sphere, we apply the following procedure:

1. Interpolate the fluid velocity at the Lagrangian marker points. This is done using the Diract Delta function $\delta_h(\mathbf{r})$ and writes

$$\mathbf{U}_l = \sum_{k,j,i} \delta_h(\mathbf{x}_{i,j,k} - \mathbf{X}_l)\mathbf{u}_{i,j,k}h^3, \tag{3.6}$$

   where $\mathbf{X}_l$ is the coordinate of the marker point, $\mathbf{U}_l$ is the interpolated velocity at that marker point, and $()_{i,j,k}$ represents the discretized quantities on the fluid grid with grid spacing h.

2. Calculate the desired fluid velocity $\mathbf{U}_l^d$ at the marker point using the discretized form of equation 2.4

$$\mathbf{U}_l^d = \mathbf{u}_p + \omega_p \times (\mathbf{X}_l - \mathbf{x}_p). \tag{3.7}$$

3. Compute the necessary force to correct for the difference between $\mathbf{U}_l$ and $\mathbf{U}_l^d$ as

$$\mathbf{F}_l = \rho_0 \frac{\mathbf{U}_l^d - \mathbf{U}_l}{\Delta t}. \tag{3.8}$$

4. Spread the forcing onto the Eulerian grid to obtain

$$\mathbf{f}_{IBM}(\mathbf{x}_{i,j,k}) = \sum_{p}^{N_p} \sum_{l}^{N_l} \delta_h(\mathbf{X}_l - \mathbf{x}_{i,j,k})\mathbf{F}_l V_l, \tag{3.9}$$

where N_p is the number of particles and N_l is the number of Lagrangian marker points for each particles, and V_l is a marker volume (see Biegert [13]).

5. Calculate the IBM force and torque applied to each particle p as

$$\mathbf{F}_{IBM,p} = -\sum_{l}^{N_l} \mathbf{F}_l V_l \tag{3.10}$$

$$\mathbf{T}_{IBM,p} = -\sum_{l}^{N_l} (\mathbf{X}_l - \mathbf{x}_p) \times \mathbf{F}_l V_l \tag{3.11}$$

3.1.2 Volume of Fluid method

The Volume of Fluid method (VoF) implemented in PARTIES (T. Kollner, private communication) allows for the transport of scalar fields in the presence of rigid particles. In this VoF approach, the diffusivity (or conductivity in the solid phase) of the scalar field is constant in each phase, and varies with the local liquid and particle volume fractions in cells that contain more than one phase. We define a global diffusivity κ in Ω_0 such that

$$\kappa = \phi_p \kappa_p + \phi_f \kappa_f, \tag{3.12}$$

where ϕ_p and ϕ_f are the particle and fluid volume fractions in a given cell respectively, and κ_p and κ_f are the diffusivities of the considered scalar in the particle and fluid phases respectively. For transport of salt ions, for instance, one could imagine that $\kappa_p = 0$. For convenience, we define the normalized diffusivity

$$\lambda^+ = 1 + \phi_p \left(\frac{\kappa_p}{\kappa_f} - 1 \right) \tag{3.13}$$

In the VoF framework, the advective velocity field $\mathbf{u}$ of the scalar field transport equation 2.5 is treated similarly to the diffusion term. An arithmetic mean of the fluid and particle

velocity is used to transport the concentration such that

$$\mathbf{u}(\mathbf{x},t) = \begin{cases} \phi_f(\mathbf{x},t)\mathbf{u}_f(\mathbf{x},t) + \phi_p(\mathbf{x},t)\underbrace{(\mathbf{U}_l + \omega_l \times (\mathbf{x}-\mathbf{X}_l))}_{\mathbf{u}_{v,l}} & \text{if } \mathbf{x} \in \Omega_l \\ \mathbf{u}_f(\mathbf{x},t), \text{ otherwise.} \end{cases} \tag{3.14}$$

Note that here, Ω_l defines the numerical space in which $\phi_p \neq 0$ due to the proximity of particle l, and $\mathbf{u}_{v,l}$ is the local solid body velocity of particle l at point $\mathbf{x}$. In the event that several particles overlap at a given location, then the average particle velocity is used instead.

The equation for transport of a scalar concentration c (eq. 2.5) becomes, in the VoF framework,

$$\frac{\partial c}{\partial t} + (\mathbf{u} + v_s \mathbf{e}_g) \cdot \nabla c = \kappa_f \nabla \cdot (\lambda^+ \nabla c). \tag{3.15}$$

3.1.3 Time stepping - without particles

Time stepping in PARTIES follows the work of Kempe and Fröhlich [78] and uses the third order Runge-Kutta (RK) method of Spalart et al. [143]. In the absence of particles, the time stepping scheme follows the classic pressure projection method [80, 102]. At time step t^n we solve for velocity $\mathbf{u}^{n,k}$ and pressure $p^{n,k}$ with substeps $k = 1, 2, 3$, where

$$\mathbf{u}^{n-1,3} := \mathbf{u}^{n,0}, \; p^{n-1,3} := p^{n,0}. \tag{3.16}$$

The time stepping scheme in the absence of particles is given by

$$-\kappa_j \nabla^2 c_j^k + \frac{c_j^k}{\Delta t^n \alpha_k} = \frac{c_j^{k-1}}{\Delta t^n \alpha_k} + \kappa_j \nabla^2 \; c_j^{k-1} \tag{3.17}$$

$$- \frac{\gamma_k}{\alpha_k} \nabla \cdot (\mathbf{u} c_j)^{k-1} - \frac{\zeta_k}{\alpha_k} \nabla \cdot (\mathbf{u} c_j)^{k-2}, \tag{3.18}$$

$$\frac{\mathbf{u}^* - \mathbf{u}^{n,k-1}}{\Delta t^n \alpha_k} = \nu \nabla^2 (\mathbf{u}^* + \mathbf{u}^{n,k-1}) - \frac{2}{\rho_0} \nabla p^{n,k-1} \tag{3.19}$$

$$- \frac{\gamma_k}{\alpha_k} \nabla \cdot (\mathbf{u}\mathbf{u})^{n,k-1} - \frac{\xi_k}{\alpha_k} \nabla \cdot (\mathbf{u}\mathbf{u})^{n,k-2} \tag{3.20}$$

$$+ 2\mathbf{g} \phi_f^k \sum_j \beta_j c_j^k, \tag{3.21}$$

$$\nabla^2 \Phi^k = \frac{\nabla \cdot \mathbf{u}^*}{2\alpha_k \Delta t^n}, \tag{3.22}$$

$$\mathbf{u}^{n,k} = \mathbf{u}^{*n,k} - 2\alpha_k \Delta t \nabla \Phi, \tag{3.23}$$

$$p^{n,k} = p^{n,k-1} + \rho_0 \Phi^k. \tag{3.24}$$

where Δt^n is the time step at iteration n, and $\alpha_k = \{\frac{4}{15}, \frac{1}{15}, \frac{1}{6}\}$, $\gamma_k = \{\frac{8}{15}, \frac{5}{12}, \frac{3}{4}\}$ and $\xi_k = \{0, -\frac{17}{60}, -\frac{5}{12}\}$ are the RK coefficients of substeps $k = \{1, 2, 3\}$ respectively. The J density-contributing scalar fields c_j of diffusivity κ_j are first advanced to the next substep k using an implicit scheme. A preliminary velocity field u^* is calculated using an implicit scheme for the diffusion terms and an explicit scheme for the advection terms. The updated concentrations fields are used in the Boussinesq term. Then, the Poisson problem for the pseudo pressure Φ^k is solved [1]. Following the projection step, the velocity and pressure are corrected, finalizing the substep.

[1]Note that ϕ_f and ϕ_p refer to the fluid and particle volume fractions respectively in the VoF method so that we refer to the pseudo-pressure as Φ instead of ϕ as done in Biegert [13] to avoid confusion.

3.1.4 Time stepping - with particles

In the presence of particles, the equations of motion of the particles and of the fluid are fully coupled following the stepping procedure of Kempe and Fröhlich [78]. We refer to [13] for a more detailed explanation of each step, but summarize the procedure to include the newly introduced VoF method (T. Köllner, internal lab report). The following steps are taken for each substep k.

1. Calculate the desired velocity of the Lagrangian marker points using equation 3.7.

2. Update the J concentration fields c_j^k by solving

$$-\kappa_{f,j}\nabla\cdot\left(\lambda^{+,k-1}\nabla c_j^k\right)+\frac{c_j^k}{\Delta t^n\alpha_k}=\frac{c_j^{k-1}}{\Delta t^n\alpha_k}+\kappa_{f,j}\nabla\cdot\left(\lambda^{+,k-1}\nabla c_j^{k-1}\right)-\frac{\gamma_k}{\alpha_k}\nabla\cdot(\mathbf{u}c_j)^{k-1}-\frac{\zeta_k}{\alpha_k}\nabla\cdot(\mathbf{u}c_j)^{k-2}.$$

3. Obtain a preliminary velocity field by solving only the explicit terms of equation 3.21 and including the Boussinseq term:

$$\frac{\tilde{\mathbf{u}}-\mathbf{u}^{k-1}}{\alpha_k\Delta t^n}=2\nu\nabla^2\mathbf{u}^{k-1}-\frac{2}{\rho_0}\nabla p^{k-1}-\frac{\gamma_k}{\alpha_k}\nabla\cdot(\mathbf{uu})^{k-1}-\frac{\zeta_k}{\alpha_k}\nabla\cdot(\mathbf{uu})^{k-2}+2\mathbf{g}\phi_f^k\sum_j\beta_j c_j^k.$$

4. Calculate the IBM forcing to enforce the no-slip condition at the Lagrangian marker points

   (a) Interpolate the fluid velocity onto the Lagrangian marker points following equation 3.6 using the preliminary fluid velocity $\tilde{\mathbf{u}}$.

   (b) Calculate the forcing at the Lagrangian marker point following equation 3.8.

   (c) Spread the IBM forcing to the Eulerian grid to obtain $\mathbf{f}_{IBM}$.

(d) Calculate the force and torque exerted by the IBM force onto the particles at the Lagrangian marker points.

5. Solve the Helmoltz equation for the implicit terms of equation 3.21 and including the IBM force, i.e.

$$\frac{\hat{\mathbf{u}} - \tilde{\mathbf{u}}}{\alpha_k \Delta t^n} = \nu \nabla^2 \hat{\mathbf{u}} - \nu \nabla^2 \mathbf{u}^{k-1} + \frac{2}{\rho_0} \mathbf{f}_{IBM} \tag{3.25}$$

6. Iterate on IBM forcing n_f times to further enforce the no-slip condition, i.e. repeating step 4 and updating the velocity at iteration (m) as

$$\mathbf{u}^{(m)} = \mathbf{u}^{(m-1)} + 2\rho_0 \alpha_k \Delta t^n \mathbf{f}_{IBM}^{(m)}. \tag{3.26}$$

See Biegert [13] for more details on the IBM iteration step. The preliminary velocity before projection-correction is given by $\mathbf{u}^* = \mathbf{u}^{(n_f)}$.

7. Solve equation 3.22 to obtain the pressure correction term. The Poisson problem is solved with a direct solver using Fast Fourier transforms in the x-z plane, and a second order central finite difference method in the y-direction.

8. Apply the pressure correction to the velocity and pressure (equations 3.23, 3.24).

9. Evaluate the sum of the forces and torques acting on each particle following equations 3.10-3.11.

10. Update the particle linear and angular velocities, as well as positions, using

$$\mathbf{u}_p^k = \mathbf{u}_p^{k-1} + \frac{2\alpha_k \Delta t}{m_p} \left(\mathbf{F}_f + \mathbf{F}_c \right) \tag{3.27}$$

$$\boldsymbol{\omega}_p^k = \boldsymbol{\omega}_p^{k-1} + \frac{2\alpha_k \Delta t}{I_p} \left(\mathbf{T}_f + \mathbf{T}_c \right) \tag{3.28}$$

$$\mathbf{x}_p^k = \mathbf{x}_p^{k-1} + \alpha_k \Delta t^n \left(\mathbf{u}_p^k + \mathbf{u}_p^{k-1} \right) \tag{3.29}$$

$$\tag{3.30}$$

3.2 2D pseudo-spectral solver

The code solves the two-dimensional Navier-Stokes equations for an incompressible flow in the streamfunction-vorticity formulation. The equations are discretized in the horizontal direction using a pseudospectral method, and in the vertical direction using a sixth-order compact finite difference scheme [86]. Time stepping is performed with a low-storage Runge-Kutta/Crank-Nicolson scheme. We refer to Burns [20] for implementation details. The code was designed to study double-diffusive processes in particle-laden flows and offer high levels of accuracy in order to fully resolve sharp gradients of concentrations of density-contributing scalars. Note that contrarily to PARTIES, this code does not allow for the resolution of the fluid flow around finite sized particles, but instead considers the particles in a Eulerian framework, modeled as a concentration field of constant settling velocity and finite diffusivity. The code was successfully employed to investigate double-diffusive processes in stratified and particle-laden flows [22, 82, 81, 1, 125, 112].

Part II

Gravity currents in stratified environments

Chapter 4

Gravity current moving down a slope into a linearly stratified ambient fluid

Authorship of this work is shared with Prof. Bruce R. Sutherland and Prof. Eckart Meiburg. Adapted from Ouillon et al. [114].

4.1 Introduction

Gravity currents are predominantly horizontal, buoyancy-driven flows of a denser fluid through a lighter fluid. When this density difference is due to the presence of suspended particles, we refer to the flow as a turbidity current. The particles are mainly suspended by turbulence and are subject to sedimentation, so that the buoyancy of the turbidity current is not conserved. The interstitial and ambient fluids are usually miscible, and the ambient fluid can be entrained into the current. The most common fluid involved in turbidity currents is fresh and/or saline water [99]. Turbidity currents play a key role in

sediment transport in aquatic environments such as oceans, reservoirs and lakes. They represent the principal means of sediment transport from shallow to deeper waters in the ocean, and they can carry large amounts of sediment over very long distances. Studying their behaviour is therefore essential to understanding the physics governing sediment transport and deposition. The destructive nature of turbidity currents is responsible for substantial damage to submarine engineering infrastructure such as pipelines and telecommunication cables. Predicting the energy content and velocity of turbidity currents is therefore essential for the design of robust engineering structures.

Most studies on turbidity currents to date, both numerical [23, 57] and experimental [34], have considered flows on flat bottoms in constant density ambient fluids. The effects of stratification on the propagation of turbidity currents were investigated experimentally for a two-layer setup [35],[126] or a constant gradient [127], while the effects of a slope were examined for a uniform ambient fluid [116]. While these studies yield important insight into the dynamics of turbidity currents, the combined effects of stratification and sloping bottom are not yet well understood. To that end, Snow and Sutherland [142] conducted a series of experiments of hyperpycnal and hypopycnal turbidity currents down a slope in a linearly stratified saline ambient fluid. The authors discuss the effects of settling velocity and stratification on the qualitative behavior of the current, and further investigate the changes in front velocity and intrusion depth for various configurations of particle sizes, stratification, and slope angle. Being able accurately to estimate the intrusion depth is paramount, as it corresponds to the point where the turbidity current lifts from the slope and loses much of its destructive potential. It also strongly affects the dynamics of settling by driving the particle-laden current away from the slope. Snow and Sutherland [142] analytically derive a scaling law for the intrusion depth that takes both entrainment and settling of particles into account. The qualitative validity of this law is verified by their experimental results and works well in the limit of short descents (high relative

stratification) and long descents (low relative stratification). This scaling law, however, relies on the predictability of the entrainment. A reference entrainment value of $E = 0.05$ or $E = 0.01$, depending on the slope, is found by fitting the intrusion depth scaling law to experimental data for particle-free gravity currents. The entrainment is not measured directly and its relative importance to settling processes is not assessed. The impact of entrainment variability on the quality of the prediction is thus not fully addressed in situations where settling of particles becomes the driving mechanism for changes in current density. By investigating this problem numerically, we are able to monitor the dynamics of the current explicitly and in a time and space resolved manner in order to analyse its velocity, its mixing and its settling behavior. By doing so, we can show directly the sensitivity of the predicted intrusion depth to the choice of entrainment coefficient in cases of settling-driven currents, and investigate more robust predictive tools for such circumstances.

Finally, the comprehensive data set provided by numerical simulations can be used to analyse the total energy budget and the dynamical energy transfers in such turbidity currents. This analysis of energy transfer rates helps build an understanding of the physical interplay of settling and entrainment and their influence on the dynamics of the current, and it supports the idea of choosing appropriate scaling tools depending on the dominant mechanism.

The initial set-up is sketched in figure 4.1. The density inside the clear ambient fluid increases linearly from ρ_T at the top to ρ_B at the bottom such that

$$\rho_2(y) = \rho_B + (\rho_T - \rho_B) \cdot \frac{y}{H} \tag{4.1}$$

The channel of width W is homogeneous in the spanwise z-direction. The particle-laden lock region of constant density ρ_1 is initially at rest. At $t = 0$, the lock is released and

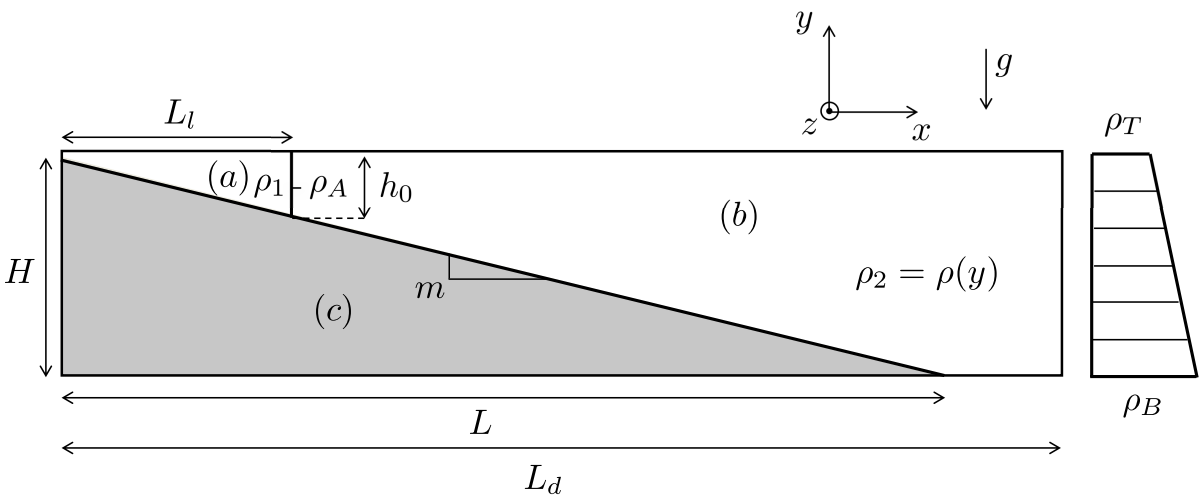

Figure 4.1: Problem set-up and configuration. (a) Particle-laden fluid; (b) ambient stratified fluid; (c) solid region. H and L denote the maximum depth and the horizontal extent of the inclined ramp, respectively. L_d is the horizontal length of the domain, h_0 and L_l denote the height and horizontal length of the lock, and m indicates the slope. ρ_1 is the bulk density of the lock, ρ_T is the initial density at the top of the ambient fluid, ρ_B is the initial density at the bottom of the ambient fluid and ρ_A is the initial density in the ambient fluid at half-lock depth.

the particle-laden flow of initial density $\rho_1 > \rho_A$ begins to move down the slope, and to interact with the ambient fluid. The local density of the fluid then depends on the particle concentration c and salinity s.

4.2 Physical modelling

The problem is governed by the three-dimensional incompressible Navier-Stokes equations. Since the suspensions considered are in the dilute regime with volume fractions well below 1%, particle-particle interactions can be neglected and the fluid and particle motion is dominated by transfer of momentum rather than volumetric displacement. Density variations due to the particles and salinity are sufficiently small for the Boussinesq approximation to hold. The density of the flow is therefore considered to be constant and equal to the reference density ρ_0, with the exception of the gravity term. The evolu-

tion of the particle and salinity concentrations is modelled using an Eulerian approach, based on convection-diffusion equations. Note that the diameter of the particles is assumed to be much smaller than the smallest length scale of the fluid motion, so that the particle inertia can be neglected and the velocity of the particles is considered to be equal to the sum of the fluid velocity and the particle settling velocity. The particle and salinity velocity fields are therefore divergence free. This approach has previously been successfully employed to investigate numerically the effects of settling on the dynamics of particle-laden flows [108], as well as their dissipation and mixing properties [109]. It was also used to study the effects of bottom topography on the mixing dynamics of turbidity currents [107]. The governing equations and choice of non-dimensional parameters are described in depth by Necker et al. [108], so that they will be summarized only briefly here.

The non-dimensional continuity, momentum, particle transport and salt transport equations are given by

$$\nabla \cdot \mathbf{u} = 0 \ , \tag{4.2}$$

$$\frac{\partial \mathbf{u}}{\partial t} + (\mathbf{u} \cdot \nabla)\,\mathbf{u} = -\nabla p + \frac{1}{Re}\Delta \mathbf{u} + (\alpha_s s + \alpha_c c)\,\mathbf{e_y} \ , \tag{4.3}$$

$$\frac{\partial c}{\partial t} + (\mathbf{u} + \mathbf{v}_s) \cdot \nabla c = \frac{1}{ReSc_c}\Delta c \ , \tag{4.4}$$

$$\frac{\partial s}{\partial t} + \mathbf{u} \cdot \nabla s = \frac{1}{ReSc_s}\Delta s \ , \tag{4.5}$$

where $\mathbf{u}$, p, s, c represent the non-dimensional fluid velocity, pressure, salinity and particle concentration, respectively. With $\tilde{(\cdot)}$ referring to variables in their dimensional form, we define the Reynolds number Re as

$$Re = \frac{\tilde{u}_b \tilde{H}}{\tilde{\nu}} \ , \tag{4.6}$$

where $\tilde{\nu}$, $\tilde{H}$ and $\tilde{u}_b$, respectively, denote the kinematic viscosity, the maximum depth (see figure 4.1) and the buoyancy velocity

$$\tilde{u}_b = \sqrt{\tilde{g}'\tilde{h}_0} = \sqrt{\frac{\tilde{\rho}_1 - \tilde{\rho}_A}{\tilde{\rho}_0}\tilde{g}\tilde{h}_0} \ . \tag{4.7}$$

Here $\tilde{\rho}_1$ is the initial lock density, $\tilde{\rho}_A$ denotes the initial ambient fluid density at mid-lock height, and $\tilde{\rho}_0$ indicates the interstitial fluid density. The variables are made non-dimensional by choosing $\tilde{H}$ and $\tilde{u}_b$ as the flow reference scales such that $\mathbf{x} = \frac{\tilde{\mathbf{x}}}{\tilde{H}}$, $\mathbf{u} = \frac{\tilde{\mathbf{u}}}{\tilde{u}_b}$, $t = \frac{\tilde{t}}{\tilde{H}/\tilde{u}_b}$, $p = \frac{\tilde{p}}{\tilde{\rho}_0\tilde{u}_b^2}$. The settling velocity is obtained by balancing the gravitational forces with the Stokes drag of a sphere in a flow of uniform velocity such that $\mathbf{v}_s = -\frac{\tilde{v}_s}{\tilde{u}_b}\mathbf{e}_y$, with

$$\tilde{v}_s = \frac{d_p^2\left(\tilde{\rho}_p - \tilde{\rho}_0\right)\tilde{g}}{18\tilde{\rho}_0\tilde{\nu}} \ . \tag{4.8}$$

The particle concentration and salinity fields are made non-dimensional as $c = \frac{\tilde{c}}{c^*}$ and $s = \frac{\tilde{s}}{s^*}$, where $c^* = \tilde{\rho}_p\frac{\tilde{\rho}_1 - \tilde{\rho}_0}{\tilde{\rho}_p - \tilde{\rho}_0}$ and $s^* = \tilde{\rho}_s\frac{\tilde{\rho}_B - \tilde{\rho}_0}{\tilde{\rho}_s - \tilde{\rho}_0}$. Here $\tilde{\rho}_p$ is the density of particles, $\tilde{\rho}_s$ is the density of salt and $\tilde{\rho}_B$ is the density at the bottom of the channel. In this way the non-dimensional particle and salt expansion coefficients are given by

$$\alpha_c = \frac{\tilde{\rho}_1 - \tilde{\rho}_0}{\tilde{\rho}_1 - \tilde{\rho}_A}\frac{\tilde{H}}{\tilde{h}_0} \ ,$$
$$\alpha_s = \frac{\tilde{\rho}_B - \tilde{\rho}_0}{\tilde{\rho}_1 - \tilde{\rho}_A}\frac{\tilde{H}}{\tilde{h}_0} \ .$$

The particle and salt Schmidt numbers, Sc_c and Sc_s, are defined, respectively, as

$$Sc_c = \frac{\tilde{\nu}}{\tilde{\kappa}_c}, \ Sc_s = \frac{\tilde{\nu}}{\tilde{\kappa}_s} \ . \tag{4.9}$$

For the sake of simplicity, and in following earlier authors, the diffusivity coefficients are

chosen to be equal to the kinematic viscosity such that $\tilde{\kappa}_s = \tilde{\kappa}_c = \tilde{\nu}$, leading to

$$Sc_s = Sc_c = 1 \ . \tag{4.10}$$

Note that while the real values of Sc_c and Sc_s are much larger than unity, the effect of molecular diffusivity on the propagation of the current in such a turbulent, high Reynolds flow, are negligible as long as $Sc \geq 1$ [52]. The Schmidt number also does not impact the destabilization of the initially two-dimensional flow through the lobe-and-cleft instability as long as $Sc \geq 1$ [56]. In order to discuss the effects of stratification, it is convenient to define a buoyancy frequency N that expresses the characteristic frequency at which a fluid would vertically oscillate in a stably stratified environment. When using the Boussinesq approximation, this is defined as

$$\tilde{N} = \sqrt{\tilde{g}\frac{\tilde{\rho}_B - \tilde{\rho}_T}{\tilde{\rho}_T \tilde{H}}} \ , \tag{4.11}$$

where $\tilde{\rho}_T$ and $\tilde{\rho}_B$ are the initial ambient fluid densities at the top and bottom of the channel, respectively. In its non-dimensional form, this can be expressed as

$$N = \tilde{N} \cdot \frac{\tilde{H}}{\tilde{u}_b} \ . \tag{4.12}$$

This non-dimensional buoyancy frequency compares the time-scale associated with stratification to the time-scale associated with the propagation of the current down to the bottom of the channel. It is therefore difficult to interpret. We therefore use the stratification magnitude S instead, defined as

$$S \equiv \frac{\tilde{\rho}_{h_0} - \tilde{\rho}_T}{\tilde{\rho}_1 - \tilde{\rho}_T} \ . \tag{4.13}$$

The above equations are solved via our immersed boundary code TURBINS [106]. Slip boundary conditions are employed at the top and right walls, and periodic conditions are implemented on the lateral boundaries. The width of the domain is chosen sufficiently large so that the periodic boundary conditions do not have a significant impact on the flow. An immersed boundary method is used to impose the no-slip condition on the slope ($\mathbf{u}_{|\Gamma_s} = 0$) [101], [106],[76]. In order to impose the boundary conditions, immersed boundary methods add a body force $\mathbf{f}$ to the Navier-Stokes equations. This force is evaluated by requiring that the velocity on the boundary $\mathbf{u}_{|\Gamma_s}$ is equal to the desired boundary velocity $\mathbf{v}_{\Gamma_s}$. If the grid node coincides with the boundary on which the condition is imposed, the forcing term is exact. This is of course rarely the case and interpolation methods are required to impose proper forces on the near-boundary nodes. [106, 76, 39, 158] provide more details about the computation of the body force and its interpolation.

4.3 Flow structure and behaviour

4.3.1 General considerations

The numerical simulations aim at reproducing the experiments conducted by Snow and Sutherland [142] and at conducting parametric studies on the settling velocity v_s and stratification parameter S. Table 4.1 summarizes the parameters for a selection of simulations. In addition, a parametric study on the Reynolds number was conducted and demonstrated that the variables of interest converge for sufficiently large values of Re. In other words, the Reynolds number did not influence the results as long as the flow quickly became fully turbulent (typically $Re > 6,000$ in the simulations).

The representative behaviour of a lock-release turbidity current down a slope into a

	exp1	exp2	exp3	S sensitivity	v_s sensitivity
Re	$16,850$	$15,000$	$35,000$	$15,000$	$15,000$
S	0.653	0.176	0.248	$0, 0.419, 0.692, 0.885, 1.028$	0.419
v_s	0.00731	0.00108	0.000463	0.001	$0, 0.001, 0.005, 0.01$
m	0.149	0.149	0.149	0.0744	0.0744

Table 4.1: Summary of relevant simulations. exp1,2,3 reproduce experiments by Snow and Sutherland [142]. The parametric studies on the stratification S and settling velocity v_s are based on realistic lab scale physical parameters and represent a small sample of the total body of simulations that were conducted.

stratified ambient fluid is shown in figure 4.2. The spanwise-averaged particle concentration is represented on a linear grey scale for various times throughout the simulation. The concentration varies between $c = 0$ and $c = 1$, where we recall that the concentration is made non-dimensional by the initial lock fluid concentration. Upon extraction of the model-gate, the flow starts to move down the slope. Soon Kelvin-Helmholtz rollers form which subsequently break down into fully three-dimensional turbulence, thereby creating smaller dissipative vortices as observed at later times ($t > 10$).

The influence of the ambient fluid stratification becomes evident at later times ($t \approx 15$) when the current separates from the surface of the ramp and intrudes into the ambient fluid. The effects of stratification on intrusion depth are key in understanding the evolution of the suspended mass, deposit profiles and energy budgets, as will be discussed later.

In most of the experiments conducted by Snow and Sutherland [142], the Reynolds number $Re = \frac{\tilde{u}_b \tilde{H}}{\tilde{\nu}}$ exceeds $15,000$. They observed turbulent mixing along the whole length of the current at its interface with the ambient fluid. Numerical simulations corroborate this behaviour as illustrated in figure 4.2. In the experiments, the lock is stirred before release to guarantee a homogeneous suspension of particles. This introduces initial turbulence that contributes to the rapid destabilisation of the flow. In our simulations a small random perturbation is applied to the initial velocity field, such that the lobe-and-

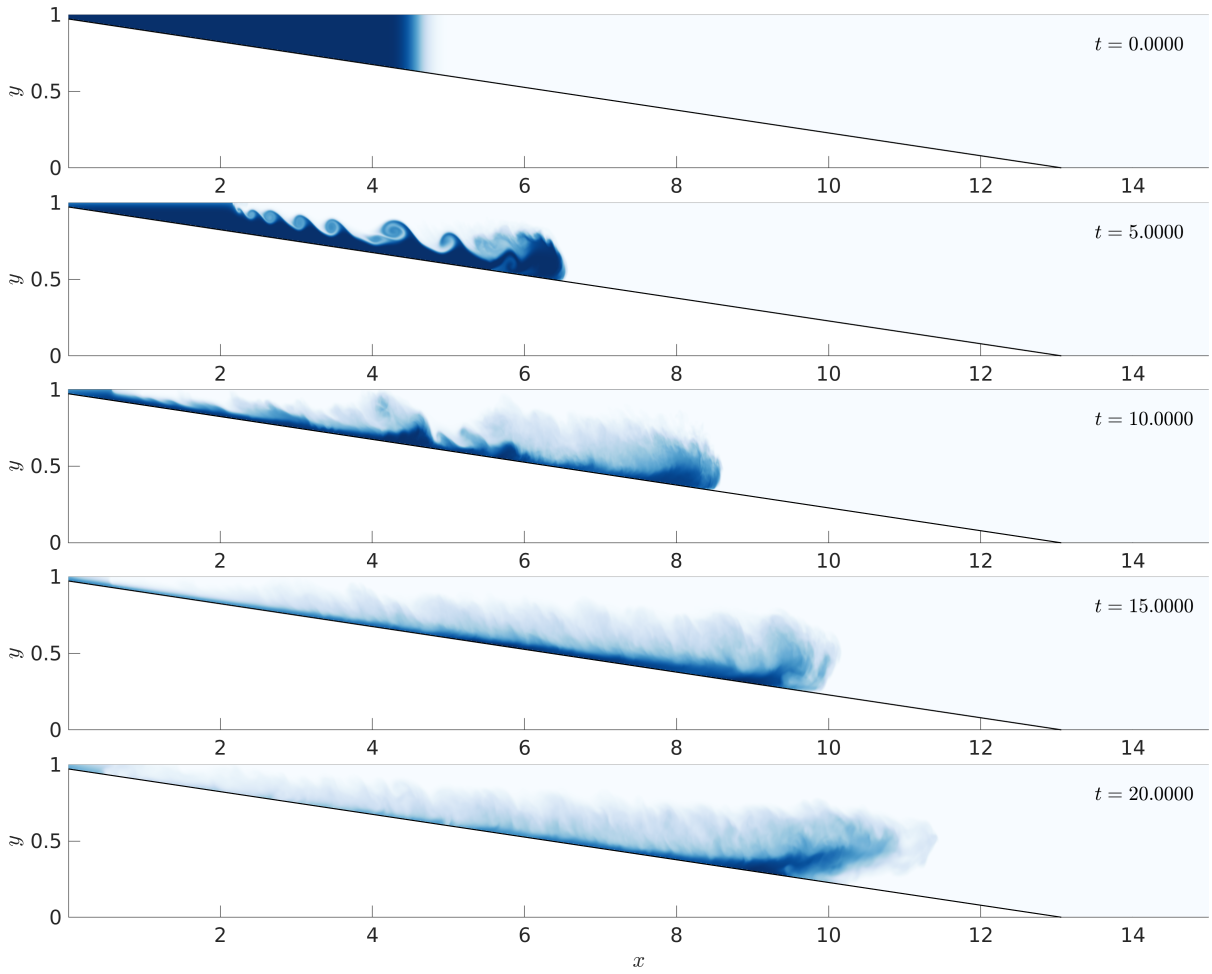

Figure 4.2: Spanwise averaged particle concentration field for various times ($Re = 15,000$, $v_s = 0.001$, $S = 0.419$, $m = 0.0744$). A 2:1 aspect ratio is used to improve readibility.

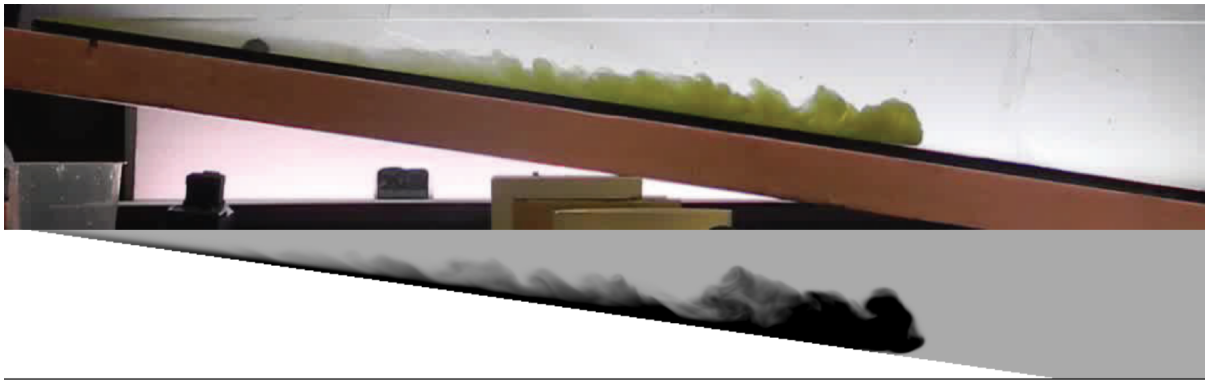

Figure 4.3: Snapshots of a turbidity current experiment (exp2, based on experiments by Snow and Sutherland [142], $S = 0.176$, $Re = 15,000$, $v_s = 0.001$, $m = 0.149$) right before separation of the current from the bottom slope. Experimental results (top) and the corresponding numerical results are compared at time $t = 12.1$.

cleft instability, initiated at the head of the current, quickly propagates along the body of the current thus destabilizing the large Kelvin-Helmholtz rollers formed after release of the lock fluid. Figure 4.3 compares the 2D averaged concentration field between the experiments and the simulations for a typical turbidity current.

4.4 Dynamic flow properties

4.4.1 Front velocity

The front velocity refers to the along-slope velocity of the head of the current. It is proportional to the time derivative of the position of the front x_f defined using a concentration threshold c_{lim} as the furthest point on the slope that verifies $c(x_f, y_s(x_f)) > c_{lim}$, where $y_s(x_f)$ is the y-position of the the forward-most point of the front. Note that here we employ the spanwise averaged concentration used, in order to be consistent with the definition of [142]. The concentration threshold is chosen as $c_{lim} = 0.05$, i.e. 5% of the initial lock concentration. We note that the concentration gradient at the head of the

current in the direction of propagation is strong, so that the result for the front velocity is independent of the choice of c_{lim}. The front velocity U_f is then computed as

$$U_f = \frac{1}{\cos\theta}\frac{dx_f}{dt} \ , \tag{4.14}$$

where θ is the angle of the slope. The front velocity for various settling velocities v_s is represented as a function of time in figure 4.4a ($Re = 15,000$, $v_s = 0.001$, $m = 0.0744$). After release, the front rapidly accelerates before an abrupt decrease in acceleration ($t \approx 2$) to a small but finite value. This behaviour differs from the inertial phase that follows the acceleration phase of planar gravity currents [24] in that the current does not reach a constant velocity after the acceleration phase. The geometry of the lock and the varying depth of the ambient fluid with the slope contribute to this behaviour [164]. In this secondary acceleration phase however, the front velocity increases slowly and is approximated in the following by a Froude number defined as the average of the front velocity

$$\mathrm{Fr} = \bar{U}_f(t_s < t < t_i) \tag{4.15}$$

where t_s and t_i are the time at the onset of the slow acceleration phase and the time when intrusion begins, respectively.

As the current is about to intrude in the ambient fluid, the front velocity decreases. Some of the fluid from the current close to the slope can then move back up the slope while the rest intrudes and moves horizontally away from the slope at a slower velocity than before intrusion, as seen in figure 4.4a. Note that the definition of the front velocity based on the rightmost location of the current differs from that of Snow and Sutherland [142] who extract the current location slightly above the slope and differentiate it to find the front velocity. Both definitions are consistent until intrusion where the rightmost

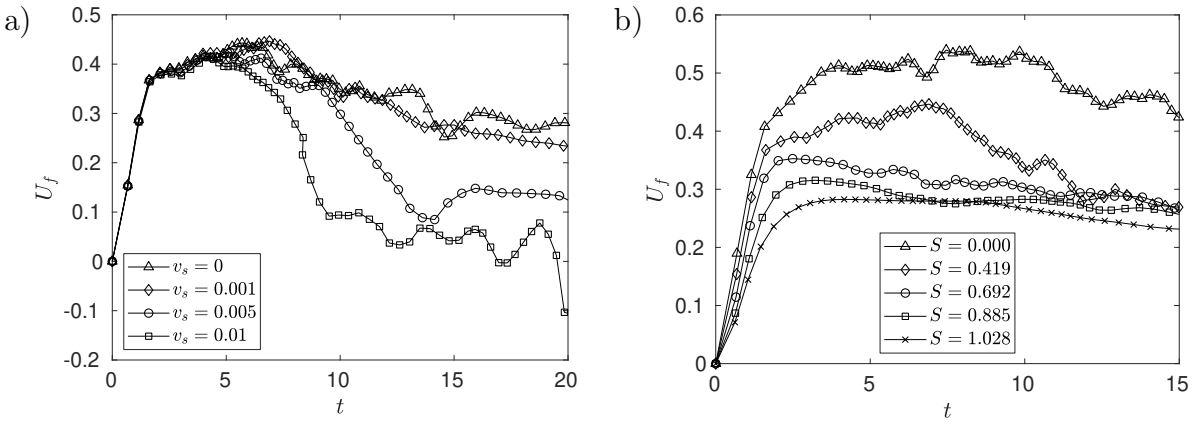

Figure 4.4: (a) Front velocity as a function of time for various settling velocities v_s ($Re = 15,000$, $S = 0.419$, $m = 0.0744$). Larger settling velocities lead to a more rapid drop in the density of current and thus decrease the time before intrusion. As intrusion occurs, the front velocity drops dramatically, and it can even oscillate around zero near the intrusion point. This is observed for $v_s = [0.005, 0.01]$ during the interval $t \sim [11, 19]$ respectively. (b) Front velocity as a function of time for various stratifications S ($Re = 15,000$, $v_s = 0.001$, $m = 0.0744$). An increase in stratification reduces the front's acceleration and its velocity plateau as less potential energy is available overall for conversion into kinetic energy.

location of the current becomes part of the intrusion but the current above the slope slows down to a halt. In the experiments, a similar increase in front velocity followed by a relatively constant front velocity is observed. As intrusion occurs, the backward motion of the current right above the slope is also observed. This can be seen in figure 6 of Snow and Sutherland [142] where the along-slope position of the front of the current is seen to oscillate around a maximum reached at intrusion. Before intrusion, it can be seen that the settling velocity has very little impact on the front velocity. The loss in head density due to settling decreases the density difference between the current and the ambient fluid and the front velocity is therefore slightly diminished by an increase in settling velocity, but this influence is small within the parameter range investigated here.

Stratification has a much stronger influence on the front velocity during and after the first acceleration phase. Figure 4.4b represents the front velocity as a function of time for various stratifications S. The increase in the front velocity during the acceleration

phase is related to the amount of kinetic energy that can be created from the initial lock configuration, which depends on the potential energy initially stored in the lock. It can be inferred that the front acceleration is related to the density difference between the lock and the ambient fluid at the bottom of the lock, i.e. $\tilde{\rho}_1 - \tilde{\rho}_{h_0}$ and thus that acceleration decreases with S. The change in front velocity after the initial acceleration phase depends on stratification, with slowly accelerating fronts for $S = [0, 0.419]$ and slowly decelerating fronts for $S = [0.692 - 1.028]$, suggesting that stratification also contributes to the difference in behaviour when compared to a classic planar gravity current [24]. Figure 4.5 presents the current simulation results, along with the experimental data of Snow and Sutherland [142], for the Froude number Fr as a function of stratification S. The experimental and numerical data are compared to theoretical predictions of Fr in the limits of no stratification ($S = 0$) and strong stratification ($S = 1$) as presented by Ungarish [163]. The author investigated a generalization of the work of Benjamin [11] to a steady gravity current propagating into a linearly stratified ambient fluid on a flat bottom. A flow-field solution of Long's model is combined with a flow-force balance over the width of the channel to yield solutions for the Froude number. We observe that the simulation data fall within the error bars of the experimental results. In the absence of stratification, the simulation results yield a Froude number of Fr $= 0.496$, which closely matches the theoretical value of Fr $= 0.5$. At $S = 1.028$, the Froude number decreases to Fr $= 0.2645$, which agrees well with the theoretical value of Fr $= 0.25$ at $S \approx 1$.

The dependence of Fr on the current to channel height ratio h_c/H is not clearly defined in the case of a sloping bottom with a flat top interface, so that the direct application of this relationship to the present set-up is not straightforward [163]. However, comparing the results of the numerical simulations to a prediction of an effective Froude number in a stratified ambient proposed by [164] yields very satisfactory agreement (figure 4.5). This effective Froude number is given, in the present geometry, by $Fr_e = 0.46\,(1 - 0.75S)^{0.5}$.

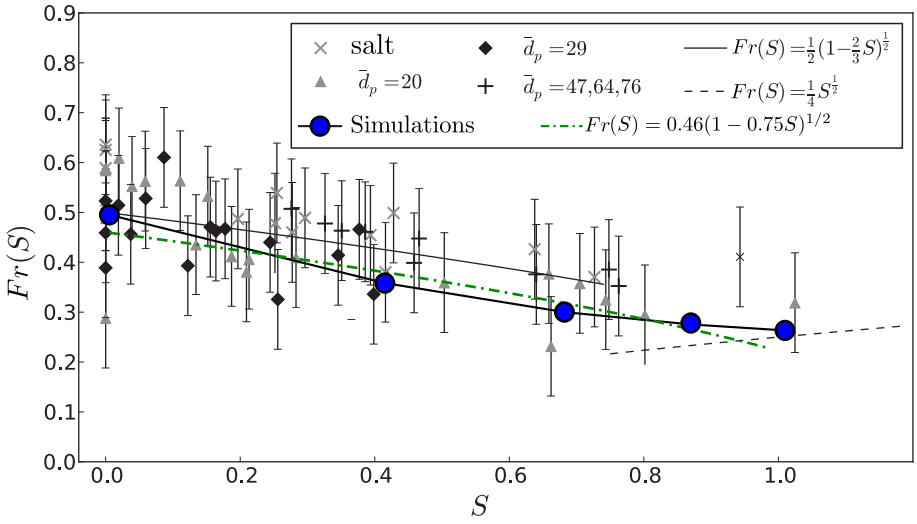

Figure 4.5: Froude number as a function of stratification - comparison with the experimental data of [142]. The numerical results are seen to fall within the margin of error of the experimental data. In the limit of no stratification ($S = 0$), the numerical simulations recover the theoretical limit of Fr = 0.5, and they approach the asymptotic value of Fr = 0.25 as $S \to 1$. Possible explanations for the wide spread of experimental results are the variability in initial turbulent kinetic energy contained in the lock due to stirring, as well as uncertainties introduced by the release of the gate.

This observation reaffirms that for small slopes (typically less than 10°), the slope does not impact the characteristics of the current [10, 19].

4.4.2 Entrainment

Entrainment of ambient fluid into the current, or detrainment of interstitial fluid from the current into the ambient fluid, contribute to the change in current density and play an important role in the intrusion phenomenon. Various approaches can be used to estimate entrainment, such as the box model description [142], which results in a constant value for the entrainment rate, independent of time and space. A time and space-resolved approach is considered here, based on the DNS simulation results. A local entrainment velocity $U_e(x, t)$ is explicitly computed at each point along the x-direction, which avoids the constant entrainment assumption made by [142].

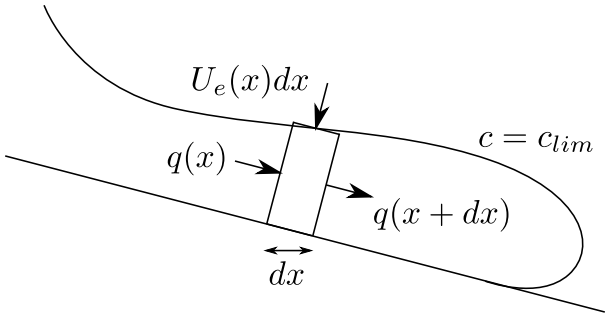

Figure 4.6: Local control volume employed to define the entrainment velocity. The balance is applied on a differential volume of length dx at location x. The envelope of the current that determines the height of the differential volume is defined based on a threshold concentration $c_{lim} = 0.01$.

Firstly, the top and bottom positions $y_{top}(x,t)$ and $y_{bot}(x,t)$ of the current are computed using a concentration threshold $c_{lim} = 0.01$. We note that the results are relatively independent of the choice of c_{lim}, in the sense that varying it by a factor of 50 from 0.001 to 0.05 typically results in a change of the entrainment velocity of less than 10%. The local volume flux balance is computed as

$$U_e(x,t) = \frac{\partial q_i(x,t)}{\partial x} = \frac{\partial}{\partial x}\int_{y_{bot}(x,t)}^{y_{top}(x,t)} (u(x,y,t)\cdot\cos\theta + v(x,y,t)\cdot\sin\theta)dy \tag{4.16}$$

where $U_e(x)$ is the entrainment velocity and $q_i(x)$ is the volume flux of the current at point x, cf. figure 4.6. The above is based on the spanwise averaged two-dimensional data. The dimensionless local rate of entrainment $E(x)$ is then computed as the ratio of the local entrainment velocity to the front velocity such that

$$E(x,t) = \frac{U_e(x,t)}{U_f(t)}\ . \tag{4.17}$$

In the present investigation, we evaluated the entrainment rate for a simulation of a set-up that corresponds to one of the experiments of [142]. The Reynolds number is

$Re = 15,000$, the settling velocity is $v_s = 0.001077$, the stratification is $S = 0.176$ and the slope is $m = 0.149$. Figure 4.7a represents a map of the computed entrainment velocity U_e as a function of both space and time. At time $t \approx 5$ (corresponding to a front location of $x_f \approx 2L_l$, where L_l is the lock-length), the flow starts destabilising and strong mixing occurs in a well defined turbulent zone behind the head of the current. Following this destabilization, one can observe the emergence of two regions of strong entrainment that evolve and spread until the intrusion forms around $t = 10$, corresponding to $x_f \approx 3L_l$. These distinct regions of high mixing can be easily understood by looking at the particle concentration in the domain as shown in figure 4.7c. The current boundary, computed using a concentration limit of $c_{lim} = 0.01$, is indicated in the figure. The current exhibits two thickness maxima behind the head that correspond to highly dissipative regions where mixing is much stronger than in the rest of the current. These regions correspond to the two high entrainment zones seen in figure 4.7a at corresponding times. Similar observations can be made at later times when more than 2 regions of high entrainment appear. This is seen in figure 4.7d, which shows the particle concentration and current boundary at $t = 9$, right before intrusion. Three regions of strong mixing are present, which can be identified by the two bumps in particle concentration in the tail of the current and the head itself.

These observations confirm the non-uniform nature of entrainment along the body of the current. Figure 4.7b shows the evolution with time of the entrainment E averaged on the length of current. There is a good match between the assumed entrainment of $E = 0.05$ in the experimental paper of [142] and the computed entrainment value of $E = 0.061$, averaged along the current. Furthermore, the computed entrainment value agrees closely with experimental observations for a current propagating over a flat surface of $E = 0.063 \pm 0.003$ [54]. Nonetheless, the numerical results highlight the strong variability of entrainment in both time and space when stratification and a slope

are present. These affect the structure of the current, and thereby change the mixing patterns along its tail.

4.4.3 Intrusion depth

The intrusion depth H_i is the depth at which the current lifts from the slope. This occurs when the density in the head of the current equals the local density of the ambient fluid. Consistent with [142], this depth is computed as the lowest point at a height $h^* = 0.5cm$ above the slope that reaches a certain threshold concentration value c_{lim}. Naturally, we expect H_i to depend on the stratification. Figure 4.8 shows the spanwise averaged particle concentration at $t = 15$ for various stratifications S, in a configuration based on the experiments by Snow and Sutherland [142]. The dashed line indicates the location of the calculated intrusion depth. Note that the value c_{lim} influences the results more so when the head of the current is diluted, and that the lowest point reached by the current before intrusion can be lower than the intrusion itself due to the inertia of the fluid. Visual representation of the measured intrusion depth is thus important to validate its calculation. The increase in buoyancy frequency, or stratification, leads to a decrease in intrusion depth. The flow intrudes earlier and higher along the slope, it propagates more slowly, and its particle concentration is higher.

For very strong stratification, the current is expected to intrude quickly after release. Under those conditions, the influence of entrainment and particle settling can be neglected, so that we can assume the current density at intrusion to be equal to its initial lock density ρ_1. Omitting the $\tilde{}$, this yields

$$\rho_1 = \rho_T + (\rho_B - \rho_T)\frac{H_i}{H} \ . \tag{4.18}$$

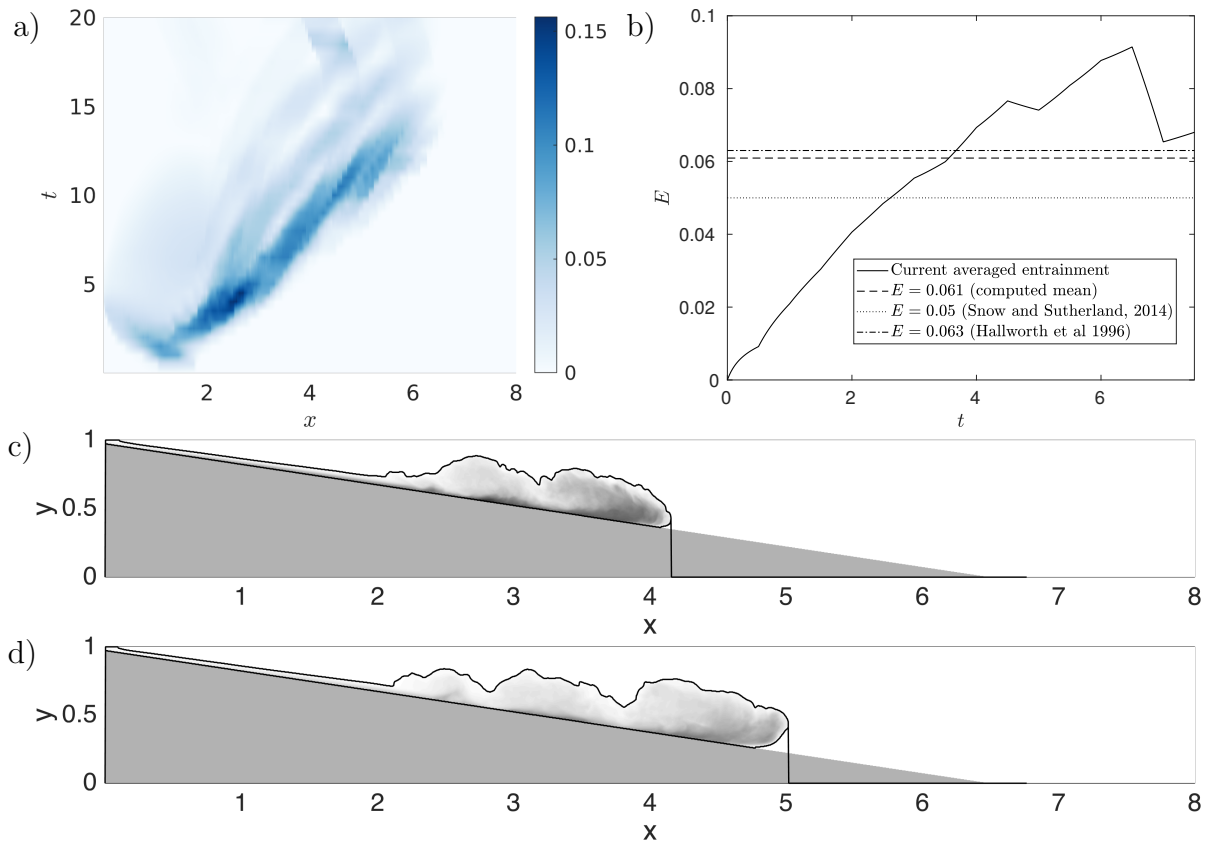

Figure 4.7: ($Re = 15,000$, $v_s = 0.001077$, $m = 0.149$ and $S = 0.176$). a) Entrainment velocity U_e mapped as a function of time and horizontal position . b) Entrainment averaged along the length of the current before intrusion as a function of time . The time averaged value of $E = 0.061$ is plotted and compared to the values of $E = 0.063$ [54] and $E = 0.05$ [142], showing good agreement on average, but highlighting the variability of E with time. Spanwise averaged particle concentration at (c) $t = 6$, and (d) $t = 9$. The concentration contour $c = c_{lim} = 0.01$ is drawn to visualize the envelope of the current, revealing regions of larger entrainment in the body of the current.

This yields an expression for the non-dimensional intrusion depth

$$\frac{H_i}{H} = \frac{\rho_1 - \rho_T}{\rho_B - \rho_T} \ , \tag{4.19}$$

which can be expressed as a function of the stratification such that

$$H_i = \frac{\rho_1 - \rho_T}{\rho_B - \rho_T} = \frac{\rho_1 - \rho_T}{(\rho_B - \rho_T)\frac{h_0}{H}} \frac{h_0}{H} = \frac{1}{S} \cdot \frac{h_0}{H} \ . \tag{4.20}$$

This constitutes a short-descent approximation of the intrusion depth. Applying this relationship to the case of figure 4.8, the intrusion depth H_i as a function of stratification S can be compared to the approximation (figure 4.9a). The short descent approximation matches the simulation results well in trend and quantitatively. The approximation slightly underestimates the intrusion depth for strong stratification, but the difference remains smaller than the thickness of the current itself. Weaker stratifications would lead to longer run-out lengths, which are prohibited by the size of the domain. For the smallest stratification tested however, the short descent approximation overestimates the intrusion depth and is expected to do so as entrainment and settling effects become more important with longer running currents.

Simulation data were also compared to experimental data from Snow and Sutherland [142] and directly plotted against the short descent approximation, in figure 4.9b. The figure shows the relative intrusion depth defined as

$$\frac{\Delta H_i}{h_0} = \frac{H_i - h_0}{h_0} \tag{4.21}$$

as a function of the relative intrusion depth predicted by the short descent approximation. The simulation results show very good agreement with the experiments, and they closely track the short descent approximation for the reference case $Re = 15,000$, $m = 0.0744$,

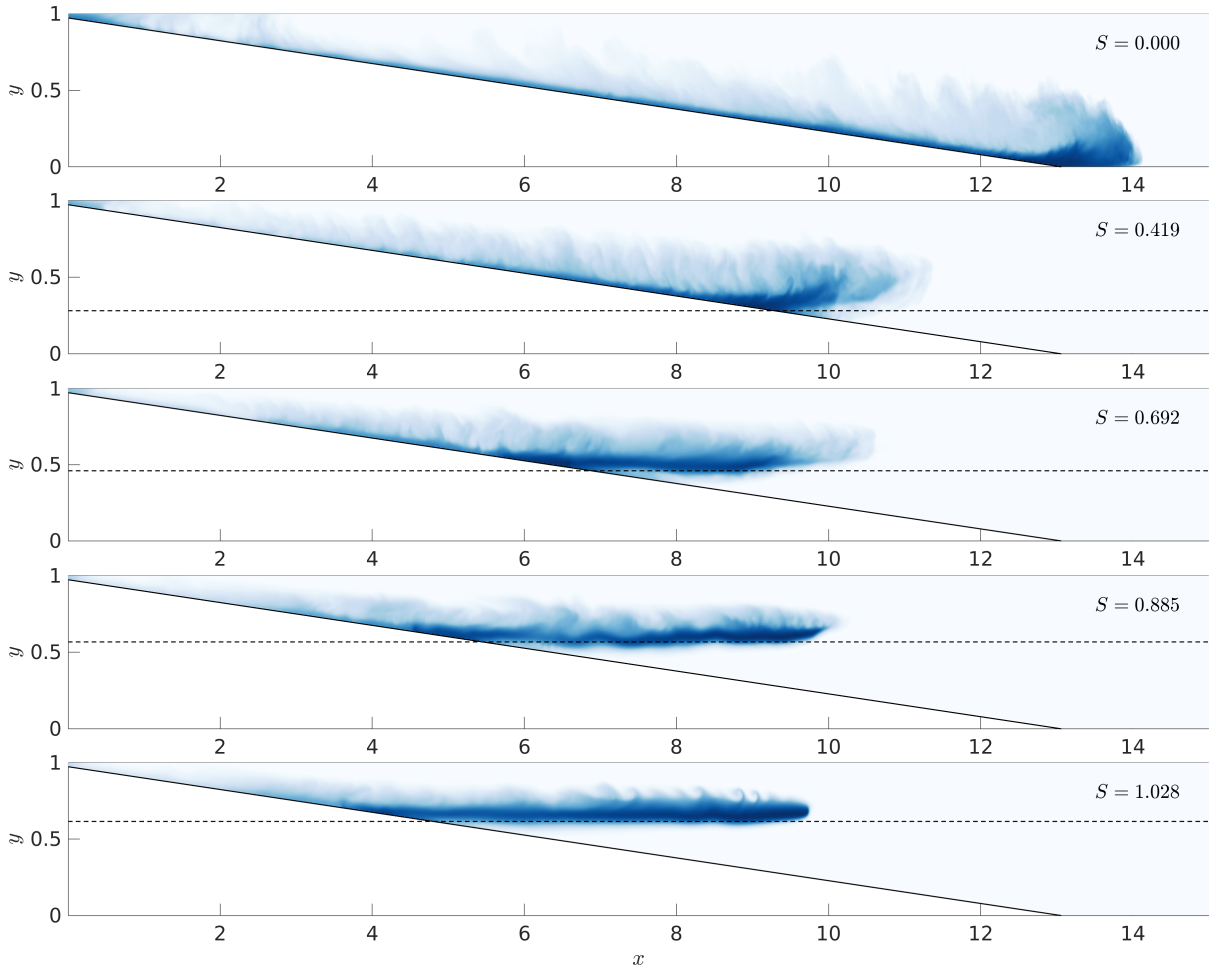

Figure 4.8: $Re = 15,000$, $m = 0.0744$, $v_s = 0.001$, $S = 0.419, 0.692, 0.885, 1.028$. Particle concentration for various stratifications S at $t = 15$. As the stratification is increased, intrusion occurs earlier and at a lower depth in the channel.

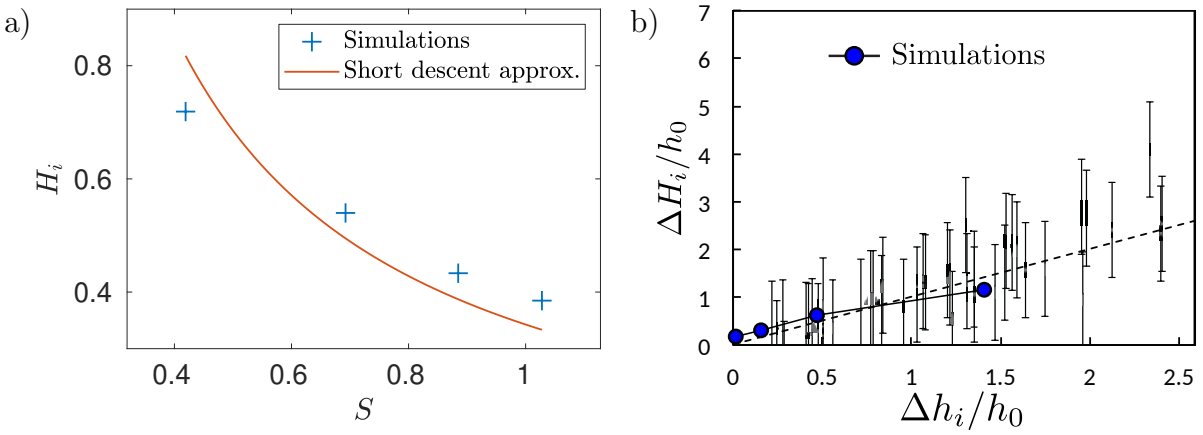

Figure 4.9: $Re = 15,000$, $m = 0.0744$, $v_s = 0.001$, $S = 0.419, 0.692, 0.885, 1.028$. (a) Intrusion depth H_i as a function of stratification S. For such a settling velocity, the short descent approximation agrees very well with simulation results even at moderately large stratification. (b) Relative intrusion depth $\Delta H_i/h_0 = (H_i - h_0)/h_0$ for experimental and numerical data as a function of the predicted relative intrusion depth $\Delta h_i/h_0 = (h_i - h_0)/h_0$ using the short descent approximation. The dashed–line corresponds to perfect agreement. Simulation results are superimposed onto the experimental results of figure 10b of Snow and Sutherland [142] and show close agreement with the short descent approximation, as well as with the experimental data.

$v_s = 0.001$ for all tested stratifications.

Despite the limited size of the numerical domain, long descents - in the sense of large variation in current density - can be investigated through a parametric study of the settling velocity. Figure 4.10 shows the particle concentration at $t = 15$ for various settling velocities v_s. Since the density of the head decreases for higher settling velocities, the flow intrudes earlier and higher along the slope, as marked by the dashed-line.

Below we will compare predictions by the various scaling laws to simulation results. Towards this end, we also recall the long descent scaling law proposed by Snow and Sutherland [142] in the form

$$\left[1 + \frac{E}{2m}\left(\frac{H_i^2}{h_0^2} - 1\right)\right]^{-\gamma-1} = S\frac{H_i}{h_0}, \tag{4.22}$$

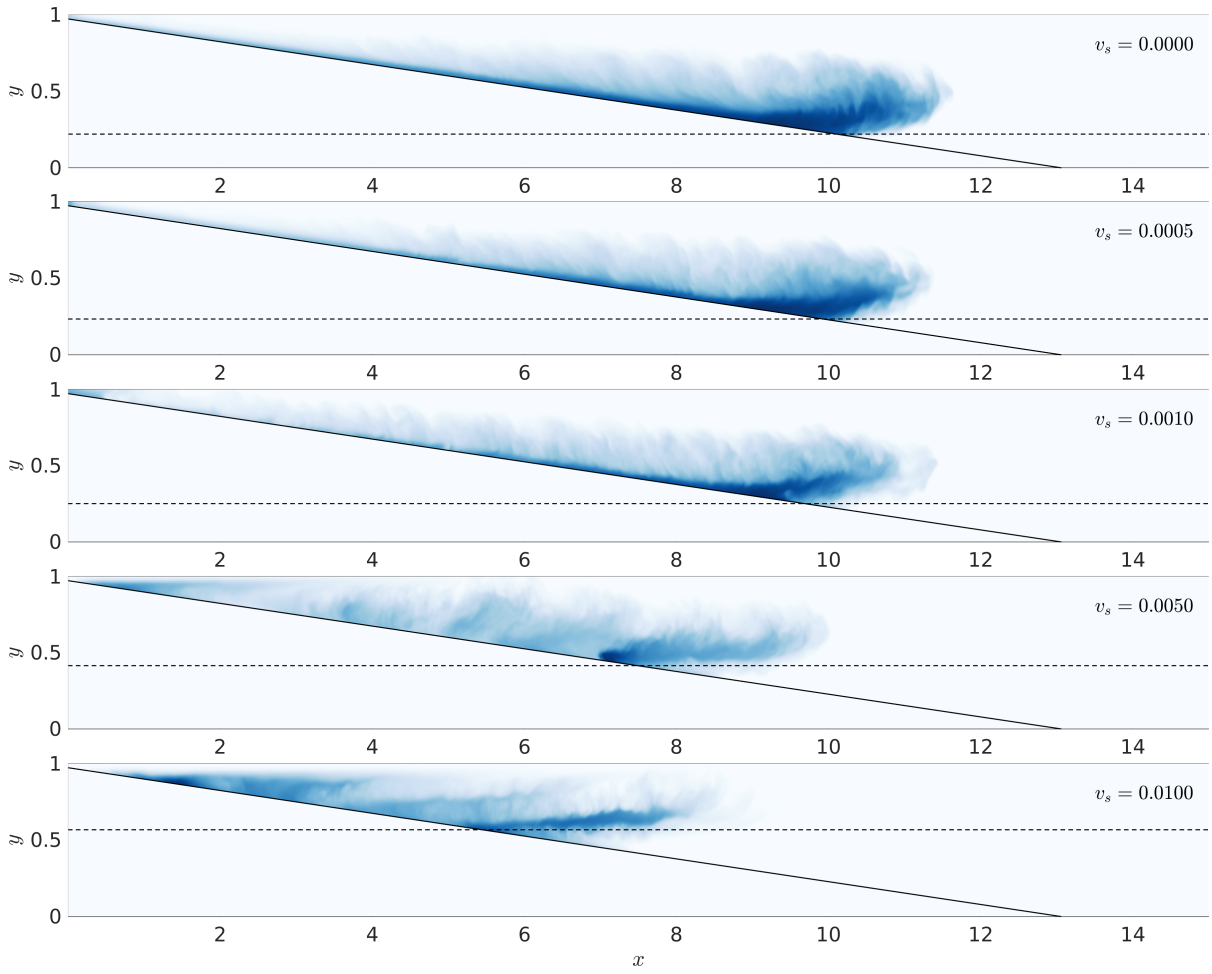

Figure 4.10: $Re = 15,000$, $S = 0.419$, $m = 0.0744$. Particle concentration for various settling velocities v_s at $t = 15$.

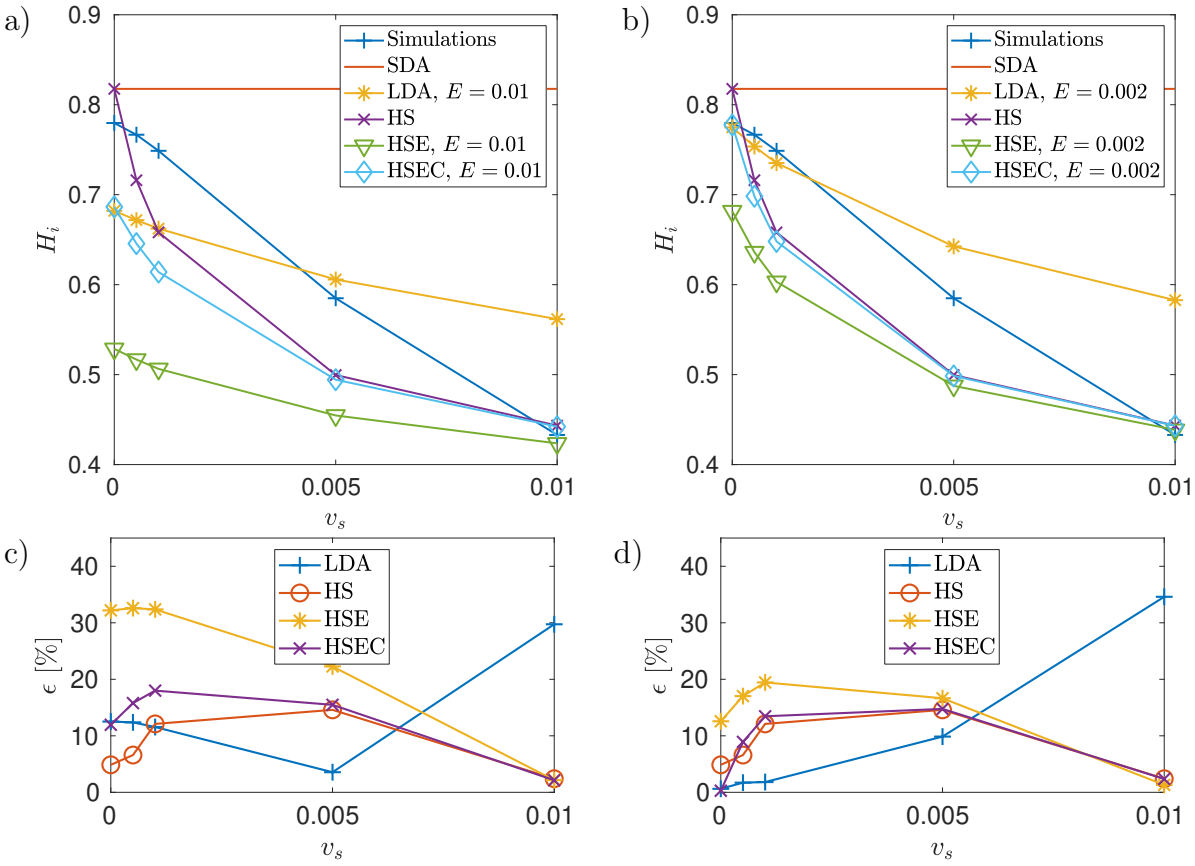

Figure 4.11: $Re = 15,000$, $S = 0.419$, $m = 0.0744$ with (a,c) $E = 0.01$ and (b,d) $E = 0.002$. (a,b): Intrusion depth H_i as a function of the settling velocity v_s. The simulation results are compared to the short descent approximation (SD), the long descent approximation (LDA) introduced by Snow and Sutherland [142], as well as the presented homogeneous settling approximations HS, HSE and HSEC. The LDA, HSE and HSEC are computed using (a) $E = 0.01$ and (b) $E = 0.002$. (c,d) Relative error $\epsilon = \frac{H_i - h_i}{H_i}$ where h_i is the approximation of H_i using LDA, HS, HSE and HSEC

where γ is the ratio of the particle-settling speed to the entrainment speed defined by

$$\gamma = \frac{v_s}{\bar{U}_e} = \frac{v_s}{E \cdot \bar{U}_f} \ . \tag{4.23}$$

In the numerical simulations, we expect settling to have a more dominant effect on the density of the current than entrainment in cases of large settling velocity and small intrusion depth. In the following, we propose two scaling relations for intrusion depth. In the first, we assume a well-mixed current of concentration c and constant volume $V = \frac{h_0 L_l}{2}$, i.e. a purely kinematic model in which entrainment is neglected, so that we have

$$\frac{h_0 L_l}{2}\frac{dc}{dt} = -v_s c L_c \ . \tag{4.24}$$

where $L_c(t)$ is the horizontal length of the current in contact with the slope. With $\bar{U}_f$ the average front velocity before intrusion, we have $L_c(t) \approx L_l + U_f t$ where we recall that L_l is the initial lock-length. For a constant settling velocity and with $c(t=0) = 1$, we thus obtain, by integrating,

$$c(t) = e^{-2\frac{v_s}{h_0}\left(t + \frac{1}{2}\frac{U_f t^2}{L_l}\right)}. \tag{4.25}$$

This is the concentration of the current under the assumption that no entrainment occurs and the volume of the current thus remains constant. The density balance between the ambient fluid and the current at the intrusion depth takes the form

$$\rho_0 + c_{H_i}(\rho_1 - \rho_0) = \rho_T + (\rho_B - \rho_T)\frac{H_i}{H}, \tag{4.26}$$

where $c_{H_i} = c(t_i)$, with t_i being the time to intrusion. This can be related to the average front speed as

$$t_i = \frac{L_c - L_l}{\bar{U}_f} = \frac{H_i - h_0}{\bar{U}_f \tan\theta} \ . \tag{4.27}$$

Here, we use the fact that after the before intrusion, the Froude number Fr is independent of v_s, as shown in 4.4a. Recasting equation 4.26 and introducing 4.27 yields the condition for H_i/h_0

$$e^{-\frac{v_s}{U_f \tan\theta}\left(\left(\frac{H_i}{h_0}\right)^2-1\right)} - \frac{\rho_T-\rho_0}{\rho_1-\rho_0} - \frac{\rho_1-\rho_T}{\rho_1-\rho_0} S\frac{H_i}{h_0} = 0. \tag{4.28}$$

This condition reduces to the short-descent approximation when $v_s = 0$. This equation can then be solved for H_i to give a prediction for the intrusion depth, and it is expected to work best in cases where settling dominates over entrainment in the change in current density.

The second model for intrusion depth incorporates entrainment similarly to [142], but in a way that explicitly separates the contributions of settling and entrainment-driven volume expansion. The change in current volume is given by

$$\frac{dh_c L_c}{dt} = L_c U_e \tag{4.29}$$

where $h_c(t) = h_0/2 + dh_c$ is the current height, which is assumed to be half the initial lock height upon release. Integrating to solve for h_c, we find

$$h_c = \frac{h_0}{2} + \frac{U_e t}{t_l + t}\left(\frac{1}{2}t + t_l\right), \tag{4.30}$$

where $t_l = \frac{L_l}{U_f}$ is defined for convenience. Assuming as previously that the current is homogeneous in concentration, but considering the change in volume due to entrainment, particle mass conservation yields, in terms of the particle mass $m_p = ch_cL_c$,

$$\frac{dm_p}{dt} = -v_s\frac{m_p}{h_c}, \tag{4.31}$$

such that

$$m_p = m_{p,0} e^{-v_s \int_0^t \frac{dt}{h_c(t)}}. \tag{4.32}$$

The particle concentration of the current at time t is thus given by

$$c = \frac{m_p}{m_{p,0}} \frac{h_0 L_l}{2 h_c L_c} = \frac{1}{2} \frac{h_0 t_l e^{-v_s \int_0^t \frac{dt}{h_c(t)}}}{\left[\frac{h_0}{2} + \frac{U_e t}{t_l + t}\left(\frac{1}{2}t + t_l\right)\right][t + t_l]}, \tag{4.33}$$

where we used that $mp_0 = c_0 \frac{h_0 L_l}{2}$ and $c_0 = 1$ is the initial non-dimensional particle concentration in the lock. Note that the numerator can be integrated analytically but the resulting expression is cumbersome to work with, so that the integration is done numerically. At this point, we note that the scaling proposed by [142] does not account for the change in density of the entrained ambient fluid with depth. This assumption can become restrictive when the initial contribution of the particles to the lock-fluid density is comparable to that of the salt in the ambient fluid. We therefore propose one model referred to as HSE (Homogeneous Settling with Entrainment) that assumes that the entrained fluid has density ρ_0 equal to the interstitial density of the fluid as in [142], and one model referred to as HSEC (Homogeneous Settling with Entrainment Corrected) that calculates the density of entrained ambient fluid as a function of current depth. In the former, the intrusion condition is given by equation 4.26 with c given by equation 4.33. In the latter, the interstitial fluid density is a result of both the change in current volume and density of entrained fluid. This density is derived from the salt mass conservation equation

$$\frac{d\rho_i V}{dt} = \bar{U}_e \rho_e L_c, \tag{4.34}$$

where $V = h_c L_c$ is the current volume and ρ_i and ρ_e are the interstitial fluid density within the current and the entrained ambient fluid density respectively. ρ_e is approximated by the density in the ambient at the top of the current head, i.e. the density of the ambient

at depth $L_c \tan\theta - h_0/2$. ρ_e can thus be approximated to leading order as

$$\rho_e = \rho_T + (\rho_B - \rho_T)\frac{L_c \tan\theta - h_0/2}{H} = \rho_T + (\rho_B - \rho_T)\frac{\bar{U}_f t + L_l/2}{H}\tan\theta. \tag{4.35}$$

Integrating equation 4.34 in time yields

$$\rho_i(t) = \frac{1}{V}\left[\rho_{i,0}V_0 + \bar{U}_e\bar{U}_f\left(\rho_T\left(\frac{t^2}{2} + t_l t\right) + (\rho_B - \rho_T)\,U_f t\left(\frac{t^2}{3} + \frac{3tt_l}{4} + \frac{t_l^2}{2}\right)\tan\theta\right)\right].$$

The HSEC intrusion condition therefore becomes

$$\rho_i(t_i) + c_{H_i}(\rho_1 - \rho_0) = \rho_T + (\rho_B - \rho_T)\frac{H_i}{H}. \tag{4.36}$$

Figures 4.11(a,c) and 4.11(b,d) present the computed intrusion depth as a function of settling velocity, the short descent approximation (SD), the so-called homogeneous settling approximation (HS) of equation 4.28 the homogeneous settling approximation with entrainment (HSE), the homogeneous settling approximation with entrainment corrected for entrained fluid density (HSEC) and the long descent approximations (LDA). The intrusion depth for the HSE, HSEC and LDA approximations was computed using a constant entrainment of $E = 0.01$, consistent with [142] for slopes of 0.0744 (figure 4.11(a,c)) and with entrainment of $E = 0.002$ (figure 4.11(b,d))

At $v_s = 0$, the simulations agree well with the short-descent approximation. This corroborates that the numerical setup is effectively made into a long-descent system by means of increasing settling, not by allowing for entrainment to act for long times. The Homogeneous Settling (HS) approximation reduces to the short descent approximation in the absence of settling and agrees well quantitatively with the measured intrusion depth, although it consistently underestimates H_i for moderate settling velocities. The absence of entrainment in this model can lead to an overestimation of the particle-concentration

at the slope which in turns leads to an overestimation of the density loss within the current, hence under-predicting intrusion. The LDA, HSE and HSEC all depend on the entrainment coefficient. For the constant value of $E = 0.01$, the LDA alternatively underestimates and overestimates the intrusion depth depending on the settling velocity, and the evolution of H_i with v_s using the LDA appears to be quasi-linear but does not reproduce the measurements of the numerical simulations. Both the HSE and HSEC agree well with the measurement at $v_s = 0.01$, but underpredict the intrusion depth at lower settling velocities. The HSEC, which accounts for the change in entrained ambient fluid density, performs much better than the HSE approximation, and suggests that the assumption of constant interstitial density made by [142] in the LDA is not always applicable. The results obtained with the LDA, HSE and HSEC suggest that the constant entrainment coefficient of $E = 0.01$ leads to an overestimation of the dilution of the current and thus leads to erroneous predictions of H_i. Quantitatively, the HS and HSEC methods produce errors that are within 20% of the measured intrusion depth for all values of v_s. An entrainment coefficient of $E = 0.002$ (figure 4.11(b,d)) was additionally used and shows far better agreement of all E-dependent predictions. In particular, the LDA leads to a reduced error at small settling velocities but overestimates the intrusion depth at larger settling velocities. At $E = 0.002$, the HSEC yields qualitatively satisfying results over the whole range of tested settling velocities. The results are almost identical to the HS although this is purely coincidental as HSEC depends on both entrainment and density of entrained fluid.

In summary, the case of long descents in the sense of strong settling and low entrainment prove particularly challenging for prediction of the intrusion depth. The LDA is particularly sensitive to the choice of entrainment coefficient E and diverges from the measurements as v_s increases. The HSE reduces to the HS as entrainment approaches zero, but underestimates intrusion depth in all tested cases. The HSEC behaves more

similarly to the measured intrusion depth as settling increases but also depends strongly on entrainment. The simpler approximation HS that neglects entrainment and solely focusses on settling-induced density changes provides robust agreement with the measured data. For practical applications, given a certain front velocity $\bar{U}_f$, lock geometry and slope, the sensitivity of each individual method to the entrainment coefficient should be explored before providing any estimate for the intrusion depth. The HSEC provides an alternative to the LDA which should be further explored with longer-descent, variable slope, numerical simulations.

4.5 Energy budget

Turbidity currents convert potential energy into kinetic energy, which is subsequently dissipated via viscous friction by the resolved small-scale structures of the flow and the unresolved Stokes flow around each settling particle [109]. Numerical simulations allow us to calculate all of these components of the energy budget, so that the effects of slope and stratification on the energy budget can be assessed. We refer to [109] for a comprehensive derivation of the energy budget. As particles settle on a slope, an additional contribution to the energy budget appears in the form of a settled particle potential energy. The average energy conservation equation writes as

$$E_{p,tot} + E_k + L = const., \tag{4.37}$$

where $E_{p,tot}$ is the total potential energy, E_k is the total kinetic energy and L is the total time-integrated losses. The total potential energy is comprised of the potential energies associated with salt (E_p, s), particle concentration (E_p, c) and deposited particles $(E_{p,dep})$

such that $E_{p,tot} = E_p + E_{p,dep} = E_{p,c} + E_{p,s} + E_{p,dep}$, where

$$E_{p,c}(t) = \alpha_c \int_\Omega cy \cdot dV \ , \tag{4.38}$$

$$E_{p,s}(t) = \alpha_s \int_\Omega sy \cdot dV \ , \tag{4.39}$$

$$E_{p,dep}(t) = \alpha_c \int_x \int_z c_{dep}(x,z,t) \cdot y_s(x) dx dz \ . \tag{4.40}$$

The total kinetic energy E_k, is given by

$$E_k(t) = \int_\Omega \frac{1}{2} u_i u_i dV. \tag{4.41}$$

The total loss is $L = L_v + L_s$ is the sum of viscous losses L_v and losses due to the Stokes flow around the settling particles L_s, where

$$L_v(t) = \int_t \epsilon(t) dt \ , \ L_s(t) = \int_t \epsilon_s(t) dt \ , \tag{4.42}$$

and

$$\epsilon = \int_\Omega \frac{2}{Re} s_{ij} s_{ij} dV \ , \ \epsilon_s = \alpha_c v_s \int_\Omega c dV \ . \tag{4.43}$$

To improve readability of the plots, the potential energies are calculated relatively to their initial values, i.e. $\Delta E_{p,i}(t) = E_{p,i}(t) - E_{p,i}(0)$.

For clarity, the energy budget is divided into two steps. First, the overall budget of potential energy variation, kinetic energy variation and losses is presented. Then, the different components of potential energy, kinetic energy and losses are separately plotted. Figure 4.12a represents the overall energy budget associated with a typical set-up ($Re = 15,000$, $S = 0.419$, $m = 0.0744$, $v_s = 0.001$). The overall potential energy steeply decreases at early times as it is converted into kinetic energy. The kinetic energy quickly reaches a maximum and then slowly decreases under the effect of dissipation. It

also decreases as it is converted back into potential energy. Indeed, the current has to lift the linearly stratified ambient fluid, increasing the salt potential energy at the expense of kinetic energy. Note that the overall energy, while not conserved exactly, remains constant to a very good degree.

Note that the potential energy starts increasing at later times ($t > 12$), after the intrusion of the current into the ambient fluid. This can be understood by looking at the potential energy budget components, presented in figure (4.12b). While the potential energy of the particles keeps decreasing, a substantial amount of the lock's initial potential energy is converted back from kinetic energy into potential energy by lifting of the stratified ambient fluid, as mentioned previously. The salt potential energy therefore increases as the current moves down the slope.

Figure 4.12c shows the time evolution of viscous and Stokes dissipation losses. Viscous losses reach a maximum slope during intrusion, indicating a maximum of instantaneous viscous dissipation. Stokes losses due to particle settling account for a small fraction of the total losses at such small settling velocities and appear to be a linear function of time. This emphasises that particle mass at small settling velocities remains almost constant on the time scale leading to intrusion. As pointed out by Necker at al. [109], the proportion of losses due to Stokes dissipation testifies to how much of the initial energy could actually be used to create motion and transport, including mixing and modification of the ambient fluid stratification; and by contrast of how much was lost to particle settling. However, the ratio of viscous to Stokes losses strongly depends on stratification and settling speed, as illustrated in figures 4.12d and 4.12e respectively.

The increase in stratification leads to a decrease in potential energy available for conversion into kinetic energy, and thus to a strong decrease in viscous dissipation (figure 4.12d). Necker et al. [109] observed that the contributions of Stokes and viscous losses in a turbidity current on a flat bottom were approximately the same. This observation does

not hold in the case of a turbidity current down a slope into a stratified ambient fluid. In the critical case of $S \to 1$, the problem reduces to a turbidity current on a flat bottom with stratification and both loss contributions are expected to be of the same order. This is indeed verified for $S = 0.692, 1.028$, but only holds true for this particular settling velocity. The losses as a function of time for various settling velocities are computed with $S = 0.419$ (figure 4.12e). The increase in settling velocity leads to a faster decrease in concentration that translates to a loss of buoyancy forces, kinetic energy and eventually viscous losses. The increase in settling velocity leads to an increase in Stokes losses, as expected, but additionally leads to a non-linear behaviour. This shows that for large settling velocities, the Stokes losses can overcome viscous losses and the mass of suspended particles decreases sufficiently rapidly that Stokes losses decrease noticeably with time. Stokes losses can be estimated by first assuming a constant suspended mass, which is expected to be a valid assumption for flows with small particle settling velocities. This linear model writes as

$$L_{s,lin} = \alpha_c v_s V_{lock} t \ , \tag{4.44}$$

where $V_{lock} = \frac{1}{2} h_0 L_l$ is the initial volume of the lock per unit width at concentration $c = 1$. A second model is proposed where the change in particle concentration is taken into account, following the derivations of the HS intrusion model of equation 4.25. The Stokes losses $L_{s,nl}$ in this model are thus given by

$$L_{s,nl} = \alpha_c V_{lock} v_s \int_0^t \int_\Omega e^{-2\frac{v_s}{h_0}\left(t + \frac{1}{2}\frac{U_f t^2}{L_l}\right)} dV dt. \tag{4.45}$$

The linear and homogeneous settling scaling laws for Stokes losses are plotted against the computed Stokes losses in figure 4.12f. Both are a perfect match at low settling velocities ($v_s = 0.001$), as expected. At larger settling velocities, the linear law fails to

capture changes in suspended mass and therefore overestimates the Stokes losses. The non-linear model yields an excellent match with the measured dissipation, even at the highest settling velocity, thus providing confidence in the ability of the HS model to predict the mean particle concentration within the current.

In summary, in a stratified ambient fluid with sufficiently large settling velocities, dissipation processes are dominated by drag losses on the settling particles. The initial potential energy available for conversion into kinetic energy strongly depends on the settling speed, and Stokes losses can represent the most important source of dissipation, and be the driving mechanism for density change in the current leading up to intrusion.

4.6 Conclusion

The behaviour of turbidity currents down a slope into a stratified ambient fluid was analysed through highly resolved numerical simulations. The general three-dimensional behaviour of the flow was discussed before quantitatively investigating its dynamic properties. Results were compared to experimental data, confirming the ability of numerical simulations to capture the experimentally observed flow dynamics.

The computed front velocity agrees well with experimental results under varying stratification and settling speed. This allows for the introduction of a combined scaling law for the front velocity based on two well known theoretical limits. Numerical data quantitatively matches the new scaling law, so that it can be used to predict the front velocity plateau of more realistic down-slope turbidity currents in a stratified ambient fluid.

Entrainment of ambient fluid into the current was investigated through a time dependent and local approach, allowing for a time and space resolved description of entrainment processes. The entrainment was found to be highly variable with time and over the length

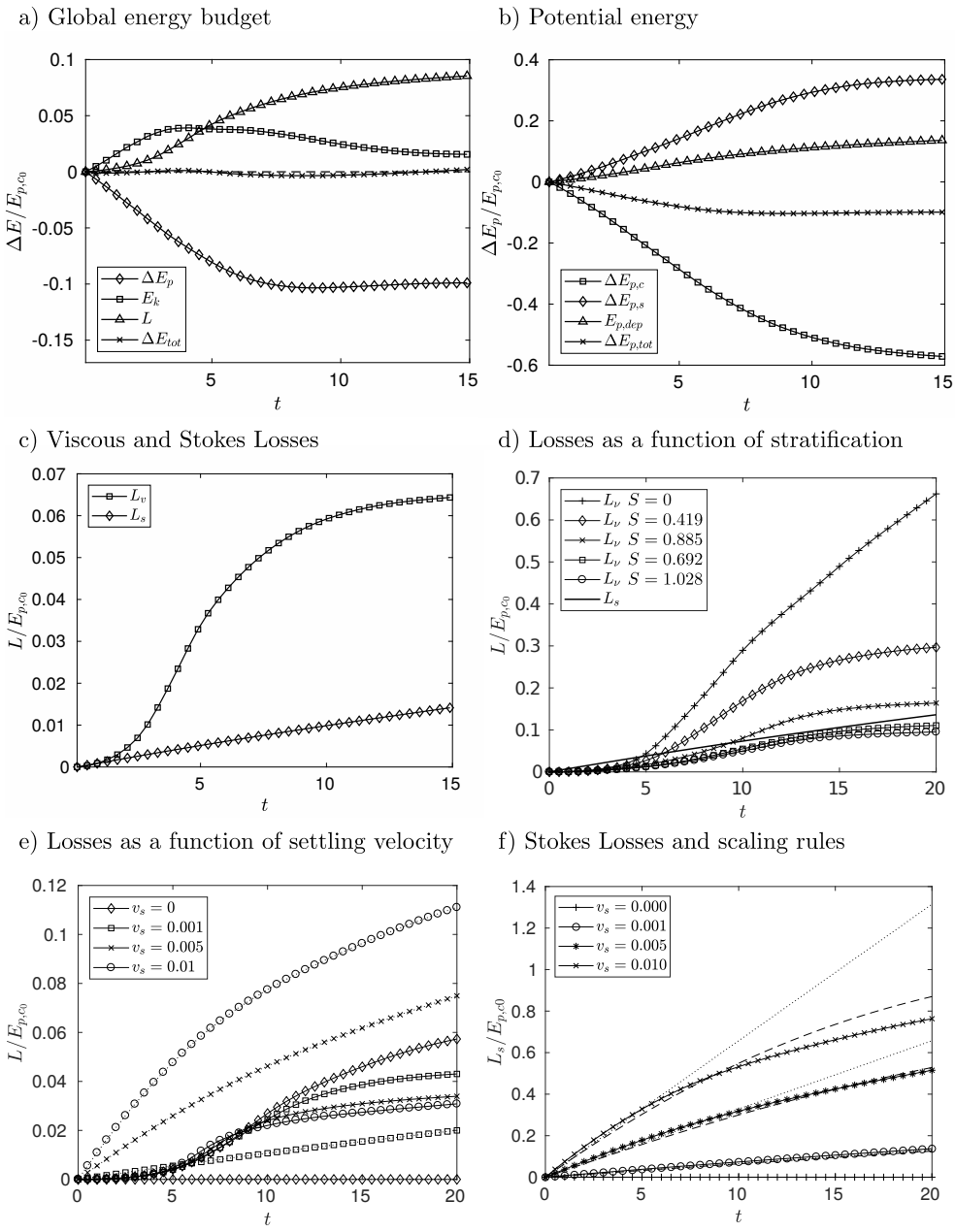

Figure 4.12: Energy budget as a function of time: **[a-c]** ($Re = 15,000$, $S = 0.419$, $v_s = 0.001$, $m = 0.0744$): **a)** Variation of the total, potential and kinetic energy and dissipation losses; **b)** Variation of total, particle, salt and deposited potential energy; **c)** Viscous and Stokes dissipation losses. **d)** ($Re = 15,000$, $S = 0, 0.419, 0.692, 0.885, 1.028$, $v_s = 0.001$, $m = 0.0744$) Viscous and Stokes dissipation losses for various stratifications; **[e-f]** ($Re = 15,000$, $S = 0.419$, $m = 0.0744$, $v_s = 0, 0.001, 0.005, 0.01$) e) Viscous and Stokes dissipation losses for various settling velocities; f) Stokes dissipation losses and settling-driven scaling.

of the current. The local variability relates to large turbulent structures in the head and tail while the space-averaged time dependence relates to the variation in turbulent kinetic energy as the flow develops and then intrudes. Averaged values of the entrainment were found to agree well with experimental data and were an even better match to theoretical results. Both the high variability of entrainment and the ability of numerical simulations to capture it suggest that it should be used as a verification tool in the investigation of intrusion depth rather than a predictable quantity.

The influence of stratification and settling velocity on intrusion depth was analyzed. Numerical results showed very good agreement with the short descent approximation in cases of large stratification and small settling velocities, as expected. High settling scenarios that depart from the constant concentration approximation of the short descent are more challenging to predict. A new scaling law based on the assumption of a homogeneous, constant volume current (HS) was proposed. This model was refined to incorporate entrainment (HSE), but the assumption of a homogeneous current yielded under prediction of the intrusion depth and proved sensitive to the chosen entrainment coefficient. Finally, a model that takes into account the change in density of the entrained ambient fluid (HSEC) was proposed and yielded satisfying results when compared to the measured intrusion depth, particularly for such low-entrainment situations. Sensitivity to entrainment coefficient in low entrainment and high settling scenarios is observed even more strongly using the long-descent approximation (LDA) of [142]. In this context, the HS approximation provides a valuable tool for estimating the intrusion depth solely based on settling. In future work, we hope to see the HSEC applied to longer descent scenarios and compared to the LDA of [142].

The energy budget of the flow highlights the effect of stratification on energy transfer from potential energy into kinetic energy and back into potential energy of the ambient fluid. Stratification directly affects the production of kinetic energy and thus the amount

of viscous dissipation, mixing and finally entrainment that occurs at the current-ambient interface. In high stratification conditions ($S \approx 1$), this means that settling can become the dominant source of energy losses in the propagating current and thus that settling most strongly affects the density of the current prior to intrusion. The HS model for current concentration is applied to predict the Stokes settling losses as a function of time for various settling velocities and is shown to accurately capture the effect of the drop is suspended mass on Stokes losses. This further validates the approach of concentration modelling in the HS approximation, and suggests that inaccuracies in the prediction of the intrusion depth can be attributed to the sensitivity of the model to the entrainment coefficient.

Chapter 5

Mixing of downslope gravity current interacting with internal waves

Authorship of this work is shared with Prof. Nicholas T. Ouellette, Prof. Jeffrey R. Koseff and Prof. Eckart Meiburg. This work has previously appeared in Ouillon et al. [113].

5.1 Introduction

Gravity currents are density-driven flows that propagate primarily in the horizontal direction. They play an important role in a host of environmental settings, as well as in a wide range of engineering applications [137, 164]. In constant-density environments, gravity currents commonly advance along top or bottom boundaries. When the ambient density field is stratified, on the other hand, gravity currents can also take the form of intrusions that propagate horizontally at intermediate heights. In geophysical applications, ambient density stratification most often is the result of temperature and salinity variations, such as in lakes and oceans [152]. The ability of stratified ambients to sustain

internal waves can then give rise to a broad range of complex interactions between gravity currents, intrusions and internal waves [41, 95, 98, 99, 30, 61, 62]. Maxworthy et al. [98] demonstrated that a gravity current released in a linearly stratified ambient fluid could, under certain circumstances, come to a stop as the waves generated by the release of the current catch up with the head of the current. The entrainment of ambient fluid through turbulent mixing frequently modifies the gravity current density by diluting it, thereby further complicating its dynamics [38, 161, 54, 109, 28].

When gravity currents flow down a slope within a continuously stratified environment, they typically intrude horizontally at their point of neutral buoyancy [7, 142, 15]. Intrusions at intermediate depths were also observed in the large-scale simulations of Marques et al. [97], which considered gravity currents propagating downslope into quiescent stratified ambients. The authors found that flow-splitting, a process in which partially mixed current fluid forms a horizontal intrusion while denser current fluid continues down the slope as a hyperpycnal current, is susceptible to occur in weakly stratified environments such as Arctic outflows. On the other hand, if the ambient consists of two constant-density layers, with a jump in the density at the interface, and if the current is denser than both of these layers, it will split into a neutrally buoyant intrusion of diluted fluid that propagates along the interface and a hyperpycnal bottom current that continues to move down the slope at a reduced velocity [129, 103, 30]. Of particular interest in the present context are gravity currents formed by the discharge of concentrated brine from desalination plants [40, 60]. Understanding the mixing of this brine under the influence of the near-coastal internal wave field, along with its transport into deeper water, is important for assessing its ecological impact on the coastal ocean environment.

Mindful of the importance of internal wave dynamics on limnology [105], Fischer and Smith [41] over the course of two fourteen-day experiments injected dye into a dense stream entering Lake Mead in order to investigate the transport of nutrients. They

found substantial amounts of the dye at the lake surface, despite theoretical predictions that the dense fluid from the stream should form a hyperpycnal current intruding at the thermocline. Without providing a detailed explanation, the authors hypothesized that large amplitude internal waves measured during the experiments might have interacted with the bottom current, thereby modifying the transport of the dense stream fluid.

Recent laboratory experiments by Hogg et al. [62] have unraveled some of the physics governing gravity current-wave interactions at a density interface. Using the tank apparatus sketched in figure 5.1, the authors initiated the gravity current and internal wave via lock-release, and subsequently studied their collision where the pycnocline meets the slope. Holding the gravity current properties constant, the authors observed a strong reduction of the gravity current mass flux for increasing wave amplitudes. Hogg et al. [62] furthermore identified a decapitation process by which the internal wave removes part of the gravity current head from its body and transports it upslope. The process differs from both detrainment and entrainment processes expected to take place in a downslope dense flow in the gravity current regime [8]. The gravity current regime is observed in the case of a dense current propagating down a gentle slope and is characterized by detrainment of dense fluid into the ambient and to a lesser extent entrainment of ambient fluid into the current, thus affecting its density [8]. In the experiments of Hogg et al. [62], the ambient fluid is stratified with a sharp pycnocline separating two homogeneous layers, such that entrainment affects the proportion of the gravity current fluid forming an intrusion at the density interface. The "decapitation" process generates mixing between the current fluid and dense ambient fluid through a new mechanism not accounted for by detrainment, entrainment or flow-splitting, further motivating a detailed analysis of its dynamics.

The current investigation analyzes and quantifies the energetics and mixing dynamics of the above current-wave interaction in depth via direct numerical simulations, and it

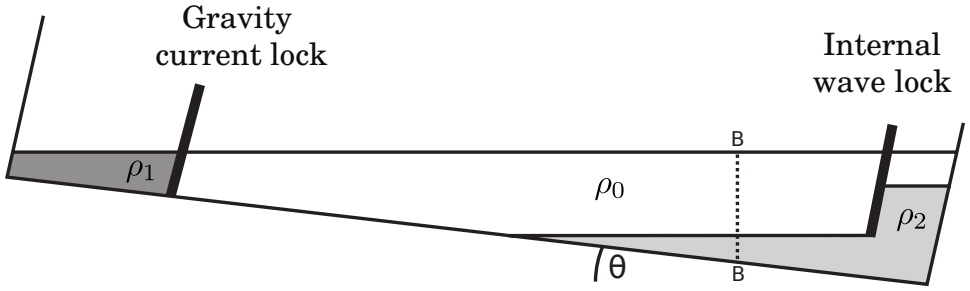

Figure 5.1: Schematic of the apparatus employed in the experiments of Hogg et al. [62]. Both the gravity current and the internal wave are initiated via lock-release. The vertical interrogation plane is shown by the dotted line.

explores its dependence on the governing dimensionless parameters. Section 2 presents the flow configuration and discusses the governing equations, along with the characteristic scales and the computational approach. Section 3 focuses on the analysis of the flow physics, beginning with the gravity current mass flux reduction as a result of the interfacial wave. The splitting of the original gravity current into an intrusion and a hyperpycnal flow is analyzed, along with the propagation velocities of the two resulting fronts. The existence of two separate parameter regimes is demonstrated, governed by distinctly different dynamics. A detailed investigation of the decapitation phenomenon follows, particularly with regard to how it contributes to the mixing of the gravity current and ambient fluids. The implications of the current-wave interaction on the various components of the overall energy budget are discussed, including viscous dissipation. Finally, the loss of available potential energy as a result of the irreversible mixing associated with the current-wave interaction is quantified. Section 4 summarizes the key findings and presents the main conclusions of the work.

5.2 Numerical set-up and governing equations

The initial configuration of the simulations is shown in figure 7.1. A lock with scalar concentration c_1 and volume V_1 is separated from the ambient by a virtual gate. The

lower, denser region of the two-layer ambient has an initial scalar concentration c_2 and volume V_2, while there is no scalar in the upper ambient region. The denser ambient is raised to a height h_u over a length l_w from the right wall whilst keeping the volume V_2 constant, causing the left part of the ambient to be lowered to height h_l. The height difference between the two parts of the dense ambient is $h_w = h_u - h_l$. The ratio of wave height to wave length h_w/l_w is referred to as the wave Froude number Fr [62]. This definition of the Froude number follows from the classical definition $U_w/\sqrt{g'_w h_w}$, where U_w denotes the wave speed and $g'_w = g\frac{\rho_2-\rho_0}{\rho_0}$, and involves using scales appropriate to the experimental setup. From wave theory we can show that $U_w \sim h_w\omega$ where ω is the wave frequency, and $\omega \sim \sqrt{h_w/D}$, where D is the depth of the dense fluid from the two-layer interface to the bottom floor. Since D is not constant but rather changes in space as the wave propagates, we use l_w which is comparable to D in the experiments, and which reflects the wavelength of the released wave. Given that l_w is a reasonable surrogate for the depth, then $U_w \sim h_w\sqrt{g'_w/l_w}$, where g'_w. The celerity associated with the wave propagation then becomes $c \approx \sqrt{g'_w l_w}$. Substituting all of this into the definition of the wave Froude number thus gives us $U_w/c \sim h_w\sqrt{g'_w/l_w}/\sqrt{g'_w l_w} = h_w/l_w$.

5.2.1 Dimensional governing equations

We solve the three-dimensional, unsteady Navier-Stokes equations for incompressible flows in the Boussinesq limit, since density changes due to salt or temperature variations are typically small in applications of interest. The scalar concentration field is governed

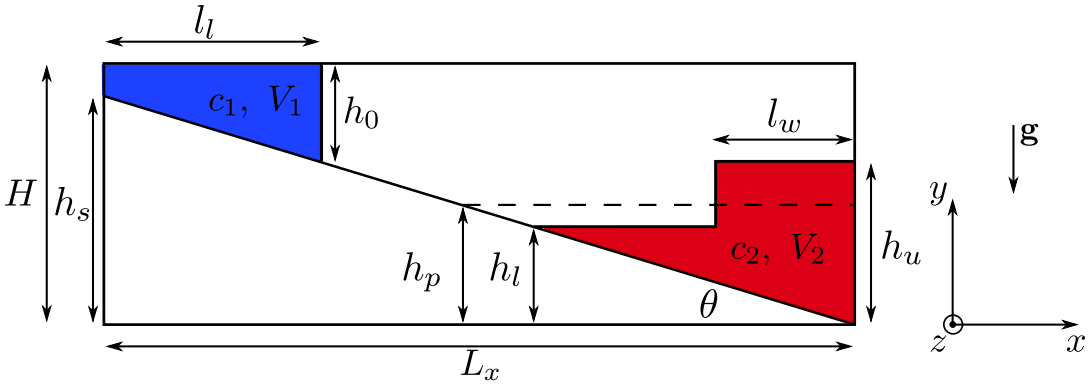

Figure 5.2: Initial set-up for studying the interaction between a lock-release gravity current and an interfacial wave. $c_1 = 1$ and $c_2 < 1$ are the initial concentrations of the lock fluid and the dense ambient fluid, respectively. V_1 and V_2 indicate the volumes of lock fluid and dense ambient fluid. At $t = 0$ the lock is released and the gravity current begins to move down the slope. At $t = t_1$ the wave lock is released and the wave starts propagating towards the slope.

by an advection-diffusion equation. The dimensional equations are given by

$$\nabla \cdot \mathbf{u} = 0 \ , \tag{5.1}$$

$$\frac{\partial \mathbf{u}}{\partial t} + (\mathbf{u} \cdot \nabla)\, \mathbf{u} = -\frac{1}{\rho_0}\nabla p + \nu \Delta \mathbf{u} + \frac{\rho - \rho_0}{\rho_0}\mathbf{g} \ , \tag{5.2}$$

$$\frac{\partial c_i}{\partial t} + \mathbf{u} \cdot \nabla c_i = \kappa_c \Delta c_i, \ \ i = \{c, w\} \ , \tag{5.3}$$

where $\mathbf{u}$ denotes the velocity vector, p represents pressure, ρ indicates the local density with the fresh water density ρ_0 serving as a reference value, and c_c and c_w are the salinity concentrations of the current and wave fluid, respectively. Note that two distinct scalar fields are defined for the current and ambient salinities, so that we can easily keep track of each fluid, similarly to what is accomplished in the experiments by adding dyes. The kinematic viscosity of water is assumed to be constant at $\nu = 10^{-6} m^2/s$. Since the influence of the scalar diffusivity κ_c on the propagation velocity of a gravity current is small as long as $\kappa_c \leq \nu$, we choose $\kappa_c = \nu$ for simplicity [57, 109, 23]. How this assumption might affect long-term observations of irreversible mixing in the flow will be discussed in

section 8.5. The gravitational acceleration is given by $\mathbf{g} = -g\mathbf{e}_y$. The density depends linearly on the salinity such that

$$\rho = \rho_0 \left(1 + \alpha c_c + \alpha c_w\right), \tag{5.4}$$

where $\alpha = \partial\rho/\partial c = \text{cst.}$ denotes the expansion coefficient.

5.2.2 Characteristic quantities and nondimensional equations

The lock height h_0 is used as a reference length, since it directly affects the propagation velocity of the gravity current. The reference concentration is chosen as the initial concentration of the lock $c_c(t = 0) = c_1$. A buoyancy velocity based on the initial density difference between the lock and the ambient fluid is used to define the velocity scale

$$u_b = \sqrt{\frac{\rho_1 - \rho_0}{\rho_0} g h_0}\ , \tag{5.5}$$

where $\rho_1 = \rho_0 \left(1 + \alpha c_1\right)$ is the density of the gravity current fluid initially contained behind the lock and ρ_0 is the density of the upper ambient fluid (figure 5.1). This defines our reference time scale $T = \frac{h_0}{u_b}$. The dimensional variables (left) are then made non-dimensional (right) as follows

$$\mathbf{x} \rightarrow \mathbf{x} h_0\ , \tag{5.6}$$

$$\mathbf{u} \rightarrow \mathbf{u} u_b\ , \tag{5.7}$$

$$t \rightarrow tT\ , \tag{5.8}$$

$$p \rightarrow p \rho_0 u_b^2\ , \tag{5.9}$$

$$c_i \rightarrow c_i c_1,\ i = \{c, w\}\ . \tag{5.10}$$

This yields the non-dimensional form of the governing equations

$$\nabla \cdot \mathbf{u} = 0 \ , \tag{5.11}$$

$$\frac{\partial \mathbf{u}}{\partial t} + (\mathbf{u} \cdot \nabla)\, \mathbf{u} = -\nabla p + \frac{1}{Re}\Delta \mathbf{u} - (c_c + c_w)\mathbf{e}_y \ , \tag{5.12}$$

$$\frac{\partial c_i}{\partial t} + \mathbf{u} \cdot \nabla c_i = \frac{1}{Pe}\Delta c_i, \ i = c, w \ , \tag{5.13}$$

where $Re = \frac{u_b h_0}{\nu}$ is the Reynolds number and $Pe = ReSc$ is the Peclet number, with $Sc = \frac{\nu}{\kappa_c}$ being the Schmidt number. As mentioned previously, the Schmidt number is set to unity. Slip boundary conditions are employed at the top and right walls, and periodic conditions are used in the spanwise direction. No-slip conditions are applied at the left wall and on the slope ($\mathbf{u}_{|\Gamma_s} = 0$). The width $L_z/H = 0.2$ of the domain is chosen sufficiently large so that the three-dimensional lobe and cleft instability can develop in the spanwise direction. No-flux boundary conditions are applied at all boundaries for the salinity.

5.2.3 Numerical method

The equations are solved by our direct immersed boundary method (IBM) code, originally developed under the name TURBINS [106]. The immersed boundary method is employed to impose the no-slip condition on the slope [101, 106, 76]. A small random perturbation is added to the u-component of the velocity field at $t = 0$, in order to facilitate the three-dimensional evolution of the flow. The computational domain is discretized by $(N_x \times N_y \times N_z) = (3000 \times 300 \times 30)$ cells, corresponding to a grid size of $\Delta x/H = \Delta y/H = \Delta z/2H = 0.0033$. The higher resolution in the x, y-plane is employed to ensure mass conservation at the immersed boundary.

Sim.	c_2	h_0/H	L_x/H	L_z/H	l_l/H	l_w/H	h_s/H	h_p/H	h_u/H	h_w/H	Re	Fr
m0 (nw)	0.8	0.31	10.0	0.2	2.405	1.287	0.915	0.568	0.568	0.0	3,200	0.0
m1	0.8	0.31	10.0	0.2	2.405	1.287	0.915	0.568	0.618	0.05	3,200	0.0389
m2	0.8	0.31	10.0	0.2	2.405	1.287	0.915	0.568	0.693	0.125	3,200	0.0971

Table 5.1: Simulation parameters employed to investigate the influence of the dimensionless wave height on the current fluid mass flux. (nw) denotes the absence of a wave.

Sim.	c_2/c_1	h_0/H	L_x/H	L_z/H	l_l/H	l_w/H	h_s/H	h_l/H	h_u/H	h_w/H	Re	Fr
p0 (nw)	0.8	0.31	10.0	0.2	2.405	1.287	0.915	0.576	0.576	0.0	3,200	0.0
p1	0.8	0.31	10.0	0.2	2.405	1.287	0.915	0.5655	0.6155	0.05	3,200	0.039
p2	0.8	0.31	10.0	0.2	2.405	1.287	0.915	0.5510	0.6760	0.125	3,200	0.097
p3	0.8	0.31	10.0	0.2	2.405	1.287	0.915	0.5464	0.6964	0.15	3,200	0.117
p4	0.8	0.31	10.0	0.2	2.405	1.287	0.915	0.5376	0.7376	0.2	3,200	0.155
p5	0.8	0.31	10.0	0.2	2.405	1.287	0.915	0.5293	0.7793	0.25	3,200	0.194
p6 (exp)	0.8	0.31	10.0	0.2	2.405	1.287	0.915	0.5233	0.8113	0.288	3,200	0.224
p7	0.8	0.31	10.0	0.2	2.405	1.287	0.915	0.5070	0.9070	0.4	3,200	0.311

Table 5.2: Simulation parameters employed to investigate the influence of the dimensionless wave height on the current-wave interaction. Simulation p6 precisely reproduces the experimental setup. The no-wave case (nw) of simulation p0 serves as reference case for quantifying the effect of the wave on mixing.

5.3 Results

5.3.1 Simulation parameters

We conduct direct numerical simulations (DNS) for the dimensionless parameter combinations listed in tables 5.1 and 5.2. Table 5.1 describes the simulations conducted to investigate the evolution of mass flux with wave height, while keeping the lower pycnocline at a constant vertical position $h_l/H = 0.568$. This is done to guarantee that the mass flux interrogation planes are equally distant from the point of contact between the slope and the pycnocline across simulations. Table 5.2 describes the parametric study of the influence of the wave height on the current-wave interaction. In these simulations the volume of the dense ambient is kept constant, in order to keep the initial background potential energy constant, cf. the discussion in section 5.3.4. Simulation p6 corresponds precisely to the experimental configuration of Hogg et al. [62].

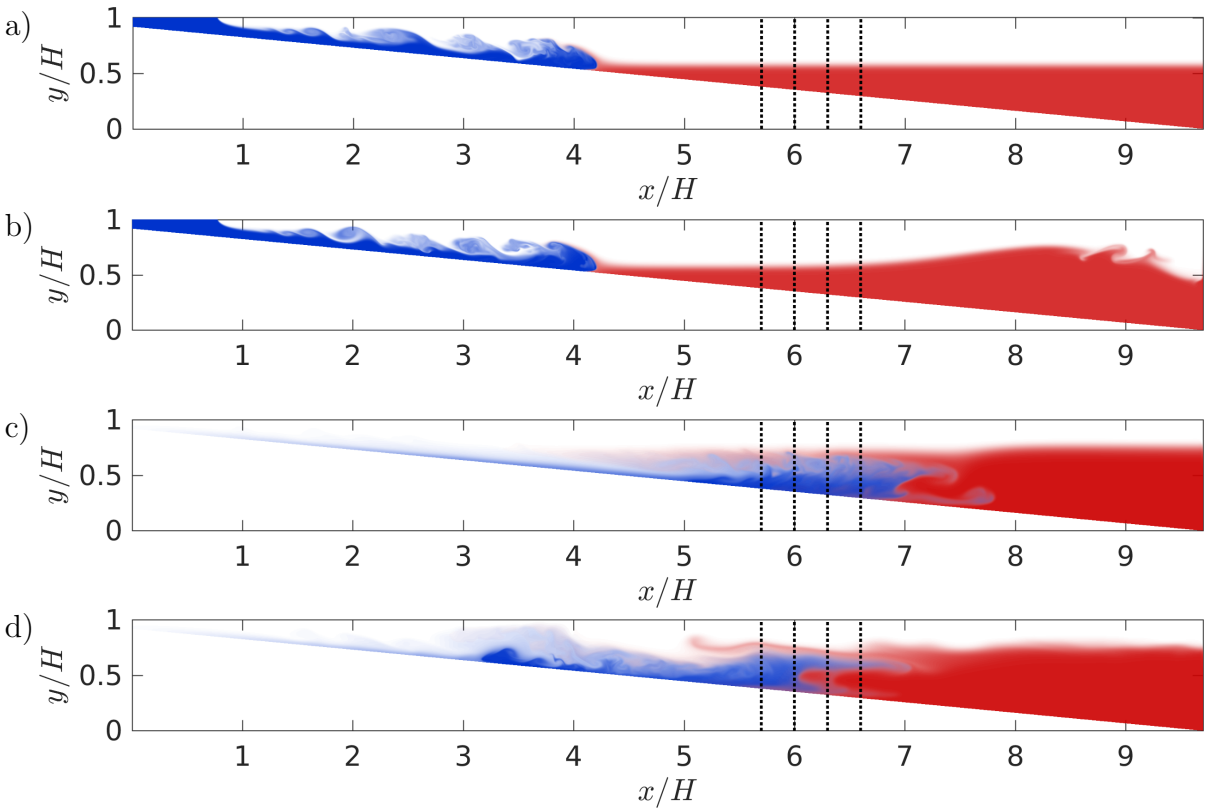

Figure 5.3: Snapshots of the gravity current concentration c_c (blue) superimposed with the lower ambient fluid concentration c_w (red) at $t/T = 12.17$ (a,b) and $t/T = 43.45$ (c,d) without (a,c) and with (b,d) an incoming wave ($Fr = 0.224$). The gravity current begins to interact with the dense bottom layer even before the wave reaches the slope. The dashed vertical lines correspond to the locations $x = x_b$ where the mass flux is evaluated.

5.3.2 Mass flux

In the following, we compare gravity current mass flux data with corresponding experimental results of [62]. Towards this end, we calculate the spanwise averaged mass flux of gravity current fluid at the four interrogation planes $x_b/H = 5.7$, 6.0, 6.3 and 6.6, as shown in figure 5.3. These locations correspond to points on the slope below the ambient pycnocline, so that the mass flux data capture both that fraction of the gravity current fluid which has penetrated through the pycnocline, as well as the fraction that is transported as an intrusion along the pycnocline. Given the statistically two-dimensional

nature of the flow, this corresponds to taking ensemble averages. The mass flux is thus calculated as

$$\dot{m} = \int_0^{L_z} \int_{y_s(x_b)}^{H} uc_c \, dydz \ , \tag{5.14}$$

where $y_s(x_b)$ indicates the vertical coordinate of the slope at the location x_b of the interrogation plane. We normalize the mass flux based on the observation that a lock-exchange gravity current propagating on a flat surface has a height close to half the lock height, and a front velocity $U_f \approx \frac{1}{2}u_b$ during the slumping phase [11, 72, 136, 18].

Normalized mass flux data are shown as functions of time in figure 5.4. Further upstream interrogation planes see higher peak mass fluxes, which reflects the significant slowdown of the gravity current as it encounters the dense lower ambient fluid. The presence of a wave reduces the mass flux, consistent with the observations of Hogg et al. [62].

Figure 5.4 furthermore indicates that the arrival of the gravity current fluid at the interrogation planes is delayed in the presence of a large wave. The energetics of this process will be analyzed in detail below. To distinguish the hyperpycnal component of the gravity current mass flux from the intrusion component, we calculate the time-averaged value $\langle uc_c(y)\rangle_\tau$ over the averaging window $\tau \in [t_p, t_{end}]$ at a $x_b = 7$. Here, t_p corresponds to the time at which the current reaches the interrogation plane, and t_{end} is chosen so as to avoid any influence from waves reflected by the right boundary of the computational domain. The profiles shown in figure 5.5a exhibit two maxima, one close to the slope, and the other one near the pycnocline. The former is associated with the hyperpycnal current component, while the latter reflects the intrusion part. The simulations indicate that both with and without a wave, the gravity current fluid transport is dominated by the intrusion component. Consistent with the observations of Hogg et al. [62], large waves are found to reduce the hyperpycnal flux component substantially. By associating the mass flux

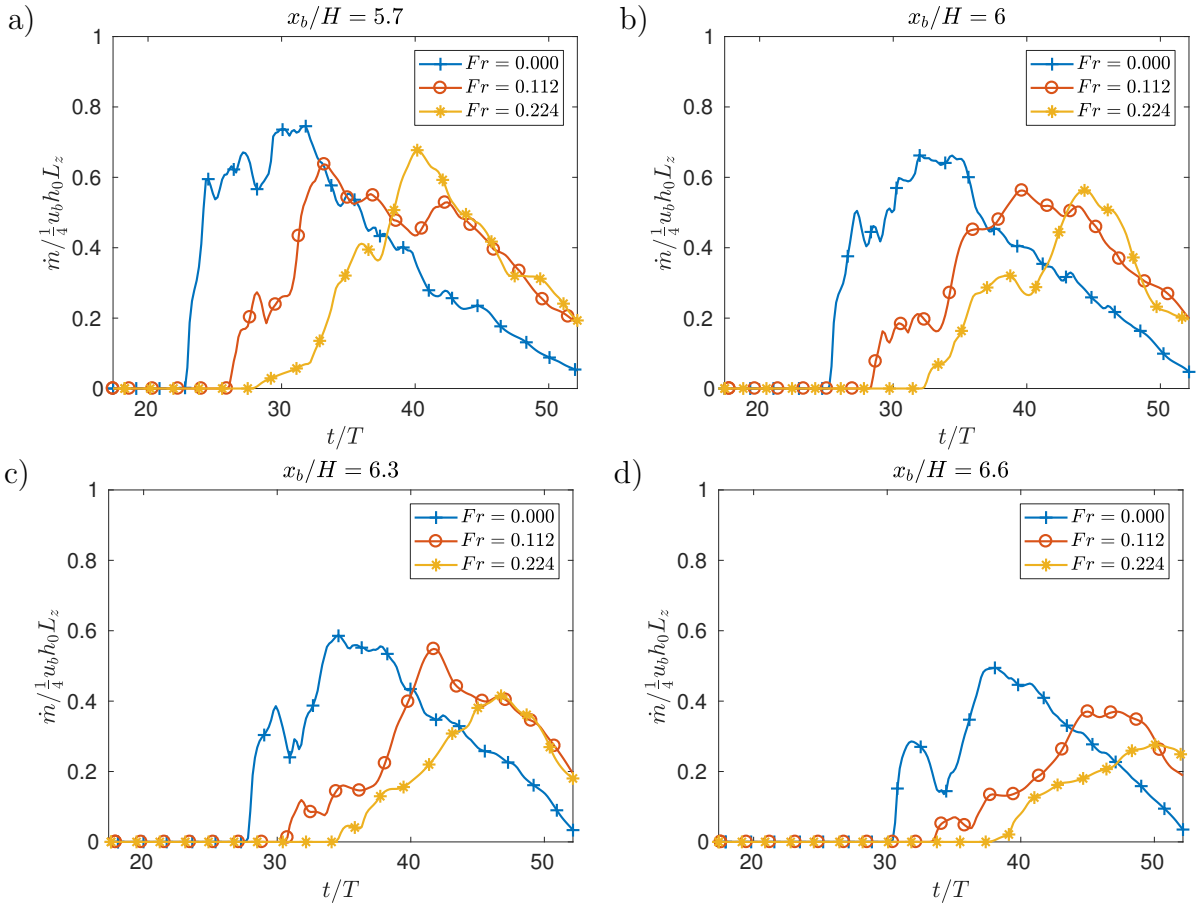

Figure 5.4: Mass flux as a function of time at interogation planes (a) $x_f/H = 5.7$, (b) $x_f/H = 6$, (c) $x_f/H = 6.3$, (d) $x_f/H = 6.6$. All locations are past the point where the pycnocline reaches the slope, and therefore reflect the ability of the current to penetrate the pycnocline for various wave sizes. The transport of gravity current fluid is both reduced and delayed by the wave.

above (below) the local minimum in the vertical profile with the intrusion (hyperpycnal current), we can quantify the two components. The results shown in figure 5.5b confirm that for the present density ratio of $c_2/c_1 = 0.8$, the gravity current fluid transport is dominated by the intrusion. The horizontal distance between the lock and the point of interaction at the pycnocline controls the amount of entrainment that occurs within the current and will therefore impact the proportion of fluid that forms the intrusion. This distance is kept constant in the mass-flux simulations and thus the entrainment prior to reaching the pycnocline remains the same across simulations, thus isolating the effect of the wave in the mass-flux calculations. Furthermore, it is evident that both the intrusive and the hyperpycnal components are reduced by the wave. Hogg et al. [62] observed a reduction of the mass flux of up to 40% for a wave with Froude number $Fr = 0.224$. The present simulations yield comparable values of 36% ($Fr = 0.112$) and 50% ($Fr = 0.224$) for the total mass flux. For the hyperpycnal component only, reductions of 45% and 75% are obtained. Thus, the current-wave interaction not only changes the overall mass flux of the gravity current into the ambient fluid, but it also redistributes these fluxes towards the intrusion. The change in mass flux depends strongly on the timing of the wave release, i.e. on $t_1 - t_0$. The effect of t_1 is not analysed systematically in this numerical study as it was previously explored in the experimental work of Hogg et al. [62]. In the experiments, the timing was adjusted to yield a maximum effect of the wave on the propagation of the current, and the value of $t_1 - t_0$ was replicated directly in the simulations. In order to obtain insight into the mechanisms responsible for these observations, we will in the following focus on the detailed dynamics of the current-wave interaction, including its energetics.

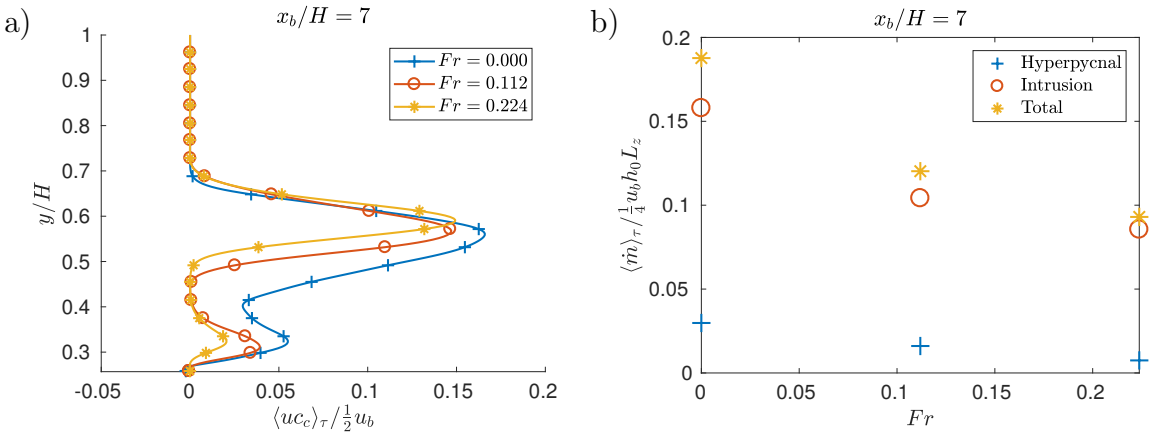

Figure 5.5: (a) Time-averaged profile of the horizontal flux of gravity current fluid uc_c as a function of y. (b) Discrete contributions of the hyperpycnal and intrusive gravity current to the total time averaged mass flux as a function of the wave Froude number. The averaging window is $t/T \in [t_p/T, 52.14]$, i.e from the beginning of the intrusion to the end of the numerical simulation.

5.3.3 The decapitation phenomenon

A striking feature of the current-wave interaction brought to light by the experiments of Hogg et al. [62] occurs when the current and the wave arrive simultaneously at the location where the pycnocline meets the slope, as shown in figure 5.6. As the current and the wave collide, the head of the current slows to a halt and lifts off the slope. A fraction of the horizontal momentum carried by the wave and the current is converted into vertical momentum, and part of the current is reflected upslope. The remainder of the current's body regenerates a head and continues moving downslope as a hyperpycnal current, while partially mixed gravity current fluid forms an intrusion that propagates horizontally along the pycnocline. The distinction between the hyperpycnal component and intrusive flow is most obvious some distance downslope from the initial point of interaction, as seen in figure 5.6. Due to inertia, the current is initially able to penetrate past the pycnocline before separation occurs. This complex interaction mechanism occurs only for sufficiently large waves, whereas for smaller waves the current merely slows down while retaining its initial head shape. This reflects the strong dependence of the current-wave interaction

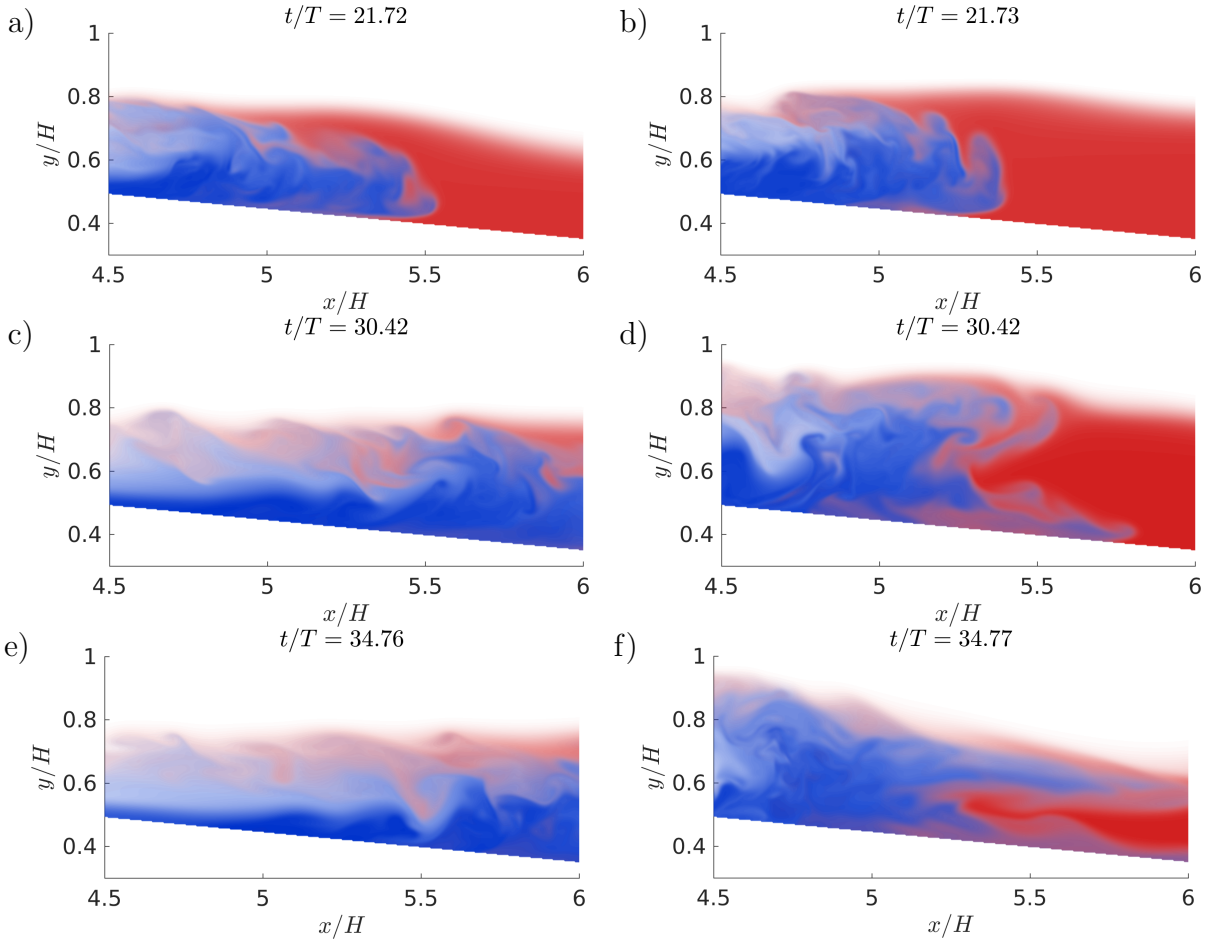

Figure 5.6: Snapshots of the gravity current concentration c_c superimposed with the lower ambient fluid concentration c_w at various times. Results are shown without (a,c,e) and with (b,d,f) an incoming wave at $Fr = 0.224$. In the presence of a strong wave (right column) the gravity current head lifts off the slope and is partially reflected upstream.

and the associated mixing on the wave height.

Closer inspection of the flow field at the location of the current-wave interaction reveals a key dynamic of the decapitation process. In the absence of a wave, the current pierces the pycnocline and maintains its downslope direction, although it loses some of its forward momentum. Strong entrainment and mixing take place along the sheared interface between the current and the ambient. This mixed fluid subsequently forms an intrusion that propagates horizontally in the ambient, as observed in figure 5.3c. Note

that while the initial concentration $c_w(t = 0) = c_2$ in the lower part of the ambient is smaller than that of the lock $c_c(t = 0) = c_1$, with $c_2/c_1 = 0.8$, strong mixing has reduced the concentration of the current head by the time it reaches the pycnocline.

In the presence of a strong wave, this picture changes drastically. Upon contact with the wave at $t/T = 22.60$, much of the gravity current head is lifted from the slope. A strong recirculation zone forms behind the head, and the current fluid splits into a downslope hyperpycnal flow, an upstream propagating reflected current, and an intrusion that moves along the pycnocline. The long term evolution is observed in figure 5.3d.

Figure 5.6 hence demonstrates that the dynamics of the current front are strongly altered by the interaction process. As described by Hogg et al. [62], the original head of the hyperpycnal current is lifted upwards by the wave, and a new current front subsequently forms from the body of the current. In order to quantify the resulting, delayed progression of the hyperpycnal flow below the pycnocline, we define the front location x_f as the rightmost horizontal position at which

$$c_c(x, y) \geq c_t \ , \tag{5.15}$$

where we choose $c_t = 0.1$, although the observations to be discussed in the following do not vary significantly with c_t. Regardless of whether a wave is present or not, the gravity current splits into an intrusion flow along $y = h_p$, and a bottom-propagating hyperpycnal component. We can identify the hyperpycnal and intrusion front locations at time t as follows: first, we determine $x_f(y)$ for all y-values. Subsequently we evaluate the slope height $y_s(x_f)$ for each value $x_f(y)$. The two front locations are then defined as

$$x_f = \begin{cases} \max(x_f(y)), \forall y \leq y_s(x_f) + \delta \text{ (hyperpycnal)} \\ \max(x_f(y)), \forall y \geq y_s(x_f) + \delta \text{ (intrusion)} \end{cases} \tag{5.16}$$

where δ is sufficiently large to encompass the hyperpycnal bottom-propagating flow, but small enough not to capture the intrusion. The intrusion occurs around $h_p/H = .576$ and the hyperpycnal flow reaches depths of $y/H \leq 0.5$ rapidly after piercing the pycnocline, suggesting that an appropriate value is $\delta/H = 0.1$. We note that within the range $0.05 \leq \delta/H \leq 0.15$ the results are not sensitive to the precise value of δ/H.

Figure 5.7 displays both front locations as functions of time. As the wave begins to interact with the current at $t/T \approx 20$, both components of the front abruptly slow down. This slowdown occurs systematically at $x/H \approx 5.5$, defining the horizontal location where the wave-current interaction occurs, and where the intrusion and hyperpycnal components of the current become distinguishable. Subsequently the intrusion front re-accelerates, and for long times its location becomes nearly independent of the wave height. The fast-moving, leftward propagating wave fluid forces the rightward propagating intrusion to accelerate, thereby reducing the long-time influence of Fr on the intrusion front location. The hyperpycnal front behaves quite differently. For small-amplitude waves with $Fr < 0.155$, the wave affects the front location only weakly, and the hyperpycnal and intrusion fronts propagate at similar speeds. For large-amplitude waves with $Fr \geq 0.155$, the hyperpyncal front comes to a nearly complete stop for a period of $t/T \approx 10$, before it eventually accelerates again. This reflects the decapitation of the original front, and the formation of a new front from the body of the current as described by Hogg et al. [62]. This dependence of the front propagation velocity on the wave height is consistent with the observation that the decapitation process exists only for sufficiently large waves with $Fr \geq 0.155$.

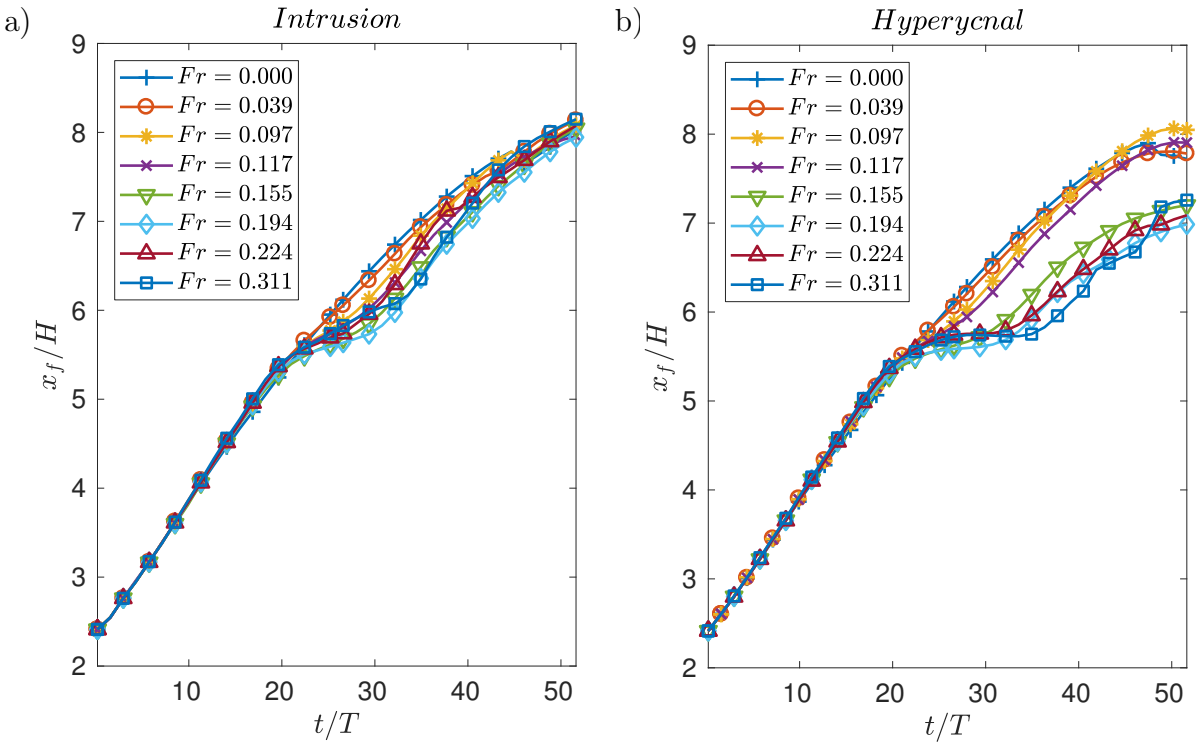

Figure 5.7: Current front location as function of time for various wave heights. During its interaction with the wave, the initial gravity current front splits into an intrusion front (a) and a hyperpycnal front (b). For large waves with $Fr \geq 0.155$, the hyperpycnal front comes to a near-complete stop and then re-accelerates, without ever catching up again with the no-wave case. In contrast, the intrusion front is slowed only temporarily by the wave.

5.3.4 Energy budget of the current-wave interaction

We now proceed to analyze how the two different current-wave interaction regimes are reflected in the various energy budget components and their temporal evolution, cf. Härtel et al. [57] for a detailed derivation. The potential energy E_p of the flow is the sum of the contributions from the gravity current and wave scalar fields

$$E_p(t) = E_{p,c}(t) + E_{p,w}(t) \ , \tag{5.17}$$

where

$$E_{p,c}(t) = \int_\Omega y c_c \ dV \quad \text{and} \quad E_{p,w}(t) = \int_\Omega y c_w \ dV \ . \tag{5.18}$$

The total kinetic energy E_k is obtained as

$$E_k(t) = \int_\Omega \frac{1}{2} u_i u_i \ dV \ , \tag{5.19}$$

while losses due to viscous dissipation from the start of the flow up to time t are given by

$$L(t) = \int_t \epsilon(t) \ dt = - \int_t \int_\Omega \frac{2}{Re} s_{ij} s_{ij} \ dV \ dt \ . \tag{5.20}$$

Here $\epsilon(t)$ denotes the volume integral over the dissipation rate, and s_{ij} indicates the rate of strain tensor $s_{ij} = \frac{1}{2}\left(\frac{\partial u_i}{\partial x_j} + \frac{\partial u_j}{\partial x_i}\right)$. In the limit of small vertical diffusion fluxes [174], energy conservation implies

$$E_{p,c} + E_{p,w} + E_k + L = cst. \tag{5.21}$$

In the limit of no mixing, the state of minimal potential energy corresponds to the configuration where the gravity current fluid collects at the bottom of the flow field,

with the lower layer ambient fluid placed immediately above. The upper ambient fresh water layer occupies the topmost region. The potential energy of this configuration is a function only of the initial volume and concentration of each fluid region. In order to be able to make meaningful comparisons between different simulations we hence keep these parameters constant between different simulations, by lowering the ambient pycnocline as we increase the wave height.

The energy budget components are displayed as functions of time in figure 5.8, for two different wave heights. Upon release of the lock, the potential energy of the current fluid is converted into kinetic energy, and viscous losses accumulate. As the current pierces the pycnocline in the absence of a wave, a fraction of its kinetic energy is used to lift dense ambient fluid, so that the overall kinetic energy of the flow peaks and then steadily declines. This picture changes in the presence of a wave. While the release of the wave at time $t_1 > 0$ initially increases the overall kinetic energy, we note that the horizontal momenta of the current and wave fluid point in opposite directions. As a result, when the current and the wave collide the kinetic energy drops significantly, while the potential energy decrease of the current fluid is temporarily delayed and, for sufficiently large waves, even reversed. This is a direct manifestation of the decapitation process, and of the formation of a reflected, upslope-propagating current. Eventually, however, the potential energy release of the current fluid resumes.

The change in the potential energy of the gravity current fluid as a function of time is given by

$$\Delta E_{p,c}(t) = E_{p,c}(t) - E_{p,c}(0) \ . \tag{5.22}$$

The work performed by the wave in order to raise the potential energy of the current

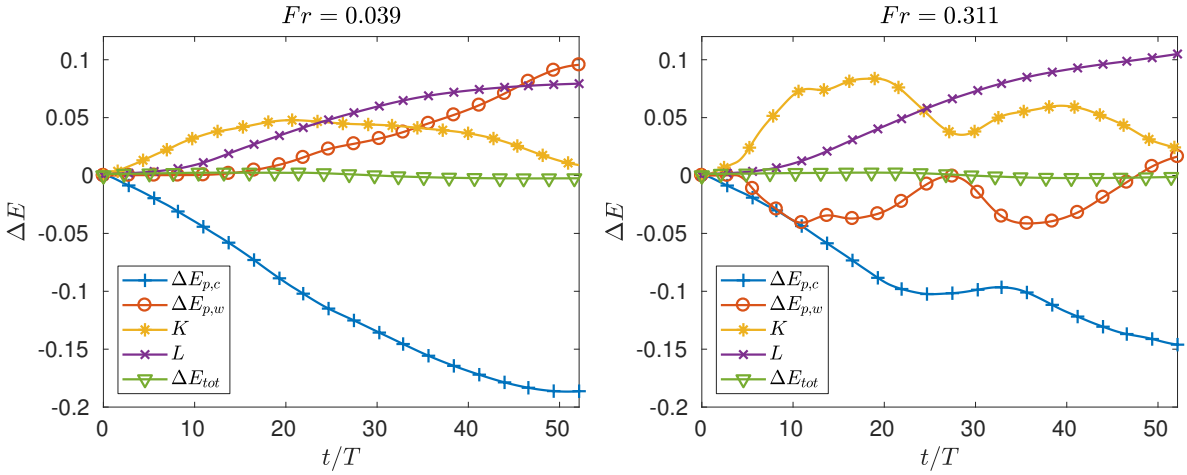

Figure 5.8: Global energy budget of the current-wave interaction for two various wave sizes and their corresponding wave Froude number $Fr = h_w/l_w$. As the wave height increases, more potential energy is released from the dense ambient fluid, impacting the production of kinetic energy, and modifying the release of potential energy of the gravity current during the current-wave interaction.

fluid can then be obtained as

$$W(t) = \Delta E_{p,c}(t) - (\Delta E_{p,c}(t))_{nw} \ , \tag{5.23}$$

where the subscript nw refers to the flow without a wave. Figure 5.9a shows the change in the gravity current potential energy $\Delta E_{p,c}(t)$ as a function of time, for various wave heights. For $Fr < 0.155$ the influence of the wave is temporary and weak, so that soon the current energy again approaches its value without a wave. A clear regime change is observed for $Fr \geq 0.155$, where the wave is seen to have a longer-lasting effect on the potential energy of the current fluid. This is confirmed by the amount of work W displayed in figure 5.9b, which demonstrates that small wave heights lead to a rapid and full recovery in the sense that soon again $W \to 0$. This suggests that small waves do not increase the amount of irreversible mixing during the current-wave interaction, a hypothesis that will be examined in more detail below. For large wave Froude numbers $Fr \geq 0.155$, on the other hand, W reaches a much higher peak, and

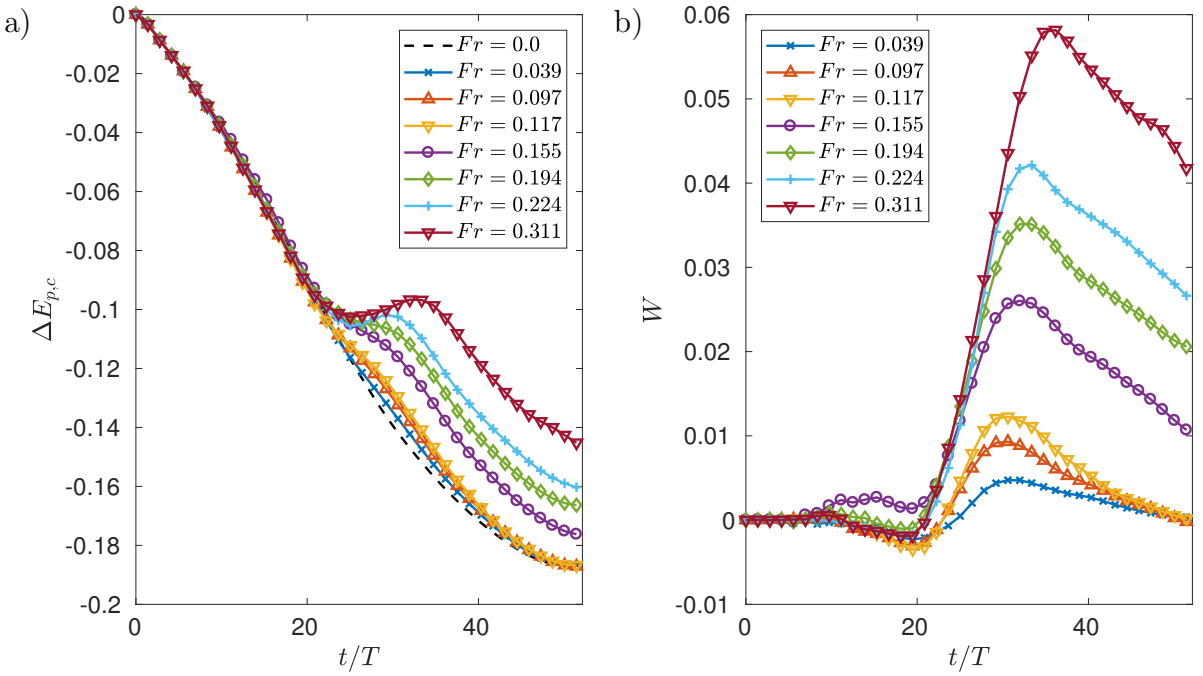

Figure 5.9: (a) Change in gravity current fluid potential energy as a function of time for various wave heights. (b) Work performed by the wave on the gravity current fluid as a function of time for various wave heights. Wave heights of $Fr \geq 0.155$ are seen to have a lasting effect on the potential energy budget of the gravity current fluid.

subsequently decreases only over a much longer time scale.

The above discussion of the energy budget indicates that for low wave Froude numbers, the wave temporarily slows down the current but does not increase the amount of mixing. Thus, the available potential energy is not reduced by the current-wave interaction, so that the current fluid can thus resume its release of potential energy upon the completion of this interaction. For large wave Froude numbers, on the other hand, the current is not only slowed down by the wave but it is also mixed, so that the potential energy available for subsequent release is reduced.

Figure 5.10a shows the volume integral $\epsilon(t)$ of the dissipation rate as function of time for various Fr-values. During the initial phase, dissipative processes in the bottom boundary layer of the current dominate (figure 5.11), while contributions from the wave propagating along the pycnocline are relatively minor. Hence, $\epsilon(t)$ is nearly independent

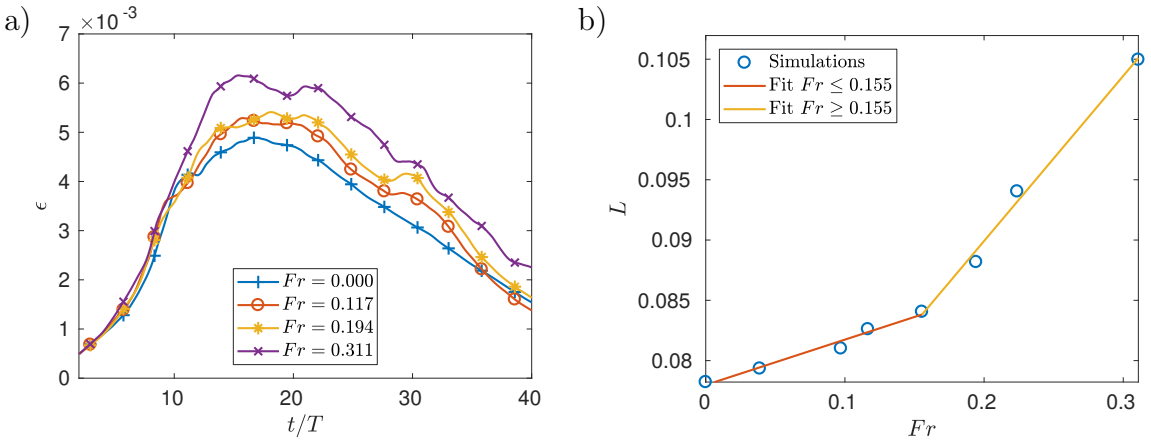

Figure 5.10: (a) Volume integral of the instantaneous viscous dissipation ϵ as a function of time for various wave Froude numbers. (b) Cumulative viscous losses L as a function of the wave Froude number. The slope of the cumulative viscous losses $vs.$ wave height increases above $Fr \approx 0.155$.

of the wave height. Once the current and the wave begin to interact at $t/T \geq 10$, however, dissipative effects within the larger region associated with the decapitation of the raised head gain importance, and $\epsilon(t)$ increases strongly with Fr. This is reflected by the cumulative losses L at the final simulation time, cf. figure 5.10b. The slope $d(L)/d(Fr)$ becomes significantly steeper above $Fr \approx 0.155$, which confirms that the current-wave interaction dominates the dissipation rate in this regime. Given the qualitative and quantitative evidence of a phenomenological change in the current-wave interaction above a certain critical wave Froude number, we will refer to waves above (below) the critical wave Froude number as supercritical (subcritical).

5.3.5 Wave-induced irreversible mixing

We proceed to analyze how the current-wave interaction affects the mixing of the gravity current fluid with the ambient, and specifically the amount of irreversible mixing that it triggers. Towards that end, we calculate the discrete probability density function (PDF), or histogram, of the current fluid concentration $c_c(t)$. We divide the concentra-

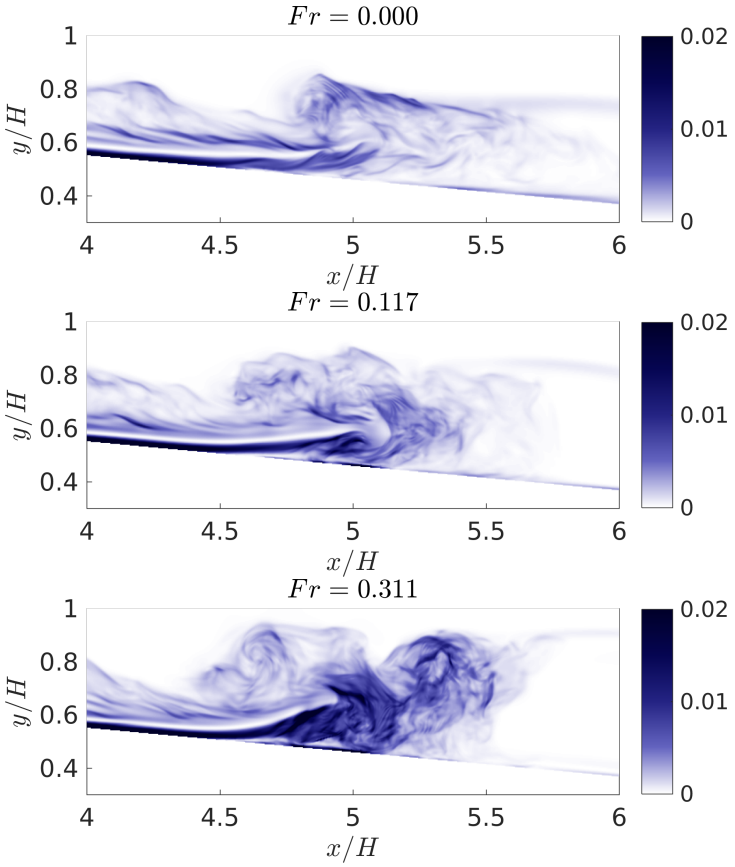

Figure 5.11: Spanwise-averaged instantaneous viscous dissipation $\langle \frac{2}{Re} s_{ij} s_{ij} \rangle_z(x, y, t)$ at $t/T = 26$ in the absence of a wave (top), in the presence of a subcritical wave (middle), and for a supercritical wave (bottom). The subcritical wave ($Fr = 0.117$) slows down the current and somewhat increases the dissipation in the vicinity of the head and close to the slope. On the other hand, the supercritical wave ($Fr = 0.311$) leads to strong dissipation away from the slope, within the uplifted current front.

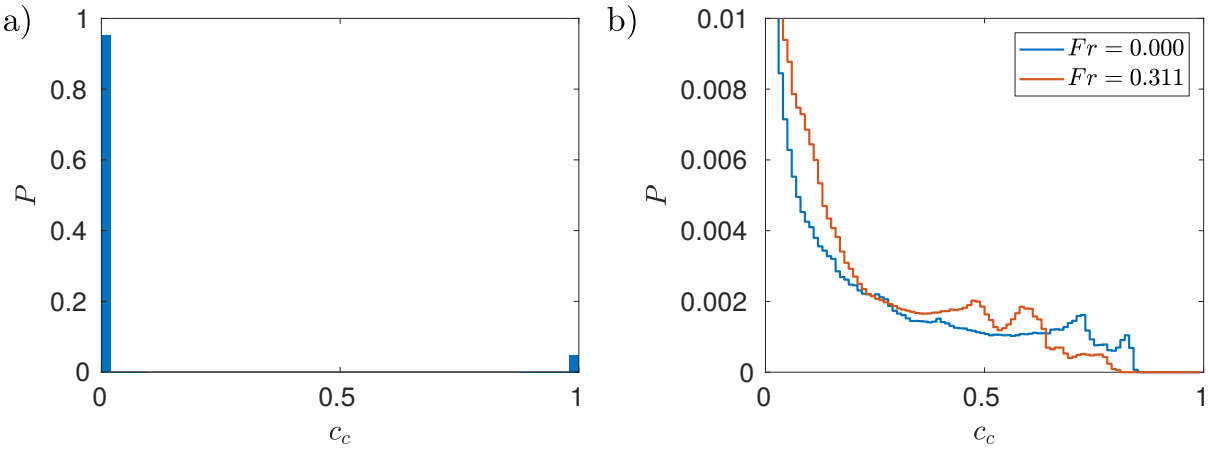

Figure 5.12: (a) Initial histogram of gravity current fluid concentration c_c. The discrete probability density function P is the same for all Froude numbers and only depends on the ratio of lock volume to total volume. (b) PDF of gravity current fluid concentration c_c at $t/T = 52.14$. The discrete probability density function P (staircase plot for readability) shows an increase in intermediate concentrations for $Fr = 0.311$ compared to the no-wave case ($Fr = 0$). Note that the vertical axis is clipped to $Pr = 0.01$ for readability, as most of the ambient remains unmixed.

tion range $[0, 1]$ into $N = 400$ equally spaced bins, and count the number of grid cells within each bin. By normalizing with the total number of cells in the entire computational domain, we obtain the relative occurrence $P_i(t),\ i = 0, N-1$ of grid cells whose concentration c falls within the range $i/N < c_c(\mathbf{x}, t) < (i+1)/N$, with $\sum_{i=0}^{N-1} P_i(t) = 1$. Initially, the concentration is either $c_c = 0$ (outside the lock) or $c_c = 1$ (inside the lock), so that $P_i(0) = 0$ for $i = [1, N-2]$, $P_{N-1}(0) = V_1/V_{tot}$ and $P_0(0) = (V_{tot} - V_1)/V_{tot}$, cf. figure 5.12a. As the current moves down the slope and mixes with the ambient, regions of intermediate concentrations form via stirring and mixing.

Figure 5.12b shows the final histograms at $t/T = 52.14$ in the absence of a wave, as well as for the largest wave height $Fr = 0.311$. By this time, both flows have succeeded in diluting the gravity current fluid, so that values $c_c > 0.85$ are no longer found. Closer inspection reveals that the $Fr = 0.311$ wave has shifted both tails of the histogram more strongly towards the center, as compared to the case without wave. The background potential energy (BPE) can now be calculated as a function of time and wave height in

order to quantify the irreversible mixing observed in the histograms.

The BPE of a variable-density flow field corresponds to the lowest amount of potential energy that the system can achieve by an optimal redistribution of the fluid elements so that the fluid density decreases with height [174]. In a closed system, it can only increase with time and its increase is a direct measure of irreversible mixing. The BPE is calculated from the sorted salinity profile written as $s(y^*)$ where y^* maps the vertical coordinate of each fluid parcel to its sorted location. $s(y^*)$ is calculated directly from the histograms of concentration for c_c and c_w and we refer the reader to Winters et al. [174] for the details of its calculation. Note that because of the slopping bottom, the calculation of the sorted profile is slightly more involved and results in a modified expression for the background potential energy given by

$$E_b(t) = \int_0^{y_N^*} s(y^*)A(y^*)y^*dy^*. \tag{5.24}$$

where $A(y^*)$ is the horizontal area of the fluid domain at height y^*. For all simulations, the rate of change of background potential energy was found to reach a maximum during the initial interaction between the current and the pycnocline, i.e. for $t_1 \leq t \leq t_2$ with $t_1/T \approx 10$ and $t_2/T \approx 30$. The difference of background potential energy with and without a wave, normalized by the initial background potential energy, is plotted in figure 5.13a as a function of time for several wave Froude numbers Fr. Note that $E_b(t = 0)$ is the same for all Fr. As expected, the presence of a wave leads to a considerable increase in irreversible mixing, which depends directly on the wave height.

Wave-induced mixing is most effective for a shorter period of time ($t_1 \leq t/T \leq t_3$ where $t_3 \approx 20$) than the peak production period. Irreversible mixing produced during the wave-current interaction is measured as the difference between background potential energy prior and post interaction, i.e. $E_b(t_2) - E_b(t_1)$. This is plotted in figure 5.13b, and

reveals once again the change in behaviour of the flow at higher wave Froude numbers. The background potential energy produced during the interaction increases monotonically with wave height but does so much more distinctively for $Fr \geq 0.155$. We also note that the amount of background potential energy produced during this time interval for the largest wave is close to twice that of the case in the absence of a wave. It is also interesting to note in figure 5.13a that the three largest waves lead to a secondary increase irreversible mixing at late times, i.e. $t/T \geq 40$. Indeed, when the reflected component of the gravity current forms an upslope current, irreversible mixing increases through entrainment (figure 5.14). Additionally, vertically transported gravity current fluid is found in higher concentrations above the slope for cases with supercritical waves. This fluid was transported during the decapitation process and is thus able to mix efficiently with ambient fluid post interaction, contributing to enhanced mixing at later times. Finally, Kelvin-Helmoltz-like structures, or numerical mimics thereof, are seen to perturb the intrusion at late times and for large waves. The size of the structures and their two-dimensional nature suggests that they contribute only little to mixing, but their existence is more likely due to the strength of the wave reflection on the right wall and is thus limited to a laboratory setting.

5.3.6 Influence of density ratio

An essential aspect of the wave-current interaction was left unexplored in the experiments of Hogg et al. [62], where the density ratio $\frac{\rho_2-\rho_0}{\rho_1-\rho_0} = \frac{c_2}{c_1}$ was held constant at 0.8. Section 5.3.4 above demonstrated the importance of the energy transfer between the wave and the current, which should be a strong function of their respective excess densities. In order to investigate this aspect, we conduct a series of simulations for a constant wave Froude number $Fr = 0.194$ and density ratios $c_2/c_1 = 0.6$, 0.4 and 0.2. Snapshots of

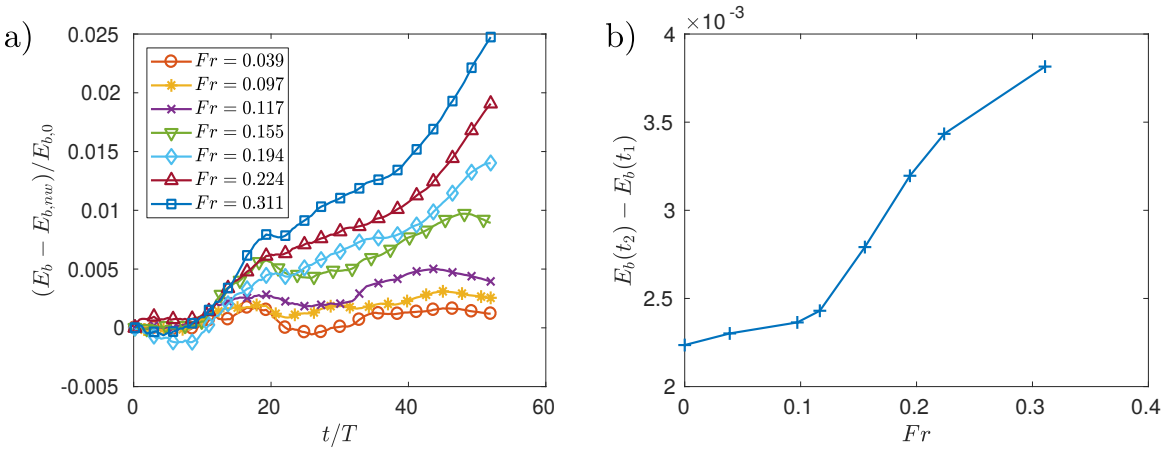

Figure 5.13: a) Difference in background potential energy $(E_b(t) - E_{b,nw}(t))/E_b(0)$ with respect to the case without a wave (nw) as a function of time for various wave Froude numbers. b) Background potential energy $E_b(t_2) - E_b(t_1)$ produced between $t_1/T = 10$ and $t_2/T = 30$, corresponding to the time interval of strong background potential energy production, plotted as a function of the wave Froude number.

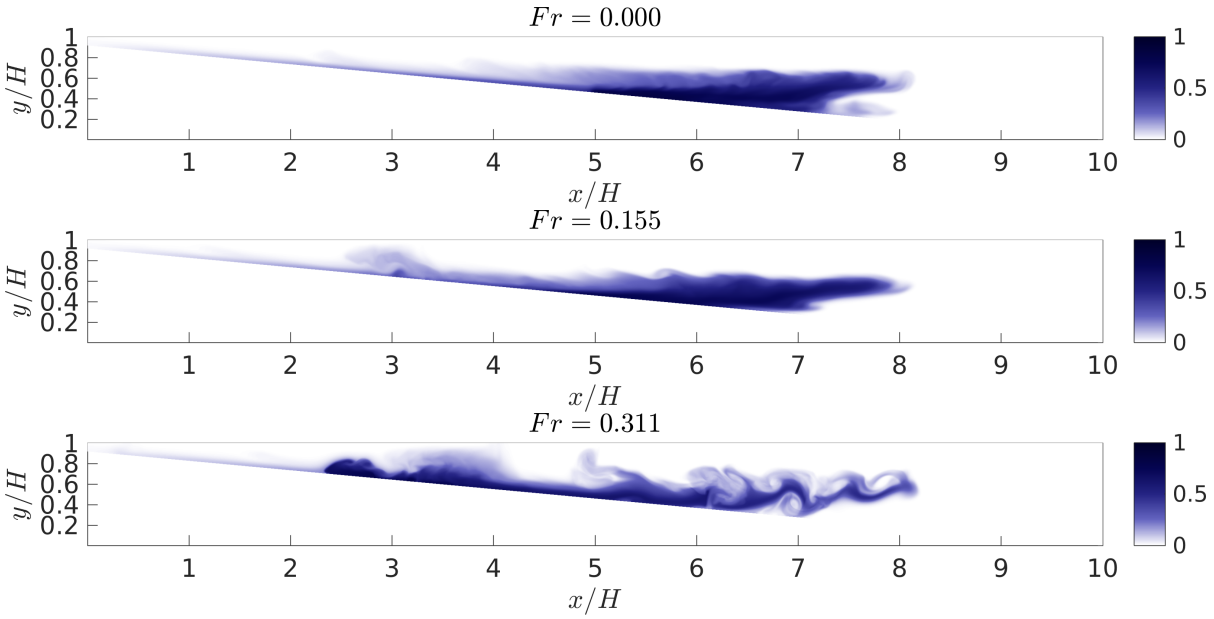

Figure 5.14: Snapshot of the depth-averaged gravity current fluid concentration at $t/T = 52.14$ for three wave Froude numbers. Mixing is induced by entrainment in the reflected, upslope propagating component of the gravity current. Interactions between the intrusion and the wave reflected off the right wall lead to additional mixing that is not directly linked to the current-wave interaction.

the corresponding spanwise-averaged gravity current fluid concentration at $t/T = 43.45$ are shown in figure 5.15. The original density ratio of $c_2/c_1 = 0.8$ leads to a complete modification of the flow in the presence of the wave, as previously described. The hyperpycnal component of the current is strongly delayed and depleted post-interaction and a strong upslope current is formed. At $c_2/c_1 = 0.6$, the head of the current is altered but persists and continues to move downslope. There is no sign of an intrusion, but the body of the current appears to be diluted on a large volume above the slope. A thin layer of gravity current fluid separates the head from the diluted body, which suggests that the wave failed to decapitate the current but strongly altered the propagation of the body of the current. At $c_2/c_1 = 0.4$, most of the head of the current retained its shape and the diluted body of the current was able to stay close to the head of the current after penetration of the pycnocline. At $c_2/c_1 = 0.2$, the gravity current completely recovers its natural dynamics with a strong head followed directly by an entrainment region forming the body of the current. As in section 5.3.2, the mass flux across an interrogation plane located at $x_b/H = 7$ is averaged over time and plotted as a function of y (figure 5.16a). The mass flux substantially increases as c_2/c_1 decreases, and transfers from an almost purely intrusive component for the largest density ratio to a purely hyperpycnal component for all other ratios. The result at $c_2/c_1 = 0.6$ is particularly interesting as the mass flux is overall strongly reduced compared to the two smaller ratios, yet no component of the flow is part of a right-ward propagating intrusion. This could indicate that the wave has had the effect of stopping the propagation of partially diluted gravity current fluid as an intrusion, yet allowed the propagation of the hyperpycnal component. Figure 5.16b illustrates the decline in total mass flux with the increase of the density ratio and stresses the idea of a transition for $0.6 < c_2/c_1 < 0.8$ to a purely intrusive flow. Predictability of current dilution and correspondingly of entrainment is paramount to determine the exact transition point from a purely hyperpycnal to a purely intrusive flow as a function of the

density ratio. The coupling of wave-induced transport with this transition is beyond the scope of the project. This nonetheless presents a new opportunity for experimental and modelling work on the effect of waves on intrusions in a strongly hyperpycnal flow (say $c_2/c_1 < 0.6$ in this particular scenario). An analysis of viscous dissipation (figure 5.17a) reveals an increase in dissipation as c_2/c_1 decreases. Indeed, less kinetic energy is conceded by the current to raise the pycnocline of the dense lower ambient, thus allowing for viscous dissipation to act on longer times as the current propagates. The change in potential energy associated with the gravity current fluid is plotted in figure 5.17b. Momentum carried by the wave decreases as c_2/c_1 decreases and thus less energy is converted back into current potential energy during the interaction. At $c_2/c_1 = 0.2$, the rate of conversion of potential energy into kinetic energy and dissipation losses is almost constant over the propagation time. The increase at the later time simply indicates that the current has reached the right wall is is thus pushed upwards. We further quantify the effect of the concentration ratio by isolating the gravity current fluid present in the upper region of the domain, defined by $y \geq h_l$, where h_l defines the initial location of the lower pycnocline of the ambient fluid. Isolating this component for a given wave height but various ratios c_2/c_1 allows us to directly measure the effect of the wave on vertical transport of gravity current fluid. We define the mass of gravity current fluid in the upper layer as

$$m^* = \int_{\Omega}^{*} c_c dV \tag{5.25}$$

where $\Omega^* = \Omega(y \geq h_l)$ and Ω represents the total fluid volume. m^* is plotted in figure 5.18a and directly explains the change in potential energy observed in figure 5.17b. Gravity current fluid upon interaction with a dense wave remains in larger amount above the pycnocline and mixes ambient fluid, while gravity current fluid interacting with a lighter wave penetrates the pycnocline, reducing vertical transport of dense gravity current fluid.

During the decapitation process and up to a time of $t/T = 30$ after release, less than 20% of the gravity current fluid is able to penetrate the lower pycnocline for the maximum ratio of $c_2/c_1 = 0.8$. In comparison, the smallest ratio of $c_2/c_1 = 0.2$ leads to 60% of the gravity fluid penetrating through the pycnocline by the same instant in time. While smaller ratios lead to more dissipation (figure 5.17a) due to the ability of the current to release its potential energy (figure 5.17b), it is expected that higher concentration ratios will lead to more mixing of gravity current fluid in the upper layer and thus away from the slope. This is shown by calculating the PDF $P^*(t)$ of gravity current fluid concentration c_c in the upper domain Ω^*. Intermediate concentrations are present in the upper region for the largest ratio c_2/c_1. This is due to the vertical transport of partially mixed fluid during the decapitation process. Naturally, only concentrations below c_2 are present in the upper domain for all simulations. This is due to the fact that any larger concentration of gravity current fluid is denser than the lower ambient fluid and can thus penetrate the pycnocline. This results in far fewer cells of intermediate concentration of gravity current fluid for lower values of c_2/c_1.

5.4 Conclusion

Experiments by Hogg et al. [62] of a downslope gravity-current interacting with an internal wave travelling at the pycnocline of a two-layer stratification were reproduced using direct numerical simulations. The simulation parameters are at scale with the experiments in terms of the Reynolds number, density ratio and wave Froude number, or wave height. The numerical simulations corroborate the experimental observations of a strong current-wave interaction for sufficiently large waves, referred to by Hogg et al. [62] as the current head decapitation. The numerical simulations also corroborate observations of a reduced mass-flux of the gravity current as it penetrates the pycnocline

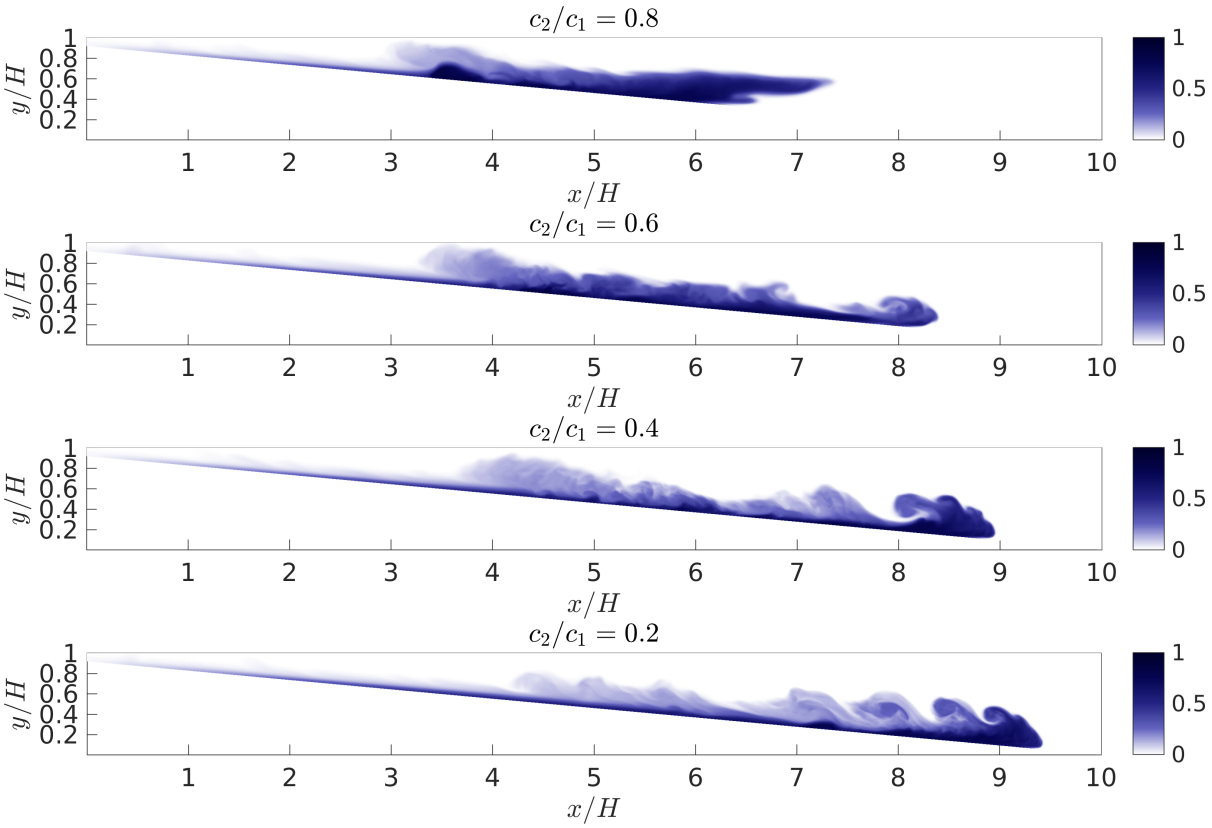

Figure 5.15: Snapshot of the spanwise-averaged gravity current fluid concentration at $t/T = 43.45$ for $Fr = 0.194$ and four density ratios c_2/c_1.

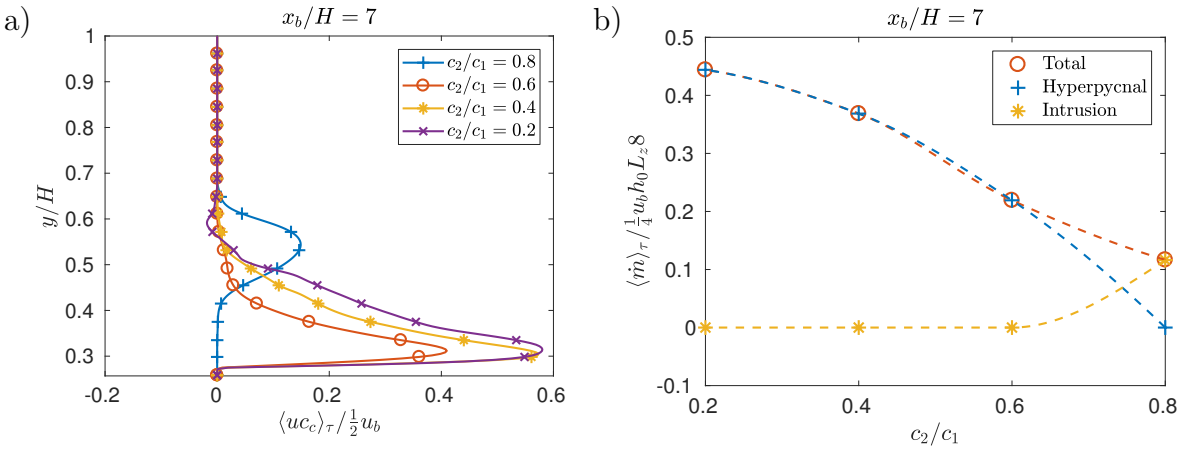

Figure 5.16: (a) Time-averaged profile of the horizontal flux of gravity current fluid uc_c as a function of y. (b) Discrete contributions of the hyperpycnal and intrusive gravity current to the total time averaged mass flux as a function of the density ratio, for $Fr = 0.194$. The averaging window is $t/T \in [26.07, 52.14]$, i.e from the beginning of the intrusion to the end of the numerical simulation.

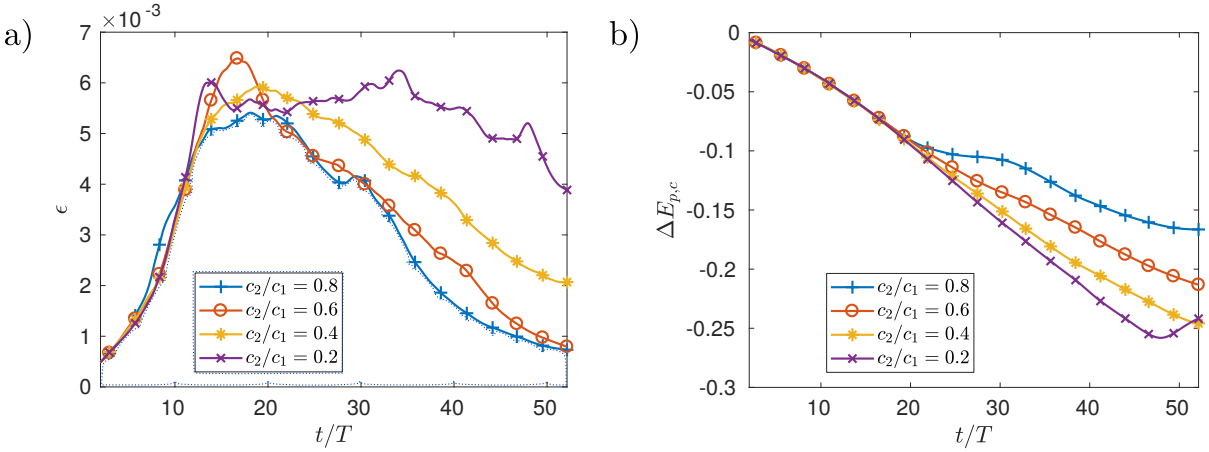

Figure 5.17: $Fr = 0.194$. (a) Viscous dissipation $\epsilon(t)$ as a function of time for various initial concentration ratios c_2/c_1 between the bottom ambient fluid and the gravity current fluid. (b) Change in potential energy $\Delta E_b(t)$ of the gravity current fluid as a function of time for various initial concentration ratios c_2/c_1.

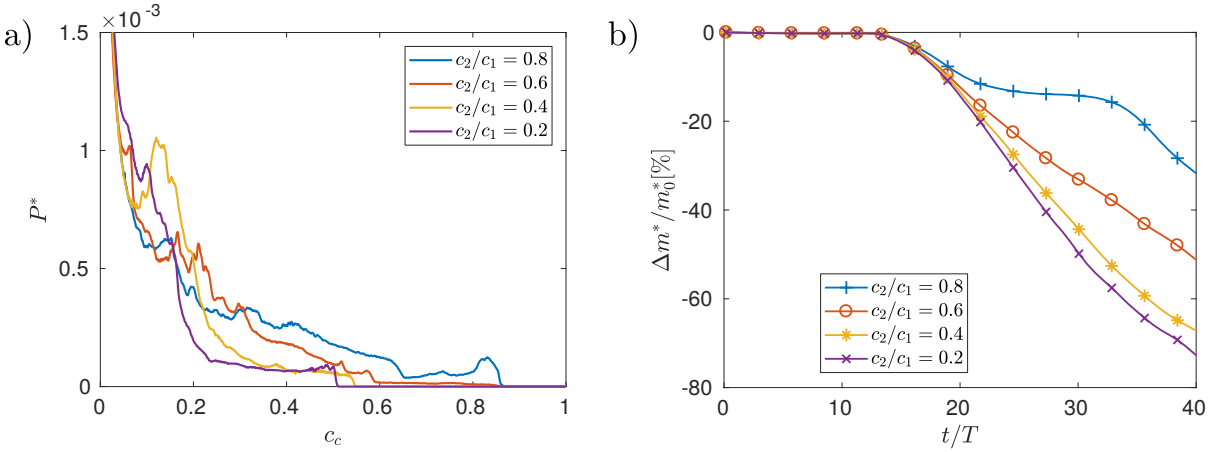

Figure 5.18: $Fr = 0.194$. (a) Relative change in mass of gravity current fluid present above the initial pycnocline defined by $y = h_l$ as a function of time for various initial concentration ratios c_2/c_1 between the bottom ambient fluid and the gravity current fluid. (b) PDF of the gravity current fluid concentration above the initial pycnocline $y = h_l$ for various initial concentration ratios c_2/c_1 at $t/T = 43.45$.

compared to a similar stratification in the absence of a wave. The mass-flux is dominated by the intrusion of partially-mixed gravity-current fluid along the pycnocline, at its height of neutral buoyancy. Both the intrusion and hyperpycnal components of the gravity current mass-flux downslope from the point where the pycnocline meets the slope are reduced in the presence of the wave. The overall mass-flux reduction for the largest tested wave height is of the order of 50%, which agrees well with the results of Hogg et al. [62]. Close inspection of the flow dynamics during interaction with the wave reveals how the decapitation process occurs: Momentum transferred by the wave into the gravity current leads to a reverse flow that separates from the head of the current and propagates back upslope. Fluid from the head is simultaneously split into a hyperpycnal component and a vertically transported component that lifts into the ambient. Part of this vertically transported - or decapitated - gravity current fluid then gets transported to the left by the reverse current occurring at the top of the domain and transported to the right as an intrusion at the pycnocline. This dynamical process translates in a change in the front velocity of the current. Individual measurements of the hyperpycnal and intrusion components of the gravity current in terms of front location reveals that both fronts are slowed down during interaction as wave height is increased. However, a change in behaviour is observed for $Fr \geq 0.155$: While the front location of the intrusion is not-strongly affected, the front of the hyperpycnal current comes to a complete stop and only resumes its progression post interaction with the wave. This observation translates the vertical transport of the decapitated head of the current, and the formation of a new hyperypcnal front from the body of the current that then resumes its along-slope propagation.

The existence of a critical wave height at which the decapitation process can occur has direct consequences on the energy budget of the flow. In the absence of a wave, kinetic energy is generated by the release of potential energy contained in the gravity

current. As it reaches the pycnocline, the gravity current loses kinetic energy to raise the potential energy of the dense lower ambient fluid. In the presence of a wave, both the gravity current fluid and the lower ambient fluid release potential energy into kinetic energy. Upon interaction, the kinetic energy drops drastically to the benefit of the potential energy of both the lower ambient and gravity current fluids. Small waves lead to no persistent change of the gravity current potential energy whereas large waves seem to irreversibly transfer kinetic energy into gravity current potential energy. This regime change of potential energy transfers in the gravity current fluid again occurs for $Fr \approx 0.155$. Viscous dissipation reaches a maximum during the current-wave interaction and increases with wave height. Viscous losses increase more rapidly with wave height past the critical value, due to stronger stirring in the vertically transported head of the current.

Time resolved quantification of irreversible mixing is achieved through calculation of the global background potential energy of the salinity field. The effect of the wave on production of background potential energy, or equivalently on destruction of available potential energy, is most strongly felt during the initial wave-current interaction. Large waves lead to continuously more irreversible mixing than in the absence of a wave while smaller waves lead to a more transient yet comparable production of background potential energy than in the absence of a wave. Production of background potential energy during the wave-current interaction goes through the same regime change as the global energy budget when the removal of the head by the wave occurs. In the decapitation regime, background potential energy change increases rapidly with wave height and reaches close to double that of the no-wave case for $Fr = 0.311$.

The effect of the density ratio $\frac{\rho_2-\rho_0}{\rho_1-\rho_0} = \frac{c_2}{c_1}$ was finally explored as it is expected to play a great role in the change in energy transfers at large wave heights. A supercritical wave Froude number of $Fr = 0.194$ is chosen and the concentration ratio was successively de-

creased. In the presence of a wave, the decrease in density ratio quickly leads to a drastic change in the behaviour of the gravity current mass flux below the pycnocline. below a critical value, the mass flux is solely due to a hyperycnal component and no intrusion of partially mixed fluid is observed to propagate to the right. Above the critical value, all the flux is comprised in the intrusion. The behaviour at the largest density ratio that still leads to no intrusion is particularly interesting, as it appears that the wave served to retain partially mixed fluid close to the point of interaction instead of this mixed fluid forming an intrusion. In addition, smaller ratios allow the gravity current to release more potential energy after reaching the pycnocline, yielding increased dissipation below the pycnocline. The effect of the wave on changes in current fluid potential energy becomes negligible at lower density ratios and it is expected that values of c_2/c_1 close to unity are necessary to observe the removal of the head of the current by the wave. While smaller ratios appear to be favourable to mixing due to the generation of additional kinetic energy during the propagation of the current, mass retention and mixing above the pycnocline is strongly reduced. Regions of intermediate concentrations formed during the decapitation process are absent at lower ratios, and only fluid of concentration below the lower ambient value are able to stay above the pycnocline. In natural settings, regions of strongly layered stratification close to shores are thus far better candidates for the observation of such high intensity events as the removal of the head by an internal waves than regions where the current is much denser than both layers. Alternatively, strong coupling events can be avoided, or intentionally generated, by adjusting the density ratio of the dense ambient to the released current.

The authors wish to thank C. Hogg for his contributions during the early stages of the investigation. EM gratefully acknowledges the support and hospitality he received as Shimizu Visiting Professor at Stanford University. Funding for this work was provided

under NSF grants CBET-1067847 (EM) and OCE-1634389 (NTO and JRK). Computational resources for this work used the Extreme Science and Engineering Discovery Environment (XSEDE), which was supported by the National Science Foundation, USA, Grant No. TG-CTS150053.

Part III

Sedimentary double-diffusive convection in natural systems

Chapter 6

Halite precipitation in double-diffusive salt fingering in the Dead Sea

Authorship of this work is shared with Dr. Nadav G. Lensky, Vladimir Lyakhovsky, Ali Arnon and Prof. Eckart Meiburg. This work has previously appeared in Ouillon et al. [112].

6.1 Introduction

Stably stratified lakes and oceans in dry regions of the world are frequently characterized by an upper, warm and salty layer that overlies colder, less salty water below (figure 6.1a). In spite of the overall stable density distribution, the difference in the diffusivities of heat and salt renders the interfacial region unstable to double-diffusive fingering [146, 123], as shown in figure 6.1b. The descending salt fingers represent downward intrusions of the saltier upper water mass (epilimnion) into the lower water body

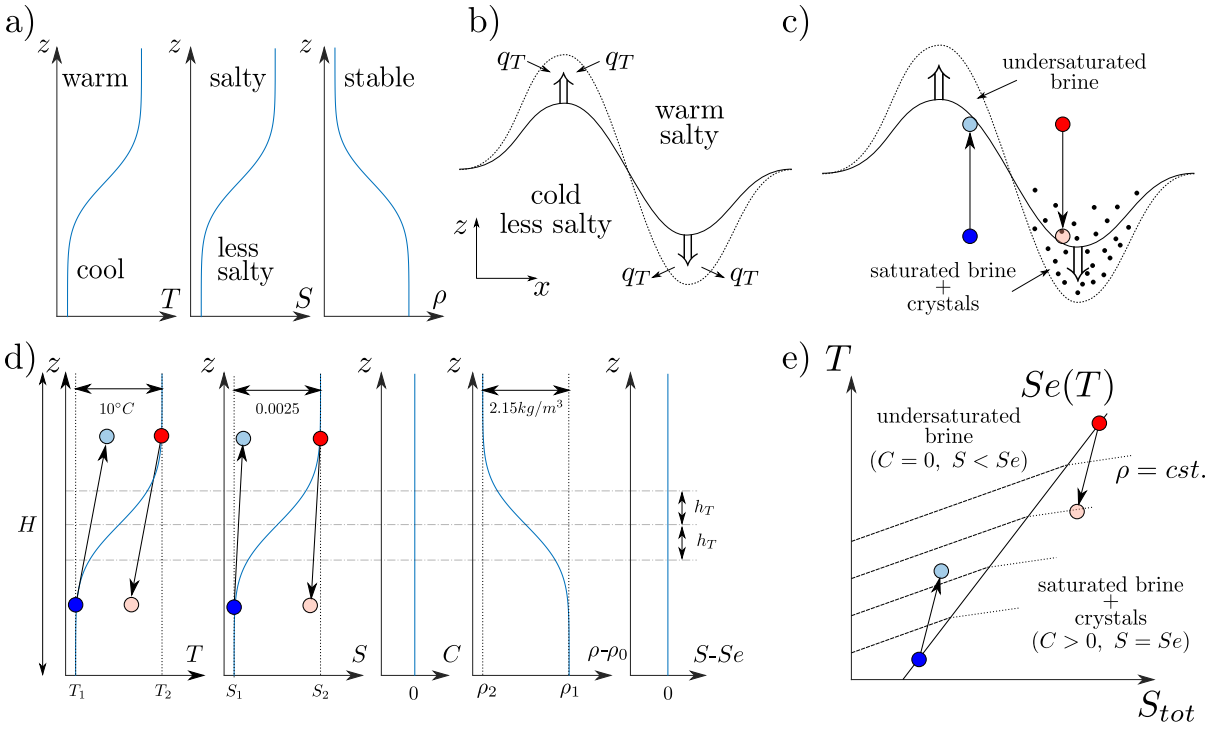

Figure 6.1: a) Temperature, salinity and density profiles in the Dead Sea during summer. b) Traditional double-diffusive salt fingering, where q_T represents the flux of heat in and out of the fingers. c) Double-diffusive salt fingering in saturated conditions, with halite precipitation. d) Initial temperature, solute salinity, halite concentration, density and saturation profiles. e) Sketch of salt water phase diagram with solubility curve and isopycnals. In c, d and e, the red (blue) fluid parcels initially in the epilimnion (hypolimnion) lose (gain) heat, while largely maintaining their salinity level.

(hypolimnion), driven by cooling in the interfacial region (metalimnion). At the same time, ascending fingers form that carry less salty hypolimnetic fluid upward into the epilimnion. The resulting net effect is a strong downward flux of dissolved salt from the epilimnion to the hypolimnion, accompanied by a weaker downward heat flux. Double-diffusive fingering has been studied in some detail both theoretically [146, 149, 71, 73], by means of numerical simulations [148, 122, 156, 125, 1], as well as through laboratory experiments [159, 92, 93] and field observations [59, 110, 175, 150, 130, 167, 3, 6].

Hypersaline stratified waterbodies, typically located in warm and extremely dry regions of the world, can exhibit salinity concentrations close to saturation, so that their

analysis needs to account for the precipitation and dissolution of salt crystals ("halite"), as shown in figure 6.1c. The Dead Sea provides a unique natural laboratory for studying the coupling between salt fingering and saturation, as it constitutes the only deep stratified hypersaline lake that presently precipitates halite. Over the last several decades, with the anthropogenic diversion of freshwater from the drainage basin [87, 88, 104], the surface water salinity of the Dead Sea increased, until it became holomictic and started to precipitate halite in 1980 [144]. Since then, the lake has been seasonally stratified with a warmer and saltier stable epilimnion during summer, and a vertically mixed water column during winter [144, 2, 3, 44, 6, 138]. Anati and Stiller [3] suggested that salt fingers reduce the salinity of the epilimnion in late summer, although they did not consider the potential role of halite precipitation. Arnon et al. [6] were able to distinguish the role of halite precipitation and double-diffusive salt fingering by in situ measurements. They provided direct evidence for significant double-diffusive salt fingering fluxes, and for the formation of halite crystals just below the thermocline, along with observations of decreasing salinity and saturation in the epilimnion. Arnon et al. [6] suggested that, in contrast to traditional thermohaline fingering, salt fingers in saturated stratified brines are asymmetrical, since descending fingers cool and precipitate halite, whereas rising fingers gain heat, become undersaturated, and have the potential to dissolve halite (figures 6.1b and c, respectively). Sirota et al. [138] as well as Sirota et al. [139] studied the basin-scale implications of these processes for the formation of halite layers in deep hypersaline bodies of water. They demonstrated the effect of dissolution in the epilimnion, and of the concurrent deposition in the hypolimnion, on the spatio-temporal variations of salt layers accumulating during hydrological crises. Following these findings, Sirota et al. [140] presented a "halite focusing" model, quantifying the basin scale increase of the halite layer thickness below the thermocline at the expense of dissolution from the shallow basin margins. This model provides an explanation of the architecture of halite

deposits observed in the geological record, which can be tens to thousands of meters thick and tens to hundreds of kilometers wide, and exhibit significant depocentral thickening [141, 43, 128].

In the following, we will employ high-resolution numerical simulations of the fluid dynamical and transport equations to test the hypothesis of Arnon et al. [6] that double-diffusive salt fingering can account for the reduction of salinity in the epilimnion during mid-summer, along with the precipitation of halite in the hypolimnion. Employing a minimum of empirical assumptions, we will explore how the traditional picture of double-diffusive salt fingering is modified when temperature-dependent halite solubility and precipitation are considered. We aim to: i) quantify the asymmetrical nature of salt fingers in a stratified saturated brine, ii) explore the role of halite crystals within the evolving fingers, along with the influence of their settling motion, and iii) evaluate the temperature, salinity, halite saturation and halite precipitation/dissolution fields as functions of the governing parameters. Based on the simulation results, we will analyze the resulting vertical fluxes of heat, solute salt and halite, as well as the rate of halite precipitation. Our main objective is to clarify the contribution of double-diffusive instabilities to the enhanced precipitation of halite in the summer months. While this work focuses on the dynamics of dissolved salt and halite crystals encountered in the Dead Sea, the same numerical approach can be applied to other hypersaline waterbodies such as evaporation ponds, as well as more generally to different combinations of fluids and minerals. Hence, the simulation approach introduced here is suitable for exploring a wide range of environmental situations involving double-diffusive flows with phase change.

This paper is structured as follows: In section 6.2, the physical problem, mathematical model and numerical methods are formulated. Section 6.3 presents the simulation results and discusses the role of crystallization within double-diffusive salt fingers. Section 6.4 presents a brief summary, along with the main conclusions.

6.2 Simulation approach and methodology

6.2.1 Setup: The context of the Dead Sea

The setup for the numerical simulations of double-diffusive salt fingers and precipitation of halite is guided by in situ observations from the Dead Sea [138, 6] in terms of temperature, salinity, saturation and halite crystallization rate (figure 6.1d). The convective fluxes and saturation conditions are strongly affected by the low diffusivity and corresponding large gradients of salinity. In order to be able to capture these small-scale features in our simulations, we consider a laboratory-scale water column of height $H = 60cm$, along with transition layer thicknesses for temperature and salinity of $h_T = h_S = 10cm$, cf. figure 6.1d. For comparison, the water depth of the Dead Sea is on the order of tens of meters, and the transition layer (metalimnion) between the well-mixed epilimnion and the hypolimnion is about a meter thick during late summer, when double diffusion is fully developed [6]. Fully resolving the fluid motion at that scale would require disproportionate computational resources while providing little additional information regarding the dynamic of double-diffusive fingering in the Dead Sea when compared to the scaled down, more accessible laboratory scale.

The temperature difference between the epilimnion and hypolimnion during summer reaches $10°C$, and the salinity difference is $\sim 2.4kg/m^3$ in quasi-salinity units (density at $25°C$ minus 1,000 kg/m^3). While the salinity of the Dead Sea is usually reported in these units [2, 44, 138, 6], here we employ the nondimensional salinity S, defined as the mass of dissolved salt per total mass of brine. In these units, the difference between epilimnion and hypolimnion amounts to 0.0025 (see appendix A for more details [49]). Assuming thermodynamic equilibrium, the salinity of brine at saturation is given by the solubility limit $Se(T)$. Once the brine reaches saturation ($S = Se$), any addition of dissolved salt results in the formation of halite crystals with concentration C. We

refer to the difference between the total salinity $S_{tot} = S + C$ and the solubility limit as the saturation $Sa = S_{tot} - Se$. While $Sa < 0$ corresponds to undersaturation, $Sa > 0$ indicates "supersaturation," which here means saturated brine containing halite crystals.

In the Dead Sea, saturation and the rate of halite production vary along the water column under a marked seasonal cycle. During the summer months the epilimnion is slightly undersaturated, whereas the hypolimnion actively precipitates halite. Arnon et al. [6] hypothesized that this "dipole" saturation stratification is a manifestation of double-diffusive salt fingering. Such a diapycnal flux explains the reduction of salinity of the epilimnion during mid-summer, the driest season, along with the continuous production of halite in the hypolimnion. To test this hypothesis, our simulations start from uniformly saturated profiles without crystals (figure 6.1d). Since halite is the most common rock forming mineral among evaporitic layers, the conditions applied in this study are the most common setting for stratified hypersaline water bodies under hydrological crisis. Above saturation, as crystals form within the saturated brine, the density changes according to the equation of state given in the Supplemental Information (figure 6.1e).

6.2.2 Mathematical model

The governing equations

We consider the two-dimensional Navier-Stokes equations for an incompressible flow with small density changes, so that the Boussinesq approximation can be employed. Advection-diffusion equations are solved for the transport of temperature (T), solute salt (S), and halite crystals (C). The crystals are assumed to be small and non-inertial, so that they settle with the Stokes settling velocity relative to the surrounding fluid. Their advection velocity $\mathbf{u}_c$ is thus given by the superposition of the fluid velocity $\mathbf{u}$ and their local settling velocity $\mathbf{v}_s = v_s \mathbf{e}_g$. The governing equations for the fluid and scalar fields

are

$$\nabla \cdot \mathbf{u} = 0 \ , \tag{6.1}$$

$$\frac{\partial \mathbf{u}}{\partial t} + (\mathbf{u} \cdot \nabla)\, \mathbf{u} = -\frac{1}{\rho_1} \nabla p + \nu \Delta \mathbf{u} + \rho' \mathbf{g} \ , \tag{6.2}$$

$$\frac{\partial T}{\partial t} + \mathbf{u} \cdot \nabla T = \kappa_T \nabla^2 T \ , \tag{6.3}$$

$$\frac{\partial S}{\partial t} + \mathbf{u} \cdot \nabla S = \kappa_S \nabla^2 S + \mathcal{F}_s(T, S, C) \ , \tag{6.4}$$

$$\frac{\partial C}{\partial t} + (\mathbf{u} + \mathbf{v}_s) \cdot \nabla C = \kappa_C \nabla^2 C + \mathcal{F}_c(T, S, C) \ . \tag{6.5}$$

Here $\mathbf{u} = (u, w)$ is the velocity vector in the two-dimensional Cartesian coordinate system $\mathbf{x} = (x, z)$, p denotes pressure, and ρ_1 indicates the reference density, which is taken as the initial density of the hypolimnion. ρ denotes the local density, $\rho' = \frac{\rho - \rho_1}{\rho_1}$ represents the reduced density, and $\mathbf{g}$ is the gravitational acceleration. $\mathbf{v}_s = -v_s \mathbf{e}_z$ is the settling velocity, κ_T and κ_S are the molecular diffusivities of heat and solute salt, respectively, while κ_C denotes the hydrodynamic diffusivity of halite crystals as a result of their mutual interactions [33, 134], which has been shown to trigger instabilities in certain types of suspension flows [21, 22, 1, 125]. Here we assume this hydrodynamic diffusivity to be equal to the molecular diffusivity of solute salt (see appendix A for details [151]). Note that as long as the convective terms are discretized with sufficient accuracy and resolution, the results obtained with the non-conservative forms of equations 6.2-6.5 will be indistinguishable from the conservative formulation.

Solubility and saturation of salt in the brine

The solubility of salt is approximated as a linear function of temperature (see appendix A for a discussion of this approximation) by

$$Se(T) - Se_1 = \sigma \cdot (T - T_1) \ , \tag{6.6}$$

where $T_1 = 24°C$ and $Se_1 = 0.280$ are taken as our reference temperature and solubility. With $\sigma = 0.25 \cdot 10^{-3}/°C$, we find that for the whole domain to be saturated, we need to set the top salinity to $S_2 = Se_1 + \sigma \cdot (T_2 - T_1) = 0.2825$ (see appendix A for accuracy of S and Se). Assuming thermodynamic equilibrium, equations 6.4 and 6.5 are constrained by the condition

$$S \leq Se(T). \tag{6.7}$$

This constraint gives rise to the source/sink terms $\mathcal{F}_s$ and $\mathcal{F}_c$ in the solute salt and halite transport equations, respectively. Their numerical treatment in the simulations will be discussed in section 6.2.3.

Equation of state

The density of the brine and suspended halite crystals is assumed to follow a linear equation of state such that

$$\rho = \rho_1 + \alpha(T - T_1) + \beta(S - S_1) + \zeta C \ , \tag{6.8}$$

where α, β and ζ denote the expansion coefficients of temperature, solute salt and crystallized salt. ρ_1 represents the reference density. Note that we allow for $\zeta \neq \beta$, so that two fluid parcels with the same overall salinity but different proportions of solute and crystal salt can have different densities. An analytical expression for ζ is given by (see

appendix A)

$$\zeta = \rho_b \frac{\rho_s - \rho_b}{\rho_s} \frac{1}{1 - Se} \ , \tag{6.9}$$

where ρ_s is the density of halite crystals and ρ_b is the brine density at saturation for an average temperature. Figure 6.1e shows the isopycnals in a temperature-salinity diagram, together with the solubility curve.

Source/sink terms

Under the assumption of thermodynamic equilibrium, crystallization and dissolution occur instantaneously, so that we do not require evolution equations for the source and sink terms $\mathcal{F}_s$ and $\mathcal{F}_c$ in the transport equations for S and C. Rather, we explicitly enforce at every time step the condition that a) all salt is dissolved if the brine is locally undersaturated, and b) if the brine is oversaturated, the concentration of dissolved salt is given by the local solubility limit. The equilibrium assumption holds given that the temperature and salinity variations within a fluid parcel are governed by diffusive time scales, which are significantly larger than the thermodynamic time scales governing the formation of halite crystals. For other systems than the Dead Sea, such a separation of time scales may not exist. In this case, one would have to employ an alternate formulation that includes an evolution equation for the halite crystal concentration, in addition to the evolution equation for the dissolved salt. These two evolution equations would then have to contain source and sink terms, respectively, that explicitly account for the thermodynamic conversion rates governing the conversion of dissolved salt into halite crystals and vice versa.

Physical properties

We consider the setup described in section 6.2.1, with $\alpha = -0.45\ kg/m^3/^\circ C$ [45] and $\beta = 0.94 \cdot 10^3\ kg/m^3$ [2] for the temperature and salinity expansion coefficients, respectively. According to equation 6.9, for the conditions of the Dead Sea $\zeta = 0.71 \cdot 10^3\ kg/m^3$ (see appendix A), so that $\zeta/\beta = 0.76$. As this ratio may take different values in other environmental systems, we will explore its influence below. The fluid viscosity, and the diffusivities of heat, solute salt and halite crystals are taken to be constant at $\nu = 10^{-6} m^2/s$, $\kappa_T = 1.4{\cdot}10^{-7} m^2/s$ [17], $\kappa_S = 1.6{\cdot}10^{-9} m^2/s$ [118] and $\kappa_C = 1.6{\cdot}10^{-9} m^2/s$, respectively (see appendix A).

Initial and boundary conditions

The initial profiles are taken to be of error function type. The bottom and top temperatures are set to $T_1 = 24^\circ C$ and $T_2 = 34^\circ C$, respectively, while the bottom and top salinities are taken as $S_1 = 0.280$ and $S_2 = 0.2825$ (figure 6.1d). The profiles are thus given by

$$T(t=0) = T_1 + \frac{\Delta T}{2}\left(1 + erf\left(\frac{z - H/2}{h_T}\right)\right)\ , \tag{6.10}$$

$$S(t=0) = S_1 + \frac{\Delta S}{2}\left(1 + erf\left(\frac{z - H/2}{h_S}\right)\right)\ , \tag{6.11}$$

where $z \in [0, H]$, $H = 60cm$ is the height of the water column, $h_T = h_S = 10cm$ is the thickness of the temperature and salinity profiles, respectively, and $\Delta T = T_2 - T_1$ and $\Delta S = S_2 - S_1$.

We employ periodic boundary conditions in the horizontal direction. At the top and bottom boundaries, we impose free-slip and Neumann conditions of vanishing diffusive flux for temperature, solute salinity and halite concentration. The simulations are initial-

ized with small random perturbations, to enable the growth of the fingering instability. We terminate the simulation before the top and bottom boundaries have a noticeable influence on the growth of the double-diffusive instability, and on the associated formation of halite.

6.2.3 Numerical implementation

Non-dimensional formulation

The above equations are rendered dimensionless by introducing characteristic quantities similar to those employed by Radko [123]. By defining a diffusive length scale d as

$$d = \left(\frac{\rho_1 \kappa_T \nu}{\alpha g \Delta T / h_T} \right)^{1/4} , \tag{6.12}$$

we can scale the remaining variables as

$$\begin{aligned} \mathbf{x} &= d\mathbf{x}' & p &= \frac{\rho_1 \nu \kappa_T}{d^2} p', \\ t &= \frac{d^2}{\kappa_T} t' & T - T_1 &= \Delta T T', \\ \mathbf{u} &= \frac{\kappa_T}{d} \mathbf{u}' & S - S_1 &= \Delta S S', \\ \mathbf{v}_s &= \frac{\kappa_T}{d} \mathbf{v}_s & C &= \Delta S C', \end{aligned}$$

where the $'$ symbol indicates dimensionless quantities. After dropping the $'$ for read-

ability, we obtain the system of governing dimensionless equations as

$$\nabla \cdot \mathbf{u} = 0 \ , \tag{6.13}$$

$$\frac{1}{Pr}\left(\frac{\partial \mathbf{u}}{\partial t} + (\mathbf{u}\cdot\nabla)\,\mathbf{u}\right) = -\nabla p' + \Delta \mathbf{u} + Ra^{1/4}\left(T + \frac{1}{R_0}S + \frac{\zeta^*}{R_0}C\right)\mathbf{e_g} \ , \tag{6.14}$$

$$\frac{\partial T}{\partial t} + \mathbf{u}\cdot\nabla T = \nabla^2 T \ , \tag{6.15}$$

$$\frac{\partial S}{\partial t} + \mathbf{u}\cdot\nabla S = \tau_S \nabla^2 S + \mathcal{F}_s \ , \tag{6.16}$$

$$\frac{\partial C}{\partial t} + (\mathbf{u}+\mathbf{v}_s)\cdot\nabla C = \tau_C \nabla^2 C + \mathcal{F}_c \ , \tag{6.17}$$

where $Pr = \frac{\nu}{\kappa_T}$ denotes the Prandtl number, $R_0 = \frac{\alpha\Delta T}{\beta\Delta S}$ represents the global density ratio, and $Ra = \frac{\alpha g \Delta T h_T^3}{\rho_1 \nu \kappa_T}$ indicates the Rayleigh number. $\zeta^* = \zeta/\beta$ is the isopycnal slope ratio in the phase diagram, while $\tau_S = \frac{\kappa_S}{\kappa_T}$ and $\tau_C = \frac{\kappa_C}{\kappa_T}$ are the solute salt to heat and crystal salt to heat diffusivity ratios, respectively. The initial density ratio is $R_0 \approx 1.915 \ll 1/\tau$, which will promote rapidly growing double-diffusive fingering instabilities [123].

Numerical method and parameters

Our simulation code solves the above equations in two dimensions by employing a pseudospectral approach in the horizontal direction, along with a compact finite difference method in the vertical direction [86]. A Crank-Nicolson scheme is used for advancing the viscous and diffusion terms in time, while the advective terms are treated by a low-storage third order Runge-Kutta method. As mentioned earlier, the assumption of thermodynamic equilibrium implies that precipitation and dissolution occur instantaneously, so that the source terms $\mathcal{F}_s$ and $\mathcal{F}_c$ are implicitly given at each time step by the difference between the solubility limit and the local solute salinity, divided by the time step. In other word, the salt flux $\mathcal{F}_s$ is calculated as a corrector that enforces the solubility limit

and needn't be computed explicitly. Instead, the solute salinity and crystal concentration are simply recalculated at the end of each Runge-Kutta substep such that the solubility condition is satisfied by the solute salt field. With T^k, S^k and C^k denoting the updated temperature, solute salinity and crystal concentration at the end of the k^{th} Runge-Kutta substep, we enforce thermodynamic equilibrium by calculating corrected values as

$$S^{k,*} = \min(S^k_{tot}, Se(T^k)), \tag{6.18}$$

$$C^{k,*} = S^k_{tot} - S^{k,*}, \tag{6.19}$$

where $S^k_{tot} = S^k + C^k$. The grid size is $N_x \times N_z = 1,024 \times 16,384 \approx 16.78M$ grid points. The code uses the *MPI* library for parallelism, along with the *FFTW* library. It has previously been validated by [1, 125].

6.3 Results and discussion

6.3.1 Asymmetrical crystallization in salt fingers

The results from direct numerical simulation of the aforementioned setup present the dynamic growth of double diffusion salt fingers, starting from stable stratified water column. Figure 6.2 shows snapshots of the temperature, brine salinity, crystal concentration and brine saturation plotted at various times. The dimensionless parameters $L_x \times H = 100 \times 800$, $h_T = h_S = 133$, $Pr = 7.143$, $Ra = 3.153 \cdot 10^8$, $R_0 = 1.915$, $\tau_S = \tau_C = 0.0114$, $\zeta/\beta = 1$ and $v_s = 0$. The characteristic length and time scales for converting these dimensionless values into dimensional ones are $d = 0.75mm$ and $d^2/\kappa_T = 4.02s$. The double-diffusive fingering instability is seen to grow from the centerline of the vertical profiles, at the point of maximum temperature and salinity gradient. The instability then propagates away from the center towards the top and bottom bound-

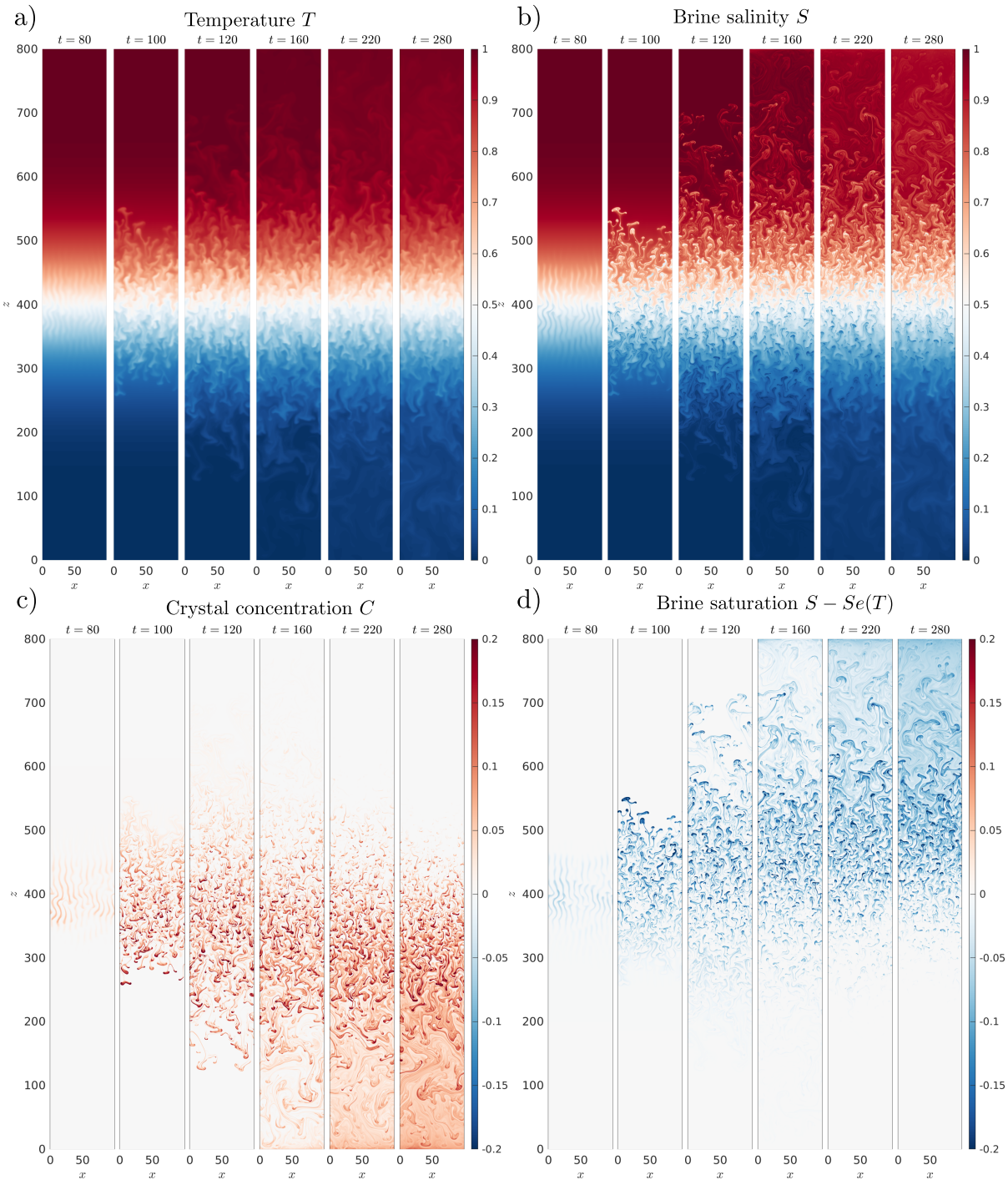

Figure 6.2: Snapshots of the scalar fields at various times: a) temperature, b) brine salinity, c) crystal concentration and d) brine saturation.

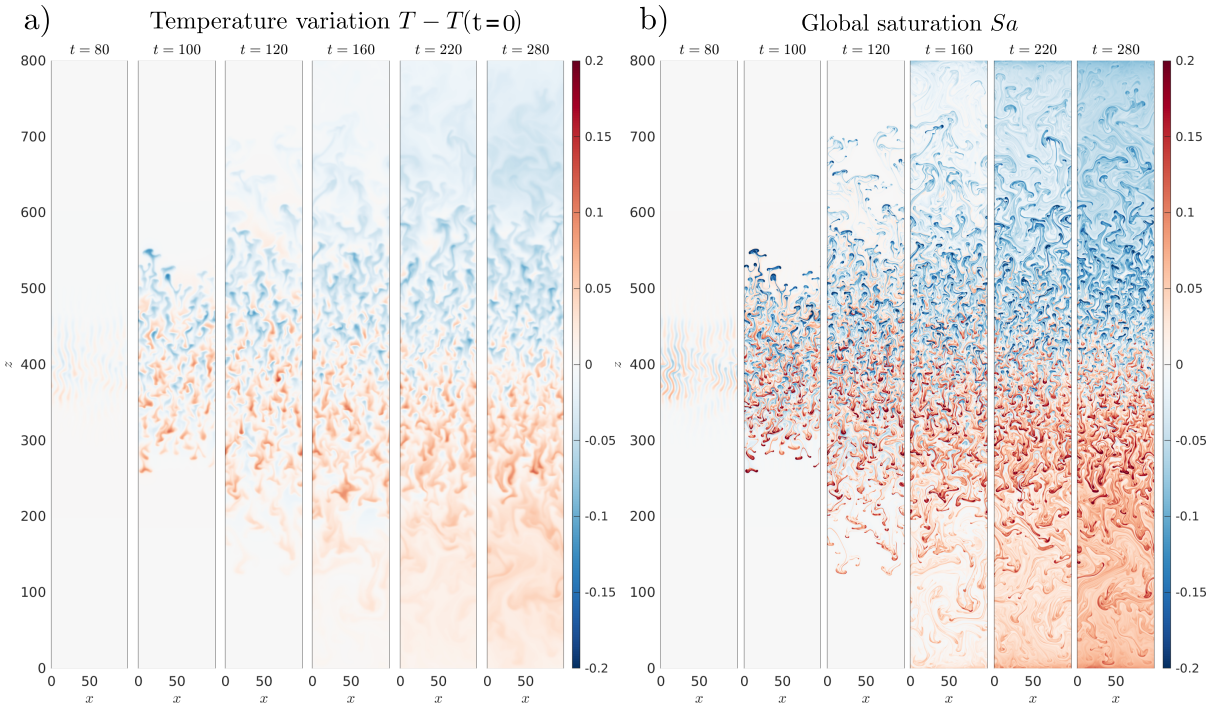

Figure 6.3: Snapshots of the scalar fields at various times: a) temperature variation from the initial profile and b) global saturation.

aries, forming warm, salty fingers below the interface and cold, fresher fingers above. The smaller diffusivity of the dissolved salt leads to sharper gradients at the finger-ambient interfaces of the salinity versus temperature fields (figure 6.2a-b). As the fingers propagate, saturation conditions change below and above the pycnocline. The warm fingers cool down rapidly in the hypolimnion thus becoming supersaturated, while the cold and fresh fingers warm up rapidly in the epilimnion thus becoming undersaturated. This leads to the formation of crystals (halite precipitation) in the hypolimnion 6.2c and to an undersaturated brine (halite dissolution) in the epilimnion 6.2d. The juxtaposition of the temperature variation $T - T(t = 0)$ and global saturation Sa in figure 6.3 reveals how the double-diffusive fingering instability can explain the profiles measured in the Dead Sea [6]: While the fingers transport heat from the top layer to the bottom layer, they also transport dissolved salt at a much faster rate, leading to a net and sustained change

in the saturation conditions. In fact, in the absence of double-diffusive fingers, purely diffusive fluxes would lead to the opposite situation, with more heat being transported from the epilimnion to the hypolimnion than dissolved salt.

Figures 6.4a-e show the scalar fields of temperature, solute salinity, halite crystal concentration, brine saturation ($S - Se$) and total saturation ($Sa = S + C - Se$) side to side at $t = 280$. We observe a double-diffusive convection regime at the center of the domain, with fingers propagating symmetrically away from the center. While the downward propagating fingers carry saltier and warmer fluid than the surroundings, those propagating upwards carry fresher, colder fluid. By $t = 280$ the influence of the computational boundaries is beginning to be felt, so that we terminate the simulation. Above the pycnocline, salinity gradients are significantly steeper than temperature gradients (figures 6.4a,b), due to the higher thermal diffusivity. Below the pycnocline, on the other hand, the T- and S-gradients are of similar magnitude. In this region, once S reaches saturation, it remains at Se. Since Se is a function of T, gradients of Se, and hence of S, scale with gradients of T. This is reflected by the halite concentration field, where crystals are mostly found in the lower half of the domain. Note that the initially saturated conditions and the absence of settling yield an approximately antisymmetric distribution for the undersaturation $S - Se(T)$ (figure 6.4d) in the epilimnion, and the halite concentration (figure 6.4c) in the hypolimnion. As a consequence, the combined saturation $Sa = C + S - Se(T)$ displays an antisymmetric distribution as well (figure 6.4e).

The time evolution of the system and the propagation in space of the diffusion-driven precipitation is shown in the horizontally averaged profiles of temperature change ($T - T_0$, where $T_0 = T(t = 0, z)$ is the initial temperature profile) and total saturation Sa (figure 6.4a-c). At early times (figure 6.4a), before fingers form, the faster diffusion of heat compared to salinity generates supersaturated conditions right above the metalimnion and undersaturated conditions right below. As fingers form, however, the net downward

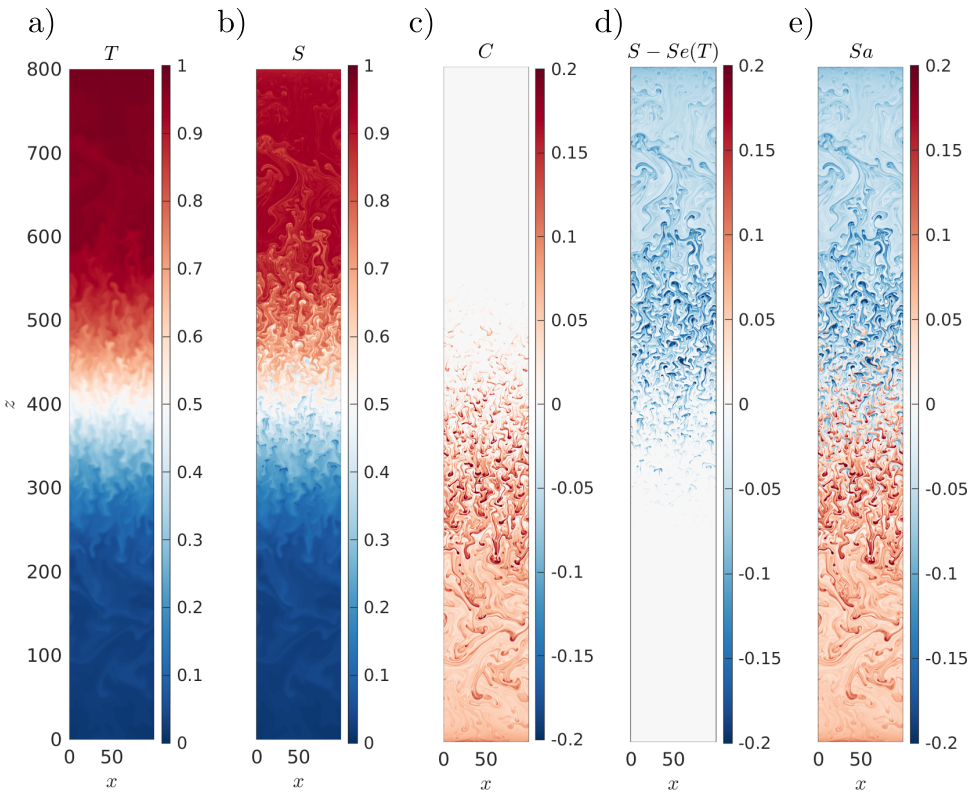

Figure 6.4: The nondimensional scalar fields, at $t = 280$: (a) temperature, (b) solute salinity, (c) halite crystal concentration, (d) brine saturation, and e) total saturation.

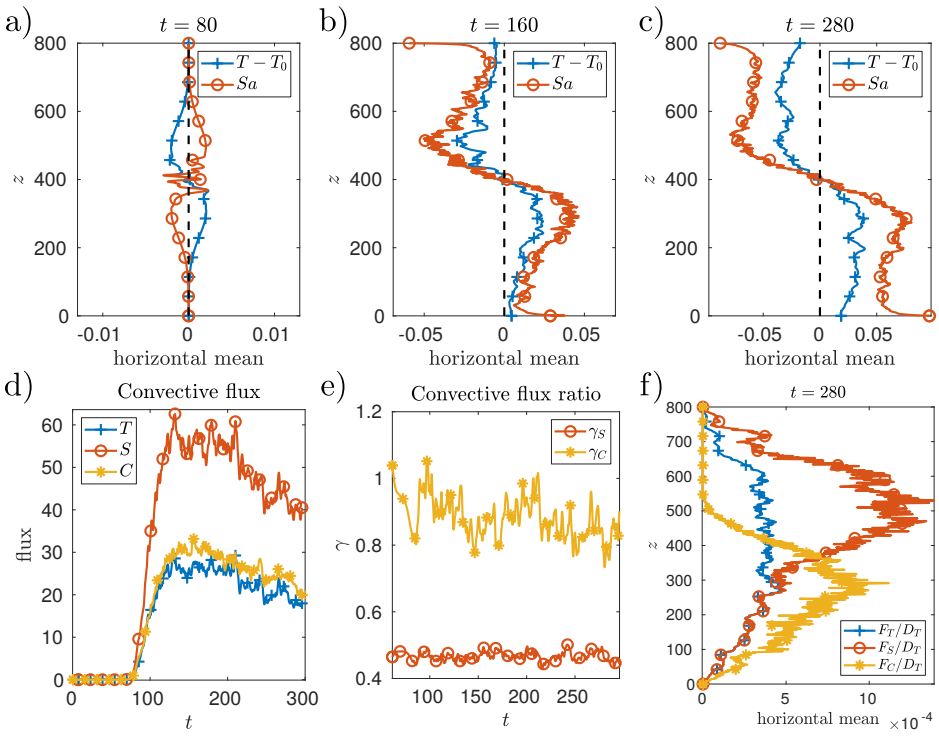

Figure 6.5: a-c) Vertical profiles of horizontally averaged temperature change $T - T(t = 0)$ and total saturation Sa at $t = 80$, 160 and 280. The vertical black dashed line indicates zero, to facilitate the interpretation of the profiles. Note that the x-axes are scaled differently for better visibility. d) Mean vertical convective fluxes of temperature, dissolved salt and halite as a function of time. e) Mean flux ratios as a function of time. f) Horizontally averaged vertical flux profiles of temperature, dissolved salt and halite.

transport of salt by the fingers becomes larger than the transport of heat and overstatturated conditions in the hypolimnion and undersaturated conditions in the epilimnion are obtained. The convective fluxes of temperature, dissolved salt and halite crystals can be computed as $F_T = \langle wT \rangle_\Omega$, $F_S = \langle wS \rangle_\Omega$ and $F_C = \langle wC \rangle_\Omega$, where $\langle \rangle_\Omega$ represents the averaging operator over the entire computational domain Ω. Figure 6.4d indicates that the vertical convective flux of salinity is roughly twice as strong as that of heat, consistent with the profiles shown in frames 6.4b,c. This is confirmed by figure 6.4e, which shows the flux ratios $\gamma_S = \frac{F_T}{F_S}$ and $\gamma_C = \frac{F_T}{F_C}$. Note that the fluxes are normalized by the diffusive flux of heat of the initial profile, i.e. $D_T = \langle \partial_z T_0 \rangle_\Omega$. The fluxes begin to grow once the system goes unstable, and reach maxima of $F_S \approx 60$ and $F_T, F_C \approx 30$ around $t = 130$. Interestingly, the flux ratios - calculated beyond the onset of instability at $t \approx 80$ - remain fairly constant in time. The thermal convective flux generated by double-diffusive fingering is more than twenty times the diffusive flux of the initial profiles imposed in the simulations. The solute salt flux is twice as large as the temperature flux, but the ratio of temperature to halite flux is close to unity. The horizontally-averaged vertical profiles of the vertical convective fluxes (figure 6.4f) show how the metalimnion converts the epilimnion's downward flux of dissolved salt into a downward halite flux in the hypolimnion. In summary, the simulation confirms the hypothesis of Arnon et al. [6] that double-diffusive salt fingering originating in the metalimnion results in the formation of antisymmetric total saturation profiles, with undersaturated brine in the epilimnion and a mixture of saturated brine and halite crystals in the hypolimnion.

6.3.2 The effect of settling

The above simulation demonstrates that salt-rich fingers induced by the classical double-diffusive convection instability can result in supersaturated conditions, and thus

in the precipitation of halite. Halite crystals are denser than the saturated brine, so that they will settle under the effect of gravity. We now explore the effects of this settling motion, under the assumption that the halite crystals have constant size and a dimensionless Stokes settling velocity v_s relative to the local fluid, as described in section 6.2. Towards this end, we will vary v_s in the range $0 < v_s < 2$. The upper bound is chosen so that the settling velocity is larger than the diffusive velocity, which has the potential to yield settling-dominated dynamics. $v_s = 2$ corresponds to a salt crystal diameter of approximately $0.03mm$, of the order of that observed by [138]. Settling should affect the overall flow via two key mechanisms: a) as the crystals exit a downward propagating finger, they will reduce the density of this finger and increase the density of the fluid they enter, and b) as the crystals enter fluid regions of different temperature and solute salinity, they will modify the local saturation level. The effects of settling on the saturation conditions in the Dead Sea are thus not obvious *a priori*.

Figure 6.6a shows the vertical profile of the horizontally averaged total saturation Sa at time $t = 210$, for settling velocities $v_s = 0, 0.5, 1$ and 2. Settling is seen to strongly reduce the oversaturation below the pycnocline, and to a lesser degree also the undersaturation above. As a result, settling breaks the antisymmetry of the saturation profile with respect to the pycnocline. As expected, the influence of settling is felt more strongly in the lower layer, where the negative buoyancy of the fingers is reduced as they lose halite. A particularly important consequence of this observation is that if the crystal size itself is proportional to the local oversaturation, as suggested by [138], halite precipitation induced by double-diffusive viscous fingering would reach an asymptote beyond which any additional growth in crystal size results in settling-induced crystal depletion from the fingers. Simulations in which the crystal size - and thus the settling velocity - varies with the local halite concentration are beyond the scope of the present study, but would constitute an interesting extension for testing this theory. The temperature profile

(figure 6.6b) reflects a similar impact of settling.

To gain additional insight into the effects of settling, we analyze the convective fluxes of heat and total salt in figure 6.6c-d: Larger settling velocities reduce the double-diffusive convective fluxes for both temperature and salinity. The settling flux (figure 6.6e), calculated as $F_{set} = \langle v_s C \rangle_\Omega$, becomes a significant contributor to the total salt flux as v_s is increased. Nevertheless the total salt flux, evaluated as the sum of the convective and settling fluxes $F_S + F_C + F_{set}$ (figure 6.6f), still decreases for larger v_s, consistent with our observation of reduced over- and undersaturation in figure 6.6a. In spite of the increased settling flux, the net effect of settling thus is a reduction in the convective and total salt fluxes, along with a loss of the antisymmetry in the saturation profile. The simulations demonstrate that the precipitation of large, rapidly settling halite crystals leads to weaker double-diffusive fingering, which in turn reduces the over- and undersaturation in the epilimninon and hypolimnion.

6.3.3 The effect of ζ

As discussed above, the density of the brine depends on the relative fractions of dissolved *vs.* crystallized salt. This effect is captured by the ratio ζ/β, whose value may vary as a function of temperature, and for different types of salt. Much like the salt depletion due to settling, the value of ζ/β directly impacts the buoyancy of the salt fingers. Its effect on the propagation of the salt-rich fingers is thus of particular importance when discussing the ability of double diffusion to generate the aforementioned saturation conditions in the epi- and hypolimnion. The saturation profiles and total salt fluxes for $\zeta/\beta = 0.83$, 1 and 1.17 are shown in figure 6.6g and h. Saturation is mostly affected in the lower layer, where an increase (decrease) of ζ/β leads to an increase (decrease) in saturation, so that precipitation of halite is accelerated (slowed down).

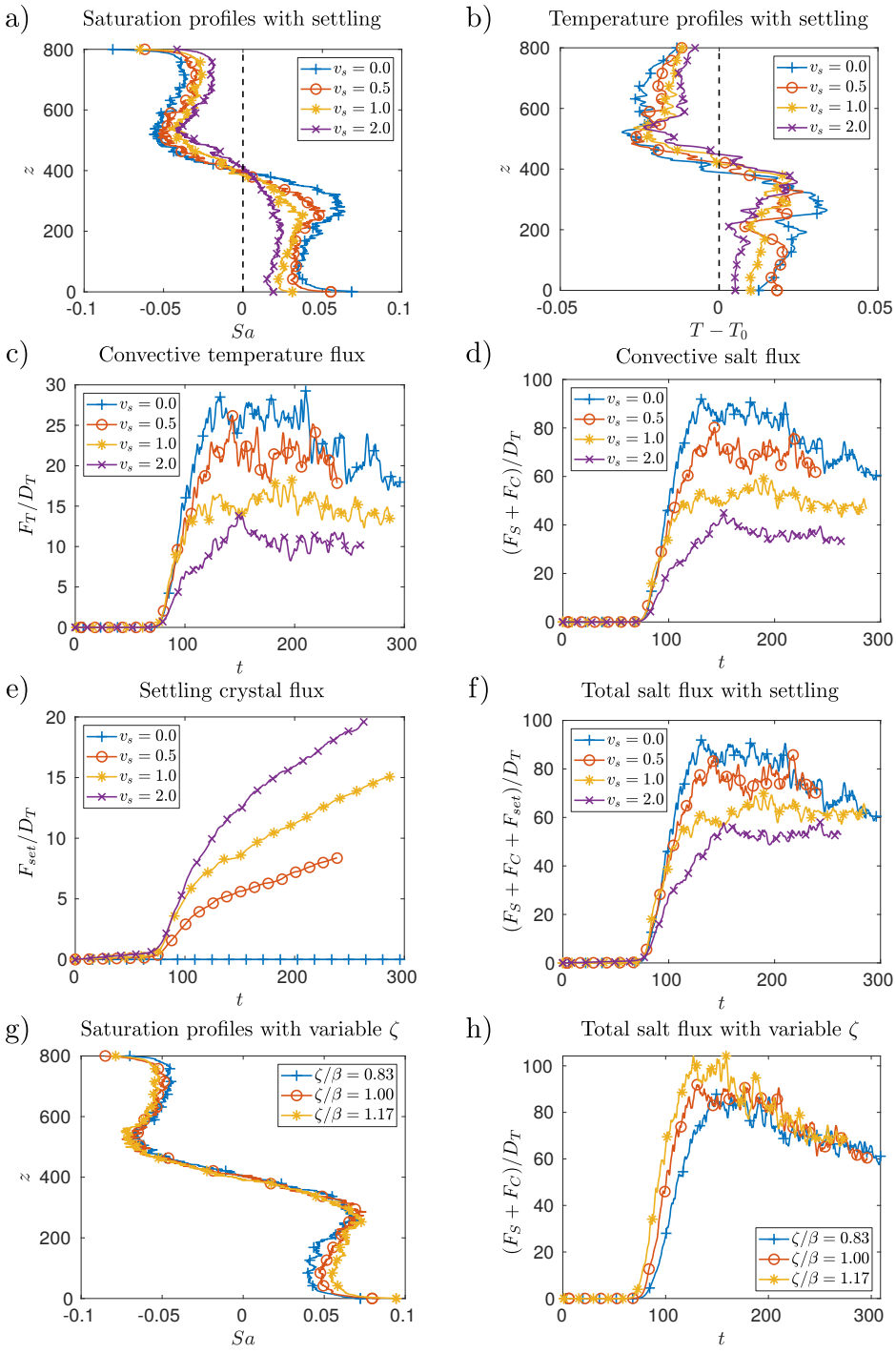

Figure 6.6: For $v_s = 0, 0.5, 1$ and 2: Vertical profile at $t = 210$ of a) total saturation Sa, and b) temperature change $T - T_0$. c) Scaled convective flux of temperature F_T/D_T. d) Scaled convective flux of salt $(F_S + F_C)/D_T$. e) Scaled settling flux of halite crystals F_{set}/D_T. f) Scaled total salt flux $(F_S + F_C + F_{set})/D_T$. For $\zeta/\beta = 0.83$, 1 and 1.17, and $v_s = 0$: g) Saturation profile Sa at $t = 210$; and h) scaled total salt flux as a function of time.

The time-resolved salt fluxes reveal that the discrepancy is mostly due to the delay in precipitation for $\zeta/\beta = 0.83$ and its acceleration for $\zeta/\beta = 1.17$ compared to the reference case. As halite precipitates, the density change impacts the buoyancy and thus the fluxes. Interestingly, for later times the convective fluxes are nearly identical for all values of ζ/β, which suggests that the overall impact of the added buoyancy for larger ratios ζ/β is small. We conclude that the influence of the ratio ζ/β on the precipitation of halite is smaller than that of settling.

6.4 Conclusions

We have employed two-dimensional direct numerical simulations in order to investigate the fluid dynamical processes governing halite precipitation in the Dead Sea. The simulations consider the configuration of warm, salty brine above cool, less salty brine, with both layers initially at saturation. Double-diffusive fingering causes a downward salinity flux that leads to undersaturation in the epilimnion, while the hypolimnion becomes oversaturated and precipitates halite. If the halite is assumed not to settle, and the slope of the density contours in the phase diagram is the same for under- and oversaturated brine ($\zeta = \beta$), the resulting saturation profile remains antisymmetric with respect to the metalimnion. The convective heat flux generated by the double-diffusive fingering is more than twenty times larger than the diffusive flux of the initial profiles imposed in the simulations. The convective flux of dissolved salt is about twice as large as the heat and halite fluxes.

Stokes settling of the halite crystals breaks the antisymmetry of the saturation profile. The crystals settle out of the downward propagating fingers that carry them, thus depleting them of some of their salinity and reducing their negative buoyancy. As a result, the convective downward flux of dissolved salt decreases, which suggests that halite

precipitation in the Dead Sea during the summer is limited by a stabilizing feedback mechanism: stronger supersaturation leads to increased precipitation and settling, which reduces the convective salinity flux and hence saturation.

The influence of the isopycnal slope ratio ζ/β in the phase diagram is less obvious. For $\zeta < \beta$ the negative buoyancy of the downward propagating fingers is reduced so that they slow down. On the other hand, this provides more time for heat to diffuse out of the fingers, which enhances halite precipitation. The simulations indicate that the resulting net effect of changing ζ/β on the downward halite flux is small.

The interfacial processes investigated here deliver dissolved salt from the epilimnion to the hypolimnion, thereby causing the hypolimnion to become supersaturated and to precipitate halite. While these processes are small-scale in nature, involving salt fingers that are millimeters to centimeters wide, we expect them to play an important role in the deposition of large-scale halite layers at the bottom of basins that are tens to hundreds of kilometers wide and tens to hundreds of meters thick. Hence, these processes can influence the dynamics of stratified hypersaline bodies of water subjected to a hydrological crisis, such as the present-day Dead Sea [6, 138, 139], or the Mediterranean during the Messinian Salinity Crisis [43]. A fundamental property of such evaporitic basins is that the thickness of the rock layers increase towards the deep parts of the basins. For instance, the Messinian salt layers below the Mediterranean Sea are found in the deeper regions of the basin and are significantly thinned or absent from the shallow parts. This architecture of the basin fill was suggested to be due to double diffusion salt fingering [140], based on field observations [138, 139, 6]. In this study we examined the small scale process of salt fingers instabilities and their role in the bulk properties of the underlying and overlying brine strata, and specifically in the formation of a "dipole" structure of undersaturated upper layer and supersaturated lower layer. The present simulations are limited to relatively short periods of time over which only a small amount of halite is

produced, since the prescribed boundary conditions do not take into account the long term effects (e.g. seasonal) of continuous evaporation and heat exchange with the atmosphere. Clearly, in reality, the proper far field boundary conditions for a basin subjected to hydrological crisis includes continuous charging of dissolved salts from above due to evaporation, which in turn will enhance the conditions for the double diffusive process investigated here. A new approach in which the impact of double-diffusive convection on the long-term precipitation of halite is modeled and which allows for the investigation of seasonal charging through evaporation will be be object of a future study. Nevertheless, it is observed that when evaporation "charges" these basins with dissolved salt at the water surface, double-diffusive fingering delivers this dissolved salt through the undersaturated epilimnion into the saturated hypolimnion. Consequently, during the crisis, the undersaturated epilimnion dissolves halite deposits whereas the hypolimnion precipitates halite layers, resulting in basin scale increase of the halite layer thickness below the thermocline at the expense of dissolution from the shallow basin margins, i.e. "halite focusing" [140].

The research was funded by the Israel Science Foundation grant number 1471/18, by the National Science Foundation under grants CBET-1438052 and CBET-1803380, and by the Army Research Office under grant W911NF-18-1-0379. The authors would also like to express their appreciation to the reviewers, associate editor and editor for their feedback and suggestions, which helped improve the reach and scope of the conclusions presented in this work. Interested readers can access the raw data at `https://datadryad.org/stash/dataset/doi:10.25349/D99G6F`.

Chapter 7

On large-scale instabilities in sedimentary double-diffusive convection

Authorship of this work is shared with Prof. Pascale Garaud, Philip Edel and Prof. Eckart Meiburg. This work is described in a manuscript in preperation for submission in *Journal of Fluid Mechanics*.

7.1 Introduction

Double-diffusive convection occurs when the density stratification of a gravitationally stable water column is caused by a fast diffusing scalar and a slowly diffusing scalar of opposite contributions to the stability [146, 160, 133, 122]. In the case where the fast and slow diffuser stabilize and destabilize the water column respectively, the resulting instability is called "double-diffusive fingering". In the opposite case, the instability is called double-diffusive convection in the diffusive regime. The former is commonly

encountered in the upper layer of the tropical and subtropical ocean. The temperature and salinity both decrease with depth in the stable water column, thus creating the necessary conditions for double-diffusive salt fingering. Fingering convection has been the object of much attention in the last 60 years, in laboratory experiments [159, 93, 84], theoretical models [9, 132] and direct numerical simulations [172, 135, 100, 148, 156, 124]. Of particular interest to the present study is the development of secondary, large-scale instabilities from a state of saturated fingering, such as thermohaline staircases [153, 131, 83, 122, 145] or gravity waves [147, 64, 156]. The unified mean-field theory of Traxler et al. [156] following the previous efforts of Radko [122] introduced a general formalism containing all previous theories on large-scale double-diffusive instabilities. However, the theory was developed with the heat-salt system in mind and therefore does not include settling of one of the scalar fields. The particular case where suspended particles, or sediment, play the role of the slow diffuser is referred to as sedimentary fingering convection [69]. While qualitatively similar to traditional double-diffusive convection [51], sedimentary fingering exhibits unique dynamics [21, 22, 125, 1]. The work of Reali et al. [125] was the first and is to the best of our knowledge the only study that introduced a mean-field theory in presence of settling. This theory however is based on the work of Radko [122] in which collective modes are not investigated.

Here, we derive a unified mean-field theory for double-diffusive instabilities in the presence of settling, in the formalism of Traxler et al. [156]. This unified theory characterizes the stability of the system in its globality and recovers previous mean-field theory results of Radko [122], Stern et al. [148], Traxler et al. [156], Reali et al. [125][1]. Our theory further reveals the existence of a new settling-driven collective instability that differs from Stern's particle-free collective instability. We show that this instability arises from

[1]Traxler further considers lateral gradients thus allowing their theory to also recover the Walsh and Ruddick [169] theory of intrusions.

the presence of a non-zero settling velocity term in the solution to the mean-field growth rate equation, even when the mean-field parameters are computed for a collectively stable system. We further examine the properties and scaling of the oscillation frequency of the new collective mode.

7.2 Modelling approach

7.2.1 Equation of state

We consider a multiphase fluid comprised of dense particles in a saline ambient fluid. The equation of state (EoS) of the liquid phase depends on the local salinity $\tilde{S}$ such that the density of the liquid is

$$\rho_l(\tilde{S}) = \rho_f + \tilde{\alpha}\tilde{S} \tag{7.1}$$

where $\tilde{\alpha} = \partial\rho_l/\partial\tilde{S}$ is the constant volumetric expansion coefficient and ρ_f is the reference density of fresh water. We define a maximum salinity $\tilde{S}_a$ in the domain for which $\rho_l(\tilde{S}_a) = \rho_a$. A non-dimensional salinity $S = \tilde{S}/\tilde{S}_a$ is then defined and equation 7.1 becomes

$$\rho_l(S) = \rho_f(1 + \alpha S), \tag{7.2}$$

where $\alpha = \frac{\rho_a - \rho_f}{\rho_f}$. This non-dimensional salinity is thus 0 in the absence of salt and 1 where salinity is maximal. The overall density of a representative fluid volume is expressed as

$$\rho = (1 - \phi_p)\rho_l(S) + \phi_p\rho_p \tag{7.3}$$

where ρ_p is the density of the particles, and ϕ_p is the volume fraction of particles. One can express a reduced density as

$$\rho' = \frac{\rho - \rho_f}{\rho_f} = \phi_p \frac{\rho_p - \rho_f}{\rho_f} + (1 - \phi_p)\alpha S. \tag{7.4}$$

Following the physical approach of previous studies [125, 1], we only consider small volume fractions of particles such that $\phi_p \ll 1$, and we assume that the particles are sufficiently small and non-inertial to be adequately represented as a continuous scalar field. Let Φ be the maximum particle volume fraction initially present in the volume. We thus define a concentration of particles as

$$C = \frac{\phi_p}{\Phi}. \tag{7.5}$$

In this continuous approach, we further assume the salinity affects the overall density such that the reduced density is simplified to

$$\rho' = \alpha S + \beta C \tag{7.6}$$

where

$$\beta = \Phi \frac{\rho_p - \rho_f}{\rho_f}, \ \alpha = \frac{\rho_a - \rho_f}{\rho_f}. \tag{7.7}$$

Note that the coefficients α, β and the variables S and C are all non-dimensional under this approach.

7.2.2 Illustration: The ash-cloud experiments [26]

The motivation for developing a generalized mean-field theory in the presence of settling particles in a double-diffusive system came from the problem of the ash-cloud experiments of Carazzo and Jellinek [25, 26]. The dynamics of cloud formation are beyond the scope of this work. Rather, we consider a simplified model for an initially quiescent cloud of particles in salt water in which both the particle concentration and salinity are linear functions of height, with salt being the stabilizing component and particles being the destabilizing component (see figure 7.1). The choice of parameters used to illustrate the stability of the system stems from density measurements conducted over the full height of the stably established cloud of experiment number 5 of Carazzo and Jellinek [26]. From this experimental data, we infer the reference density of fresh water ρ_f ($\approx 996\,\mathrm{kg/m^3}$), the reference density of salty water at the bottom of the tank ρ_a ($\approx 1008\,\mathrm{kg/m^3}$), the density at the top and bottom of the cloud ρ_b ($\approx 1005\,\mathrm{kg/m^3}$) and ρ_t ($\approx 1000\,\mathrm{kg/m^3}$) and the thickness of the cloud h ($\approx 20\,\mathrm{cm}$). There are no directly available measurements of salinity and particle concentration at the top and bottom of the cloud, referred to as S_t, S_b and C_t, C_b. During formation of the cloud in the experiments, strong entrainment occurs at the interface between the upward jet and the ambient salt water. During the process of cloud formation, the particle-laden jet initially overshoots the line of neutral buoyancy before collapsing back, thereby leading to most particles being at the top of the cloud [26]. We thus consider that the maximal volume fraction of particles is initially found at the top of the cloud, such that the non-dimensional concentration at the top of the cloud is $C_t = 1$. We further assume that the overall density elevation at the top of the cloud is only due to the presence of particles (i.e., that $S_t = 0$). This assumes that in the center of the jet, no ambient salt water was entrained and thus the top of the cloud is without salinity. Similarly, we consider that

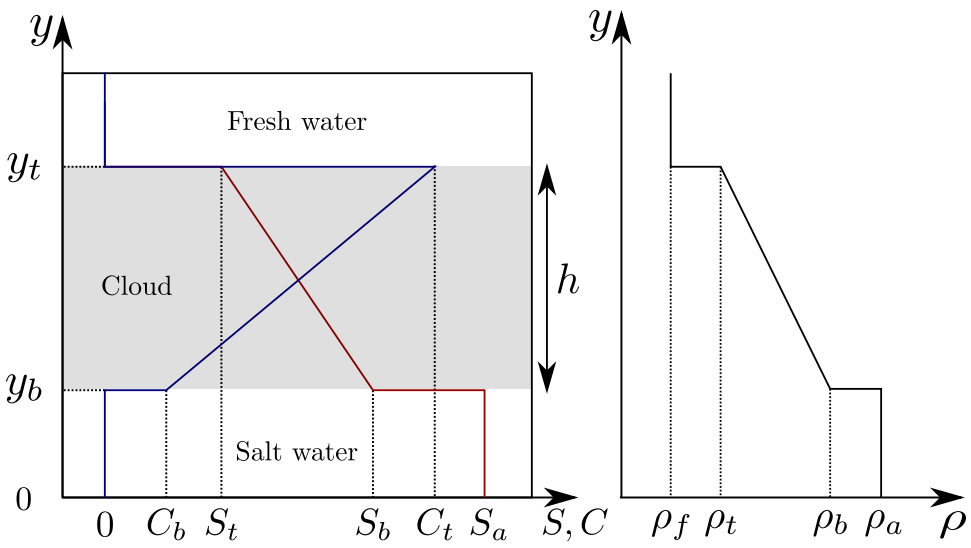

Figure 7.1: Sketch of the ash-cloud experiment [26] simplified to consider linear profiles of salinity and particle concentration.

particle concentration is minimal at the bottom of the cloud. Given that the phenomena of particle diffusion and sedimentation have effects on the cloud scale at much larger times than the time of cloud formation, we suppose that $C_b = 0$. Under these assumptions we find

$$S_t = 0, \quad S_b = \frac{\rho_b - \rho_f}{\rho_a - \rho_f} \approx 0.75, \quad C_t = 1, \quad C_b = 0. \tag{7.8}$$

The corresponding values for α and β are

$$\alpha = \frac{\rho_a - \rho_f}{\rho_f} \approx 0.012, \quad \beta = \frac{\rho_b - \rho_f}{\rho_f} \approx 0.004. \tag{7.9}$$

Within the cloud, the y-gradients of salinity and particle concentration are thus $\bar{S}_y = (S_t - S_b)/h \approx -3.75 m^{-1}$ and $\bar{C}_y = (C_t - C_b)/h \approx 5 m^{-1}$.

7.2.3 Governing equations

We consider a two-dimensional domain of fluid initially at rest and a Cartesian coordinate system (x,y) with y increasing upward. We assume that the fluid is characterized

by a constant kinematic viscosity ν ($\approx 10^{-6}\,\mathrm{m^2 s^{-1}}$) and a density ρ, which depends on two diffusive components : salinity S and particle concentration C, through the equation of state 7.6. The governing equations are the two-dimensional Navier-Stokes equations for an incompressible flow. The density variations due to salinity and particle-loading are considered to be small such that the Boussinesq approximation is employed and a buoyancy source term is added to the momentum equations.

The salinity S and the particle concentration C each follow an advection-diffusion equation. Under the aforementioned assumptions, the motion of the particles relative to the fluid flow is due to a constant Stokes settling velocity. The velocity of the particle scalar field is thus $\boldsymbol{u}_p = \boldsymbol{u} - V_{st}\boldsymbol{e}_y$, where V_{st} is the constant Stokes settling velocity. For spherical particles of density ρ_p and radius R, the Stokes settling velocity is given by

$$V_{st} = \frac{2}{9}\frac{(\rho_p - \rho_f)}{\rho_f}\frac{gR^2}{\nu}. \tag{7.10}$$

The set of governing equations is therefore given by

$$\nabla \cdot \boldsymbol{u} = 0, \tag{7.11}$$

$$\frac{\partial \boldsymbol{u}}{\partial t} + (\boldsymbol{u} \cdot \nabla)\boldsymbol{u} = -\frac{1}{\rho_f}\nabla p + \nu \Delta \boldsymbol{u} + (\alpha S + \beta C)\boldsymbol{g}, \tag{7.12}$$

$$\frac{\partial C}{\partial t} + \boldsymbol{u} \cdot \nabla C - V_{st}\frac{\partial C}{\partial y} = \kappa_c \Delta C, \tag{7.13}$$

$$\frac{\partial S}{\partial t} + \boldsymbol{u} \cdot \nabla S = \kappa_s \Delta S. \tag{7.14}$$

where $\boldsymbol{u} = (u, v)$ denotes the velocity field, p the pressure, $\boldsymbol{g} = -g\boldsymbol{e}_y$ is the acceleration due to gravity ($g \approx 9.81\,\mathrm{ms^{-2}}$), κ_s and κ_c are the salt and particle diffusivities, assumed here to be constant ($\kappa_s \approx 10^{-9}\,\mathrm{m^2 s^{-1}}$ and $\kappa_c \approx 10^{-14}\,\mathrm{m^2 s^{-1}}$) [26].

7.2.4 Initial and boundary conditions

The fluid is initially at rest and salinity and particle concentration are initially x-independent. Local flow dynamics are controlled by double-diffusive processes, which, as will be derived in the following sections, act on length scales of mm. The vertical extent of the cloud in Carazzo and Jellinek [26] is thus several orders of magnitude larger than the initial double-diffusive dynamics and is not expected to be a determinant parameter in the formation of layers. We thus only consider a section of the cloud as our numerical domain such that the initial background salinity and concentration profiles have constant y-gradients equal to $\bar{S}_y$ and $\bar{C}_y$ respectively. Periodic boundary conditions are imposed in the x-direction as well as in the y-direction for the fluctuation from the background profiles. The two-dimensional window within the cloud is of length L_x and height $L_y \ll h$ where h is the depth of the cloud.

7.2.5 Non-dimensional perturbation equations

From here on we decompose all the fields into a background component and a perturbation component such that

$$S = \bar{S}_y y + \tilde{S}, \quad C = \bar{C}_y(y + V_{st}t) + \tilde{C}, \quad p = p_0 + \tilde{p}, \quad \boldsymbol{u} = \tilde{\boldsymbol{u}}. \tag{7.15}$$

Injecting into the governing equations 7.11-7.14, the governing equations for the perturbations become

$$\nabla \cdot \tilde{\boldsymbol{u}} = 0, \tag{7.16}$$

$$\frac{\partial \tilde{\boldsymbol{u}}}{\partial t} + (\tilde{\boldsymbol{u}} \cdot \nabla)\tilde{\boldsymbol{u}} = -\frac{1}{\rho_f}\nabla \tilde{p} + \nu \Delta \tilde{\boldsymbol{u}} - (\alpha \tilde{S} + \beta \tilde{C}) g \boldsymbol{e}_y, \tag{7.17}$$

$$\frac{\partial \tilde{C}}{\partial t} + \tilde{\boldsymbol{u}} \cdot \nabla \tilde{C} + v \bar{C}_y - V_{st}\frac{\partial \tilde{C}}{\partial y} = \kappa_c \Delta \tilde{C}, \tag{7.18}$$

$$\frac{\partial \tilde{S}}{\partial t} + \tilde{\boldsymbol{u}} \cdot \nabla \tilde{S} + v \bar{S}_y = \kappa_s \Delta \tilde{S}. \tag{7.19}$$

where the background pressure p_0 has been chosen such that

$$\nabla p_0 = -\rho_f g \left(\alpha \bar{S}_y y + \beta \bar{C}_y (y + V_{st} t)\right) \boldsymbol{e}_y.$$

The perturbation equations 7.16-7.19 are made non-dimensional following the formalism of Radko [123]. A velocity scale $U = \frac{\kappa_s}{d}$ and time scale $T = \frac{d^2}{\kappa_s}$ are introduced based on the fast diffuser. The diffusion length is

$$d = \left(\frac{\nu \kappa_s}{\alpha g |\bar{S}_y|}\right)^{\frac{1}{4}}. \tag{7.20}$$

Although salinity and concentration are already non-dimensional quantities, it is convenient to re-scale them with $d|\bar{S}_y|$ and $\frac{\alpha}{\beta} d|\bar{S}_y|$ respectively. By choosing $\delta p = \rho_f \nu \kappa_s / d^2$ as the pressure scale, the non-dimensional equations become

$$\nabla \cdot \tilde{\boldsymbol{u}} = 0, \tag{7.21}$$

$$\frac{1}{Pr}\left(\frac{\partial \tilde{\boldsymbol{u}}}{\partial t} + (\tilde{\boldsymbol{u}} \cdot \nabla)\tilde{\boldsymbol{u}}\right) = -\nabla \tilde{p} + \Delta \tilde{\boldsymbol{u}} - (\tilde{S} + \tilde{C})\boldsymbol{e_y}, \tag{7.22}$$

$$\frac{\partial \tilde{C}}{\partial t} + \tilde{\boldsymbol{u}} \cdot \nabla \tilde{C} + \frac{v}{R_0} - V\frac{\partial \tilde{C}}{\partial y} = \tau \Delta \tilde{C}, \tag{7.23}$$

$$\frac{\partial \tilde{S}}{\partial t} + \tilde{\boldsymbol{u}} \cdot \nabla \tilde{S} - v = \Delta \tilde{S}. \tag{7.24}$$

where $\tau = \frac{\kappa_c}{\kappa_s}$ is the diffusivity ratio, $Pr = \frac{\nu}{\kappa_s}$ ($\approx 10^3$) is the Prandtl number[2] and $V = \frac{V_{st}d}{\kappa_s}$ is the non-dimensional settling velocity. The density ratio is $R_0 = \frac{\alpha|\bar{S}_y|}{\beta|\bar{C}_y|}$ (≈ 2.25 in the reference setup of the ash-cloud experiments of Carazzo and Jellinek [26]).

The system 7.21-7.24 is identical to that of Alsinan et al. [1]), to the only exception that the authors considered a temperature-particle system. This impacts the signs of initial y-gradients, leading to sign differences in the perturbation equations. For constancy with the literature [156, 1, 125], we define a new variable $\tilde{\Theta}$ analogous to the temperature in classic double diffusive convection. This new variable is simply defined as $\tilde{\Theta} = -\tilde{S}$. From a physics standpoint, the salinity gradient is negative, and thus salinity contributes to making the system more stable. The pseudo-temperature has a positive gradient and also contributes to making the system more stable. This allows us to re-write equations 7.21-7.24 as

[2]Although it is understood here as a Schmidt number, we choose to call it a Prandtl number in order to stay consistent with the existing literature on double-diffusion, which is mainly focused on heat-salt systems.

$$\nabla \cdot \tilde{\boldsymbol{u}} = 0, \tag{7.25}$$

$$\frac{1}{Pr}\left(\frac{\partial \tilde{\boldsymbol{u}}}{\partial t} + (\tilde{\boldsymbol{u}} \cdot \nabla)\tilde{\boldsymbol{u}}\right) = -\nabla \tilde{p} + \Delta \tilde{\boldsymbol{u}} + (\tilde{\Theta} - \tilde{C})\boldsymbol{e_y}, \tag{7.26}$$

$$\frac{\partial \tilde{C}}{\partial t} + \tilde{\boldsymbol{u}} \cdot \nabla \tilde{C} + \frac{v}{R_0} - V\frac{\partial \tilde{C}}{\partial y} = \tau \Delta \tilde{C}, \tag{7.27}$$

$$\frac{\partial \tilde{\Theta}}{\partial t} + \tilde{\boldsymbol{u}} \cdot \nabla \tilde{\Theta} + v = \Delta \tilde{\Theta}. \tag{7.28}$$

This model is now identical to the system of equations used by Alsinan et al. [1], Reali et al. [125] , which further reduces to the standard double-diffusive equation when $V = 0$ (e.g. [123]).

7.2.6 Numerical method

We use a hybrid pseudospectral-compact finite differences spatial scheme combined with a low-storage Runge-Kutta/Crank-Nicolson time stepping method to solve the set of 2D equations. It uses stream functions and vorticity. This code was designed to run efficiently on massively-parallel supercomputers using the *MPI* and *FFTW* libraries. Small-scale simulations were run on 12 cores on a local server while large-scale simulations were run on up to 2048 cores on the TACC Stampede2 supercomputer.

7.3 Generalized stability analysis

7.3.1 Small-scale instability

In the absence of settling, a linear stability analysis of the linearized non-dimensional equations (eq. 7.25 to 7.28) yields the well-known stability condition to double-diffusive

fingering, i.e. that $R_0 < 1/\tau$ [123]. Alsinan et al. [1] derived the linear stability of the linear background stratification in the presence of settling and showed that settling leads to a new instability mode. This instability leads to the growth of inclined waves, and is active even when the two scalars diffuse at identical rates. If the scalar components have unequal diffusivities, the settling-driven instability mode competes with the elevator mode of the classical fingering instability. The linear stability of the system is derived by linearizing the governing equations and using normal modes in the form

$$(u, v, S, C) \sim \Re\left((\hat{u}, \hat{v}, \hat{S}, \hat{C}) \exp(\lambda t + ilx + iky)\right) \tag{7.29}$$

where $\lambda \in \mathbb{C}$ is the complex growth rate, l the horizontal wavenumber and k the vertical wavenumber (so as to be consistent with the literature, see Alsinan et al. [1]). The resulting cubic equation for the growth rate of small-scale instabilities in the presence of settling is found to be

$$\lambda^3 + a_2\lambda^2 + a_1\lambda + a_0 = 0, \tag{7.30}$$

where

$$\begin{aligned}
a_2 &= (1 + \tau + Pr)|\boldsymbol{k}|^2 - ikV, \\
a_1 &= (\tau + Pr + \tau Pr)|\boldsymbol{k}|^4 + \frac{Prl^2}{|\boldsymbol{k}|^2}(1 - R_0^{-1}) - ikV|\boldsymbol{k}|^2(1 + Pr), \\
a_0 &= \tau Pr|\boldsymbol{k}|^6 - Prl^2(R_0^{-1} - \tau) - \frac{ikVPr}{|\boldsymbol{k}|^2}(l^2 + |\boldsymbol{k}|^6),
\end{aligned}$$

and $|\boldsymbol{k}|^2 = k^2 + l^2$.

7.3.2 Mean-field theory

Large-scale structures such as intrusions, collective instabilities or the γ-instability can emerge from the fingering regime of double diffusion. Mean-field models have been employed to investigate these instabilities, under the foundational assumption that they operate on scales much larger than that of individual fingers. By considering the spatial average over several finger widths of the small-scale fields, we can construct the evolution equations of the large-scale fields and analyse their stability through linear stability analysis. Following the work of Traxler et al. [156], we obtain the generalized mean-field equations by averaging the set of non-dimensional equations 7.25-7.28, which govern the dynamics of perturbations from a linearly stratified base state. The equations should be averaged over space-time scales that greatly exceed the finger scales. We refer to section Appendix B for more a detailed description of the averaging of the fingering regime. The averaging operator marked as $\overline{}$ is assumed to commute with temporal and spatial differentiation operators. Each field $\boldsymbol{u}$, p, Θ, C can be separated into a space-time average and a fluctuation from this average, i.e,

$$\tilde{\boldsymbol{u}} = \overline{\tilde{\boldsymbol{u}}} + \boldsymbol{u}', \quad \tilde{p} = \overline{\tilde{p}} + p', \quad \tilde{\Theta} = \overline{\tilde{\Theta}} + \Theta' \quad \text{and} \quad \tilde{C} = \overline{\tilde{C}} + C'.$$

Fluctuations from the average are such that $\overline{\boldsymbol{u}'} = \overline{p'} = \overline{\Theta'} = \overline{C'} = 0$. The averaged governing equations are, omitting the tilde, given by

$$\nabla \cdot \overline{\boldsymbol{u}} = 0, \tag{7.31}$$

$$\frac{1}{Pr}\left(\frac{\partial \overline{\boldsymbol{u}}}{\partial t} + (\overline{\boldsymbol{u}} \cdot \nabla)\overline{\boldsymbol{u}}\right) = -\nabla \overline{p} + \Delta \overline{\boldsymbol{u}} + (\overline{\Theta} - \overline{C})\boldsymbol{e}_y, \tag{7.32}$$

$$\frac{\partial \overline{C}}{\partial t} + \overline{\boldsymbol{u}} \cdot \nabla \overline{C} + \frac{\overline{v}}{R_0} - V\frac{\partial \overline{C}}{\partial y} + \frac{\partial F_c}{\partial y} = \tau \Delta \overline{C}, \tag{7.33}$$

$$\frac{\partial \overline{\Theta}}{\partial t} + \overline{\boldsymbol{u}} \cdot \nabla \overline{\Theta} + \overline{v} + \frac{\partial F_\theta}{\partial y} = \Delta \overline{\Theta}. \tag{7.34}$$

where $\boldsymbol{R}_{ij} = \overline{u_i' u_j'}$ is the Reynolds stress tensor, $\boldsymbol{F}_c = \overline{\boldsymbol{u}' C'}$ is the turbulent flux of particles and $\boldsymbol{F}_\theta = \overline{\boldsymbol{u}' \Theta'}$ is the turbulent flux of salinity. Similarly to Traxler et al. [156], two hypotheses are made: (i) the Reynolds stress term is small and can be neglected (this can be verified *a posteriori*, see Appendix B) and (ii) the vertical turbulent fluxes of particles and salt $F_c = \overline{v' C'}$ and $F_\theta = \overline{v' \Theta'}$ are much more significant than the horizontal fluxes $\overline{u' C'}$ and $\overline{u' \Theta'}$, such that $\boldsymbol{F}_c \approx F_c \boldsymbol{e}_y$ and $\boldsymbol{F}_\theta \approx F_\theta \boldsymbol{e}_y$. This can also be verified *a posteriori* (see Appendix B). Assuming the problem is 2D allows us to eliminate the explicit dependence on pressure by cross-differentiation of the x and y momentum equations. In order to express the flux terms $\frac{\partial F_c}{\partial y}$ and $\frac{\partial F_\theta}{\partial y}$ as a function of the mean field parameters, we introduce as in Radko [122]

$$Nu = \frac{F_\theta - (1 + \frac{\partial \overline{\Theta}}{\partial y})}{-(1 + \frac{\partial \overline{\Theta}}{\partial y})} \quad \text{and} \quad \gamma = \frac{F_\theta}{F_c}, \tag{7.35}$$

where Nu is the Nusselt number[3] and γ is the turbulent flux ratio. The Nusselt number is to be understood as the ratio of the total salt (or pseudo-temperature) flux $F_\theta^{tot} = F_\theta - (1 + \frac{\partial \overline{\Theta}}{\partial y})$ (talking into account both fluctuation and molecular fluxes) to the molecular

[3]Like the Prandtl number, this is a Nusselt number only to be consistent with the existing literature.

salt flux. The particle and salt turbulent fluxes can thus be expressed as

$$F_\theta = (1 - Nu)\left(1 + \frac{\partial\overline{\Theta}}{\partial y}\right), \tag{7.36}$$

$$F_c = \frac{1}{\gamma}(1 - Nu)\left(1 + \frac{\partial\overline{\Theta}}{\partial y}\right). \tag{7.37}$$

The key hypothesis of the mean-field theory [122, 156] resides in assuming that for given values of Pr, τ and V, Nu and γ depend only on the local density ratio defined as

$$R_\rho = R_0\left(\frac{1 + \frac{\partial\overline{\Theta}}{\partial y}}{1 + R_0\frac{\partial\overline{C}}{\partial y}}\right) \tag{7.38}$$

The validity of this assumption crucially depends on the fingers being short compared with the scale of variation of $\bar{\Theta}$ and $\bar{C}$. By assuming that $R_0\frac{\partial\overline{C}}{\partial y} \ll 1$ we linearize this expression to

$$R_\rho = R_0 + R'_\rho \quad \text{where} \quad R'_\rho = R_0\left(\frac{\partial\overline{\Theta}}{\partial y} - R_0\frac{\partial\overline{C}}{\partial y}\right).$$

Then we linearize Nu and $1/\gamma$ to

$$Nu(R_\rho) \approx Nu(R_0) + \frac{\mathrm{d}Nu}{\mathrm{d}R_\rho}(R_0)R'_\rho,$$

$$\frac{1}{\gamma(R_\rho)} \approx \frac{1}{\gamma(R_0)} + \frac{\mathrm{d}(1/\gamma)}{\mathrm{d}R_\rho}(R_0)R'_\rho.$$

By injecting these expressions into equations 7.36 we finally obtain linearized expressions for the turbulent fluxes:

$$F_\theta = -A_2\left(\frac{\partial\overline{\Theta}}{\partial y} - R_0\frac{\partial\overline{C}}{\partial y}\right) - (Nu_0 - 1)\left(1 + \frac{\partial\overline{\Theta}}{\partial y}\right), \tag{7.39}$$

$$F_c = -A_1\left(\frac{\partial\overline{\Theta}}{\partial y} - R_0\frac{\partial\overline{C}}{\partial y}\right)(Nu_0 - 1) + \frac{1}{\gamma_0}F_\theta, \tag{7.40}$$

where we have introduced the four constants $Nu_0 = Nu(R_0)$, $\gamma_0 = \gamma(R_0)$, $A_1 = R_0 \frac{\mathrm{d}(1/\gamma)}{\mathrm{d}R_\rho}(R_0)$ and $A_2 = R_0 \frac{\mathrm{d}Nu}{\mathrm{d}R_\rho}(R_0)$.

The system of equations 7.31 can now be linearized to

$$
\begin{aligned}
&\frac{\partial \overline{u}}{\partial x} + \frac{\partial \overline{v}}{\partial y} = 0, \\
&\left(\frac{1}{Pr}\frac{\partial}{\partial t} - \Delta\right)\left(\frac{\partial \overline{u}}{\partial y} - \frac{\partial \overline{v}}{\partial x}\right) + \frac{\partial \overline{\Theta}}{\partial x} - \frac{\partial \overline{C}}{\partial x} = 0, \\
&\frac{\partial \overline{C}}{\partial t} + \frac{\overline{v}}{R_0} - V\frac{\partial \overline{C}}{\partial y} + \frac{1}{\gamma_0}(\Delta\overline{\Theta} - \overline{v} - \frac{\partial \overline{\Theta}}{\partial t}) - A_1\left(\frac{\partial^2 \overline{\Theta}}{\partial y^2} - R_0\frac{\partial^2 \overline{C}}{\partial y^2}\right)(Nu_0 - 1) - \tau\Delta\overline{C} = 0, \\
&\frac{\partial \overline{\Theta}}{\partial t} + \overline{v} - (Nu_0 - 1)\frac{\partial^2 \overline{\Theta}}{\partial y^2} - A_2\left(\frac{\partial^2 \overline{\Theta}}{\partial y^2} - R_0\frac{\partial^2 \overline{C}}{\partial y^2}\right) - \Delta\overline{\Theta} = 0.
\end{aligned}
$$

The linearized system is then examined by using normal modes in the form

$$(\overline{u}, \overline{v}, \overline{\Theta}, \overline{C}) \sim \Re\left((\hat{u}, \hat{v}, \hat{\Theta}, \hat{C})\exp(\lambda t + ilx + iky)\right)$$

where $\lambda \in \mathbb{C}$ is the complex growth rate and l and k are horizontal and vertical wavenumbers respectively. After algebraic manipulation, we obtain the following cubic eigenvalue equation

$$\lambda^3 + a_2\lambda^2 + a_1\lambda + a_0 = 0, \tag{7.41}$$

where

$$
\begin{aligned}
a_2 &= b_1 + Pr|\boldsymbol{k}|^2, \\
a_1 &= b_2 + Pr|\boldsymbol{k}|^2 b_1 + Pr\frac{l^2}{|\boldsymbol{k}|^2}\left(1 - \frac{1}{R_0}\right), \\
a_0 &= Pr|\boldsymbol{k}|^2 b_2 + Pr\frac{l^2}{|\boldsymbol{k}|^2}\left[|\boldsymbol{k}|^2\left(\tau - \frac{1}{R_0}\right) + \left(\frac{1}{\gamma_0} - \frac{1}{R_0}\right)\left(A_2(1-R_0) + Nu_0 - 1\right)k^2\right. \\
&+ \left. A_1 k^2 (Nu_0 - 1)(1 - R_0) - ikV\right],
\end{aligned}
$$

and

$$
\begin{aligned}
b_1 &= (1+\tau)|\boldsymbol{k}|^2 + k^2\left(A_2\left(1 - \frac{R_0}{\gamma_0}\right) + (Nu_0 - 1)(1 - A_1 R_0)\right) - ikV, \\
b_2 &= (|\boldsymbol{k}|^2 + k^2(A_2 + Nu_0 - 1))(\tau|\boldsymbol{k}|^2 - A_1 R_0 k^2 (Nu_0 - 1) - ikV) \\
&+ A_2 R_0 k^2\left(A_1 k^2 (Nu_0 - 1) - \frac{|\boldsymbol{k}|^2}{\gamma_0}\right).
\end{aligned}
$$

This cubic generalizes the work of Traxler et al. [156] to include settling. The coefficients in the cubic are complex due to the contribution from settling. In the absence of settling ($V = 0$) we recover the real coefficients of the cubic from Traxler et al. [156], eqs. 2.13a-c. When only considering the horizontally invariant $l = 0$ modes, we recover the cubic of Reali et al. [125]. Note that the roots of the polynomial depend explicitly on the mean-field parameters Nu_0, γ_0, A_1 and A_2, all of which are functions of the fluxes $F_c = \overline{v'C'}$ and $F_\theta = \overline{v'\Theta'}$. Therefore, determination of the roots for any given system (Pr, τ, R_0, V) first requires knowledge of the fluxes. The latter can only be obtained through non-linear simulations of the full set of equations.

Mean-field theory predicts the existence of several large scale instabilities. Intrusions require horizontal gradients of the background fields [169] and are thus not considered

here. The collective instability, first derived in the work of Stern et al. [148] is obtained in the limit of discarding the diffusion terms for the diffusing scalar fields and neglecting the possible dependence of γ on R_0 (i.e. $A_1 = 0$). In the absence of settling, the collective instability is known to excite oscillatory modes, eventually leading to the formation of internal gravity waves that compete with fingering. As pointed out by Stern et al. [148], these oscillatory modes can be seen as analogous to the diffusive regime of the small-scale double-diffusive instability. Indeed, in the fingering regime, the mean flux of the slow molecular diffuser is larger than the mean flux of the fast molecular diffuser such that in the averaged fields, the roles of fast and slow diffusers are reversed.

The γ-instability, first derived in Radko [122] in the absence of settling and later generalized in the presence of settling in Reali et al. [125], is obtained when considering horizontally invariant perturbations ($l = 0$) with zero mean flow. The averaged equations 7.31 then become

$$\frac{\partial \overline{C}}{\partial t} = -\frac{\partial F_c^{tot}}{\partial y} + V\frac{\partial \overline{C}}{\partial y}, \tag{7.42}$$

$$\frac{\partial \overline{\Theta}}{\partial t} = -\frac{\partial F_\Theta^{tot}}{\partial y}, \tag{7.43}$$

where $F_\Theta^{tot} = F_\Theta - (-1 + \frac{\partial \overline{\Theta}}{\partial y})$ and $F_c^{tot} = F_c - \tau(\frac{1}{R_0} + \frac{\partial \overline{C}}{\partial y})$ are particle and salt total fluxes, which take into account both fluctuation and molecular components. These total fluxes are introduced for the sake of consistency with the literature. They are linearized using similar considerations as in the general mean-field framework, i.e., by introducing a flux ratio and a Nusselt number

$$Nu = \frac{F_\Theta^{tot}}{1 - \frac{\partial \overline{\Theta}}{\partial y}} \quad \text{and} \quad \gamma^{tot} = \frac{F_\Theta^{tot}}{F_c^{tot}}$$

which depend only on the local density ratio R_ρ. Note that the Nusselt number is exaclty the one defined in 7.35 but that the total flux ratio γ^{tot} is generally different from the turbulent flux ratio γ. Examining the stability of the linearized system by using modes in the form

$$(\overline{\Theta}, \overline{C}) \sim \Re\left((\hat{\Theta}, \hat{C}) \exp(\lambda t + iky)\right)$$

yields exactly the eigenvalue equation found in Reali et al. [125]:

$$\lambda^2 + a_1\lambda + a_0 = 0, \tag{7.44}$$

where

$$a_1 = k^2\left(A_2\left(1 - \frac{R_0}{\gamma_0^{tot}}\right) + (1 - A_1^{tot}R_0)Nu_0\right) - ikV, \tag{7.45}$$

$$a_0 = -k^4 A_1^{tot} R_0 Nu_0^2 - ik^3 V(A_2 + Nu_0), \tag{7.46}$$

and $A_1^{tot} = R_0 \frac{\mathrm{d}(1/\gamma^{tot})}{\mathrm{d}R_\rho}(R_0)$ is generally different from A_1. In the absence of settling ($V = 0$) all imaginary terms disappear and we arrive at the result of Radko [122]. In this case, we find that $A_1^{tot} > 0$ is a sufficient condition for the free term in the quadratic equation to be negative. A sufficient condition for instability is therefore $A_1^{tot} > 0$, or, equivalently, that γ^{tot} is a decreasing function of R_ρ. Radko [122] identified the variation of the flux ratio γ^{tot} in time and space as the key mechanism driving the instability, hence its name. Reali et al. [125] showed that settling broadens the range of the γ-instability, in the sense that systems which are γ-stable in the absence of settling can become γ-unstable with the addition of a settling velocity. Furthermore, settling has been seen to affect the fluxes, in most cases leading to increased growth rates of instability.

7.3.3 Characterization of stability

Following the method of Traxler et al. [156], we determine the Nusselt number and flux ratio for a given Pr, τ, R_0 and V by running small-scale 2D simulations (i.e., a simulation in a small-enough domain for the overall density ratio R_0 to be identical to the local density ratio R_ρ). More details on the space-time integration used to obtain turbulent fluxes and validation of this method against existing data is found in Appendix B. The simulations are additionally run with a slightly greater density ratio $R_0 + dR$ and a slightly lower density ratio $R_0 - dR$ such that an estimate for the first derivative of the Nusselt number and of the inverse flux ratio can be derived as

$$\frac{dNu}{dR_\rho}(R_0) = \frac{Nu(R_0 + dR) - Nu(R_0 - dR)}{2dR} + \mathcal{O}(dR^2), \tag{7.47}$$

$$\frac{d(1/\gamma)}{dR_\rho} = \frac{\frac{1}{\gamma(R_0+dR)} - \frac{1}{\gamma(R_0-dR)}}{2dR} + \mathcal{O}(dR^2). \tag{7.48}$$

With this methodology, mean-field parameters of any system with given Pr, τ, R_0 and V can be computed by running three small-scale simulations. dR is set to 0.25 for the results presented in table 7.1 and subsequently reduced to 0.1 for the results presented in tables 7.2 and 7.3.

7.4 High-Prandtl non-sedimentary systems

7.4.1 Collective stability in γ unstable systems

We are interested in the mean-field instabilities that exist high Prandtl numbers and in the presence of settling. As an illustration, we conduct small-scale simulations with fluid parameters that are based on the experiments of Carazzo and Jellinek [26]. The generalized mean-field theory can then be used to characterize the linear stability of the

	Nu	γ	γ^{tot}	A_2	A_1	A_1^{tot}
Σ_{exp}	27.4 ± 4.2	0.534 ± 0.037	0.555 ± 0.036	-91.2	0.6	0.3

Table 7.1: Estimations of the Carazzo and Jellinek mean-field parameters in the absence of settling ($V = 0$).

system. In the experiments, the choice of particles and the properties of salt imposes that the diffusivity ratio τ between the particulate field and the salinity field is $\mathcal{O}(10^{-5})$ [26]. Such a small value of the diffusivity ratio would require mesh resolutions that are computationally prohibitive and numerical studies often assume unrealistic values for the diffusivity of the slow-diffusing particle concentration [1, 125]. In addition, the fast-diffuser is often assumed to be a temperature scalar field, resulting in small, manageable values of the Prandtl number. Large Prandtl number flows indeed require very fine grids to fully capture local gradients. While artificially increasing the diffusivity ratio has few repercussions on the dynamics of the flow, the Prandtl number directly affects the nature of the larger-scale instabilities. Using the parameters described in section 7.2.2, we consider the system $\Sigma_{exp} = (R_0 = 2.25, Pr = 10^3, \tau = 0.01)$ to be a good approximation of the system investigated experimentally in Carazzo and Jellinek [26]. Note that while the diffusivity ratio is much larger than the realistic value of $\mathcal{O}(10^{-5})$, it is assumed to be small enough to yield similar predicted maximum growth rate and associated wavenumber (see Appendix B).

The stability of the system Σ_{exp}, in the absence of settling, is investigated and yields the results consigned in table 7.1. As described in Appendix B, the domain size is 37×74 units of length and we choose a 256×516 resolution, which is found to be sufficient to accurately estimate the fluxes. Note that it is important to recall that 2D simulations are known to underestimate the fluxes compared to more realistic 3D simulations [125, 148]. Hence, the data in table 7.1 (and following tables) is presented as a first estimate of the fluxes. Given that $R_0 < 1/\tau$ in the system $\Sigma_{exp} = (R_0 = 2.25, Pr = 10^3, \tau = 0.01)$,

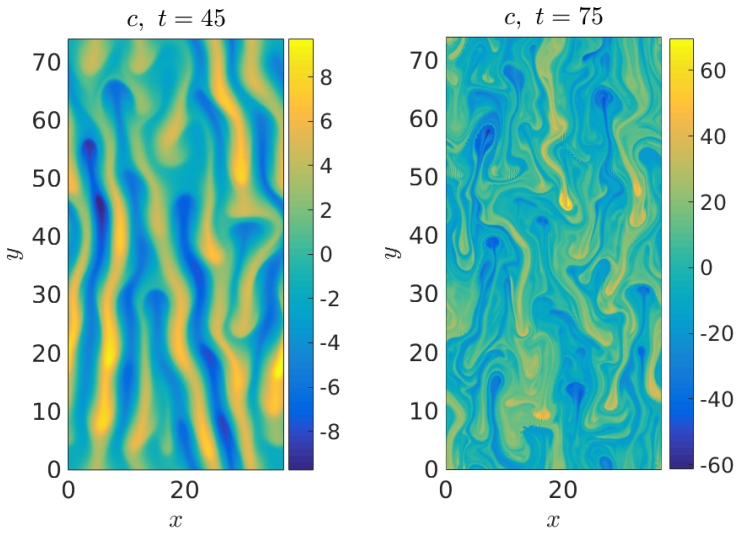

Figure 7.2: Small scale simulation of the $\Sigma_{exp} = (R_0 = 2.25, Pr = 10^3, \tau = 0.01)$ system. (Left) Double-diffusive fingers in the concentration field at early times. (Right) Concentration field in the state of fingering convection.

it is known to be unstable to the finger instability as confirmed by the formation of particle-rich fingers at the beginning of the small-scale simulations (figure 7.2). The fingers eventually saturate to form a homogeneous and statistically stationary state of fingering convection (figure 7.2) during which the fluxes are measured.

From table 7.1, we find that the sufficient condition for γ-instability $A_1^{tot} > 0$ is satisfied. More surprisingly, the system is also found to be stable to collective instabilities. This is seen by solving the general cubic (eq. 7.41) for the aforementioned mean-field values and plotting the resulting positive real part of the growth rate in the so-called "flower-plot" (figure 7.3). While the γ-instability is observed, the "leaf' of the oscillatory collective modes as described in figure 4 of Traxler et al. [156] is absent from the high-Prandtl system. The Σ_{exp} system without settling can therefore be characterized as (i) unstable to the fingering instability, (ii) collectively stable and (iii) γ-unstable. We argue that this characterization is crucial in understanding the dynamics of layer formation in the experiments of Carazzo and Jellinek [26]. To our knowledge, γ-unstable systems have

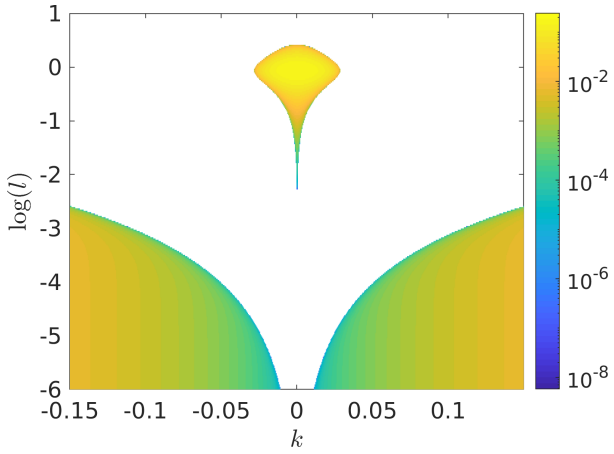

Figure 7.3: Positive real part of the growth rate obtained by solving generalized mean-field theory cubic (eq. 7.41) for settings $\Sigma_{exp} = (R_0 = 2.25, Pr = 10^3, \tau = 0.01)$ at $V = 0$.

only been found in collectively unstable systems [122, 156] but never in collectively stable systems.

Conducting *DNS* of the large-scale instabilities of the Σ_{exp} system, even in two-dimensions, is computationally prohibitive. Thus, a set of parameters (Pr, τ, R_0) which leads to similar dynamics as the Σ_{exp} system while being numerically convenient is constructed. This system should be simultaneously (i) unstable to the finger instability, (ii) collectively stable without settling, (iii) γ-unstable and (iv) cost effective. Satisfying the last point will essentially be achieved by decreasing the Prandtl number and increasing the diffusivity ratio. It is to be noted however, that τ cannot be increased too much for the condition $R_0 < 1/\tau$ to remain satisfied and that R_0 cannot be increased too much for the system to remain γ-unstable [122, 156]. Following a methodology presented in Appendix B, we choose to consider the system $\Sigma_{num} = (R_0 = 1.5, \tau = 0.1, Pr = 200)$, which verifies points i) to iv) expressed above.

As with the original system Σ_{exp}, the stability of the Σ_{num} system is explored through small-scale 2D simulations (see table 7.2) and is found, as expected, to be stable to Stern's collective instability but unstable to the γ-instability.

	Nu	γ	γ^{tot}	A_2	A_1	A_1^{tot}
Σ_{num}	76.42 ± 6.98	0.6839 ± 0.016	0.6926 ± 0.015	-447.8	0.58	0.47

Table 7.2: Estimations of mean-field parameters for $\Sigma_{num} = (R_0 = 1.5, \tau = 0.1, Pr = 200)$.

Solving the most general eigenvalue cubic 7.41 for the first three γ-modes $(0, k_1)$, $(0, k_2)$ and $(0, k_3)$, where $k_n = \frac{2n\pi}{L_y}$ denotes the vertical wavenumber and $L_y = 40fgw$ is the domain height, we find growth rates of 0.0023, 0.0091 and 0.020 respectively for the first three γ-modes.

7.4.2 DNS results

Large-scale simulations of the $\Sigma_{num} = (R_0 = 1.5, \tau = 0.1, Pr = 200)$ system in the absence of settling are carried out to investigate the long-term evolution of the double-diffusive fingers and check the stability to large-scale instabilities as described by the mean-field theory. The domain size is $20 \times 40fgw$ thus containing the equivalent of 16 small-scale $5 \times 10fgw$ domains ($1fgw$ = one non-dimensional fastest growing wavelength of finger instability). Periodic boundary conditions in both x and y are considered and the salinity and particle concentration fields have a constant y-gradient initially and are homogeneous in the x-direction. All fields are initially perturbed with low-amplitude white noise. Note that the domain is still small enough to be fully immersed into the particle-laden cloud of the experiments of Carazzo and Jellinek [26] such that the influence of the cloud boundaries do not need to be considered in the present study.

Figure 7.4 shows snapshots of the concentration field throughout the simulation. First, thin elongated particle-rich fingers appear ($t = 25$), rapidly followed by a long homogeneous state of fingering convection ($t = 50$) which remains qualitatively stable until layering begins ($t = 2750$), and becomes established ($t = 3000$). This visually confirms the possibility of a double-diffusive system with unbounded gradients to form

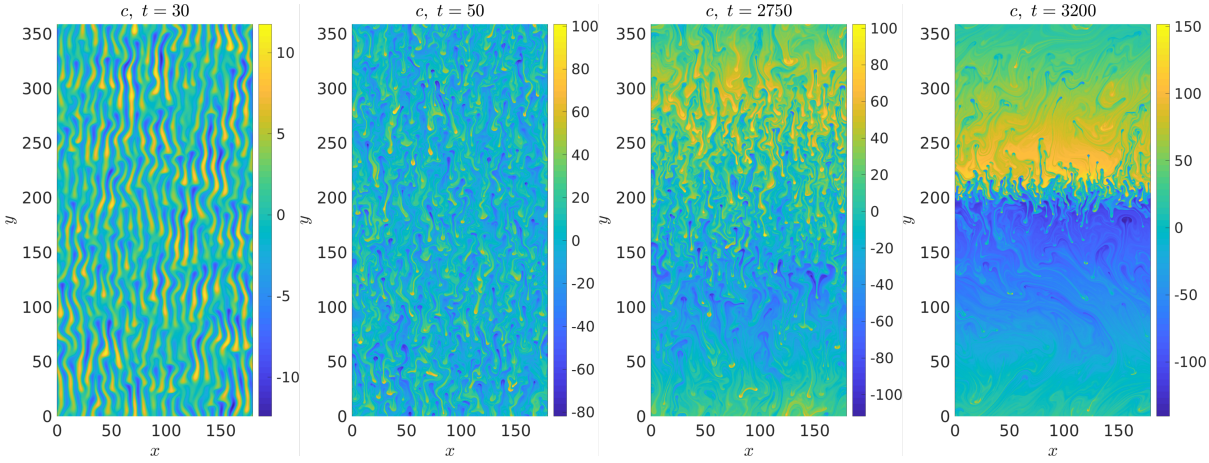

Figure 7.4: $\Sigma_{num} = (R_0 = 1.5, \tau = 0.1, Pr = 200)$. Snapshots of the concentration perturbation field at $t = 25$ (begining of fingering), $t = 50$ (established fingering convection), $t = 2750$ (onset of layering), and at $t = 3000$ (layering is established).

layers [122], despite the absence of collective instability. This result is of particular importance as it confirms the hypothesis that collective instabilities are not required to be present for the γ-instability to generate layers.

Inspection of the amplitude of the first three vertical modes of spectral concentration (figure 7.5) reveals that the γ-instability is indeed active, as had been theoretically predicted. The growth of $(0, k_1)$, starting at $t = 1100$ and on-going at the end of the simulation is indeed typical of γ-instabilities (see [122] and [145]). This result further demonstrates that in the absence of settling, the γ instability is able to grow despite the absence of collective instabilities, as predicted by mean-field theory. The measured growth rate of the $(0, k_1)$ mode is 0.00145, which agrees well with the predicted value of 0.0023 using the generalized cubic of equation 7.41. However, the $(0, k_2)$ and $(0, k_3)$, which are expected to grow much more rapidly than the $(0, k_1)$ (see figure 7.3) have growth rates of $6.97 \cdot 10^{-4}$ and $5.44 \cdot 10^{-5}$ respectively. A hypothesis for the discrepancy between the mean-field theory and the direct numerical simulations is that at such high Prandtl numbers, the fingers remain vertically coherent over lengths much longer than their width. From figure 7.4, it can be estimated that fingers remain vertically coherent

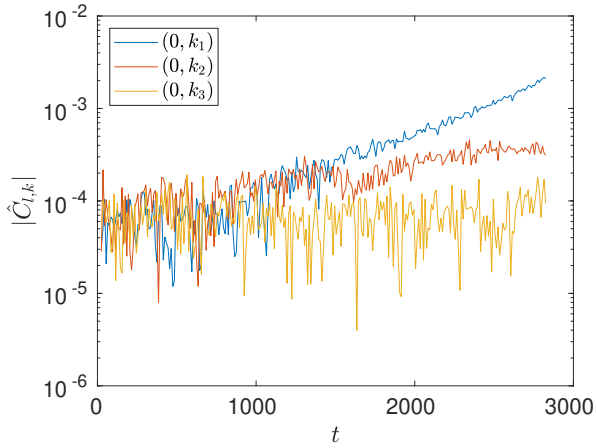

Figure 7.5: Times series of the purely vertical $(0, k_1)$, $(0, k_2)$ and $(0, k_3)$ modes of concentration in the $V = 0$ system.

over lengths of 20-50d. At such high-Prandtl, and in the absence of the collective instabilitiy, there are no inclined waves that destabilize the vertical coherence of the fingers, in stark contrast with low Prandtl problems (see figure 1 in Radko [122]). It was observed by Stellmach et al. [145] that any γ-mode significantly smaller than the most dominant collective mode would be suppressed by this mode. They also noted that the growth rate of the collective instability was only well predicted for instabilities larger than approximately 5 finger widths. Here, it appears that the elongated fingers act as a similar filter on γ-modes, where modes smaller than 5 finger heights (or up to approximately 250d) are unable to grow at the predicted growth rate.

7.5 High-Prandtl sedimentary systems

7.5.1 A settling-driven collective instability

The dynamics in the presence of settling is investigated by allowing the particles to settle at a velocity V, varied between $V = 0$ and $V = 10$. We run numerous small-scale simulations to estimate mean-field parameters for different values of the settling velocity

V	Nu	γ	γ^{tot}	A_2	A_1
0	76.42 ± 6.98	0.6839 ± 0.016	0.6926 ± 0.015	-447.8 ± 134.8	0.58
0.25	73.51 ± 6.5	0.6801 ± 0.016	0.6891 ± 0.016	-439.8 ± 138.3	0.55
0.5	77.36 ± 6.0	0.6800 ± 0.014	0.6885 ± 0.014	-428.1 ± 111.8	0.53
0.7	79.03 ± 8.13	0.6741 ± 0.020	0.6824 ± 0.020	-470.4 ± 156.0	0.53
0.9	77.29 ± 6.5	0.6691 ± 0.020	0.6775 ± 0.020	-443.4 ± 191.0	0.35
1	83.57 ± 8.57	0.666 ± 0.021	0.6744 ± 0.021	-478.3 ± 143.9	0.60
1.5	99.00 ± 12.84	0.6553 ± 0.025	0.6618 ± 0.024	-599.5 ± 238.2	0.68
2	107.13 ± 13.57	0.6323 ± 0.030	0.6281 ± 0.030	-720.7 ± 185.6	0.85
5	234.7 ± 38.40	0.5560 ± 0.0458	0.5536 ± 0.046	-798.05 ± 97.1	0.362
10	486.6 ± 117.95	0.4752 ± 0.1216	0.4740 ± 0.1218	-1986.6 ± 465.1	0.463

Table 7.3: Estimations of mean-field parameters for $\Sigma_{num} = (R_0 = 1.5, \tau = 0.1, Pr = 200)$ in presence of different settling velocities V. Having noticed a high sensibility to the value of A_2, we now focus on an interval rather than just a mean.

V (table 7.3).

Figure 7.6 juxtaposes the positive real part of the growth rate predicted by the mean-field cubic (eq. 7.41) and the small-scale cubic (eq. 7.30) for $V = 0, 2, 10$. Here we use the fact that in the absence of horizontal gradients, the growth rate is symmetric around $k = 0$ and only present the half flower plot of both cubics. The γ-instability and its UV catastrophe are observed as $|k|$ increases for low l for all three settling speeds. Interestingly, a substantial proportion of the basic modes that are predicted to have a positive growth rate by the small-scale linear stability analysis are suppressed in the mean-field theory. The "fingering" modes in particular are unstable on a very wide range of vertical wavenumbers at such high Pr, and are entirely suppressed above a certain vertical wavenumber k that decreases with V. In the absence of settling, the absence of instability-driven collective, gravity-wave modes predicted by the general cubic is observed.

At $V = 2$, the mean-field theory predicts the existence of a large scale settling-driven instability (the "leaf" of the "flower-plot") that admits a maximum growth rate for vertical wave numbers $k = \mathcal{O}(10^{-2})$ and horizontal wave numbers $l < \mathcal{O}(10^{-2})$. At

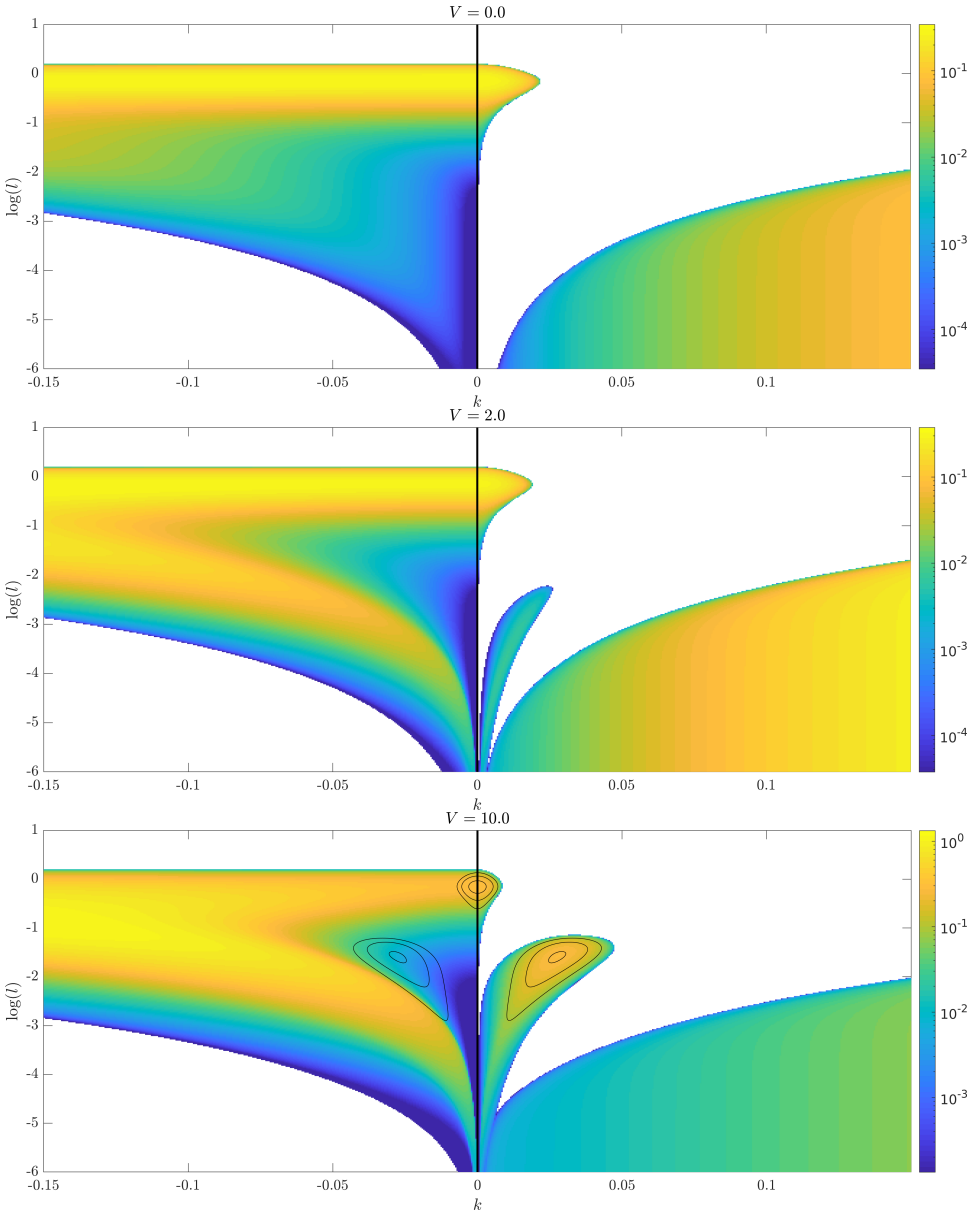

Figure 7.6: Predicted real part of growth rates for the fastest growing perturbations for $\Sigma_{num} = (R_0 = 1.5, \tau = 0.1, Pr = 200)$ with $V = 0$, $V = 2$ and $V = 10$, where colour is scaled to $log(Re(\lambda))$. The left hand side is calculated using the small-scale cubic (eq. 7.30) while the right hand side corresponds to the growth rates calculated using the generalized mean-field theory (eq. 7.41. Here, we use the symmetry with respect to $k = 0$ to only represent half of the wavenumber space of each solution. The black lines represents contours $(0.1, 0\ .2,\ 0.3)$ of the growth rate predicted by mean-field theory, superimposed to both sides of the plot.

$V = 2$, this unstable region cannot be differentiated visually from the unstable modes predicted by the small-scale theory at similar wavenumbers. At $V = 10$ however, the new unstable region of the mean-field theory induced by settling admits a maximum growth rate that is much larger than that of the basic mode at the same wavenumbers. This suggests that the unstable region driven by settling in mean-field theory is not simply a consequence of the mode suppression, but possibly a new form of large-scale instability. Contours of growth rate predicted by the mean field theory have been added to figure 7.6 at $V = 10$ on both sides of the flower plot to better visualize the offset between the mean-field, settling-driven unstable modes and the basic modes. The imaginary part of λ corresponding to the fastest growing mode is plotted in figure 7.7 for $V = 10$. The oscillation frequency observed in the 'leaf' corresponding to the new large-scale instability increases rapidly with l and decreases with k, suggesting that this imaginary term corresponds to the second term of a_1 in the cubic 7.41, which is due to the diffusion of the background profiles. Thus, the newly identified instability oscillates at a frequency dependent on the buoyancy frequency, and not on the settling velocity. This is analogous to the collective instability [148, 145] and suggests that settling induces a new form of collective, oscillatory instability.

The generalized mean-field cubic (eq. 7.41) is solved to determine the growth rate as a function of wavenumber. The positive real part is plotted in figure 7.8 for several settling speeds. The new region of collective instability is defined by the region of positive growth rate that is absent from the non-sedimentary simulations, and is visually identified by the symmetric leaves extending outward in the "flower plot" 7.8. The maximum growth rate, associated horizontal wavenumber l_{max} and vertical wavenumber $\pm k_{max}$ of the collective instability all increase with V. The area of the region of collective instability, i.e. the area of the leaf, also increases with V. The growth rate of the fastest growing collective mode (figure 7.8) goes through a regime change at $V \approx 3$, and is observed to scale with

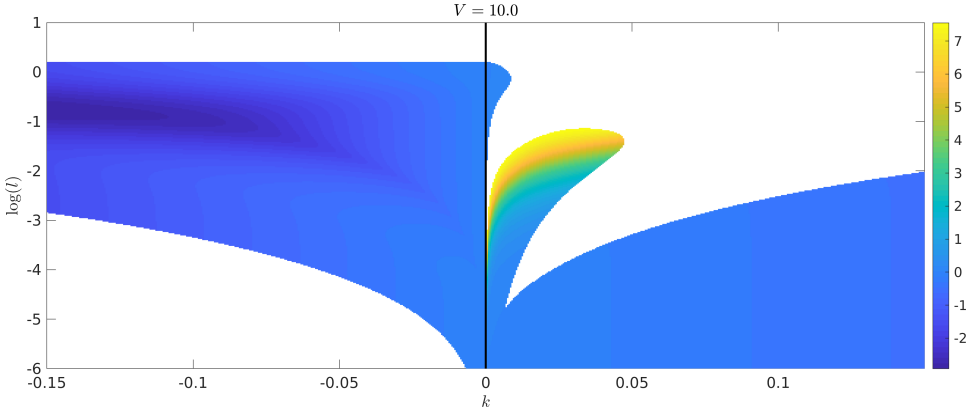

Figure 7.7: Predicted imaginary part of growth rates for the fastest growing perturbations for $\Sigma_{num} = (R_0 = 1.5, \tau = 0.1, Pr = 200)$ with $V = 10$. The left hand side is calculated using the small-scale cubic (eq. 7.30) while the right hand side corresponds to the generalized mean-field theory (eq. 7.41. Here, we use the symmetry with respect to $k = 0$ to only represent half of the wavenumber space of each solution.

powers of V is both regimes. The wavenumbers of the most unstable mode (figure 7.9b) also increase monotonically with V but are observed to converge to an asymptotic value for large settling velocities. Note that at $V = 5$, the wavenumbers of the fastest growing mode are $(l_{max}, k_{max}) \approx (0.020, 0.033)$, such that the associated wavelengths remain much larger than individual fingers, and the mean-field theory assumptions are respected.

7.5.2 Physical interpretation of the settling-driven collective instability

The origin of the settling-driven collective instability can be understood by isolating the relative contribution of the settling term V and of the mean field parameters in the solution of the general cubic 7.41. We compute the maximum positive real part of the solution to the cubic with settling velocity $V = V_1$ but with mean field parameters (mfp) computed from a small-scale simulation at $V = V_2$, denoted mfp$(V = V_2)$. The results are presented for $V_1 = 0, 2$, $V_2 = 0, 2$ and $V_1 = 0, 10$, $V_2 = 0, 10$, for the real and imaginary part of the fastest growing mode (figures 7.10 and 7.11). The cases $V_1 = V_2$ correspond

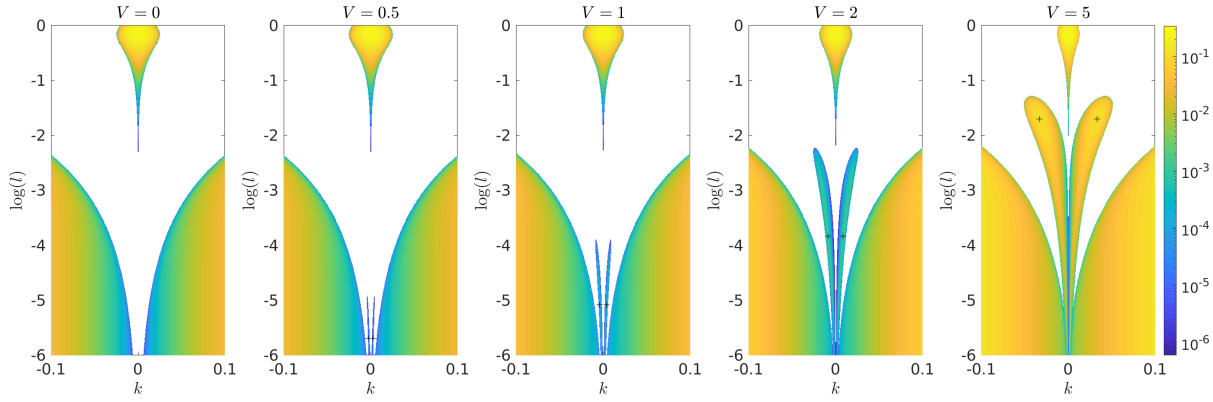

Figure 7.8: Positive real part of the growth rate obtained by solving generalized mean–field theory cubic (eq. 7.41) for various settling velocities V. The black crosses indicate the location of the fastest growing settling-driven collective mode. The boundaries of the mode are defined by the region of positive growth rate that is absent from the non-sedimentary simulations, i.e. small scale modes and γ modes.

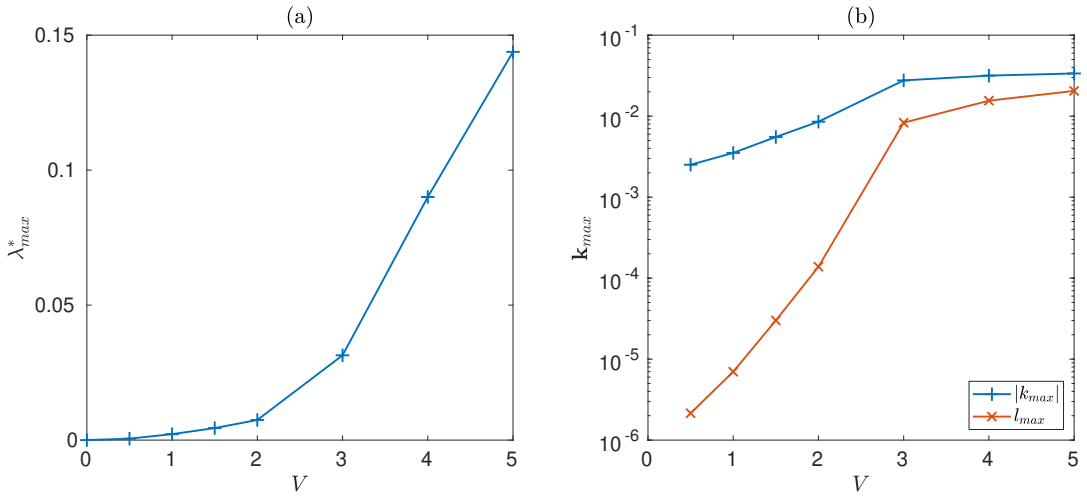

Figure 7.9: (a) Growth rate λ^*_{max} of the fastest growing collective mode, i.e. the fastest growing mode of the newly identified large-scale settling driven instability, as a function of settling velocity V. (b) Horizontal wavenumber l_{max} and vertical wavenumber $|k_{max}|$ of the fastest growing collective mode as a function of settling velocity V.

to the standard solution of the cubic while the cases $V_1 \neq V_2$ are artificially investigated to isolate the effect of settling and turbulence on the stability of the sedimentary system.

Firstly, no collective instability is observed when $V = 0$ in the cubic with mfp($V = 2$), similarly to the case in which $V = 0$ and mfp($V = 0$). This shows that for such a settling speed, the change in turbulent properties induced by settling in the small-scale simulations do not lead to the collective instability. This is however not true at larger settling speeds, and for $V = 0$, mfp($V = 10$), turbulence induced by settling results in collectively unstable mean field parameters. More interestingly, setting $V = 2$ with $mfp(V = 0)$ leads to the formation of a leaf of collectively unstable modes, despite the mean field parameters being calculated in the absence of settling. This suggests that simply from the presence of a non-zero V term in the general cubic, new unstable modes emerge from the collectively stable mean-field parameters computed at $V = 0$. This is also observed when setting $V = 10$ and mfp($V = 10$). Anecdotally, changes in turbulence due to settling increase the range and growth rate of the new collective instability compared to the case $V = 2, 10$, mfp($V = 0$), as seen when the settling velocity is set to $V = 2, 10$ and the mean field parameters are mfp($V = 2, 10$) respectively.

Particular attention must be paid to the sign of the imaginary part of the settling-driven collective mode. Contrarily to the classic collective instability, which admits both the negative and positive solution for the imaginary part of the fastest growing mode, the settling-driven mode "picks" the sign of the imaginary part, hence restricting the solution to be dependent on the sign of k. This is most apparent when comparing the imaginary parts computed at $V = 10$ and mfp($V = 10$) with the imaginary parts computed at $V = 0$ and mfp($V = 10$).

This suggests that the regime change observed in figure 7.9 for the growth rate and

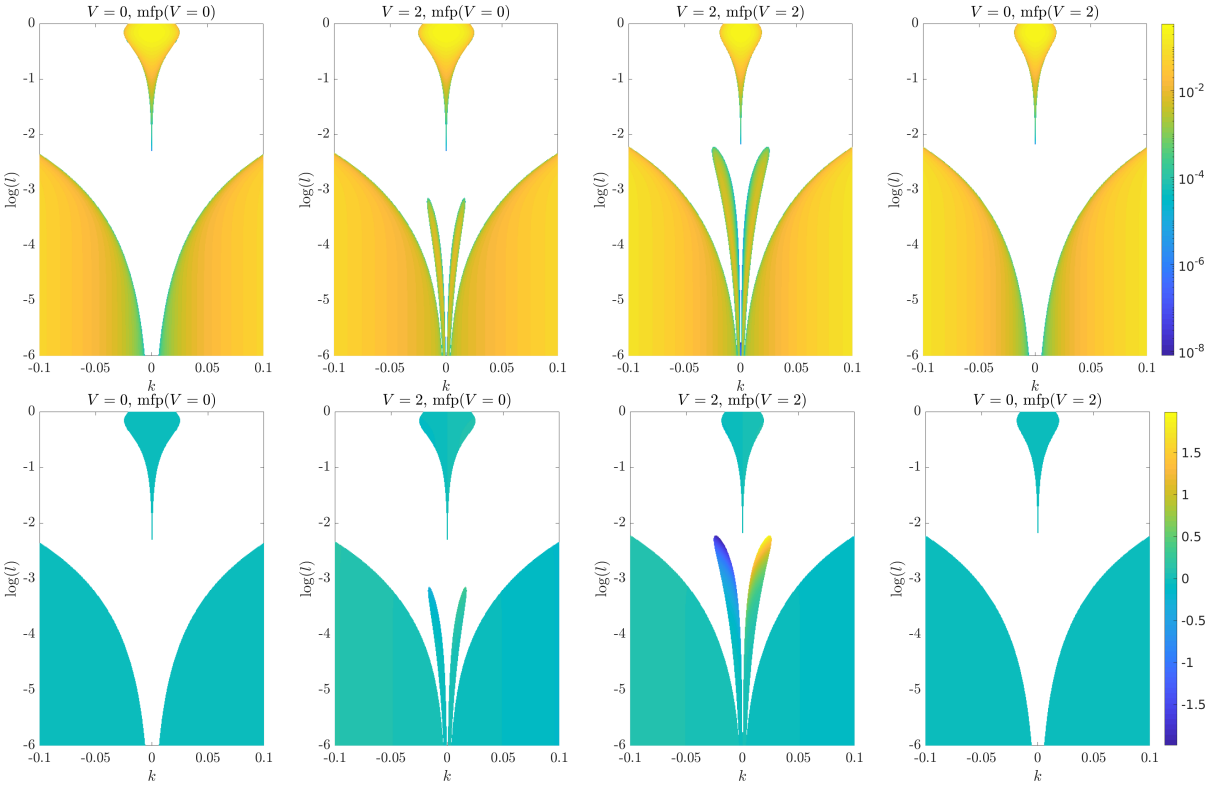

Figure 7.10: Real and imaginary part of the solution to the generalized cubic 7.41 for the fastest growing mode for various combinations of settling velocity V_1 and mean field parameters mfp(V_2) computed from small scale simulations that use a settling velocity V_2. Here, $V_1, V_2 = 0, 2$.

most unstable wavenumbers of the new collective mode reflects the relative contribution of the settling term V in the cubic and of the change in mean field parameters due to turbulence induced by settling, to the stability of the collective mode. At low settling speeds, the turbulence in generally unchanged from the non-sedimentary case, but the non-zero settling term in the cubic leads to a new instability. At high settling speeds, the changes in turbulence induced by settling lead to a collectively unstable mean field in the classical sense, and the presence of settling in the cubic simply forces the sign of the imaginary part. The underlying mechanisms of these two regimes are described in the following.

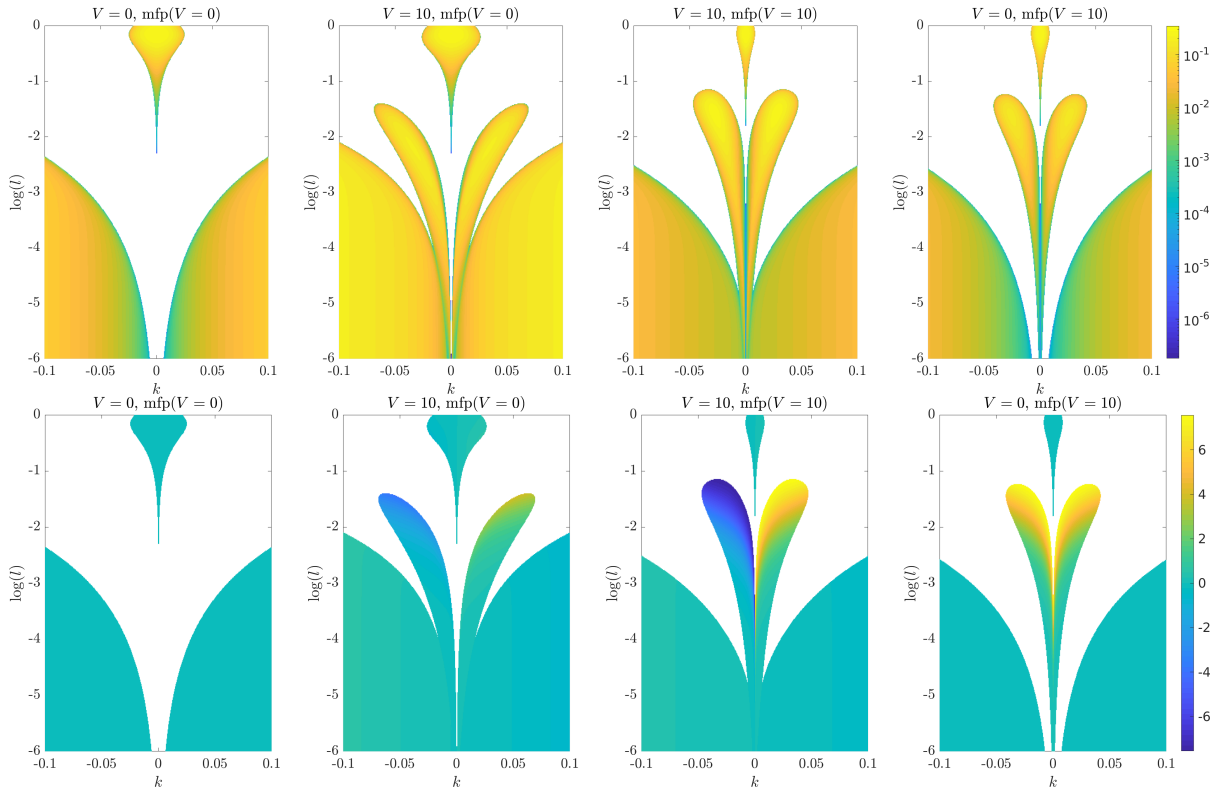

Figure 7.11: Real and imaginary part of the solution to the generalized cubic 7.41 for the fastest growing mode for various combinations of settling velocity V_1 and mean field parameters mfp(V_2) computed from small scale simulations that use a settling velocity V_2. Here, $V_1, V_2 = 0, 10$.

Low-settling regime

A simple interpretation to the emergence of the settling-driven collective mode at small settling velocities is found by investigating the stability of inclined gravity waves in the presence of two density-contributing fields where one settles under the effect of gravity. We again consider the case of a gravitationally stable linearly stratified fluid in which the non-settling field is stably stratified while the settling field is unstably stratified. As will be shown, differential diffusion, or diffusion in general, is not necessary for this instability mechanism to operate, and we thus consider the linear governing equations

$$\nabla \mathbf{u} = 0, \tag{7.49}$$

$$\frac{1}{Pr}\frac{\partial \mathbf{u}}{\partial t} = -\nabla p + (\Theta - C)\boldsymbol{e_y}, \tag{7.50}$$

$$\frac{\partial C}{\partial t} + \frac{v}{R_0} - V\frac{\partial C}{\partial y} = 0, \tag{7.51}$$

$$\frac{\partial \Theta}{\partial t} + v = 0 \tag{7.52}$$

Using normal modes in the form $(u, v, \Theta, C) = \mathcal{R}\left((\hat{u}, \hat{v}, \hat{\Theta}, \hat{C})\exp(\lambda t + ilx + iky)\right)$, we find the growth rate cubic

$$\lambda^3 + \lambda^2(-ikV) + \lambda\frac{l^2}{|\mathbf{k}|^2}\left(1 - \frac{1}{R_0}\right) - \frac{l^2}{|\mathbf{k}|^2}ikV = 0. \tag{7.53}$$

The fastest growing mode is plotted as a function of k, l in figure 7.12 for $R_0 = 1.5$, $Pr = 200$ and various values of V. The corresponding imaginary part is plotted in figure 7.13 for modes of non-negligible growth rate. Unstable inclined gravity waves are excited as soon as $V \neq 0$. This instability mechanism is easily understood physically (see sketch in figure 7.14): The inclined waves transport upwards denser fluid from below, and downwards lighter fluid from above. As the destabilizing particle field settles, the

perturbation of concentration shifts downwards, thus increasing the density of the upward moving and already dense fluid relatively to the downward moving lighter fluid. Once the direction of the inclined wave reverses, the dense fluids and lighter fluids thus overshoot their former point of neutral buoyancy, and the instability is amplified. An intuitive condition for this amplification to occur is that the frequency associated to the settling of the particle field is of the same order as the oscillation frequency of the wave ω_w, i.e.

$$\omega_w \sim 2\pi k V, \tag{7.54}$$

where $\omega_w = Pr\,(1 - 1/R_0)\,\frac{l}{|\mathbf{k}|}$. We restrict our analysis to modes for which $l \ll k$ such that $|\mathbf{k}|^2 \approx k^2$, and verify a posteriori that this holds true for the considered modes. Under this approximation, the condition for amplification becomes

$$l \sim 2\pi \frac{k^2 V}{Pr\,(1 - 1/R_0)}. \tag{7.55}$$

This scaling is represented as the red line in figure 7.12 and shows excellent agreement with the predicted most unstable mode for a wide range of small horizontal wavenumbers l.

We therefore postulate that the condition for the growth of the new settling-driven instability in the low-settling regime simply derives from equation 7.55. Indeed, in this regime, the effect of the settling velocity on the turbulence, and thus the mean field parameters, is small. This assumption can be used to compute the solution to the general cubic with constant mean field parameters mfp($V = 0$) but varying the value of V in the cubic. The maximum growth rate and associated wavenumbers are plotted in figure 7.15. By removing the effect of settling on turbulence, we find that the growth rate of the new settling-driven collective instability scales as $\lambda(V) = \hat{\lambda} V^2$, and the corresponding

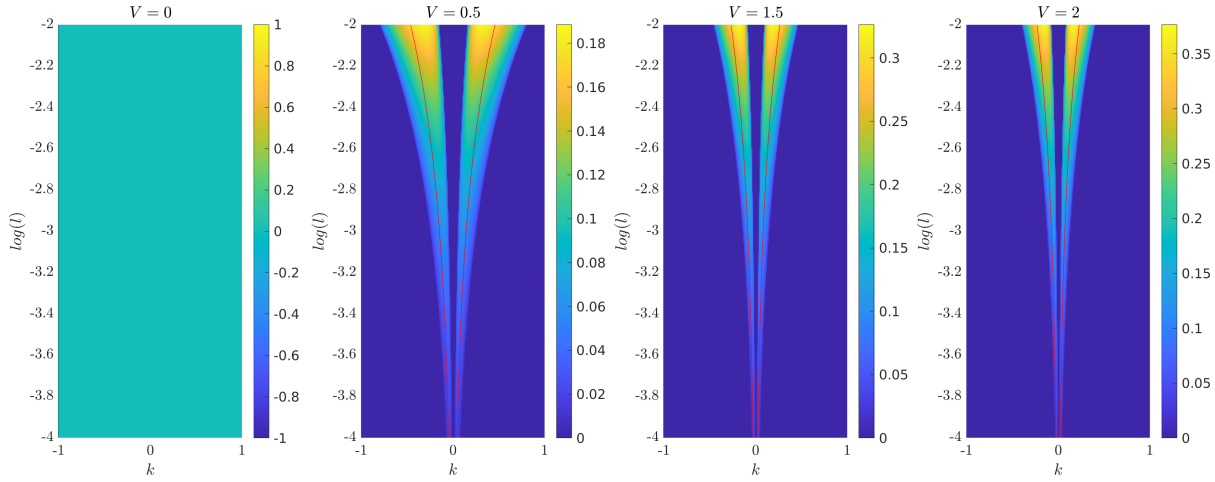

Figure 7.12: Growth rate of instability in a linearly stratified fluid in the presence of a settling destabilizing field and a non-settling stabilizing field. $R_0 = 1.5$, $Pr = 200$.

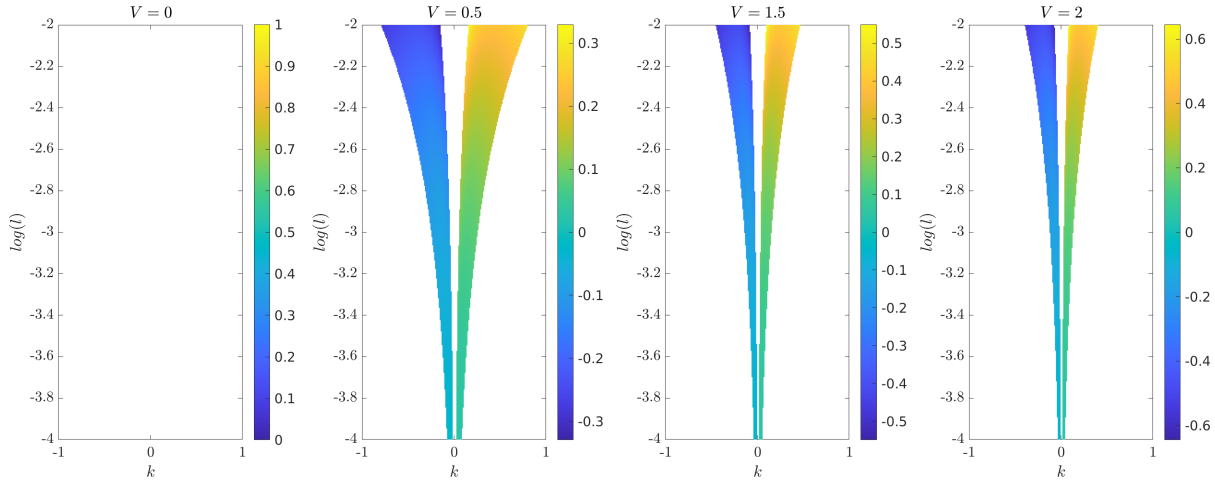

Figure 7.13: Corresponding imaginary part to the fastest growth modes under the condition $\lambda > 10^{-12}$. $R_0 = 1.5$, $Pr = 200$.

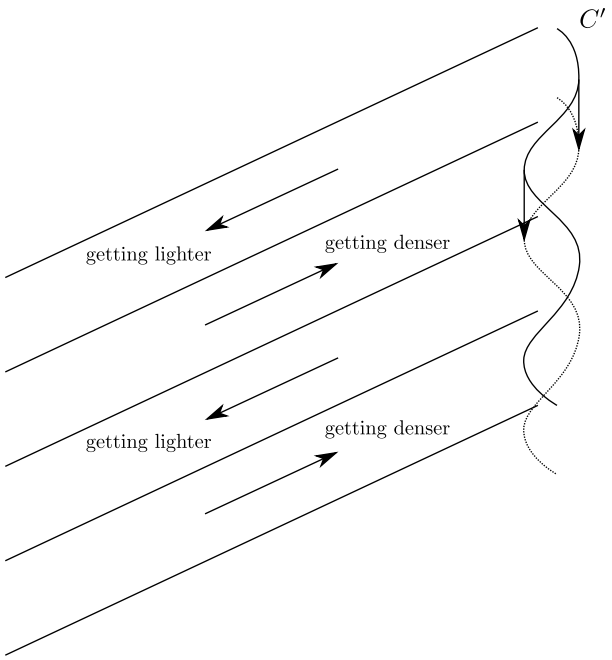

Figure 7.14: Sketch of the gravity wave amplification mechanism in the presence of a settling destabilizing field and a non-settling stabilizing field.

wavenumbers scale as $k(V) = \hat{k}V$ and $l(V) = \hat{l}V^3$.

We first note that the amplification conditions of equation 7.55 automatically enforces the scaling of $l(V)$ with respect to $k(V)$. We can now consider the general cubic of equation 7.41 and verify that the scaling of k, l and λ for the fastest growing mode of the settling-driven collective instability is a direct consequence of the amplification condition. Consider the following scaling of λ, k and l under the amplification condition

$$\lambda = \hat{\lambda}V^{\beta}, \quad k = \hat{k}V^{\alpha}, \quad l = \hat{k}^2V^{2\alpha+1}, \tag{7.56}$$

where α and β are coefficients to be determined. Then, for the scaled growth rate $\hat{\lambda}$ to be in fact independent of V, the scaling

$$V^{3\beta} \sim a_2(V)V^{2\beta} \sim a_1(V)V^{\beta} \sim a_0, \tag{7.57}$$

must hold true. Here, a_2, a_1, a_0 are the coefficients of the polynomial of equation 7.41. Under the amplification condition of equation 7.55 and for small wavenumber k, we have $l \ll k$, i.e. $|\mathbf{k}|^2 \approx k^2$. Scaling of the coefficients of equation 7.41 yields

$$a_2 \sim \hat{k}^2 V^{2\alpha} - i\hat{k} V^{\alpha+1} \tag{7.58}$$

$$a_1 \sim \hat{k}^4 V^{4\alpha} - i\hat{k}^3 V^{3\alpha+1} + \hat{k}^2 V^{2\alpha+2} \tag{7.59}$$

$$a_0 \sim \hat{k}^6 V^{6\alpha} + \hat{k}^4 V^{4\alpha+2} - i\hat{k}^3 (V^{5\alpha+1} + V^{3\alpha+3}). \tag{7.60}$$

The constraint of equation 7.57 thus yields two linearly independent equations

$$3\beta = 2\alpha + 2\beta, \tag{7.61}$$

$$3\beta = \alpha + 2\beta + 1, \tag{7.62}$$

which admit the unique solution $\beta = 2$ and $\alpha = 1$. This proves that the amplification condition that allows for settling to amplify the oscillations of an inclined gravity wave is a sufficient condition to obtain the correct scaling of the collective growth rate and corresponding wavenumnber, as shown in figure 7.15.

7.5.3 High-settling regime

The growth rate of the collective modes at $V = 10$ is almost identical when computed using the true mean field parameters (mfp($V = 10$) regardless of whether V is set to 0 or 10 in the cubic (see figure 7.11). In the high-settling regime, settling thus induces changes to the turbulence field that lead to a collectively unstable system in the classic sense of Stern et al. [148]. The growth rate of the classic collective instability additionally increases more rapidly with V than the settling-driven collective instability, and the most unstable wavenumbers become V independent (see figure 7.9). A physical interpretation

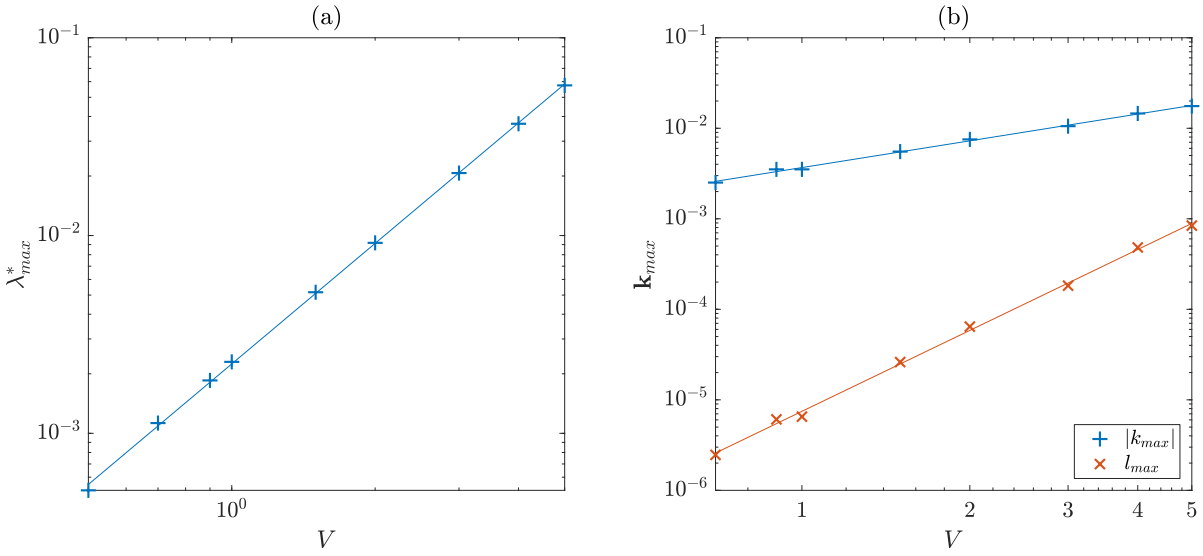

Figure 7.15: (a) Growth rate λ^*_{max} of the fastest growing collective mode as a function of settling velocity V, using constant mean field parameters computed from simulations at $V = 0$. (b) Horizontal wavenumber l_{max} and vertical wavenumber $|k_{max}|$ of the fastest growing collective mode as a function of settling velocity V.

for the collective instability was proposed by Stern et al. [148], which identified the variations in salt-finger buoyancy flux induced by the wave to feed the instability (see figure 6 of Stern et al. [148] or figure 6.3 of Radko [123]). This mechanism is very similar to the amplification mechanism identified in the low-settling regime (figure 7.14). In the high-settling regime, the addition of settling to the classic collective instability mechanism simply has the effect of damping the mode that opposes the direction of settling, and reinforcing the mode that acts in the direction of settling. Thus, settling simply restricts the sign of the imaginary part of λ for the fastest growing mode of the collective instability. This is observed directly in figure 7.11. The imaginary part of the growth rate of the fastest growing mode in the case where the cubic is solved with $V = 0$ and mfp($V = 10$) can indifferently be negative and positive, and does not depend on the sign of k. This contrast with the solution at $V = 10$ and mfp($V = 10$), where the imaginary part only admits one solution for the fastest growing mode and depends on the sign of k.

7.6 Conclusion

The mean-field theory approach has been successfully employed to describe layering modes in non-sedimentary [122] and sedimentary systems [125], as well as to recover the collective instability of Stern et al. [148] and intrusion modes of [169] [156]. However, none of these studies considered high-Prandtl systems, such as a linearly stratified particle-laden salt water column. In this work, we extend the mean-field theory of Traxler et al. [156] to include sedimentary systems, in which one of the diffusing scalars settles at a constant settling velocity V. We analysed the stability of a characteristic high-Prandtl problem, both in the presence and absence of settling. We found that such non-sedimentary systems can be collectively stable yet unstable to γ-modes and showed with 2D DNS that layering occurred despite the absence of inclined gravity waves. We additionally found that the growth rate of the γ-modes did not scale as predicted by the mean-field theory and proposed that larger wavenumber modes are filtered by the presence of elongated fingers. In collectively unstable systems, it was observed by Stellmach et al. [145] that inclined gravity waves were responsible for the filtering of the γ-modes of wavenumbers comparable or larger than the most unstable collective mode. Here, the high viscosity of the fingers stabilizes shear-induced instability such that they remain coherent over large vertical distances, up to $50d$. γ-modes with wavelength $\mathcal{O}(50d)$ or more are thus filtered by the fingering modes, favoring in our simulations the formation of a single layer.

In the presence of settling, this picture changes markedly. The presence of settling in the mean-field theory equation for the growth rate of large-scale instability leads to a novel type of collective modes that differs from the classical collective instability. Through small-scale simulations, we computed the mean-field parameters for various settling ve-

locities V and found that the growth rate increases linearly with V for sufficiently large V. Isolating the effect of settling on the turbulence, i.e. on the mean-field parameters from the effect of the settling velocity V in the solution of the growth rate gave additional insight into the nature of the instability. At low settling velocities, turbulence is relatively unaffected by settling, and the system remains collectively stable in the classical sense. However, settling induces a new type of instability that only relies on the presence of two density-contributing scalars, one of which that settles, by amplifying inclined gravity waves. The amplification occurs when the wave oscillation frequency is of the same order as the frequency associated with settling, leading to an amplification constraint that relates the horizontal wave number and the vertical wave number to the settling velocity. This condition was found to be sufficient to explain the scaling of the growth rate and wavenumbers of the most unstable settling-driven collective mode. Higher settling velocities change the turbulent properties of the flow such that it becomes collectively unstable in the sense of Stern et al. [148]. However, through the same mechanism that describes the low-settling regime instability, settling favors one of the two modes of the collective instability, such that the sign of the imaginary part associated with the fastest growing mode of the collective instability is enforced by the direction of settling.

The relevance of such collective modes in environmental systems is not immediately obvious, as it requires that the stabilizing component of the double-diffusive system be a slow diffuser, such as dissolved salt ions. The time scale associated with fingering modes scales with $\kappa_s^{-1/2}$ and thus reduces the ability of fingering to adapt to changes in the background conditions when compared to fingering in heat-salt systems. However, it is equally important to note that in non-dimensional form, the particle settling velocity is scaled with $\kappa_s^{3/4}$, and thus non-dimensional settling velocities in such high-Prandtl problems can be very large even within the limits of Stoke's law. For instance, particles

of diameter $d_p = 100\mu m$ and relative density 2.5 that of water settle under Stoke's law at $V_{st} \approx 8.2mm/s$, yielding a particle Reynolds number $\mathcal{O}(1)$. With a typical salt ions diffusivity of $\kappa_s \approx 10^{-9}\,\mathrm{m^2 s^{-1}}$ and typical diffusive lengths $d \approx 200\mu m$, the non-dimensional settling velocity is $V \approx 1.7 \cdot 10^3$. This suggests that even very small particles can lead to double-diffusive systems in which instabilities that arise from the sedimentary nature of the problem dominate the flow dynamics.

Part IV

Swarms of inertial swimmers in stratified fluids

Chapter 8

Biogenic mixing in vertically migrating swarms of inertial swimmers

Authorship of this work is shared with Dr. Isabel O. Houghton, Prof. John Dabiri and Prof. Eckart Meiburg. Part of this work has been submitted for publication in *Journal of Fluid Mechanics*.

8.1 Introduction

In recent years a picture has begun to emerge of the ways in which biologically generated turbulence could contribute to oceanic transport and mixing [70, 36, 77, 32]. In particular, it has been suggested that swarms of self-propelled organisms, such as copepods and zooplankton, may significantly modify the properties of the water column in marine ecosystems [173, 68]. In support of this idea, the collective upward migration of *cm*-scale swimmers in stably stratified salt water has been shown to generate a downward

jet that triggers substantial mixing at the swarm scale, resulting in effective diffusivities up to three orders of magnitude larger than the molecular diffusivity [68].

The motion of self-propelled organisms in the Stokes regime has been explored in some detail both theoretically and computationally, as surveyed in the comprehensive review by Pak and Lauga [115]. In comparison, swimming at moderate Reynolds numbers, where inertia plays a significant role, has received far less attention to date [170], due to the modeling challenges and computational cost associated with resolving the details of the animal-fluid interaction in this parameter regime. Large zooplankton such as copepods that straddle the boundary between inertial and viscous-dominated flows, are particularly relevant with regard to biologically induced mixing, since these mm to cm-scale swimmers account for the majority of living organisms in the mesopelagic and aphotic zone [166]. Hence there exists a strong motivation to develop accurate computational modeling approaches for analyzing their collective action, along with the resulting fluid motion [170].

A popular model for self-propelled swimmers in the Stokes regime was introduced by Lighthill, and corrected by Blake [91, 16]. This so-called squirmer model replaces the individual motion of the cilia around a spherical swimmer by a wave envelope, and it evaluates the resulting incompressible axisymmetric flow. It has been used extensively in studying the motion of sub-mm scale organisms in viscous flows [85, 96, 74]. More recently, this model has been extended to finite Reynolds number flows in order to analyze swimming regimes that are inaccessible to fully resolved numerical simulations of the interaction between flexible appendages and the surrounding fluid [37, 170, 79, 171, 4]. The squirmer model represents an excellent candidate for numerical investigations of biogenic mixing, as it enables the analysis of hydrodynamically interacting swimmers and their collective contribution to the large-scale fluid motion. To that end, Li and Ardekani [90], Wang and Ardekani [171] and Li et al. [89] employ a distributed Lagrangian mul-

tiplier approach that approximately imposes the surface velocity of the swimmer within its interior. Based on this technique, Wang and Ardekani [171] analyze groups of up to eight swimmers at moderate Reynolds numbers in linearly stratified environments, along with the resulting mixing efficiency, effective diapycnal diffusivity and other statistical properties. In addition, the authors assess the combined effects of background decaying isotropic turbulence and swimming on those quantities. They report enhanced diapycnal mixing and increased mixing efficiency for swimmers in the inertial regime for $Re \leq 10$.

Following a similar modeling approach, the present investigation analyzes biogenic transport and mixing processes generated by the migration of swarms of up to 373 self-propelled organisms. It specifically focuses on identifying the differences between the mechanisms that govern mixing at the swimmer and swarm scales. Guided by accompanying laboratory observations, we employ a novel use of the Immersed Boundary Method (IBM) coupled with a Volume of Fluid (VoF) approach for scalar transport, in order to simulate swarms of phototactic, hydrodynamically interacting swimmers migrating through density-stratified interfacial regions. Towards this end, we adapt the squirmer model so that the individual organisms can actively modify their swimming orientation in response to an external light source, much like *Artemia salina* [68]. After reviewing the laboratory experiments in section 8.2 and the simulation approach in section 8.3, we will explore the process of jet formation in section 8.4. The swimmer- and swarm-scale mixing processes will be analyzed as functions of the animal number density in section 8.5. In addition, we will employ the insight gained from the discrete swimmer simulations in order to develop a continuum model in section 8.6 that is capable of capturing the generation of large-scale jets by the collective action of a swarm.

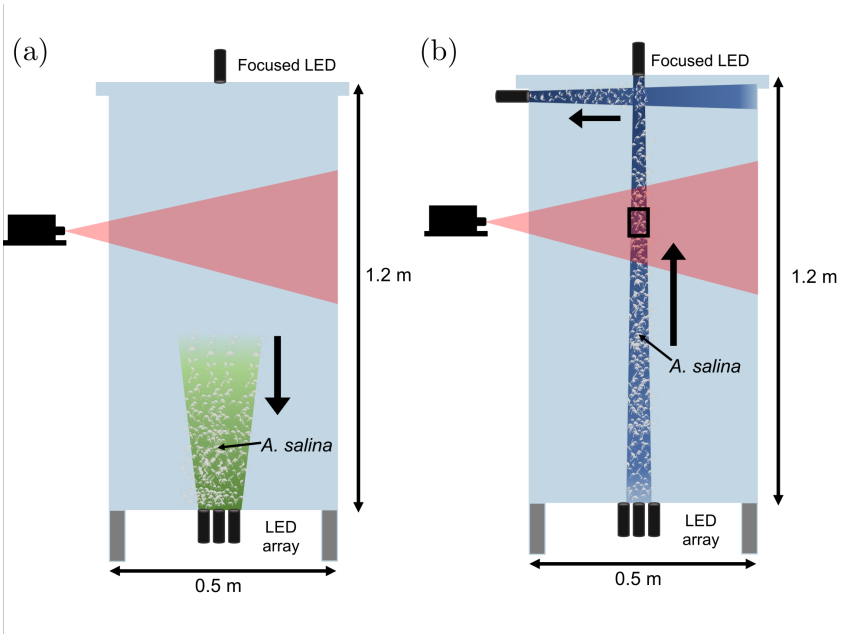

Figure 8.1: Experimental setup to measure jet velocity: (a) Animals grouped at bottom initially; (b) Animals drawn to the surface, and then to the side, with a focused LED from above. A two-dimensional red laser sheet illuminates particles seeded in the flow.

8.2 Experimental methods

Controllable vertical migrations were achieved in the laboratory utilizing the brine shrimp *Artemia salina*, a zooplankton species approximately 1 cm in length. The experiments leveraged the strong phototactic response of the animals to control their vertical motion in laboratory tanks 1 - 2 meters tall.

Two different experimental protocols were used to study the collective vertical migrations, one to assess the flow field dependency on animal number density [66] and one to measure irreversible mixing by the aggregation [68].

8.2.1 Jet velocity experiments

Following methods in Houghton and Dabiri [66], the fluid velocity induced by the aggregation was assessed with simultaneous volumetric animal number density and two-

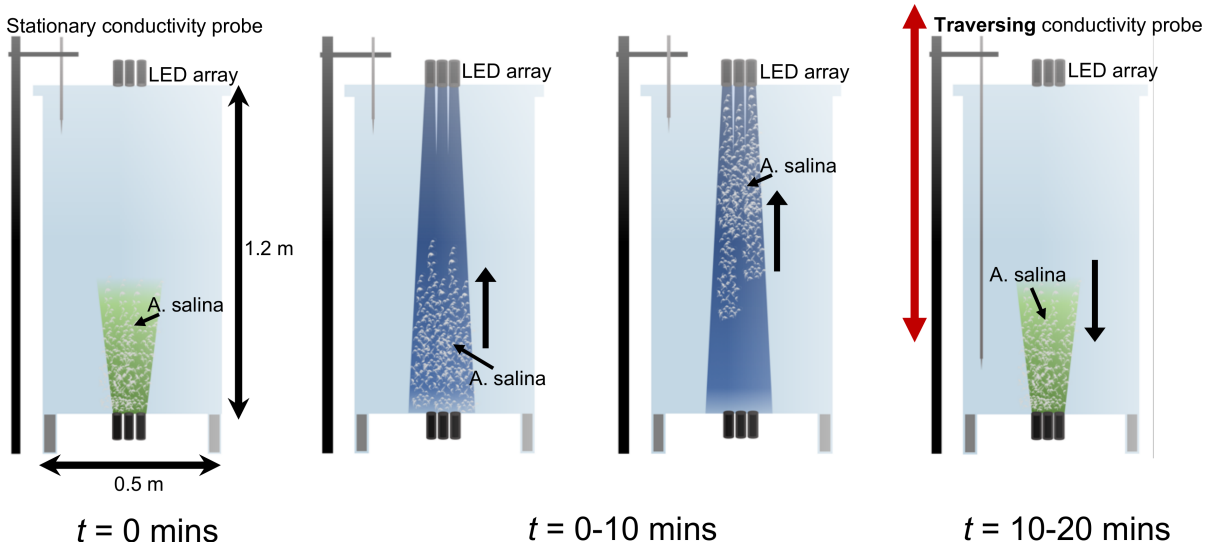

Figure 8.2: Experimental setup to measure irreversible mixing: A 20 minute cycle was repeated six times. A density profile was obtained during each downward migration period. Repeated density profiles were obtained at the end of the experiment to confirm consistency of the density profiles indicating the tank was horizontally homogeneous. Adapted from Houghton et al. [68].

dimensional velocity measurements in a $0.5m \times 0.5m \times 1.2m$ tall, well-mixed tank.

Lights were utilized to control the animal motion, with an LED array pointing upward through the clear acrylic bottom of the tank and a single focused LED pointed vertically downward from the top of the tank (figure 8.1). Another focused LED was pointed horizontally just below the water surface intersecting the vertical beam in order to draw the animals to the edge of the tank after they reached the surface. The lower LED array was used to group the animals at the bottom of the tank initially, and the strong phototactic response of the swimmers resulted in a steady upward migration following activation of the upper LED and deactivation of the lower LED array (Supplementary Video). Experimental studies focused solely on the upward migrations.

Image analysis was used to measure the local animal number densities within the aggregation by obtaining the animal count within the known illuminated volume created by the focused LED. Local animal densities were of the same order of magnitude as

reported values for oceanic swarms, which range from 10,000-450,000 animals/m^3 [55, 70, 111]. Estimates of the animal swimming velocities were obtained using object centroid tracking and were averaged in one second bins.

To measure the fluid velocity within the aggregation, the experimental tank was seeded with $13\mu m$ neutrally buoyant glass beads and illuminated with a two-dimensional red laser sheet. Pairs of subsequent frames ($\Delta T = 0.04s$) were used to conduct particle image velocimetry (PIV) using PIVLab [155]. Vertical and horizontal velocities within the two-dimensional slice through the center of the aggregation were obtained using a multi-pass method with two iterations and a decreasing window size from 64×64 pixels to 32×32 pixels and a 50% overlap. Animals were masked out prior to processing, with the identical mask applied to the pair of processed images.

For full experimental details, including complete experimental tank conditions and image analysis methods, see Houghton and Dabiri [66].

8.2.2 Density stratified experiments

Two experimental setups are presented in a density-stratified environment, one focused on transient dynamics in a linear stratification and one measuring irreversible mixing in a two layer stratification. Transient dynamics within a linearly salt-stratified water column were studied in a $0.9m \times 0.9m \times 2m$ tall tank, with a buoyancy frequency of $N = 0.05s^{-1}$ to assess the importance of a restratifying force. A $1W$, $447nm$ (blue) laser was used as the light stimulus rather than focused LEDs for increased illumination intensity over larger height. Transient perturbations to the density stratification in the tank were measured as the animals swam upward toward the light using a vertically traversing density probe (Precision Measurement Engineering) located $5cm$ horizontally from the centerline of the migration. Following each migration and measurement of the

perturbations, the animals could be returned to the bottom of the tank by powering off the upper blue laser and powering on a lower green laser.

Long-term impacts to the density profile (i.e. mixing) were measured in the $0.5m \times 0.5m \times 1.2m$ tank. Animals were introduced at a tank averaged value of 46,000 $\pm$ 5,000 animals m^{-3} to 138,000 $\pm$ 5,000 animals m^{-3}. These experiments used a two-layer stratification with buoyancy frequencies across the $0.2m$ thick interface of $N = 0.04 - 0.13s^{-1}$. This corresponded to a salt concentration of 26.0 ppt in the upper mixed layer and 26.1 - 26.5 ppt in the lower mixed layer for the range of stratification strengths used. To simulate the passage of a swarm through a pycnocline, animal migrations were repeatedly induced over 120 minutes, switching the LED light stimulus between the top and bottom (upward and downward migration) every 10 minutes (figure 8.2). The long-term evolution of the initial two-layer stratification was measured with the same vertically traversing probe located $20cm$ laterally from the migration. Density profiles were obtained every twenty minutes throughout a migration experiment, with repeated density profiles obtained at the end of a 120 minute experiment to confirm that the tank was fully settled and horizontally homogeneous. For full density mixing experimental details, see Houghton et al. [68].

8.3 Simulation approach

We conduct direct numerical simulations of model swimmers reacting to a virtual light source, to generate a controlled vertical migration of a swarm similar to the one observed in the experiments. The simulations are designed to fully capture the local hydrodynamic interactions that lead to the large-scale spatial and temporal collective dynamics found experimentally.

8.3.1 Governing equations

We employ the squirmer model introduced by Lighthill [91] and adapted by Blake [16] for Stokes flows to represent the swimmers. The squirmer model replaces the individual motion of numerous cilia around a spherical swimmer by a wave envelope and then evaluates the corresponding incompressible axisymmetric Stokes flow around the sphere. This model has been studied extensively and its usage has recently been extended to inertial finite Reynolds number flows, both analytically [170, 79] and numerically [90, 171, 89, 29]. The squirmer swimmer generates thrust by imposing a radial and tangential velocity at the surface of the sphere such that, in polar coordinates,

$$u_\rho(\rho = R, \theta) = \sum_{n=0}^{\infty} A_n P_n \cos\theta, \tag{8.1}$$

$$u_\theta(\rho = R, \theta) = \sum_{n=1}^{\infty} \frac{2}{n(n+1)} B_n \sin\theta P_n' \cos\theta, \tag{8.2}$$

where θ is the polar angle to the swimming direction, R is the radius of the sphere, A_n and B_n are the n^{th} mode of the radial and tangential squirming velocity components, and P_n and P_n' are the n^{th} Legendre polynomial and its derivative, respectively. It is common to consider a reduced order model by neglecting the radial velocity and only retaining the first two modes of the squirming motion, such that the surface velocity of a squirmer reduces to a tangential component, as shown in figure 8.3 [29]. In the reference frame of the moving object, this tangential velocity is given by

$$u_\theta(\rho = R, \theta) = B_1 \sin\theta + B_2 \sin\theta\cos\theta \ . \tag{8.3}$$

The amplitude B_1 of the first mode is responsible for propulsion, while that of the second mode B_2 accounts for the stress field generated by the swimmer [16]. In a Stokes

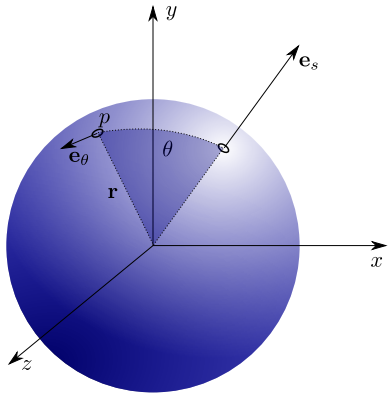

Figure 8.3: Sketch of the squirmer swimmer. $\mathbf{e}_s$ defines the swimming direction. $\mathbf{r}$ is the vector from the center of the sphere to a point at its surface, where the tangential velocity u_θ is imposed in the direction of $\mathbf{e}_\theta$. θ denotes the angle between $\mathbf{r}$ and the swimming direction $\mathbf{e}_s$.

flow, the terminal velocity $U = \frac{2}{3}B_1$ reached by a single squirmer is independent of B_2. The ratio $\beta = B_2/B_1$ determines the squirming mode, i.e. how thrust is generated by the squirmer. Squirmers with $\beta > 0$ are defined as pullers, while those with $\beta < 0$ are pushers. A puller generates thrust by accelerating fluid backwards in front of its body, while a pusher accomplishes the same by accelerating fluid behind its body, as shown in figure 8.4. The resulting effect on the fluid velocity field and on the transport of a diffusing scalar field varies with the magnitude of β and with the Reynolds and Peclet numbers. Figure 8.5 illustrates the qualitative influence of the swimming mode on the flow field and on the concentration contours of a passive scalar field, for $Re = 20$ and $\beta = -3, 0, 3$. At this Reynolds number, the recirculation region typically present above a pusher is quite thin. The streamline pattern associated with the neutral swimmer is fairly symmetric, while the puller gives rise to a pronounced recirculation region in its near wake. The velocity field corresponding to the swimming mode directly affects the transport of a passive scalar. While a pusher tends to carry along resident fluid near its front stagnation point, a puller drags along fluid in its near wake.

To simulate the flow field associated with a swarm of squirmers, we solve the three-

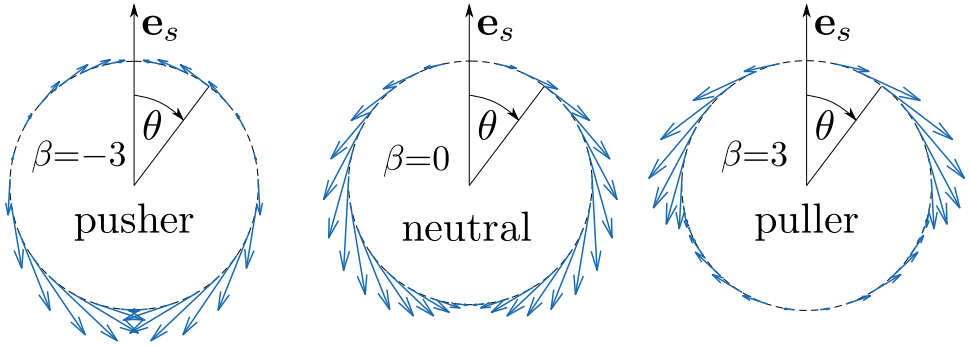

Figure 8.4: Axisymmetric surface velocity vectors in the reference frame of the squirmer, for a pusher, neutral swimmer, and puller.

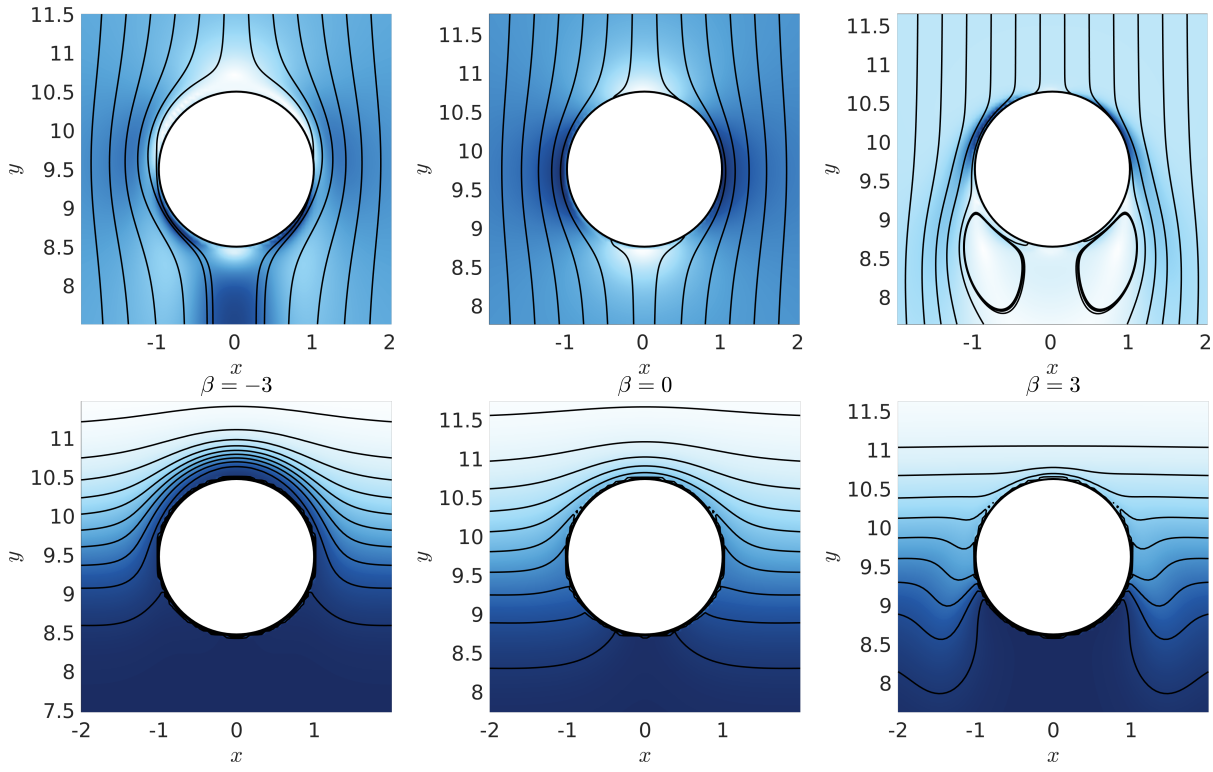

Figure 8.5: Axisymmetric flow due to an inertial squirmer swimming across a passive scalar gradient at $Re = 20$, for $\beta = -3$ (left), $\beta = 0$ (center), and $\beta = 3$ (right). The streamlines and velocity magnitude field in the reference frame of the swimmers (top), along with the concentration field and contour lines (bottom), illustrate the differences among the swimming modes.

dimensional incompressible Navier-Stokes equations in the Boussinesq limit, in conjunction with an advection-diffusion equation for the density field. In addition, the conservation equations of linear and angular momentum are solved for each squirmer. We account for the effect of the squirmers on the fluid via the Immersed Boundary Method (IBM) [101, 14]. This approach adds a forcing term $\mathbf{f}$ to the momentum equation in order to enforce boundary condition (8.3) at the surface of the squirmer. The dimensional governing equations for the fluid motion and scalar transport in conservative form hence take the form

$$\nabla \cdot \mathbf{u} = 0, \tag{8.4}$$

$$\frac{\partial \mathbf{u}}{\partial t} + \nabla \cdot (\mathbf{u}\mathbf{u}) = -\frac{1}{\rho_f}\nabla p + \nu \Delta \mathbf{u} + c\alpha \xi_f \mathbf{g} + \mathbf{f}_{IBM}, \tag{8.5}$$

$$\frac{\partial c}{\partial t} + \nabla \cdot (\hat{\mathbf{u}} c) = \nabla(\kappa \nabla c), \tag{8.6}$$

where $\mathbf{u}$ represents the fluid velocity in Cartesian coordinates, p indicates the pressure, and ν is the constant kinematic viscosity. As reference density ρ_f we choose the value $1,000 kg/m^3$, and α denotes the expansion coefficient associated with the concentration field c. The gravity term of equation (8.5) was derived by assuming a linear relationship between the local density and the scalar concentration

$$\rho = \rho_f(1 + \alpha c). \tag{8.7}$$

Here κ represents the scalar diffusivity, and $\hat{\mathbf{u}}$ is the compound velocity defined as the fluid velocity inside the fluid domain and the particle velocity within each particle, i.e., the solid body motion of the rotating and translating swimmer. $\xi_f(\mathbf{x})$ denotes the indicator

function of the fluid phase

$$\xi_f(\mathbf{x}) = \begin{cases} 1 \text{ if } \mathbf{x} \in \Omega_f, \\ 0 \text{ if } \mathbf{x} \in \Omega_p, \end{cases} \tag{8.8}$$

where Ω_f and Ω_p indicate the volumes occupied by the fluid and particle phases, respectively. The governing equations are solved inside the numerical domain $\Omega = \Omega_f \bigcup \Omega_p = [0, L_x] \times [0, L_y] \times [0, L_z]$ with edge lengths L_x, L_y, L_y, where x and z denote the horizontal directions and y points in the upward vertical direction of swimming.

In order to track the concentration field as it is convected and diffused within the fluid, without crossing into the swimmers, we employ the Volume of Fluid (VoF) approach [5]. Within this VoF framework, the diffusivity κ takes the constant value κ_f in the fluid phase and the constant value $\kappa_p = 0$ in the particle phase. We represent the tangential velocity discontinuity at the surface of the swimmers by a smoothing function, to transition from fluid to particle velocity over a thickness of one grid cell Δx. Physically, this transition layer represents the boundary layer from the tip of the cilia to the ciliated edge of the swimmer. We impose a no-flux condition at the true swimmer surface, so that scalar concentration trapped in the thin modelled ciliated region is able to diffuse into the fluid.

The particle motion is governed by the conservation of linear and angular momentum

$$m_p \frac{d\mathbf{u}_p}{dt} = \int_{\Gamma_p} \tau \cdot \mathbf{n} dA - V_p \left(\rho_p - \rho_f\right) \mathbf{g} + \mathbf{F}_c, \tag{8.9}$$

$$I_p \frac{d\omega_p}{dt} = \int_{\Gamma_p} \mathbf{r} \times \left(\tau \cdot \mathbf{n}\right) dA + \mathbf{T}_c, \tag{8.10}$$

where m_p, I_p, V_p and ρ_p are the mass, moment of inertia, volume, and density of the particle. The hydrodynamic stress tensor $\tau = -p\mathbf{I} + \rho_f \nu \left[\nabla \mathbf{u} + (\nabla \mathbf{u})^T\right]$ is projected onto the outward surface normal vector $\mathbf{n}$ along the particle surface Γ_p. $\mathbf{F}_c$ and $\mathbf{T}_c$ account for collision forces during particle-particle or particle-wall interactions. Normal

collision forces are evaluated from a simple linear spring-dashpot model, while tangential collision forces are neglected. In addition, we employ a lubrication model when two swimmers approach each other. A detailed description of the fluid solver and collision model, along with corresponding validation information, is provided in Biegert et al. [14].

In the classical form of the IBM, the forcing term $\mathbf{f}_{IBM}$ accounts for the no-slip condition at the surface Γ_p of a particle by enforcing the condition (see equation 3.7 for general framework)

$$\mathbf{u} = \mathbf{u}_p + \omega_p \times \mathbf{r} \text{ on } \Gamma_p, \tag{8.11}$$

where $\mathbf{u}_p$ and ω_p denote the translational and angular velocities of the particle, respectively, and $\mathbf{r}$ indicates the position vector from the center of the particle to a point on its surface. For the present squirmer simulations, this traditional form of the IBM is modified, and the forcing term $\mathbf{f}$ is instead calculated such as to impose the relative squirming velocity at the Lagrangian marker points on the particle surface

$$\mathbf{u} = \mathbf{u}_p + \omega_p \times \mathbf{r} + u_\theta \mathbf{e}_\theta \text{ on } \Gamma_p, \tag{8.12}$$

where $u_\theta \mathbf{e}_\theta$ is the squirmer slip velocity imposed at the marker point, acting in the direction of the coordinate vector $\mathbf{e}_\theta$.

8.3.2 Nondimensional formulation

The equations are rendered dimensionless by employing the swimmer radius R and the terminal velocity of a squirmer in the Stokes regime, $\frac{2}{3}B_1$ [16], as characteristic length and velocity scales, respectively. For all simulations, the characteristic concentration C is chosen such that the dimensionless concentration varies between 0 and 1. The

nondimensional variables are thus given by

$$\mathbf{x} \to R\mathbf{x}', \qquad \mathbf{u} \to \frac{2}{3}B_1\mathbf{u}',$$
$$t \to \frac{3R}{2B_1}t', \qquad p \to \rho_f\left(\frac{2}{3}B_1\right)^2 p',$$
$$c \to Cc', \qquad F_c \to \rho_f\left(\frac{2}{3}B_1\right)^2 R^2 F_c',$$
$$T_c \to \rho_f\left(\frac{2}{3}B_1 R\right)^2 R^3 T_c.$$

Dropping the prime, the dimensionless governing equations become

$$\nabla \cdot \mathbf{u} = 0, \tag{8.13}$$
$$\frac{\partial \mathbf{u}}{\partial t} + \nabla \cdot (\mathbf{u}\mathbf{u}) = -\nabla p + \frac{1}{Re}\Delta\mathbf{u} + Ri\xi_f \mathbf{e}_g c + \mathbf{f}_{IBM}, \tag{8.14}$$
$$\frac{\partial c}{\partial t} + \nabla \cdot (\mathbf{u}c) = \frac{1}{Pe}\Delta c. \tag{8.15}$$

where $Re = \frac{2}{3}\frac{B_1 R}{\nu}$, $Ri = gC\alpha R/\rho_f(2/3B_1)^2$, $Pe = \frac{2}{3}\frac{B_1 R}{\kappa_f}$. Additionally, a reference density variation is defined as $\Delta\rho = C\alpha$. The particle momentum equations become

$$\hat{\rho}_p V_p \frac{d\mathbf{u}_p}{dt} = \frac{1}{Re}\int_{\Gamma_p} \tau \cdot \mathbf{n} dA - V_p\left(\hat{\rho}_p - 1\right)\hat{\mathbf{g}} + \mathbf{F}_c, \tag{8.16}$$
$$I_p \frac{d\omega_p}{dt} = \frac{1}{Re}\int_{\Gamma_p} \mathbf{r} \times (\tau \cdot \mathbf{n})\, dA + \mathbf{T}_c, \tag{8.17}$$

with $\hat{\mathbf{g}} = \mathbf{g}R/(\frac{2}{3}B_1)^2$, $\hat{\rho}_p = \rho_p/\rho_f$, $V_p = \frac{4}{3}\pi$ and $I_p = \frac{8}{15}\pi$. The non-dimensional squirmer velocity boundary condition becomes $u_\theta = \frac{3}{2}\left(\sin\theta + \beta\sin\theta\cos\theta\right)$.

Parameter name	Symbol	Definition
Reynolds number	Re	$\frac{2B_1R}{3\nu}$
Peclet number	Pe	$\frac{2B_1R}{3\kappa_f}$
Nondim. gravity	$\hat{\mathbf{g}}$	$\frac{\mathbf{g}R}{(2B_1/3)^2}$
Richardson number	Ri	$\frac{gC\alpha R}{\rho_f(2B_1/3)^2}$
Relative particle density	$\hat{\rho}_p$	ρ_p/ρ_f
Squirming mode	β	B_2/B_1

Table 8.1: List of the simulation parameters.

8.3.3 Active control of swimming direction

The phototactic response of the brine shrimp drives the vertical migration of the swarm, which in turn leads to the formation of a large-scale jet and the associated irreversible mixing [68]. To reproduce this scenario in our simulations, we model the shrimp's phototactic response by modifying the squirming velocity in order to actively control the orientation of the swimmer. This is accomplished by imposing a stronger velocity on the side of the swimmer that is oriented away from the target than on the side facing the target, so that the squirmer rotates towards the target. We take the velocity non-symmetry to be proportional to the misalignment θ_t between the swimming and target directions, as shown in figure 8.6, so that

$$\cos\theta_t = \mathbf{e_s} \cdot \mathbf{e_t}. \tag{8.18}$$

Locally, the value of the velocity modulation at a given point on the surface of the spherical swimmer further depends on the angle ϕ between the projection of the position vector $\mathbf{r}$ and the projection of the target vector $\mathbf{e_t}$ onto the plane normal to $\mathbf{e_s}$. This

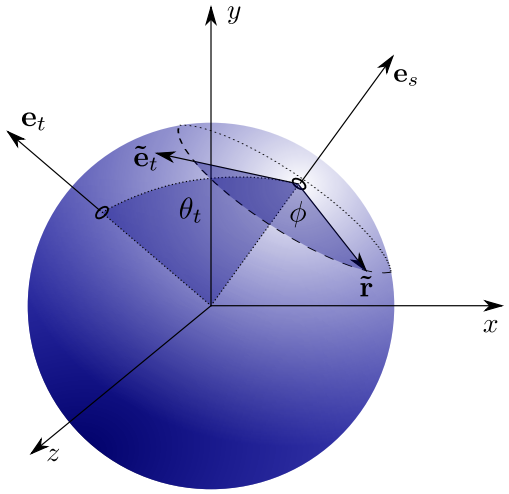

Figure 8.6: Sketch of an active squirmer with phototactic response. The misalignment θ_t is the angle between the swimming direction $\mathbf{e_s}$ and the desired target direction $\mathbf{e_t}$. ϕ is the angle between the projection of $\tilde{\mathbf{r}}$ and the projection of $\tilde{\mathbf{e}}_\mathbf{t}$ onto the plane normal to the swimming direction $\mathbf{e_s}$.

angle is given by

$$\cos\phi = \frac{\tilde{\mathbf{r}} \cdot \tilde{\mathbf{e}}_\mathbf{t}}{||\tilde{\mathbf{r}}|| \cdot ||\tilde{\mathbf{e}}_\mathbf{t}||}, \tag{8.19}$$

where $\tilde{\mathbf{r}}$ and $\tilde{\mathbf{e}}_\mathbf{t}$ are defined as

$$\tilde{\mathbf{r}} = \mathbf{r} - (\mathbf{r} \cdot \mathbf{e_s})\mathbf{e_s} \text{ and } \tilde{\mathbf{e}}_\mathbf{t} = \mathbf{e_t} - (\mathbf{e_t} \cdot \mathbf{e_s})\mathbf{e_s}. \tag{8.20}$$

We introduce a modulation function

$$G(\theta_t, \phi) = \sqrt{1 - A(\theta_t)\cos(\phi)}\ , \tag{8.21}$$

where $A(\theta_t)$ controls the magnitude of the asymmetry and is such that $0 < A < 1$. We propose to evaluate A as

$$A_{q,\gamma} = q + (1-q)\,\mathrm{erf}\left(\gamma\,(1 - \cos\theta_t)\right)\ . \tag{8.22}$$

The amplitude of the asymmetry using this model jumps to the step value q as soon as a non-negligible misalignment is measured, and it smoothly increases to unity using an error function. γ is used to modulate how sharply the swimmer will transition from a weak correction to a strong correction of its swimming direction, depending on the value of θ_t. Finally, the asymmetric squirming velocity is given by

$$u_\theta = F(\theta) \cdot G(\theta_t, \phi) \ , \tag{8.23}$$

where $F(\theta) = B_1 \sin\theta + B_2 \sin\theta\cos\theta$ is the original squirming velocity.

8.3.4 Numerical setup

The governing parameters are chosen to closely match the experimental values. As described in section 8.4, the typical animal velocity observed in the experiments is $1cm/s$. We base the size of the spherical squirmer on the length of the *A. salina* appendages of order $1cm$, which also represents the characteristic length scale over which the fluid is being accelerated. Hence, we select as the squirmer radius $R = 0.5cm$. For a fluid viscosity of $10^{-6}m^2/s$, this yields a Reynolds number $Re = 50$, which fits within the range of inertial flows recently investigated using the squirmer model [29, 89].

The simulations are conducted with our in-house code PARTIES, a second-order accurate finite difference solver based on a staggered uniform Cartesian grid [14]. Time integration is performed by a low-storage, third-order Runge-Kutta method, based on a pressure-projection approach for satisfying the continuity constraint. The volume fraction of the swimmers in the simulations is chosen to mimic the animal number density of the experiments. The appropriate fluid velocity and concentration field boundary conditions at the surface of the swimmers are enforced via the IBM and VoF techniques, as described above. The above simulation approach allows us to consider a variety of flows, for different

boundary and initial conditions.

8.4 Coherent jet velocity

8.4.1 Experimental observations

A. salina exhibit slight negative buoyancy, similar to most marine zooplankton [119], and therefore must overcome both gravity and fluid drag to propel themselves upward. The required thrust for this upward swimming is produced via the rearward propulsion of fluid by the metachronal beating of the animal appendages [173], similar to the swimming modes of many marine zooplankton such as Antarctic and Pacific krill [27].

In the laboratory migrations, as the animal number density within the aggregation increased, the distance between each swimmer decreased and the fluid wakes of individual swimmers began to interact, as seen in figure 8.7. Previous work found that the individual flow fields combined to form a coherent downward jet-like flow within the aggregation, even in the presence of strong stratification relative to oceanic values [68]. Here, we present the dependence of the jet-like flow on animal number density.

During the laboratory migrations conducted, following activation of the upper focused LED, animal number density within the field of view gradually increased over the first 80-100 seconds. At first, fluid motion within the illuminated plane was limited to individual wakes visualized due to animals swimming in the laser sheet. Over time, animal number density asymptoted and a spatially coherent downward flow developed 8.8. The initially high normalized spatial standard deviation of the vertical fluid velocity decreased as the coherent downward jet developed within the swarm. The period from 100-155 seconds was used for asymptotic values, chosen for the relatively constant animal number densities among all experiments. The average of all the vertical velocity values within the field

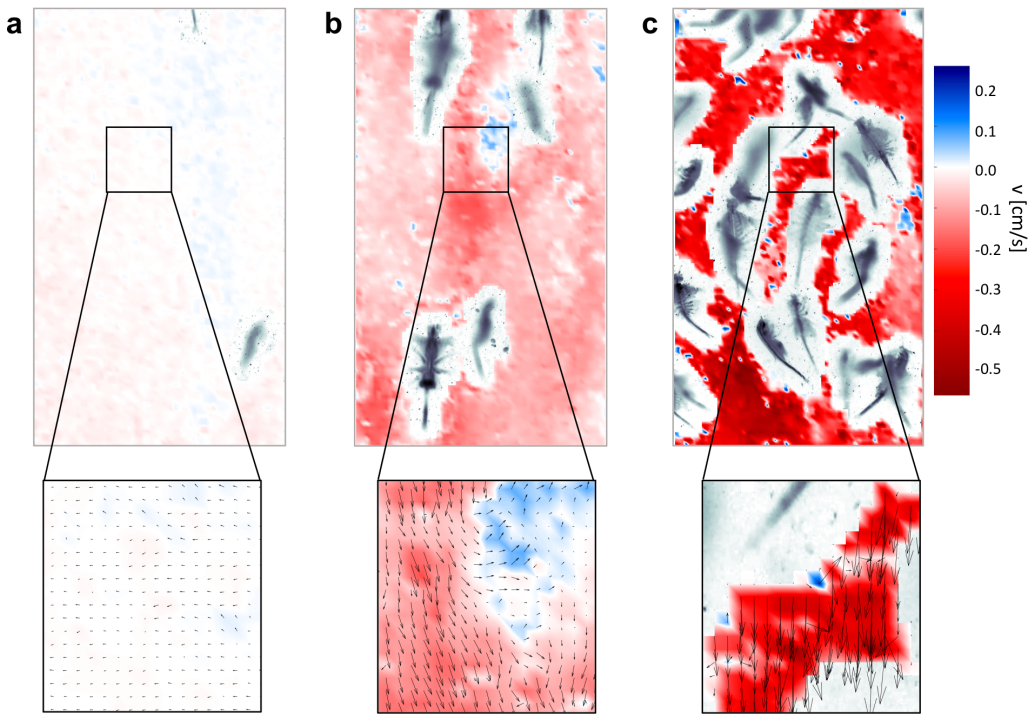

Figure 8.7: Experimental measurements. Upper row: Pseudo-color plot of instantaneous vertical velocity in illuminated plane at three times. Lower row: Zoom of region with in-plane velocity vectors at three different times: (a) $t = 16.4s$, (b) $t = 56.4s$, and (c) $t = 100s$.

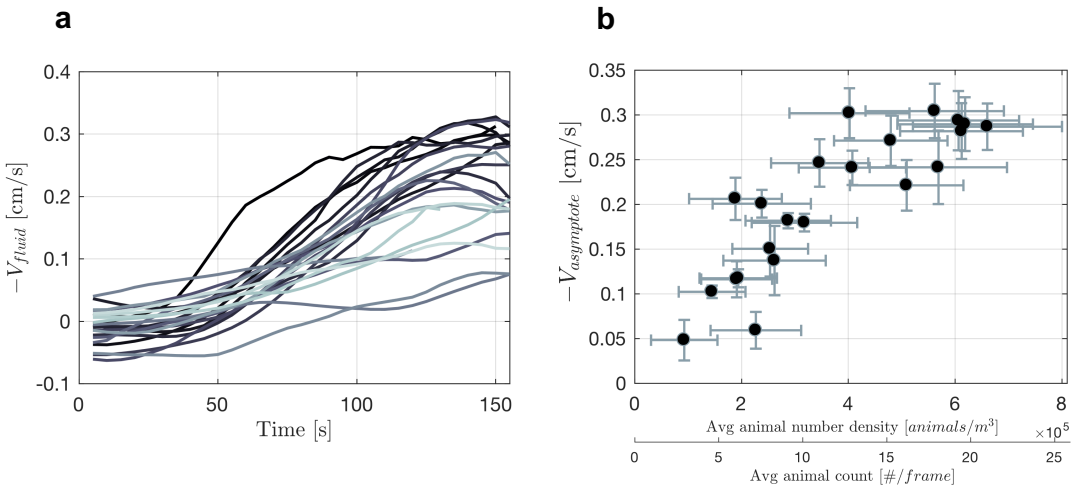

Figure 8.8: Experimental measurements. (a) Instantaneous animal count in the field of view, in 1 second bins. (b) Average animal swimming speed over time, in 1 second bins. Colored lines from dark to light correspond to the first experiment to the last experiment run. Animal count within the migration decreased over time, either due to reduced phototaxis or overall endurance. Animal velocities were higher at early times, either because they were naturally faster or did not have to contend with the flow fields of preceding animals.

of view were averaged over the time interval from 100-155 seconds to obtain an average asymptotic fluid velocity. As would be expected, migrations with higher asymptotic animal number density resulted in a larger asymptotic downward jet velocity 8.9. More animals propelling themselves upward against gravity and drag required more thrust to be produced, in the form of a downward induced velocity, explaining the monotonic increase in jet velocity with increasing animal number density within the range of animal number densities tested.

8.4.2 Discrete swimmer simulations

We employ numerical simulations in order to investigate the formation of a jet by a homogeneous swarm of squirmers moving in a constant fluid density fluid, for various animal number densities. Towards this end, we consider a group of neutrally buoyant

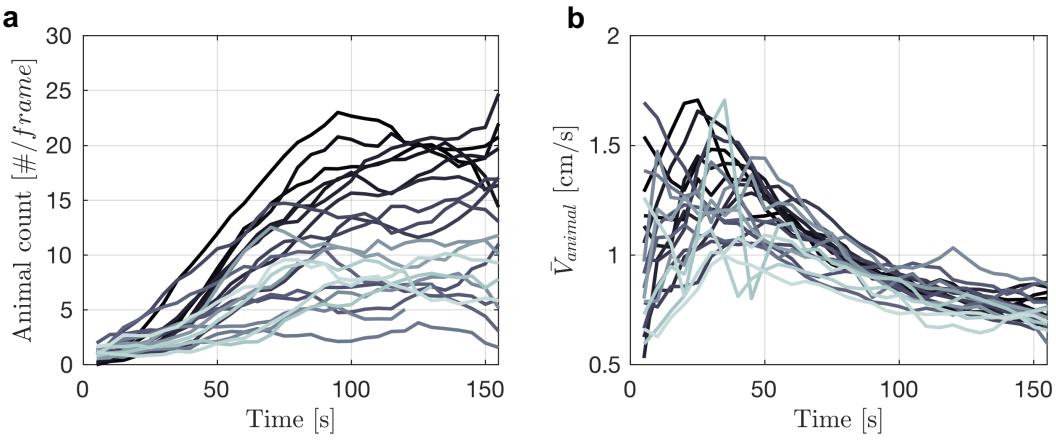

Figure 8.9: Experimental measurements: (a) Average vertical fluid velocity during each migration over time (b) Asymptotic jet velocity as a function of animal number density. Error bars represent the standard deviation of the animal count (horizontal) and fluid velocity (vertical). The standard deviation of the animal count is due to animal density variability during the asymptotic period as well as large noise in the counting algorithm. Adapted from Houghton and Dabiri [66]

swimmers that are initially distributed randomly in fluid at rest. We apply periodic conditions in the swimming direction y and the spanwise z-direction, so that the swimmers can exit the computational domain at one boundary and re-enter it at the opposite one (figure 8.10). Slip walls are employed in the spanwise x-direction. The volume fraction of the swimmers is determined by their number and the size of the simulation domain. All simulations have $Re = 50$ and $\beta = -3$, and they employ a domain size of $20 \times 40 \times 10$ with a constant grid spacing of $1/30$. The target light source is placed at height $2L_y$, centered in the horizontal plane, so that the swimmers move upwards. We conducted four simulations with 47, 94, 187 and 373 neutrally buoyant swimmers, corresponding to volume fractions of 2.46%, 4.92%, 9.79%, and 19.53%, in order to closely match experimental conditions, as well as estimates of the packing density in the ocean [171, 70].

As the swimmers move through the domain and interact, they influence each other's velocity and direction. Figure 8.11 shows a two-dimensional slice of a typical configuration, along with the fluid velocity vectors and contours of the velocity magnitude. The

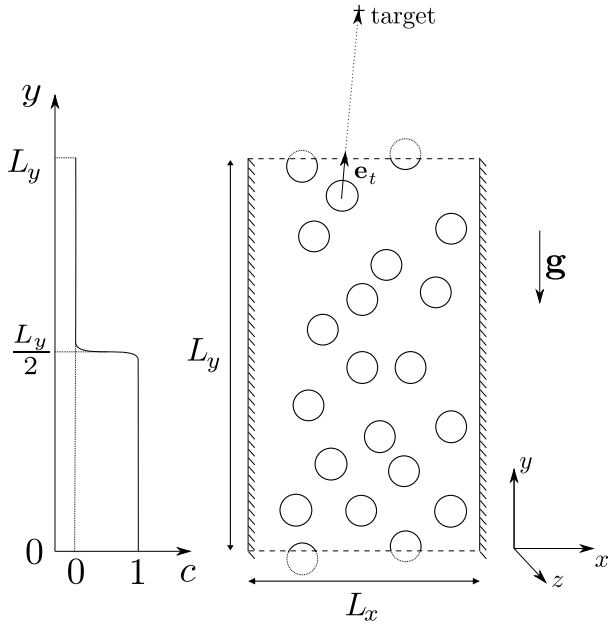

Figure 8.10: Numerical set-up for simulating the formation of a jet by a homogeneous swarm of swimmers in a periodic domain.

figure demonstrates that the hydrodynamic interactions among the swimmers occur both at the scale of the swimmers themselves, but also at scales several times larger than the swimmer size due to the substantial extent of their wakes.

The experiments discussed earlier had indicated that the jet velocity produced by the global swarm depends on the local volume fraction of swimmers, i.e., on the animal number density. Since the swarm extends over the entire computational domain in the simulations, we compute the volume average of the vertical fluid velocity as

$$V_{fluid}(t) = \frac{1}{L_x L_y L_z (1-\bar{\phi}_p)} \int_\Omega v\,(1-\phi_p)\,dV \ . \tag{8.24}$$

where ϕ_p is the local particle volume fraction. For all four global volume fractions, figure 8.4.2 displays the results for V_{fluid} as a function of time in dimensional form, so that they can be directly compared to the corresponding experimental data.

The jet velocity rapidly reaches a quasi-steady value, despite the nonlinearity of the

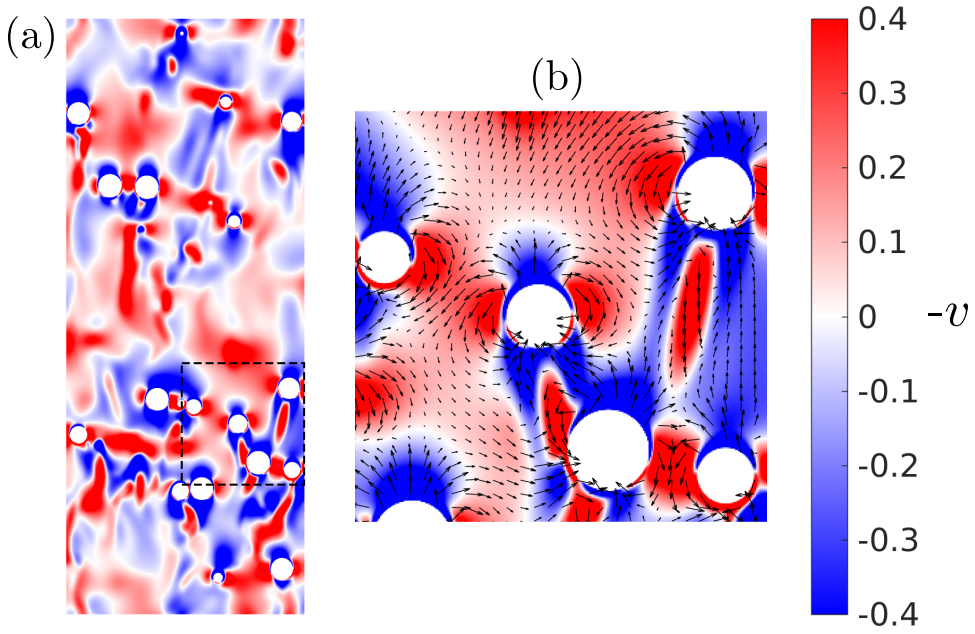

Figure 8.11: Discrete swimmer simulation of the jet formation with a volume fraction of swimmers of 9.79%. (a) Pseudo-color plot of the vertical velocity in a slice of the three-dimensional domain. (b) Zoomed-in view corresponding to the dashed-line square in the right frame, with the planar component of the velocity vector field.

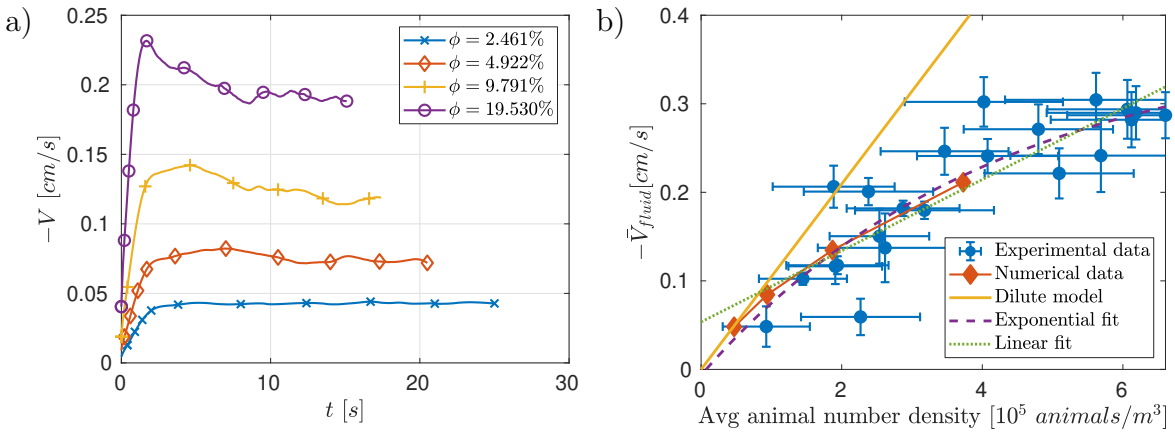

Figure 8.12: Simulation results: (a) Average vertical fluid velocity for various mean volume fractions of swimmers $\bar{\phi}_p$ over time. (b) Asymptotic jet velocity as a function of the animal number density, i.e., the mean volume fraction of swimmers.

local particle-particle interactions. In agreement with the experiments, the jet velocity depends strongly on the number of swimmers per unit volume. This is more easily characterized by the average jet velocity in the quasi-steady regime defined as

$$\bar{V}_{fluid} = \frac{1}{\tau}\int_{t^*}^{t^*+\tau} V_{fluid}(t)dt. \tag{8.25}$$

where τ is an integration window sufficiently large so that $\bar{V}_{fluid}$ does not depend on τ. The results are presented in figure 8.4.2 as a function of the mean volume fraction of swimmers $\bar{\phi}_p$ and suggest a nonlinear relationship between jet velocity and mean volume fraction, or equivalently animal number density. The dimensional jet velocity and animal number density can be calculated from those results and compared to the experiments. The mean volume fractions of swimmers $\bar{\phi}_p = 2.46\%$, 4.92%, 9.79% and 19.53% correspond to animal number densities of $4.7{\cdot}10^4\ m^{-3}$, $9.4{\cdot}10^4\ m^{-3}$, $1.87{\cdot}10^5\ m^{-3}$ and $3.73 \cdot 10^5\ m^{-3}$, respectively. Recalling the reference velocity of $U = 1cm/s$, the dimensional numerically measured jet velocities are $0.048cm/s$, $0.084cm/s$, $0.135cm/s$ and $0.202cm/s$. The animal number densities observed in the simulations overlap with the values measured in the experiments, and the agreement with experimentally measured jet velocities for such animal densities is excellent. This suggests that the squirmer model quantitatively captures the thrust generation by the collective action of the animals.

Given that the swimmers and the fluid are initially at rest, and that there is no external momentum transfer to the fluid or swimmers, the total momentum of the fluid has to remain equal and opposite to that of the swimmers for all times, so that

$$\bar{V}_p\bar{\phi}_p = -\bar{V}_{fluid}(1-\bar{\phi}_p)\ , \tag{8.26}$$

where $\bar{V}_p$ is the average swimmer velocity in the quasi-steady regime. For small animal

volume fractions, we can assume the fluid velocity to be uniform throughout the domain, and the swimmers to move with their terminal velocity V_{term}, so that

$$\bar{V}_p - \bar{V}_{fluid} = V_{term}(\beta, Re) \ . \tag{8.27}$$

Equations (8.26) and (8.27) can then be solved for $\bar{V}_p$ and $\bar{V}_f$ as functions of $(\bar{\phi}_p, \beta, Re)$, yielding

$$\bar{V}_{fluid} = -\bar{\phi}_p V_{term} \ , \tag{8.28}$$

$$\bar{V}_p = (1 - \bar{\phi}_p) V_{term} \ . \tag{8.29}$$

Note that the velocities are made dimensionless by the terminal velocity of a squirmer in the Stokes regime, such that $V_{term}(\beta, 0) = 1$ for all β. Scaling of the terminal velocity with the Reynolds number is thoroughly investigated by Chisholm et al. [29]. In order to evaluate the terminal velocity of an individual swimmer for the specific values of $\beta = -3$ and $Re = 50$, we conduct a simulation of a single swimmer in an unstratified fluid column, which shows a terminal velocity $V_{term} \approx 2$. This is consistent with the results of Chisholm et al. [29], who found a terminal velocity of approximately 2.5 for $\beta = -5$. Pushers in an inertial regime exhibit faster swimming speeds than in the viscous regime such that $V_{term} > 1$ for all values of $\beta < 0$.

Figure 8.4.2 compares the prediction from equation (8.28), referred to as the dilute model, to the results of the numerical simulations and experimental measurements. Additionally, a linear and an exponential fit are computed as described below. The dilute model passes through the origin and through the numerical data point associated with the smallest volume fraction. This demonstrates that the homogeneous flow assumption is valid at low volume fraction and that the dilute model is accurate at low volume

fractions. The figure also shows that the swarm jet velocity depends sub-linearly on the animal number density, and that nonlinear interactions of the wakes impact the jet formation as soon as $\bar{\phi}_p > 2.5\%$. The least-square exponential and linear fits, respectively, take the form $V_{exp.} = ae^{bn} + c$ and $V_{lin.} = a'n + b'$ where n is the animal number density and a, b, c, a', b' are constants. The optimal fit is computed over the whole set of numerical and experimental data. Interestingly, the exponential fit obtained from the combined data agrees remarkably well with the numerical data and, without any arbitrary constraints, recovers the $c = -a$ condition that guarantees that $V_{exp.} = 0$ at $n = 0$, i.e. that the jet velocity is zero in the absence of swimmers. Thus, models for the large-scale effects of *A. Salina* swarms on the water column can rely on jet velocity predictions based on the estimated animal number density. Such efforts are described in section 8.6. Additionally, there is a simple upper boundary to the maximum jet velocity produced by the swarm, determined by momentum conservation and terminal swimmer velocity and that assumes that individual swimmers encounter a perfectly homogeneous flow. This idealized dilute scaling agrees well with numerical and experimental data for low volume fractions.

8.5 Mixing in the presence of a density stratification

8.5.1 Experimental observations

In order to assess the ability of swarms of swimmers to contribute to oceanic mixing processes, it is important to account for the effects of density stratification on the swarm-induced fluid transport processes described in the previous section. Values of the oceanic buoyancy frequency $N = \sqrt{-\frac{g}{\rho}\frac{\partial \rho}{\partial y}}$ typically fall into the range $10^{-3}s^{-1} \leq N \leq 10^{-2}s^{-1}$, whereas the present laboratory experiments employed significantly larger values of N,

up to $10^{-1}s^{-1}$, due to laboratory constraints. Nevertheless, a strong downward jet was observed to transport less dense fluid against the stable background density gradient, as seen in figure 8.13. The downward fluid transport within the jet was balanced by an upward counterflow outside of the swarm.

The transient measurements shown in figure 8.13b show fluid with approximately the surface density transported to the lower extent of the aggregation, rather than a series of smaller-scale overturns that would reduce transport and mixing. The vertical extent of fluid transport varied over time, due to variability in the balance between the swarm propelling fluid downward and the buoyant restoring force on the displaced fluid. We note that these density profiles were obtained during an active migration with significant fluid motion. Therefore, the local density profile is not representative of the entire tank cross-section and thus the one-dimensional density transect is not expected to conserve mass.

The transient profiles illustrate a mechanism for altering the density stratification via large-scale fluid transport. The resulting turbulent mixing increases the surface area and gradient strength between fluid parcels of different densities, which in turn enhances the rate of scalar diffusion and irreversible mixing. In the long-term mixing experiments, the density profiles measured along a single vertical line (see section 8.2) show significant smoothing of the two-layer stratification, indicative of irreversible mixing due to the migration of the swarm. Two different stratification strengths, $N_{int} = 0.10s^{-1}$ and $N_{int} = 0.05s^{-1}$ are presented in figure 8.14, illustrating the significantly enhanced mixing for a range of restratifying forces. By fitting the solution of the one-dimensional vertical diffusion equation with variable diffusivity to the measured profiles, Houghton et al. [68] argued that this enhanced mixing reflects an effective diffusivity approximately three orders of magnitude larger than the molecular diffusivity of salt. Interestingly, mixing across the interface was vertically asymmetric, with mixing extending further above the

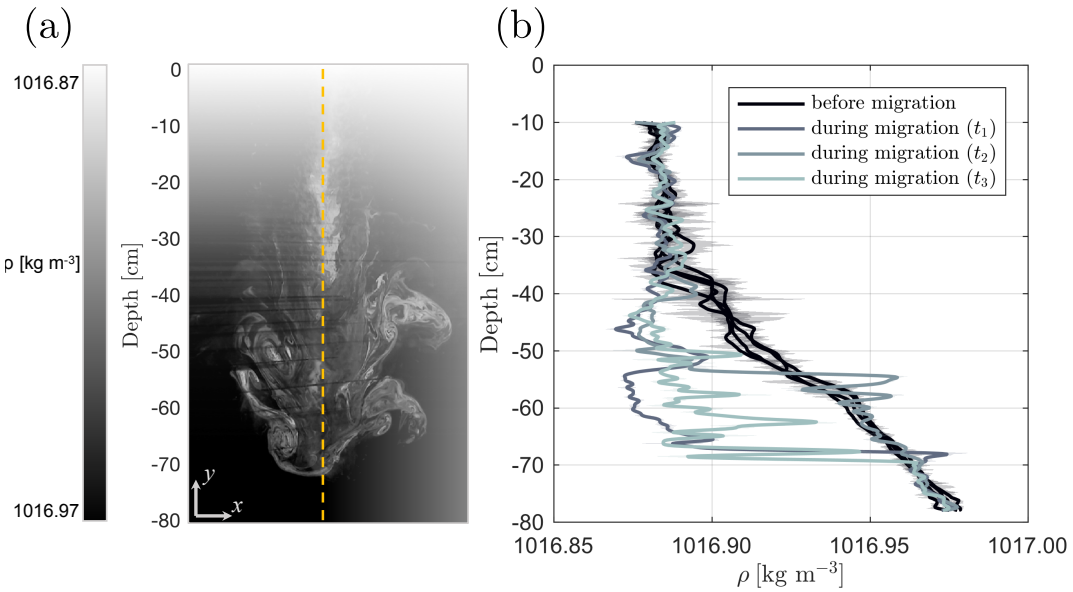

Figure 8.13: (a) Schematic describing transient flow in linearly stratified tank. Grayscale coloring corresponds to fluid density, with the jet transporting light colored, low density fluid downward. Arrows indicate fluid motion. Yellow dashed line corresponds to a representative location to obtain the vertical density profiles presented in the frame on the right. (b) Four control density profiles were obtained prior to a migration. Three separate profiles during the migration were obtained at $t_1 = 18min$, $t_2 = 24min$, and $t_3 = 28min$.

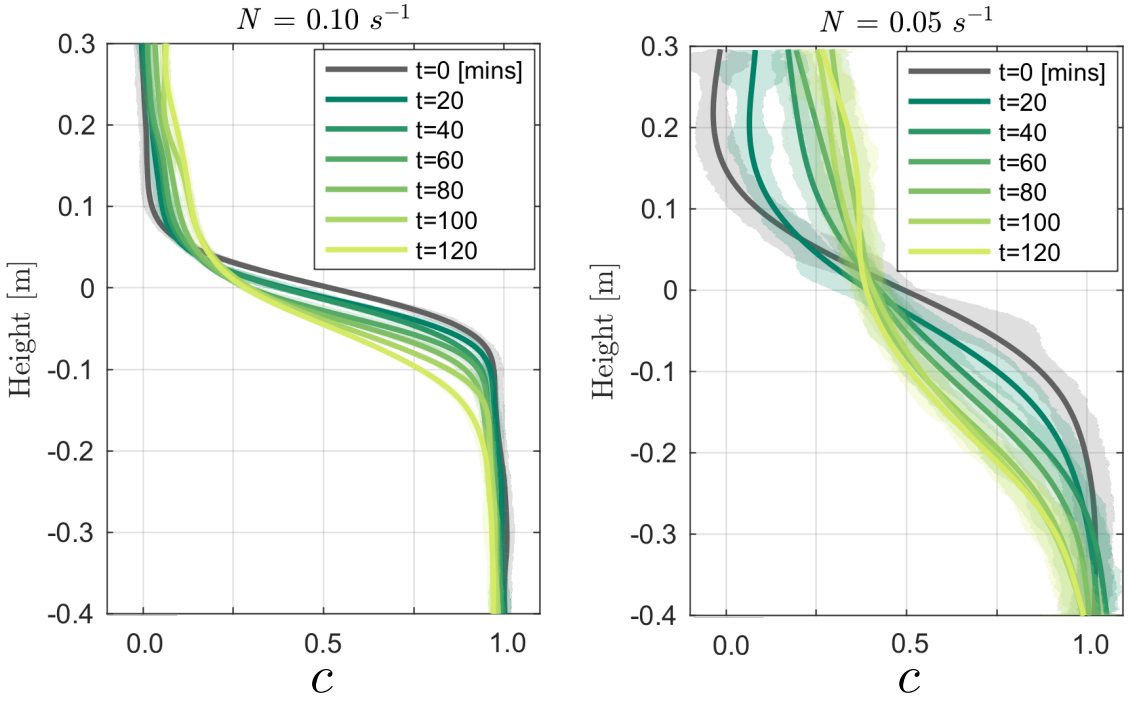

Figure 8.14: Concentration profile evolution from the original two-layer stratification for two stratification strengths. Repeated final profiles were constant, indicating the tank was fully quiescent and horizontally homogeneous and the density profile change was due to irreversible mixing. Concentration profiles are shifted and normalized to span a range from 0 to 1 for ease of comparison where a concentration of 0 corresponds to the minimum initial salt concentration of the upper layer and 1 corresponds to the maximum initial salt concentration of the lower, denser layer for a given experiment. Adapted from Houghton et al. [68]

interface than below.

8.5.2 Simulations: Irreversible mixing within the swarm

The post-migration experimental density profiles shown in figure 8.14 demonstrate the swarm's ability to generate substantial irreversible mixing. The associated flow visualization images provided in figure 8.13 suggest that this mixing occurs both within the swarm as well as at the edge of the swarm-induced jet. In order to analyze the dependence of this irreversible mixing on the animal number density, we apply the same

simulation set-up as in section 8.4.2, but now for a two-layer stratified ambient, as shown in figure 8.10. We continue to employ periodic boundaries in the vertical direction for the swimmers and the fluid velocity field, but impose a vanishing normal derivative at those boundaries for the concentration variable. We calculate the Richardson number directly from the experimental setup, which has a density difference $\Delta\rho = 0.051\text{kg/m}^3$. For the gravitational acceleration $g = 9.81\text{m/s}^2$ and the reference density $\rho_f = 1,000\text{kg/m}^3$, we obtain $Ri = \frac{R\Delta\rho g}{\rho_f U^2} = 0.025$. In order to reduce the computational cost, we employ $Sc = \frac{\nu}{\kappa_f} = 1$, which is $O(10^3)$ smaller than the experimental value for salt ions [176]. The initial density profile has an error function shape $\frac{1}{2}(1 - erf(\frac{y-H/2}{\delta_p}))$, with a pycnocline thickness $\delta_p = \frac{1}{3}R$.

All simulations employ $Re = 50$ and $\beta = -3$, in a domain of size $20 \times 40 \times 5$ with a constant grid spacing of $1/30$. The target light source is placed at the height $2L_y$, centered in the horizontal plane, so that the swimmers move upwards. We conducted three simulations with 24, 48 and 93 swimmers, corresponding to volume fractions of 2.51%, 5.03%, and 10.05%.

We quantify irreversible mixing by employing the concept of background potential energy as introduced by Winters et al. [174]. Changes in the background potential energy E_b directly measure the irreversible transfer of energy that goes into mixing. For a given system, E_b is defined as the lowest potential energy that can be obtained via the reversible rearrangement of fluid parcels. We write

$$E_b = g \int_\Omega \rho y^* dV \ , \tag{8.30}$$

where the mapping $y^*(\mathbf{x}, t)$ gives the vertical position of a fluid parcel of density $\rho(y^*)$ originally at position $(\mathbf{x}, t)$. The corresponding sorted concentration profile $c(y^*)$ represents the configuration of the lowest potential energy, in which the fluid parcels are

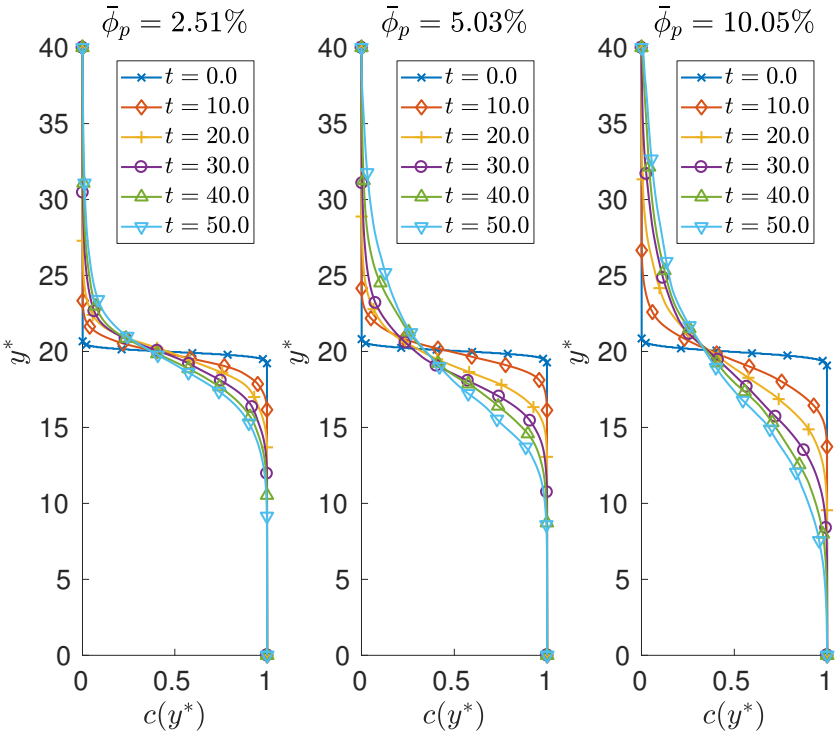

Figure 8.15: Time series of sorted concentration profiles for various mean swimmer volume fractions in the periodic, two-layer stratified domain.

arranged in layers of upward decreasing densities. The numerically computed, sorted concentration profiles shown in figure 8.15 are qualitatively similar to the experimental profiles of figure 8.14.

In order to quantify the increase in mixing due to the presence of the swimmers, we calculate an effective diffusivity κ_{eff} from the sorted concentration profiles $c(y^*)$, by solving the minimization problem

$$r = \min_{\kappa_{eff}} \left(\| c(y^*) - c_{\kappa_{eff}} \| \right) \ . \tag{8.31}$$

Here $c_{\kappa_{eff}}$ represents the solution to the one-dimensional heat equation for a two-layer problem with a diffusivity κ_{eff} that is constant in space and time. $\kappa_{eff}/\kappa = 1$ initially since the swimmers and the fluid are initially at rest, cf. figure 8.5.2. As the swimmers

cross the pycnocline, they displace fluid and lead to a monotonic increase in effective diffusivity. The simulation results show an effective diffusivity that is more than an order of magnitude larger than the molecular diffusivity for the largest volume fraction, suggesting a strong impact of the swimmers on interfacial mixing. The final ratio of effective to molecular diffusivity increases approximately linearly with the swimmer volume fraction, which agrees well with results for squirmers in a linearly stratified environment [171]. Figure 8.5.2 compares the horizontally averaged concentration profiles to the sorted ones employed for the effective diffusivity calculation.

We note that Houghton et al. [68] calculated a depth-dependent effective diffusivity, which they found to have a maximum in the upper fluid layer, and a minimum in the lower layer. The authors reported effective diffusivities up to three orders of magnitude larger than the molecular diffusivity of salt ions, although we have to keep in mind that the molecular diffusivity in the experiments was $O(1,000)$ smaller than in the simulations. This results in much smaller ratios of effective to molecular diffusivity in the simulations than in the experiments.

8.5.3 Simulations: Preferential direction of scalar transport

As shown in figure 8.14, experimentally measured density profiles between migrations reveal an asymmetry with respect to the centreline of the profile. Since we are in the Boussinesq regime, we hypothesize that this asymmetry, or skewness, in the profiles results from the swimming direction, rather than from the density stratification.

In order to explore this issue, we simulate the migration of a swarm of swimmers across a stably stratified density interface within a closed domain, as sketched in figure 8.17. Initially the swimmers are randomly distributed in the lower (upper) half of the domain for an upward (downward) moving swarm, such that the initial volume fraction

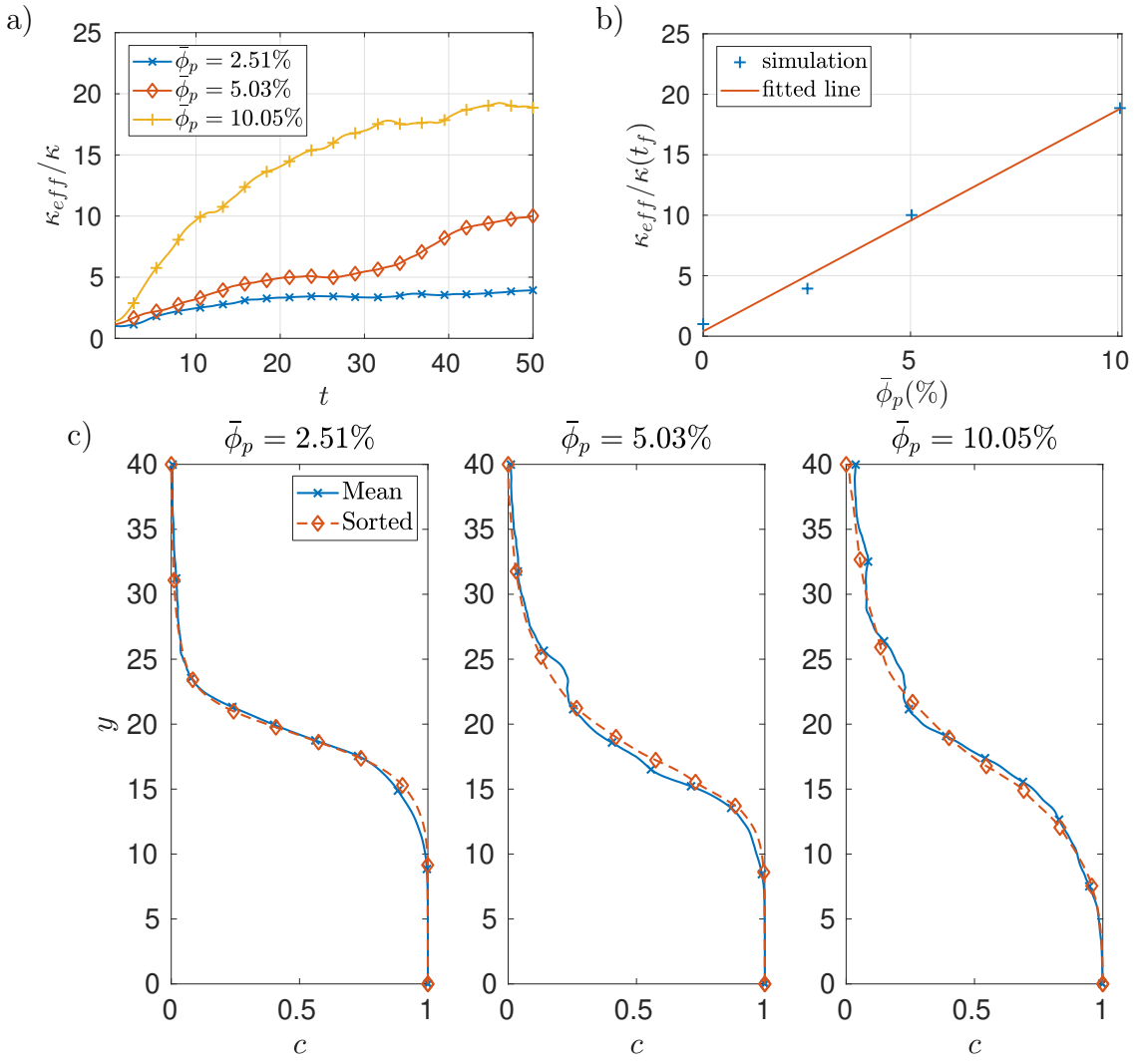

Figure 8.16: Ratio of effective to molecular diffusivity for various mean swimmer volume fractions in the periodic, two-layer stratified domain. (a) Variation with time. At $t = 0$, $\kappa_{eff}/\kappa = 1$ as swimmers are initially static. (b) Final computed value as a function of swimmer volume fraction, and linear fit. (c) Comparison of horizontally averaged profiles and sorted profiles at $t = 50$.

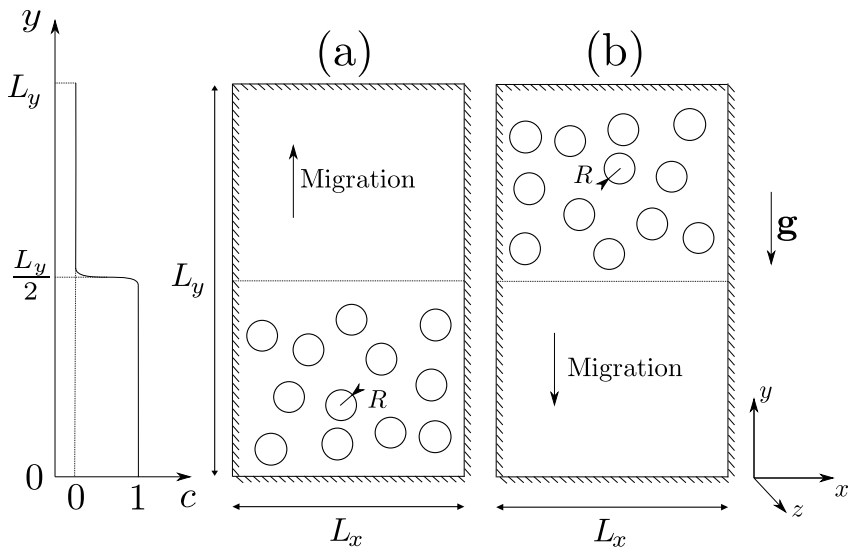

Figure 8.17: Sketch of the initial configuration for simulations of swarms migrating across a stably stratified density interface. (a) upward moving swarm, and (b) downward moving swarm.

is $\bar{\phi}_p = 0.1$ in the populated half, equivalent to an animal number density of $1.9 \cdot 10^5\ m^{-3}$. In both cases, the swimmers are neutrally buoyant with respect to the upper fluid layer. The target light source is placed at $y = 2L_y$ ($y = -L_y$) for the upward (downward) moving swarm. We employ the closed domain setup in order to prevent a mean flow from developing. The parameters of the numerical simulations are summarized in table 8.2. Under the Boussinesq approximation, the only feature that prevents the two cases from being equivalent to each other is the swimmer density, which equals the density of the upper fluid layer in both cases. In the lower layer, the upward moving swarm thus experiences a buoyancy force in the direction of swimming, while the downward moving swarm experiences a force opposed to the swimming direction. Hence a comparison of the two cases will enable us to assess the influence of the animal density on the transport.

Snapshots of a two-dimensional plane of the density field at different times are presented in figure 8.18 for the case of the upward moving swimmers. Swimmers that are sliced by the plane appear as white disks, whose size depends on the relative position

(L_x, L_y, L_z)	(N_x, N_y, N_z)	$N_{swim.}$	R	Re	Pe	Ri	$\hat{\rho}_p$	β	$\mathbf{e}_{s,i}$
$(30, 40, 5)$	$(900, 1200, 150)$	72	1	50	50	0.025	1	-3	$\mathbf{e}_y$
$(30, 40, 5)$	$(900, 1200, 150)$	72	1	50	50	0.025	1	-3	$-e_y$

Table 8.2: Numerical parameters for simulating the migration of a swarm across a density interface.

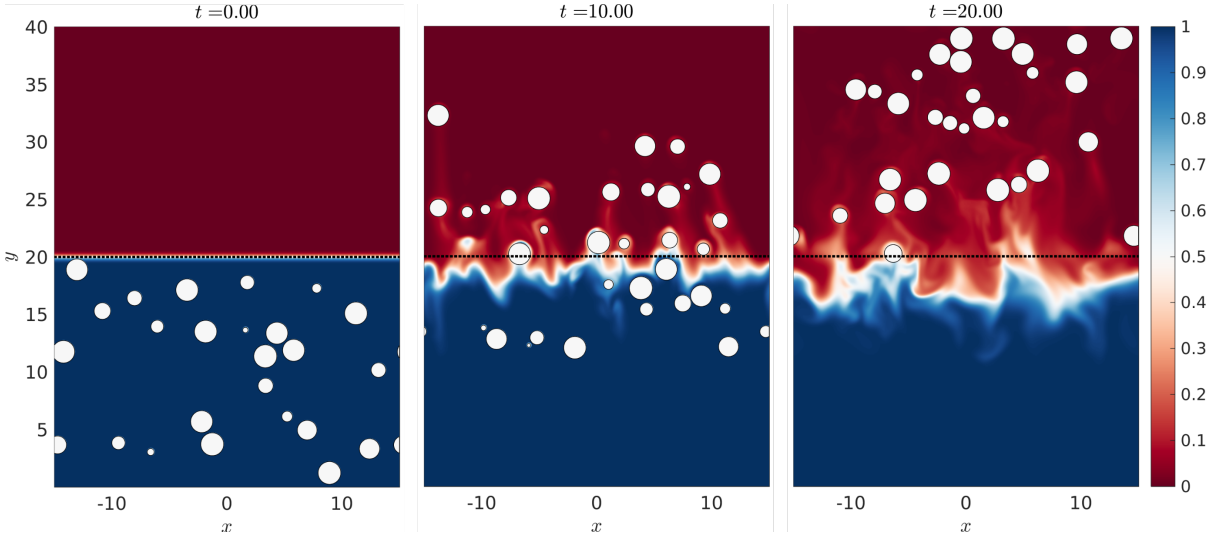

Figure 8.18: Two-dimensional slice of the density field for upward moving swimmers, at three different times. The black dotted line denotes the initial location of the pycnocline ($c = 0.5$).

of the swimmer with respect to the plane. The motion of the swimmers is observed to deform the density interface, whose initial location is marked by the dotted black line. The squirmers carry dense fluid with them above the interface, while their wake pushes lighter fluid below the interface.

The scalar transport is seen to be skewed in the direction of swimming, which confirms that the experimentally observed skewness is indeed an intrinsic properties of the swimming-induced transport. We can define a quantitative indicator of the skewness in the form of the transport length

$$L_{skew} = L_{up} - L_{down} \ , \tag{8.32}$$

where L_{up} and L_{down} represent the first moments of the scalar field

$$L_{up} = \frac{\int_{h_p}^{L_y} \bar{c}|y - h_p|)dy}{\int_{h_p}^{L_y} cdy} \ , \ L_{down} = \frac{\int_{0}^{h_p} (1-\bar{c})|y - h_p|)dy}{\int_{0}^{h_p} (1-\bar{c})dy} \ . \tag{8.33}$$

Here $\bar{c}$ denotes the horizontally averaged concentration field. h_p represents the instantaneous vertical position of the pycnocline, which is evaluated as

$$h_p = \frac{L_y}{2} \frac{1 - \bar{\phi}_0}{1 - \bar{\phi}_t} \ , \tag{8.34}$$

where $\bar{\phi}_t$ indicates the time-dependent volume fraction of swimmers in the lower fluid layer. This definition of h_p reflects the fact that conservation of volume causes the y-location where $c = 0.5$ to shift downward as the swimmer volume is transferred from the lower to the upper layer. Since $\bar{\phi}_t$ itself is a function of h_p, this equation is solved numerically at each time in order to compute L_{up} and L_{down}.

Figure 8.5.3 presents results for L_{skew} as function of time for both upward and downward moving swarms. The transport length is positive (negative) for upward (downward) migration. The absolute values are very similar, suggesting that under the current conditions the swimmer density has little impact on the skewness of transport. This confirms that the experimentally observed skewness is a result of preferential transport in the direction of the swarm, and not due to the effect of the swimmer buoyancy.

The above observations suggest that the preferred transport is driven by the amount of resident fluid that a swimmer carries along next to its surface, which is a function of the squirmer mode β. Figure 8.5.3 compares the transport length L_{skew} for a single pusher with $\beta = -3$ and a neutral swimmer with $\beta = 0$. We exclude pullers from the comparison, since at Reynolds numbers $\mathcal{O}(100)$ they produce an unstable wake [29], so that the

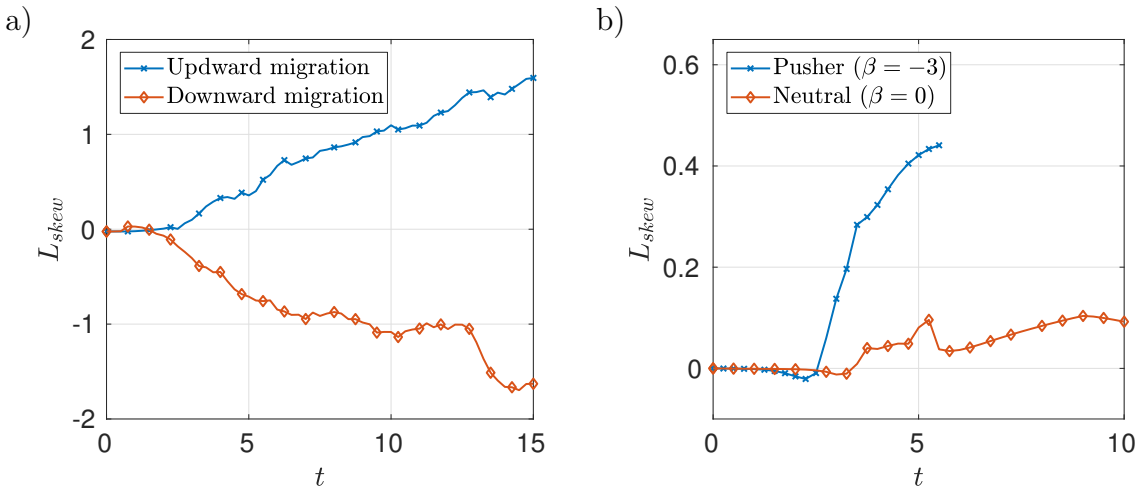

Figure 8.19: (a) Transport length L_{skew} as a function of time for upward and downward moving swarms. (b) Transport length generated by a single swimmer moving through a pycnocline for two squirming modes: puller ($\beta = -3$) and neutral ($\beta = 0$).

squirmer model is unlikely to represent animals in the *cm*-size range. The figure demonstrates that pushers generate a much stronger skewness than neutral swimmers. Pushers travel faster than neutral swimmers, but even for corresponding vertical swimmer locations pushers transport dense fluid over longer distances, and perturb the interface more strongly than their neutral counterpart, as seen in figure 8.20. This suggests that a comparison of experimental and computational skewness can potentially provide information on whether a particular animal functions more like a pusher or a neutral swimmer.

8.6 Continuum model for mixing at the swarm scale

As mentioned earlier, we distinguish between squirmer-scale mixing processes due to the motion of individual animals, and swarm-scale mixing events involving the jet generated by the collective action of all swimmers. Understanding and quantifying the respective roles of the processes at these different scales is essential for developing realistic biogenic mixing models for the ocean. The swimmer-resolving simulations described in

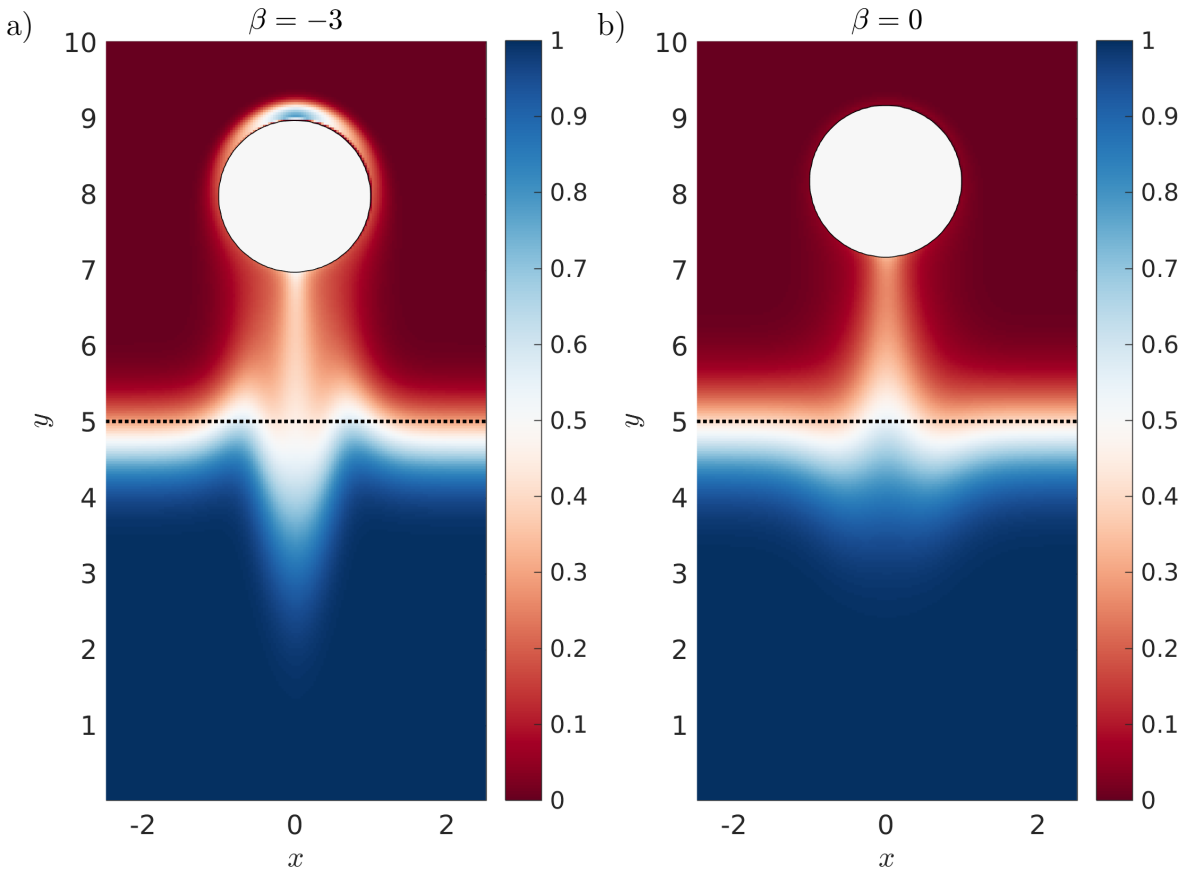

Figure 8.20: Slice of the scalar concentration field for a single swimmer moving through a sharp pycnocline for (a) a pusher squirmer, and (b) a neutral squirmer.

the previous section successfully reproduced the mixing dynamics at the scale of each animal, as well as the jet formation due to their collective action. In the following, we aim to develop a continuum model capable of capturing the mixing events at the scale of this jet, as observed in the flow visualization experiments of figure 8.13a.

Consider the momentum balance of a neutrally buoyant individual swimmer migrating upward. If the swimmer moves at a steady velocity, the drag it experiences is balanced by its thrust, so that it does not impart any net momentum onto the fluid. Consequently the upward momentum transferred by the swimmer onto fluid parcels near its head, equals the downward momentum imparted on fluid parcels in the wake of the swimmer, which form the swimmer-scale jet. For a negatively buoyant swimmer moving at a steady velocity, the balance between thrust and drag is modified by the gravitational force. When many swimmers migrate upwards within close proximity of each other in a dense swarm, these swimmer-scale upward and downward-moving fluid parcels partially neutralize each other due to viscous diffusion. However, at the swarm scale the collective action of the swimmers still results in the net upward acceleration of fluid parcels ahead of the swarm, and in the downward acceleration of fluid parcels in its wake. This downward moving fluid forms the swarm-scale jet observed in the experiments of figure 8.13a.

We model the jet formation by the collective action of the swimmers at the swarm scale via a source term in the vertical momentum equation that extends over the scale of the swarm R_s, and travels with the swarm velocity V_s. The Navier-Stokes equations with the swarm source term take the form

$$\nabla \cdot \mathbf{u} = 0 \ , \tag{8.35}$$

$$\frac{\partial \mathbf{u}}{\partial t} + (\mathbf{u} \cdot \nabla)\, \mathbf{u} = -\frac{1}{\rho_0} \nabla p + \nu \nabla^2 \mathbf{u} + \mathbf{f} \ , \tag{8.36}$$

where the forcing term $\mathbf{f}$ is defined as

$$\mathbf{f} = -f_0 \chi(t, \mathbf{x}) \mathbf{e}_y \ . \tag{8.37}$$

The upward migrating swarm injects downward momentum into the swarm-scale jet. As a first step we assume a spherical swarm shape, with an error-function-type transition zone at its edge, and fluctuations along the spherical coordinates θ and ϕ to mimic the spatial variability of a real swarm. Hence the swarm radius has the form

$$R_s(\theta, \phi, t) = \bar{R}_s \left(1 + \epsilon \cdot \sin\left[2\pi(\phi + \delta_1)\right] \cdot \sin\left[2\pi(\theta + \delta_2)\right]\right), \tag{8.38}$$

where δ_1 and δ_2 are random numbers between 0 and 1 selected at each time step, and the perturbation amplitude $\epsilon = 0.1$. The source function $\chi(t, \mathbf{x})$ is defined as

$$\chi(t, \mathbf{x}) = \frac{1}{2}\left(1 + erf\left(\frac{r(t, \mathbf{x}) - R_s(\theta, \phi, t)}{\delta_s}\right)\right) \ , \tag{8.39}$$

where $r(t, \mathbf{x})$ is the radial distance from the swarm center $\mathbf{X}_s = \mathbf{X}_0 + V_s t \mathbf{e}_y$, with $\mathbf{X}_0$ denoting the initial swarm location at $t = 0$. In order to quantify the strength f_0 of the source term, consider a spherical swarm of radius $\bar{R}_s$ that migrates upward with velocity V_s. We model this swarm as a self-propelled porous sphere subject to a dimensional drag force

$$F_D = C_D \rho_0 \phi_p V_s^2 \bar{R}_s^2 \ , \tag{8.40}$$

where C_D represents the drag coefficient. Consequently, we obtain

$$f_0 = C_D \phi_p \frac{V_s^2}{\bar{R}_s} \ . \tag{8.41}$$

We render the Navier-Stokes equation dimensionless with the prescribed swarm velocity

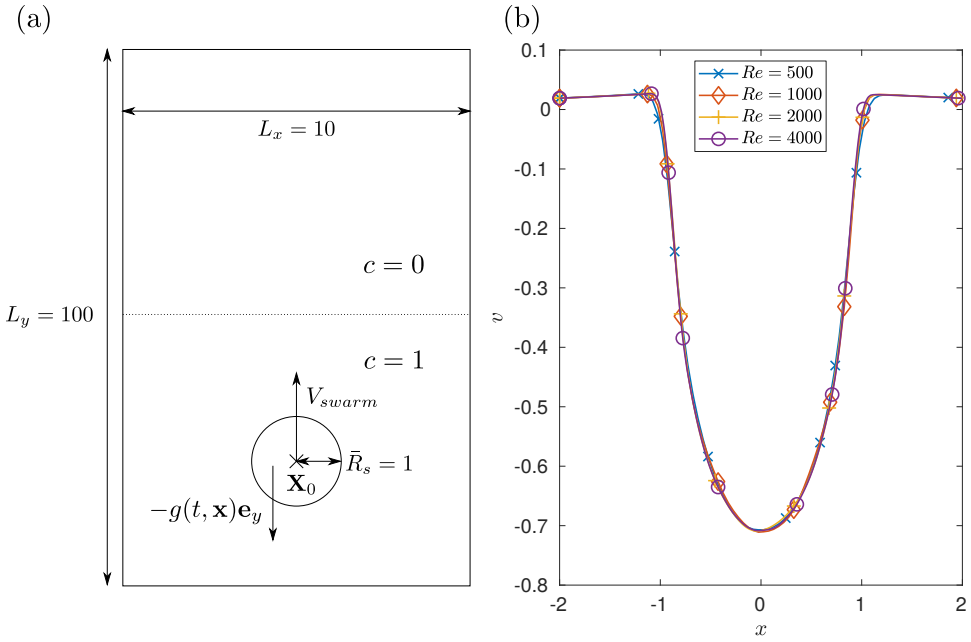

Figure 8.21: (a) Setup for swarm simulations. (b) Vertical velocity profile as a function of x on a slice in the z direction going through the center of the swarm and at $y = y_s - 2\bar{R}_s$ and $t = 50$.

V_s and the mean radius of the swarm $\bar{R}_s$, so that it takes the form

$$\frac{\partial \mathbf{u}}{\partial t} + (\mathbf{u}\cdot\nabla)\,\mathbf{u} = -\nabla p + \frac{1}{Re}\Delta\mathbf{u} - C_D\phi_p\chi(t,\mathbf{x})\mathbf{e}_y\ . \tag{8.42}$$

The swarm Reynolds number $Re = \frac{V_s\bar{R}_s}{\nu}$ is orders of magnitude larger than the Reynolds number of a single swimmer.

Based on the above approach, we conduct a series of simulations for increasingly large swarm Reynolds numbers. To this end, we employ a computational domain of size $L_x \times L_y \times L_z = 10 \times 100 \times 10$, with free-slip top and bottom walls and periodic boundaries in x and z. The swarm is initially placed at the center of the x, z-plane, and at $y = 40$. The passive concentration interface is located at mid-height $y = 50$, cf. figure 8.21a. Since we do not know the precise value of the effective drag coefficient C_D, we make an arbitrary choice $C_D\phi_p = 1$.

For the early time $t = 50$, when the jets are still stable, figure 8.21b displays representative velocity profiles through downward jets, recorded at a distance $2\bar{R}_s$ below the swarm center. Independent of the Reynolds number, the jets have peak velocities of $V_{jet} \approx 0.7V_s$, so that the jet Reynolds number $Re_{jet} = \frac{V_{jet}\bar{R}_s}{\nu} \approx 0.7Re$. Snapshots of the concentration field for various Reynolds numbers reflect the destabilization of the jet at time $t = 200$, along with the resulting mixing, cf. figure 8.22.

In contrast to the fully resolved squirmer simulations discussed earlier, mixing at the swarm scale results in a strongly asymmetric sorted concentration profile $c(y^*)$, which cannot be captured by a constant effective diffusivity, cf. figure 8.6. Following Houghton et al. [68], we thus introduce an effective diffusivity κ_{eff} that varies with y, and which can be obtained by solving the transport equation

$$\frac{\partial c}{\partial t} = \frac{\partial}{\partial y}\left(\kappa_{eff}(y)\frac{\partial c}{\partial y}\right) \tag{8.43}$$

to obtain the best fit with the computed profile $c(y^*)$. Towards this end we employ a fully implicit backward Euler time stepping scheme, in combination with second order central finite differences for the spatial discretization. The objective cost function $\mathcal{L}\left(\kappa_{eff}\right) = \sum_i (c^*(y_i) - c_{\kappa_{eff}}(y_i))^4$ is minimized using MATLAB's built-in nonlinear `fsolve` function. The choice of $\kappa_{eff}(y) = \kappa$ as the initial guess is critically important, since the effective diffusivity away from the pycnocline carries little meaning as the error-function-type solution flattens out. The above initial guess thus allows us to identify regions of strong mixing where the effective diffusivity is much larger than the molecular value.

Figure 8.6 indicates that $\kappa_{eff}(y^*)$ is largest in the lower section of the pycnocline. Figure 8.6 shows that the maximum ratio of effective to molecular diffusivity increases approximately linearly with the jet Reynolds number. For $Re_{jet} = 2,800$ this ratio

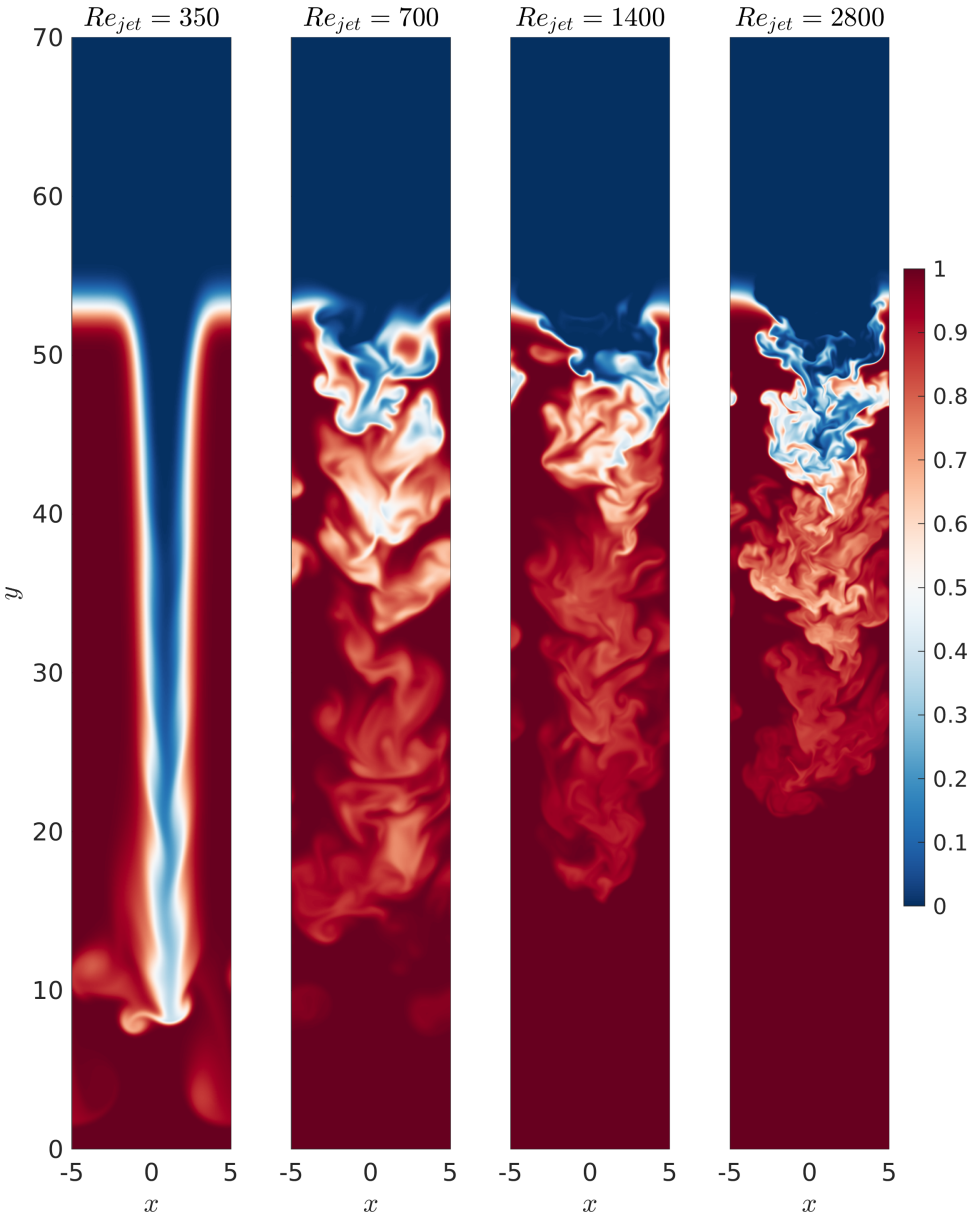

Figure 8.22: Snapshots of the concentration field at $t = 200$ for four jet Reynolds numbers in the x, y-plane centered in the z-direction.

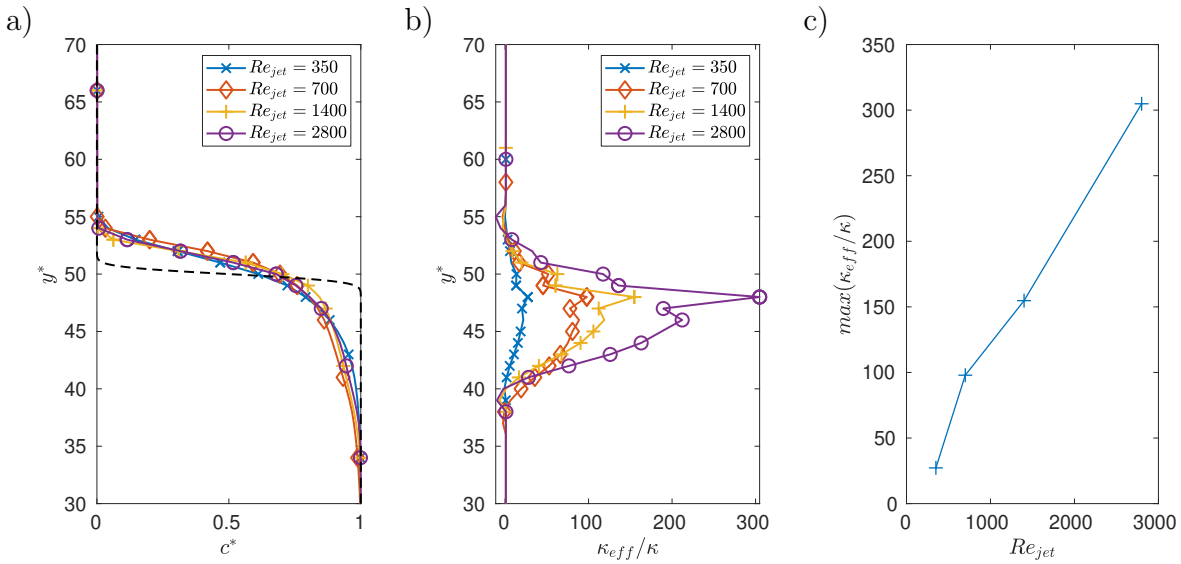

Figure 8.23: (a) Sorted concentration profiles at $t = 200$ for various jet Reynolds numbers. The dashed line corresponds to the initial concentration profile. (b) Ratio of effective to molecular diffusivity as a function of the sorted vertical height for different Reynolds and Peclet numbers ($Re = Pe$). (c) Maximum ratio of the effective to molecular diffusivity ratio as a function of the Reynolds number.

already reaches a value above 300. This is equivalent to a swarm Reynolds number of 4,000, which corresponds to a moderate size swarm of radius $40cm$ migrating at $1cm/s$. For reference, schools of Antarctic krill have been observed to range from as few as 150 individuals in a volume of $2{,}000cm^3$, up to swarms larger than $30m$ in horizontal extent [55].

As a key observation we note that even for a moderate size swarm, the effective diffusivity associated with the jet is much larger than that of the mixing processes at the swimmer scale, cf. figure 8.6. We hence expect larger swarms to generate most of their mixing through the swarm-scale coherent jet that they form, rather than through the small-scale processes within the swarm. The amount of mixing generated by the swarm is thus mainly controlled by its size, and by the velocity of the coherent jet which itself was shown to depend on the volume fraction of swimmers. We thus postulate that models for diapycnal mixing induced by swarms of swimmers have to account for the

swarm size as well as the associated jet velocity.

8.7 Conclusion

We have explored the collective vertical migration of a swarm of inertial swimmers through a stably stratified density interface. Towards this end, we conducted closely coordinated laboratory experiments and computational simulations that provide fundamental insight into the associated transport and mixing processes, both at the swimmer and at the swarm scale.

The laboratory experiments exploit the phototactic response of *Artemia salina*, by employing light sources in order to trigger controlled swarm migrations. The computational approach successfully duplicates this key experimental feature, by adapting the inertial squirmer model in order to provide the hydrodynamically interacting individual swimmers with the ability to direct their motion towards a specified target. The computational parameters such as the swimmer- and swarm-scale Reynolds numbers, the Richardson number, as well as the number of swimmers and the animal number density in the swarm closely match the experimental values. In the direct Navier-Stokes simulations the individual swimmers are represented by means of an Immersed Boundary Method approach, while the evolution of a scalar concentration field is tracked via the Volume of Fluid concept.

Both the experiments and the simulations demonstrate intense mixing at the scale of the individual swimmers, due to the fluid motion that these induce. The hydrodynamic interaction of the individual swimmers furthermore produces a spatially coherent source of thrust that leads to the formation of a swarm-scale jet in the direction opposite to the migration. Numerically calculated jet velocities closely match experimental measurements for equivalent animal number densities. The jet velocity is seen to increase

monotonically with the animal number density, although at a sublinear rate. For steadily moving dilute swarms, the jet velocity is well predicted by a simple analytical model that assumes spatially uniform jet and swimmer velocities.

The migrating swarm causes strong irreversible mixing that can be quantified via the effective diffusivity concept. The experiments demonstrate that locally this effective diffusivity can be up to three orders of magnitude larger than the molecular value. This observation is consistent with the numerical simulation results, although these employ a larger molecular diffusivity, so that the ratio of effective to molecular diffusivity is smaller. We find that the effective diffusivity increases linearly with the volume fraction of the swimmers, or equivalently with the animal number density.

Even though a steadily moving, neutrally buoyant swimmer does not impart any net momentum on the fluid, we find that its action leads to preferential scalar transport in the swimming direction. By analyzing the resulting skewness of the scalar concentration field, we find that this preferential scalar transport strongly depends on the specific squirmer mode of the individual swimmer. Comparisons between experimental and computational observations suggest that *A. Salina* behaves more like a pusher than a puller.

As a final step, we propose a continuum model for the generation of a large-scale jet by a swarm, based on an idealization of the swarm as a self-propelled porous sphere. This model reproduces the large ratios of effective to molecular diffusivity observed in the experiments, and it suggests that large swarms generate most of their mixing through the coherent jet that they form at the scale of the swarm, rather than by processes at the swimmer-scale.

Acknowledgements

EM gratefully acknowledges the support and hospitality he received as Shimizu Visiting Professor at Stanford University. Funding for this research was provided under NSF

grants CBET-1510615 to EM, and CBET-1510607 to JOD. Computational resources for this work used the Extreme Science and Engineering Discovery Environment (XSEDE), supported by the National Science Foundation, USA, Grant No. TG-CTS150053.

Chapter 9

Conclusions

9.1 Summary of findings

Fundamental processes in stratified fluid flows, driven by density differences due to one or more fluid properties or by the presence of active or passive particles, were investigated. Emphasis was placed on exploring relevant parametric spaces in order to derive scaling laws, predictive models, or approximations that describe said processes, and can help future research or be applied directly in the relevant fields. Here, we provide a summary of the main findings, and refer to the conclusions of the individual chapters for more details.

Part II discusses two configurations of lock-release gravity currents moving down a slope into a stratified medium. In chapter 4, the ambient fluid is linearly stratified and the lock fluid is dense due to small, dense particles. Upon release, the dense fluid flows down the slope into the stratified ambient and its density decreases as the suspended particles settle and ambient fluid is entrained at the head of the current. The current additionally encounters regions of increasing ambient fluid density, thus leading to a point

of intrusion, corresponding to the location from the free surface where the density of the current head matches that of the ambient fluid at the head of the current. After quantifying the dynamics of the flow and intrusion for a range of stratification intensities and settling velocities, we propose novel models for predicting the depth at which the current is expected to intrude and show good agreement with the numerical results and with experimental results of the parent study of Snow and Sutherland [142]. Furthermore, intrusion depth prediction in strongly stratified ambient fluids is shown to be highly sensitive to the choice of entrainment coefficient in existing scaling laws. Finally, an energy budget analysis emphasizes the role of settling in changing the dynamics of intrusion, from a secondary process to entrainment at low settling speeds, to a first order effect at higher settling rates. This work was published in Ouillon et al. [114].

In chapter 5, the ambient fluid is stratified in two layers separated by a sharp interface, and the density differences in the ambient and in the lock fluid are cause by differences in dissolved salt concentration. In order to replicate the experiments of Hogg et al. [62], the two-layer interface of the ambient fluid is partially raised, such that an internal wave forms upon release and propagates towards the slope. The process by which the internal wave can remove the head of the gravity current as they interact at the slope was identified by Hogg et al. [62] and is reproduced numerically. A parametric study on the effect of wave Froude number reveals that there exist a Froude number beyond which this process can occur, and that it leads to marked phenomenological changes in the behavior of the current. While for small waves, the current recovers its natural behavior in the absence of a wave, large waves lead to a rapid increase in irreversible mixing, energy budget, and distribution of mixed and entrained fluid post-interaction. Such behavior is only observed when the density ratio of the lower ambient to the initial lock fluid density is smaller than, but close to unity, suggesting that such processes are likely to occur in natural environments where strongly layered stratification is present. This work was

published in Ouillon et al. [113].

Part III discusses two studies that investigate double-diffusive processes in multi-phase flows. Chapter 6 presents numerical simulations of a simplified model of the Dead Sea during summer months, in which the water column consists of a stable two-layer stratification. The top layer, or epilimnion, is warm and salty, while the hypolimnion is colder and less salty, resulting in a hydrostatically stable density profile. The initial profile is everywhere at salt saturation. Salt precipitation is accounted for numerically by enforcing the saturation condition in a two-dimensional Navier-Stokes solver. The numerical simulations show that in the Dead Sea in the summer, the double-diffusive fingering instability is active at the metalimnion, and the downward propagating fingers are oversaturated to salt (or halite). This results in the formation of salt crystals, which a represented numerically by a particulate concentration field undergoing settling at a constant Stokes settling velocity. We explore the effect of the settling of the newly formed crystals in the downward fingers and find that it does not affect the long term fluxes of salt compared to classical double-diffusive fingering. The simulations demonstrate that double-diffusive fingering is sufficient to explain the flux of salt from the epilimnion to the hypolimnion, resulting in undersaturated conditions in the former and supersaturated conditions in the latter. This work is of particular importance for understanding salt layer formation in the historical record, and is the basis for a joint research project with Dr. Nadav Lensky and his team at the Geological Survey of Israel. This work was published in Ouillon et al. [112].

Chapter 7 investigates the formation of large-scale instabilities from a state of fingering convection in high-Prandtl sedimentary double-diffusive systems. The generalized mean-field theory introduced in Traxler et al. [156] is extended to sedimentary system. We consider a high-Prandtl system representative of a particle-laden flow in which salinity

plays the role of the fast, stabilizing diffuser, and particles play the role of the slow, destabilizing diffuser. In the absence of settling, the flow is found to be stable to collective modes identified by [147], but susceptible to the γ-instability [122]. DNS of this system results in the formation of layers, a strong indication that the γ-instability is sufficient to obtain layering despite the absence of the oscillatory collective instability. At high Prandtl numbers, the mean-field theory is also found to suppress most basic modes, fingering or settling-driven, predicted by linear stability of the non-averaged equations. In the presence of settling, a region of instability predicted by the mean-field theory that is not suppressed by the averaging of the equations appears and admits increasing growth rates with settling velocity. For sufficiently large values of the settling velocity, this unstable region differs from that predicted by the basic stability analysis of the small-scale modes, both in growth rate and oscillatory frequency. Whether this unstable region is an artifact of mean-field theory or a new, settling-driven collective instability will require further analysis.

In part IV, chapter 8, we investigate the migration of swarms of small inertial swimmers and its effect on mixing, both at the scale of individual swimmers and at the scale of the swarm through a momentum source model. The swimmers are represented by rigid spheres and we employ the squirmer model [91, 16] to allow the sphere to self-propel. The simulation parameters are based on joint experimental work [68, 66]. Mixing within the swarm is found to be enhanced by the presence of swimmers and increases with volume fraction. The swarm generates a jet-like coherent vertical velocity in the opposite direction to the moving swarm. The jet velocity obtained numerically agrees well with the experimental results in the whole range of tested animal number densities and the jet velocity is shown to agree well with a simple model based on momentum conservation in the limit of small animal number densities. At larger animal number densities, the jet

velocity is found to increase sub-linearly with animal number density, due to non-linear interactions between the wakes of the swimmers. Modeling the swarm as a momentum source and mapping the strength of the forcing to yield the desired jet velocity for a given animal number density, we can show that mixing induced by the interaction between the jet and the ambient fluid is much stronger than mixing induced within the swarm by individual swimmers. This result motivates further research into quantifying the impact of diurnal migration of large swarm of moderate Reynolds number animals, from the perspective of the swarm and not just of the within-swarm dynamics.

Appendix A

Supporting information to Chapter 6

A.1 Equation of state

We present the solubility and equation of state of brine saturated to halite salt (NaCl).

A.1.1 Equation of state for undersaturated brine

The equation of state (EoS) for undersaturated brine of the Dead Sea [2, 45] is given as:

$$\rho(T,S) = \rho_0 + \alpha(T - T_0) + \beta(S - S_0), \tag{A.1}$$

where ρ is the density of the brine (kg/m^3), T is the temperature ($^\circ C$), S is the salinity (kg/kg), $\alpha = -0.45 kg/m^3/^\circ C$ is the thermal expansion coefficient [45], $\beta = 0.936 \cdot 10^3 kg/m^3$ is the dissolved salts expansion coefficient, and the reference values are $\rho_0 = 1.2350 \cdot 10^3 kg/m^3$, $T_0 = 20^\circ C$ and $S_0 = 0.277$ [2].
The salinity, S, is defined as the mass of dissolved salts (M_s) per mass of brine (M_t) which is the the sum of mass of water (solvent) M_w and M_s:

$$S = \frac{M_s}{M_t} = \frac{M_s}{M_w + M_s}. \tag{A.2}$$

From the measuring perspective, direct determination of salinity is not accurate enough to follow depth and seasonal variations in salinity in the Dead Sea (recent salinity determination is 0.280, for a density of $1.2424 \cdot 10^3 kg/m^3$ at $25^\circ C$ [49]; this salinity value is in accordance with equation A.1, within the analytical error of S). Instead, quasi-salinity is measured as very high accuracy density measurements are readily available [2, 44, 138, 139]. Quasi-salinity is the density anomaly of brine from $1000 kg/m^3$, at a given temperature.

A.1.2 Solubility

The solubility of salt in water, $Se(T)$, is a function of temperature and it is approximated by a linear relation

$$Se(T) - Se_1 = \sigma(T - T_1), \tag{A.3}$$

where Se_1, T_1 are constants and σ is the temperature induced solubility change $\sigma = \frac{dSe}{dT}$. In the case of the Dead Sea brines, and for small temperature variations around the reference temperature, we can assume that $\sigma = 0.25 \cdot 10^{-3} K^{-1}$ [151]. The salinity value 0.280 at $25^\circ C$ is slightly below solubility of salt in water. Saturation is achieved by cooling down to $T = 24^\circ C$, therefore we use $Se_1 = 0.280$ and $T_1 = 24^\circ C$.

A.1.3 Equation of state for crystal bearing brine

More generally, for a brine-crystal mixture with mass of crystals M_c, the total salinity S_{tot} is defined as

$$S_{tot} = \frac{M_s + M_c}{M_w + M_s + M_c}. \tag{A.4}$$

We assume that in the crystal-brine mixture the saturated brine is at thermodynamic equilibrium. Any salinity increase and/or temperature decrease leads to crystallization, while the residual brine itself remains at saturation. The equation of state for a brine with total salinity larger than saturation ($S_{tot} > Se$) is developed here, where M_c is accounted for. We use two additional quantities, i.e the salinity of the brine S as defined in equation A.2 and the crystal concentration C given by the mass ratio:

$$C = \frac{M_c}{M_w + M_s + M_c}. \tag{A.5}$$

It should be noted that

$$S + C = S_{tot} + S \cdot C \approx S_{tot}. \tag{A.6}$$

The approximation is made given that for typical values of S and C, their product can be neglected, i.e. $S_{tot} \gg S \cdot C$. The density is defined as the total mass divided by the total volume:

$$\rho(T, S_{tot}) = \frac{M_t}{V_t} = \frac{M_w + M_s + M_c}{V_b + V_c} = \frac{M_w + M_s + M_c}{V_b + \frac{M_c}{\rho_s}}, \tag{A.7}$$

where ρ_s is the density of salt crystals, V_b and V_c the brine and crystal volumes respectively, and $V_t = V_b + V_c$ the total volume. With equations A.4 and A.7, we calculate the partial derivatives

$$\frac{\partial S_{tot}}{\partial M_c} = \frac{M_w + M_s + M_c - (M_s + M_c)}{(M_w + M_s + M_c)^2} = \frac{1 - S_{tot}}{M_t} \tag{A.8}$$

$$\frac{\partial \rho}{\partial M_c} = \frac{1}{V_b + \frac{M_c}{\rho_s}} - \frac{M_b + M_c}{(V_b + \frac{M_c}{\rho_s})^2 \rho_s} = \frac{1}{V_t}\left(1 - \frac{\rho}{\rho_s}\right) \tag{A.9}$$

Combining equations A.8 and A.9, we obtain the differential equation

$$\frac{\partial \rho}{\partial S_{tot}} = \frac{M_t\left(1 - \frac{\rho}{\rho_s}\right)}{V_t\,(1 - S_{tot})} = \frac{\rho\left(1 - \frac{\rho}{\rho_s}\right)}{1 - S_{tot}}. \tag{A.10}$$

Integration by separation of variables yields

$$\int \frac{d\rho}{\rho\left(1 - \frac{\rho}{\rho_s}\right)} = \int \frac{dS_{tot}}{1 - S_{tot}}, \tag{A.11}$$

such that

$$\rho(T, S_{tot}) = \rho_s \left[1 + \left(\frac{\rho_s}{\rho_0 + \alpha(T - T_0) + \beta(Se(T) - S_0)} - 1\right)\left(\frac{1 - S_{tot}}{1 - Se(T)}\right)\right]^{-1}. \quad \text{(A.12)}$$

Using equation A.4 and notation $\rho_b(T) = \rho_0 + \alpha(T - T_0) + \beta(Se(T) - S_0)$ for the density of the saturated brine , equation A.12 is rewritten in the form:

$$\rho(T, S_{tot}) = \frac{\rho_b(T)}{1 - \frac{\rho_s - \rho_b(T)}{\rho_s(1 - Se(T))}C}. \quad \text{(A.13)}$$

Assuming small crystal concentration ($C \ll 1$) and keeping the first term of the Taylor series expansion , we obtain

$$\rho(T, S_{tot}) = \rho_b(T) + \rho_b(T)\frac{\rho_s - \rho_b(T)}{\rho_s(1 - Se(T))}C. \quad \text{(A.14)}$$

Thus, the linearized form of the EoS is given by

$$\rho(T, S_{tot}) = \rho_0 + \alpha(T - T_0) + \beta(Se(T) - S_0) + \zeta C, \quad \text{(A.15)}$$

with ζ defined as

$$\zeta = \rho_b(T)\frac{\rho_s - \rho_b(T)}{\rho_s(1 - Se(T))} \quad \text{(A.16)}$$

Strictly speaking the ζvalue depends on the temperature, but for the Dead Sea conditions these variations are small. For practical use we adopt a constant value

$$\zeta \approx 0.71 kg/m^3. \quad \text{(A.17)}$$

which corresponds to $\rho_s = 2.1 \cdot 10^3 kg/m^3$, $\rho_b = 1.24 \cdot 10^3 kg/m^3$, and $Se = 0.28$. Under the specified Dead Sea conditions we thus have $\zeta < \beta$. In this study we explore the impact of different ζvalues on the dynamics of salt fingers.

A.2 Linear stability analysis

We present the results of a linear stability analysis of the base profiles to small perturbations. The equations are linearized around the base state. In the absence of crystals from the base state, we consider the non-dimensional equations but omit the equation

for the transport of crystals, such that the system to be linearized is

$$\nabla \cdot \mathbf{u} = 0, \tag{A.18}$$

$$\frac{1}{Pr}\left(\frac{\partial \mathbf{u}}{\partial t} + (\mathbf{u}\cdot\nabla)\,\mathbf{u}\right) = -\nabla p' + \Delta \mathbf{u} + Ra^{1/4}\left(T + \frac{1}{R_0}S\right)\mathbf{e_g}, \tag{A.19}$$

$$\frac{\partial T}{\partial t} + \mathbf{u}\cdot\nabla T = \nabla^2 T, \tag{A.20}$$

$$\frac{\partial S}{\partial t} + \mathbf{u}\cdot\nabla S = \tau_S \nabla^2 S. \tag{A.21}$$

Taking the curl of the momentum equations yields the vorticity formulation and drops the explicit dependence on pressure such that the equations become

$$\nabla \cdot \mathbf{u} = 0, \tag{A.22}$$

$$\frac{1}{Pr}\left(\frac{\partial \omega}{\partial t} + (\mathbf{u}\cdot\nabla)\,\omega\right) = \Delta \omega + Ra^{1/4}\left(\frac{\partial T}{\partial x} + \frac{1}{R_0}\frac{\partial S}{\partial x}\right)\mathbf{e_g}, \tag{A.23}$$

$$\frac{\partial T}{\partial t} + \mathbf{u}\cdot\nabla T = \nabla^2 T, \tag{A.24}$$

$$\frac{\partial S}{\partial t} + \mathbf{u}\cdot\nabla S = \tau_S \nabla^2 S. \tag{A.25}$$

The linearization takes the form

$$\begin{aligned} \omega &= 0 + \omega' \\ u &= 0 + u' \\ w &= 0 + w' \\ T &= \bar{T} + T' \\ S &= \bar{S} + S' \end{aligned}$$

where $\bar{T} = \bar{S} = \frac{1}{2}\left(1 + erf\left(\frac{z-H/2}{h_T}\right)\right)$. Assuming a solution of the form $Q = \hat{Q}(z)e^{ilx+\sigma t}$ for all the variables and neglecting the diffusion of the base state (quasi-steady assumption), we obtain by linearizing the equations the generalized eigenvalue problem

$$\sigma \mathbf{A}\mathbf{x} = \mathbf{B}\mathbf{x}, \tag{A.26}$$

where $\mathbf{A}$ and $\mathbf{B}$ are such that

$$A = \begin{bmatrix} \frac{1}{Pr}D_2 & 0 & 0 \\ 0 & 1 & 0 \\ 0 & 0 & 1 \end{bmatrix} \quad \text{and} \quad B = \begin{bmatrix} D_2^2 & Ra^{1/4}l^2 & \frac{Ra^{1/4}}{R_0}l^2 \\ -\partial_z \bar{T} & D_2 & 0 \\ -\partial_z \bar{S} & 0 & \tau D_2 \end{bmatrix},$$

in which D_2 is the Laplacian operator $D_2 = \partial_z^2 - l^2$. The problem is discretized in the vertical direction z using a finite difference method. We look for bounded solutions to equation A.26 where σ represents the growth rate associated to a certain horizontal and vertical mode, with a positive real part indicates an unstable solution. Difficulties arise when solving the eigenvalue problem with a finite domain in the vertical extent. The vertical extent needs to be sufficiently large for perturbations to decay, resulting in a narrow interfacial region that requires a high resolution. However, we are mainly interested in the fastest growing mode that correspond to the setup of the numerical simulations and we only require for the horizontal wavenumber l to be varied over its parameter space whilst looking for the most unstable mode. A second-order central finite difference scheme is employed and the resolution in the vertical direction is successively increased to guarantee convergence of the fastest growing mode. The fastest growing mode is obtained for $l_{max} \approx 0.711$, i.e. for a wavelength of $\lambda = 2\pi/k_{max} \approx 8.837$. Note that this wavelength corresponds to the width of the salt fingers that initially form in the system.

The main limitation of the continuous approach for the transport of crystallized salt is the difficulty in simulating realistic hydrodynamic crystal diffusivities. This hydrodynamic diffusivity depends on particle size, and is typically orders of magnitude smaller than the molecular diffusivity of salt ions. Crystal salt has no impact on the linear stability of the initial system, which is considered to be at saturation but devoid of any crystals. In addition, the potential energy that can be released through double diffusion in the system is initially entirely contained in the solute salt above the interface. Nonetheless, one might ask what the influence of the small fraction of crystallized salt on the system might be when using an artificially large diffusivity: in the numerical simulations the diffusivity is set to that of the diffusivity of solute salt to reduce computational cost. The physical argument for choosing such a value is that the double-diffusive dynamic is controlled primarily by the solute-salt/temperature interface and that the small mass of crystallized salt would have a negligible impact on the dynamic of the system. Indeed, the growth rate of the downward (upward) propagating fingers is controlled by the difference in outward (inward) flux of heat and inward (outward) flux of salt. When the diffusivity ratio of the slow to fast diffuser drops below a certain threshold, this growth rate is thus essentially a function of the fast diffuser, i.e. heat. This suggests that for such diffusivity ratios, further reducing the diffusivity of crystal salt to its true hydrodynamic value would have a negligible impact on the fingering regime.

This can be intuited by varying the diffusivity of the slow diffuser in the linear stability analysis. The growth rate and most unstable horizontal wavenumber are plotted in figure A.1 as a function of the diffusivity ratio. The red marker indicates the diffusivity ratio $\tau_S = \tau_C = 0.0114$ of solute salt diffusivity to thermal diffusivity used in the simulations. As expected, the results of the linear stability analysis converge asymptotically with decreasing values of τ. The value of σ obtained using the diffusivity ratio of the numerical simulations is only 3% smaller than the asymptote, and the horinzontal wavenumber of the most unstable mode differs by 1.6% from the asymptote. This shows that even if

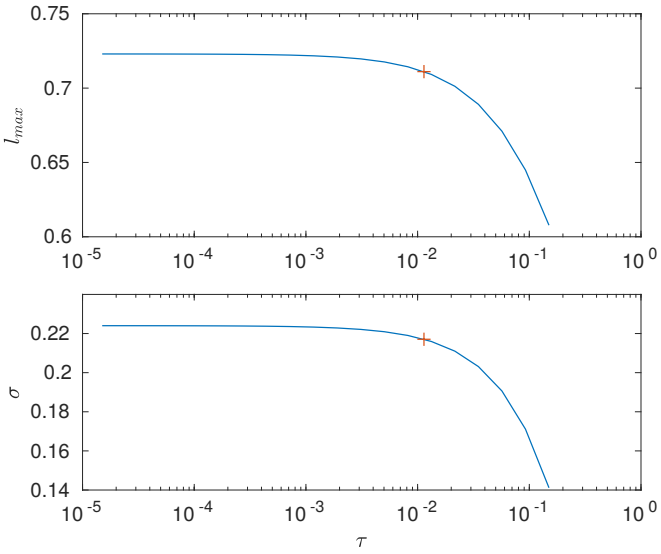

Figure A.1: Horizontal wavenumber of the fastest growing mode (top) and corresponding growth rate (bottom) as a function of the diffusivity ratio τ. The red marker '+' indicates the value of $\tau_S = \tau_C = 0.0114$ used in the numerical simulations.

most of the solute salt immediately crystallized, the growth rate and width of the fingers would remain almost the same as it would be with solute salt. We thus conclude that the assumption of $\tau_C = \tau_S$ does not influence the initial fingering regime.

Appendix B

Supporting information to Chapter 7

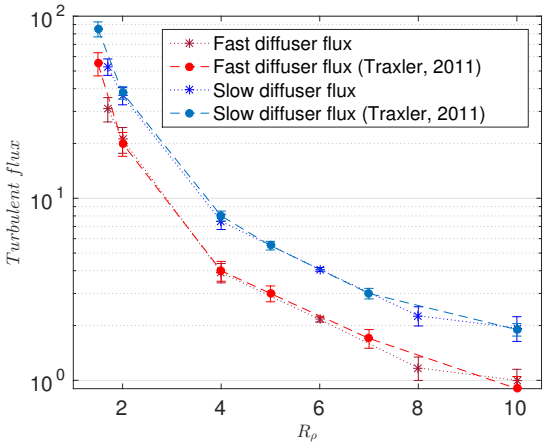

Figure B.1: Fluxes for various values of the density ratio R_ρ in the case $Pr = 7$, $\tau = 0.01$ from our simulations as compared to available data.

B.1 Protocol for computing mean-field parameters

B.1.1 Method for computing the fluxes

Boundary and initial conditions

The computational domain is periodic in x and y so as to avoid altering the dynamics near the boundaries. It has to be large enough to fit a few fingers so as to provide good estimates of the fluxes but at the same time it should not be too large lest secondary instabilities should appear. In the absence of settling, we ran our small-scale simulations in a domain of 5×10 *fgw*. In the presence of settling, we ran the small-scale simulations in 100×100 boxes. These choices, following Radko [122], Reali et al. [125], are purely empirical but seem to be a good compromise.

In order to perturb the system from the linearly stratified base state, we initiate all fields with low-amplitude white noise.

B.1.2 Validation

We run numerous small-scale simulations with $Pr = 7$ and $\tau = 0.01$ for different values of the density ratio. The output of each simulation is post-processed to obtain a value for the salt and particle flux, using the above protocol. The data is then compared to that obtained by Traxler (see [156]). Figure B.1 shows very good agreement between our 2D fluxes and that obtained by Traxler, thus validating our computational method.

B.2 Verification of mean-field hypotheses

B.2.1 Reynolds stress tensor

A key hypothesis that is made to derive mean-field theory is that the Reynold stress tensor

$$\boldsymbol{R} = \begin{pmatrix} \overline{u'^2} & \overline{u'v'} \\ \overline{v'u'} & \overline{v'^2} \end{pmatrix}$$

has a negligible divergence. We check that this is the case by computing the quantity

$$||\nabla \cdot \boldsymbol{R}||^2 = \left(2\overline{u'\frac{\partial u'}{\partial x}} + \overline{u'\frac{\partial v'}{\partial y}} + \overline{v'\frac{\partial u'}{\partial y}}\right)^2 + \left(2\overline{v'\frac{\partial v'}{\partial y}} + \overline{u'\frac{\partial v'}{\partial x}} + \overline{v'\frac{\partial u'}{\partial x}}\right)^2$$

where averaging is done in post-processing accordingly to the protocol presented in appendix A.1.. Analysis of our small-scale simulations reveals that the quantity $||\nabla \cdot \boldsymbol{R}||$ never exceeds 10^{-15}, hence verifying the validity of our hypothesis.

B.2.2 Vertical transport

The other key hypothesis is that the salt flux $\boldsymbol{F}_s = \overline{u'\Theta'}\boldsymbol{e}_x + \overline{v'\Theta'}\boldsymbol{e}_y$ is mainly vertical. One can re-write the salt flux as

$$\boldsymbol{F}_\theta = \overline{v'\Theta'}(\epsilon \boldsymbol{e}_x + \boldsymbol{e}_y)$$

where $\epsilon = \overline{u'\Theta'}/\overline{v'\Theta'}$. Computing the ϵ time series and time averaging it reveals that $\epsilon \ll 1$, thus the hypothesis is verified. This is true in non-sedimentary simulations, where $\epsilon = \mathcal{O}(10^{-4})$, as well as in presence of settling, where $\epsilon = \mathcal{O}(10^{-3})$.

B.3 Effect of diffusivity ratio on growth rate of most unstable fingering mode

The largest growth rate λ_{max} of the fingering instability and associated horizontal wavenumber l_{max} as functions of τ can be calculated by solving the cubic equation for the small-scale instabilities (eq. 7.30), for the values of Pr and R_0 corresponding to the experiments (figure B.2).

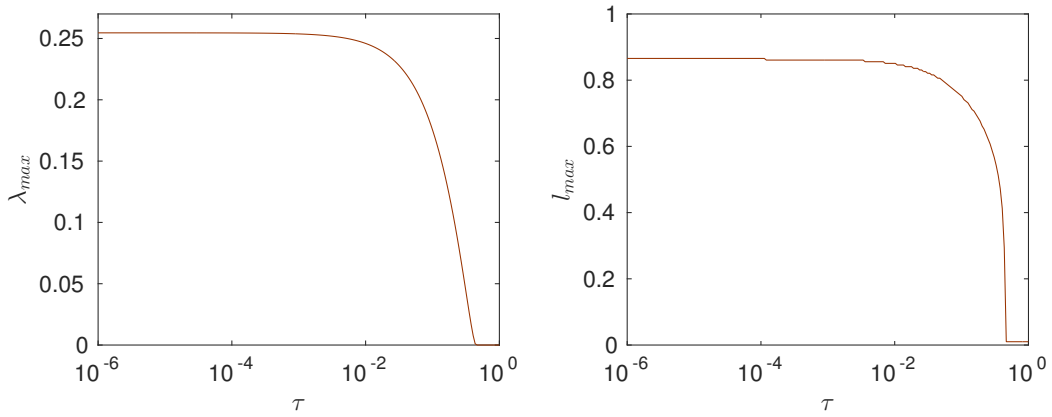

Figure B.2: Largest growth rate λ_{max} and associated horizontal wavenumber l_{max} as functions of τ for $Pr = 1000$ and $R_0 = 2.25$. Note that the growth rate and wavenumber are not defined beyond $\tau = 1/R_0$ because instability only arises for diffusivity ratios $\tau < 1/R_0$.

Bibliography

[1] Alsinan, A., E. Meiburg, and P. Garaud

2017. A settling-driven instability in two-component, stably stratified fluids. *J. Fluid Mech.*, 816:243–267.

[2] Anati, D. A.

1997. The hydrography of a hypersaline lake. In *Dead Sea lake its setting*, T. M. Niemi, Z. Ben-Avraham, and J. Gat, eds., chapter 8, Pp. 89–103. Oxford Univ. Press, Oxford.

[3] Anati, D. A. and M. Stiller

1991. The post- 1979 thermohaline structure of the Dead Sea and the role of double-diffusive mixing. *Limnol. Oceanogr.*, 36(2):342–353.

[4] Ardekani, A. M., A. Doostmohammadi, and N. Desai

2017. Transport of particles, drops, and small organisms in density stratified fluids. *Phys. Rev. Fluids*, 2(10):100503.

[5] Ardekani, M. N., L. A. Asmar, F. Picano, and L. Brandt

2018. Numerical study of heat transfer in laminar and turbulent pipe flow with finite-size spherical particles. *Int. J. Heat Fluid Flow*, 71:189–199.

[6] Arnon, A., J. S. Selker, and N. G. Lensky

2016. Thermohaline stratification and double diffusion diapycnal fluxes in the hypersaline Dead Sea. *Limnol. Oceanogr.*, 61(4):1214–1231.

[7] Baines, P. G.

2001. Mixing in flows down gentle slopes into stratified environments. *J. Fluid Mech.*, 443:237–270.

[8] Baines, P. G.

2008. Mixing in downslope flows in the ocean - plumes versus gravity currents. *atmosphere-ocean*, 46(4):405–419.

[9] Baines, P. G. and A. E. Gill

1969. On thermohaline convection with linear gradients. *J. Fluid Mech.*, 37(2):289–306.

[10] Beghin, P., E. J. Hopfinger, and R. E. Britter

1981. Gravitational convection from instantaneous sources on inclined boundaries. *J. Fluid Mech.*, 107(-1):407.

[11] Benjamin, T. B.

1968. Gravity currents and related phenomena. *J. Fluid Mech.*, 31(02):209.

[12] Bianchi, D., E. D. Galbraith, D. A. Carozza, K. A. S. Mislan, and C. A. Stock

2013. Intensification of open-ocean oxygen depletion by vertically migrating animals. *Nat. Geosci.*, 6(7):545–548.

[13] Biegert, E.

2018. *Eroding Uncertainty: Towards Understanding Flows Interacting with Mobile Sediment Beds Using Grain-Resolving Simulations*. PhD thesis, University of California, Santa Barbara.

[14] Biegert, E., B. Vowinckel, and E. Meiburg

2017a. A collision model for grain-resolving simulations of flows over dense, mobile, polydisperse granular sediment beds. *J. Comput. Phys.*, 340:105–127.

[15] Biegert, E., B. Vowinckel, R. Ouillon, and E. Meiburg

2017b. High-resolution simulations of turbidity currents. *Prog. Earth Planet. Sci.*, 4(1):33.

[16] Blake, J. R.

1971. A spherical envelope approach to ciliary propulsion. *J. Fluid Mech.*, 46(01):199.

[17] Blumm, J. and A. Lindemann

2003. Characterization of the thermophysical properties of molten plymers and liquids using the flash technique. *High Temp. Press.*, 35/36(6):627–632.

[18] Borden, Z. and E. Meiburg

2013. Circulation based models for Boussinesq gravity currents. *Phys. Fluids*, 25(10):101301.

[19] Britter, R. E. and P. F. Linden

1980. The motion of the front of a gravity current travelling down an incline. *J. Fluid Mech.*, 99(03):531.

[20] Burns, P.

2013. *Double-diffusive instabilities in sediment-laden systems.* PhD thesis, University of California, Santa Barbara.

[21] Burns, P. and E. Meiburg

2012. Sediment-laden fresh water above salt water: linear stability analysis. *J. Fluid Mech.*, 691:279–314.

[22] Burns, P. and E. Meiburg

2015. Sediment-laden fresh water above salt water: nonlinear simulations. *J. Fluid Mech.*, 762:156–195.

[23] Cantero, M. I., S. Balachandar, M. H. García, and D. Bock

2008. Turbulent structures in planar gravity currents and their influence on the flow dynamics. *J. Geophys. Res.*, 113(C8):C08018.

[24] Cantero, M. I., J. R. Lee, S. Balachandar, and M. H. Garci

2007. On the front velocity of gravity currents. *J. Fluid Mech.*, 586:1.

[25] Carazzo, G. and M. A. Jellinek

2012. A new view of the dynamics, stability and longevity of volcanic clouds. *Earth Planet. Sci. Lett.*, 325-326:39–51.

[26] Carazzo, G. and M. A. Jellinek

2013. Particle sedimentation and diffusive convection in volcanic ash-clouds. *J. Geophys. Res. Solid Earth*, 118(4):1420–1437.

[27] Catton, K. B., D. R. Webster, S. Kawaguchi, and J. Yen

2011. The hydrodynamic disturbances of two species of krill: implications for aggregation structure. *J. Exp. Biol.*, 214(11):1845–1856.

[28] Cenedese, C. and C. Adduce

2010. A new parameterization for entrainment in overflows. *J. Phys. Oceanogr.*, 40(8):1835–1850.

[29] Chisholm, N. G., D. Legendre, E. Lauga, and A. S. Khair

2016. A squirmer across Reynolds numbers. *J. Fluid Mech.*, 796(2016):233–256.

[30] Cortés, A., W. E. Fleenor, M. G. Wells, I. de Vicente, and F. J. Rueda

2014. Pathways of river water to the surface layers of stratified reservoirs. *Limnol. Oceanogr.*, 59(1):233–250.

[31] Dabiri, J. O.

2010a. Role of vertical migration in biogenic ocean mixing. *Geophys. Res. Lett.*, 37(11):1–5.

[32] Dabiri, J. O.

2010b. Role of vertical migration in biogenic ocean mixing. *Geophys. Res. Lett.*, 37(11).

[33] Davis, R. H.

1996. Hydrodynamic diffusion of suspended particles: a symposium. *J. Fluid Mech.*, 310:325.

[34] De Rooij, F. and S. B. Dalziel

2009. Time- and Space-Resolved Measurements of Deposition under Turbidity Currents. In *Part. Gravity Curr.*, number 200 I, Pp. 207–215. Oxford, UK: Blackwell Publishing Ltd.

[35] De Rooij, F., P. F. Linden, and S. B. Dalziel

1999. Saline and particle-driven interfacial intrusions. *J. Fluid Mech.*, 389:S0022112099005078.

[36] Dewar, W. K., R. J. Bingham, R. L. Iverson, D. P. Nowacek, L. C. St. Laurent, and P. H. Wiebe

2006. Does the marine biosphere mix the ocean? *J. Mar. Res.*, 64(4):541–561.

[37] Doostmohammadi, A., R. Stocker, and A. M. Ardekani

2012. Low-Reynolds-number swimming at pycnoclines. *Proc. Natl. Acad. Sci.*, 109(10):3856–3861.

[38] Ellison, T. H. and J. S. Turner

1959. Turbulent entrainment in stratified flows. *J. Fluid Mech.*, 6(03):423.

[39] Fadlun, E., R. Verzicco, P. Orlandi, and J. Mohd-Yusof

2000. Combined Immersed-Boundary Finite-Difference Methods for Three-Dimensional Complex Flow Simulations. *J. Comput. Phys.*, 161(1):35–60.

[40] Fernández-Torquemada, Y., J. M. Gónzalez-Correa, A. Loya, L. M. Ferrero, M. Díaz-Valdés, and J. L. Sánchez-Lizaso

2009. Dispersion of brine discharge from seawater reverse osmosis desalination plants. *Desalin. Water Treat.*, 5(1-3):137–145.

[41] Fischer, H. B. and R. D. Smith

1983. Observations of transport to surface waters from a plunging inflow to Lake Mead. *Limnol. Oceanogr.*, 28(2):258–272.

[42] Forel, F. A.

1885. Les ravins sous-lacustres des fleuves glaciaires. *C. R. Acad. Sci. Paris*, 101:725.

[43] Garcia-Castellanos, D. and A. Villaseñor

2011. Messinian salinity crisis regulated by competing tectonics and erosion at the Gibraltar arc. *Nature*, 480(7377):359–363.

[44] Gertman, I. and A. Hecht

2002. The Dead Sea hydrography from 1992 to 2000. *J. Mar. Syst.*, 35(3-4):169–181.

[45] Gertman, I., N. Kress, B. Katsenelson, and P. Zavialov

2010. Equations of state for the Dead Sea and Aral Sea : Searching for common approaches . *IOLR Rep. IOLR/12/2010*, (April).

[46] Gerz, T., U. Schumann, and S. E. Elghobashi

1989. Direct numerical simulation of stratified homogeneous turbulent shear flows. *J. Fluid Mech.*, 200:563–594.

[47] Gill, A. E.

2016. *Atmosphereocean dynamics*. Elsevier.

[48] Glowinski, R., T.-W. Pan, T. Hesla, and D. Joseph

1999. A distributed Lagrange multiplier/fictitious domain method for particulate flows. *Int. J. Multiph. Flow*, 25(5):755–794.

[49] Golan, R., I. Gavrieli, J. Ganor, and B. Lazar

2016. Controls on the pH of hyper-saline lakes A lesson from the Dead Sea. *Earth Planet. Sci. Lett.*, 434:289–297.

[50] Gouesbet, G. and A. Berlemont

1999. Eulerian and Lagrangian approaches for predicting the behaviour of discrete particles in turbulent flows. *Prog. Energy Combust. Sci.*, 25(2):133–159.

[51] Green, T.

1987. The importance of double diffusion to the settling of suspended material. *Sedimentology*, 34(2):319–331.

[52] Gualtieri, C., A. Angeloudis, F. Bombardelli, S. Jha, and T. Stoesser

2017. On the Values for the Turbulent Schmidt Number in Environmental Flows. *Fluids*, 2(2):17.

[53] Guermond, J.-L. and L. Quartapelle

2000. A Projection FEM for Variable Density Incompressible Flows. *J. Comput. Phys.*, 165(1):167–188.

[54] Hallworth, M. A., H. E. Huppert, J. C. Phillips, and R. S. J. Sparks

1996. Entrainment into two-dimensional and axisymmetric turbulent gravity currents. *J. Fluid Mech.*, 308:289.

[55] Hamner, W. M., P. P. Hamner, S. W. Strand, and R. W. Gilmer

1983. Behavior of Antarctic Krill, Euphausia superba: Chemoreception, Feeding, Schooling, and Molting. *Science (80-.).*, 220(4595):433–435.

[56] Härtel, C., F. Carlsson, and M. Thunblom

2000a. Analysis and direct numerical simulation of the flow at a gravity-current head. Part 2. The lobe-and-cleft instability. *J. Fluid Mech.*, 418(2000):S0022112000001270.

[57] Härtel, C., E. Meiburg, and F. Necker

2000b. Analysis and direct numerical simulation of the flow at a gravity-current head. Part 1. Flow topology and front speed for slip and no-slip boundaries. *J. Fluid Mech.*, 418.

[58] Hetsroni, G.

1989. Particles-turbulence interaction. *Int. J. Multiph. Flow*, 15(5):735–746.

[59] Hoare, R. A.

1966. Problems of Heat Transfer in Lake Vanda, a Density Stratified Antarctic Lake. *Nature*, 210(5038):787–789.

[60] Hodges, B. R., J. E. Furnans, and P. S. Kulis

2011. Thin-layer gravity current with implications for desalination brine disposal. *J. Hydraul. Eng.*, 137(3):356–371.

[61] Hogg, C. A. R.

2014. *The flow of rivers into lakes : experiments and models*. PhD thesis.

[62] Hogg, C. A. R., G. C. Egan, N. T. Ouellette, and J. R. Koseff

2018. Shoaling internal waves may reduce gravity current transport. *Environ. Fluid Mech.*, 18(2):383–394.

[63] Holt, S. E., J. R. Koseff, and J. H. Ferziger

1992. A numerical study of the evolution and structure of homogeneous stably stratified sheared turbulence. *J. Fluid Mech.*, 237(-1):499.

[64] Holyer, J. Y.

1981. On the collective instability of salt fingers. *J. Fluid Mech.*, 110:195–207.

[65] Hopfinger, E. J.

1987. Turbulence in stratified fluids: A review. *J. Geophys. Res.*, 92(C5):5287.

[66] Houghton, I. A. and J. O. Dabiri

2019. Alleviation of hypoxia by biologically generated mixing in a stratified water column. *Limnol. Oceanogr.*, P. lno.11176.

[67] Houghton, I. A., J. R. Koseff, S. G. Monismith, and J. O. Dabiri

2018a. Vertically migrating swimmers generate aggregation-scale eddies in a stratified column. *Nature*, 556(7702):497–500.

[68] Houghton, I. A., J. R. Koseff, S. G. Monismith, and J. O. Dabiri

2018b. Vertically migrating swimmers generate aggregation-scale eddies in a stratified column. *Nature*, 556(7702):497–500.

[69] Houk, D. and T. Green

1973. Descent rates of suspension fingers. *Deep Sea Res. Oceanogr. Abstr.*, 20(8):757–761.

[70] Huntley, M. and M. Zhou

2004. Influence of animals on turbulence in the sea. *Mar. Ecol. Prog. Ser.*, 273:65–79.

[71] Huppert, H. E.

1971. On the stability of a series of double-diffusive layers. *Deep Sea Res. Oceanogr. Abstr.*, 18(10):1005–1021.

[72] Huppert, H. E. and J. E. Simpson

1980. The slumping of gravity currents. *J. Fluid Mech.*, 99(4):785–799.

[73] Huppert, H. E. and J. S. Turner

1981. Double-diffusive convection. *J. Fluid Mech.*, 106(-1):299.

[74] Ishikawa, T., M. P. Simmonds, and T. J. Pedley

2006. Hydrodynamic interaction of two swimming model micro-organisms. *J. Fluid Mech.*, 568:119.

[75] Itsweire, E. C., K. N. Helland, and C. W. Van Atta

1986. The evolution of grid-generated turbulence in a stably stratified fluid. *J. Fluid Mech.*, 162(-1):299.

[76] Kang, S.

2008. *An improved immersed boundary method for computation of turbulent flows with heat transfer*. PhD thesis, Stanford University.

[77] Katija, K. and J. O. Dabiri

2009. A viscosity-enhanced mechanism for biogenic ocean mixing. *Nature*, 460(7255):624–626.

[78] Kempe, T. and J. Fröhlich

2012. An improved immersed boundary method with direct forcing for the simulation of particle laden flows. *J. Comput. Phys.*, 231(9):3663–3684.

[79] Khair, A. S. and N. G. Chisholm

2014. Expansions at small Reynolds numbers for the locomotion of a spherical squirmer. *Phys. Fluids*, 26(1):011902.

[80] Kim, J. and P. Moin

1985. Application of a fractional-step method to incompressible Navier-Stokes equations. *J. Comput. Phys.*, 59(2):308–323.

[81] Konopliv, N., L. Lesshafft, and E. Meiburg

2018. The influence of shear on double-diffusive and settling-driven instabilities. *J. Fluid Mech.*, 849:902–926.

[82] Konopliv, N. and E. Meiburg

2016. Double-diffusive lock-exchange gravity currents. *J. Fluid Mech.*, 797:729–764.

[83] Krishnamurti, R.

2003. Double-diffusive transport in laboratory thermohaline staircases. *J. Fluid Mech.*, 483:287–314.

[84] Kunze, E.

2003. A review of oceanic salt-fingering theory. *Prog. Oceanogr.*, 56(3-4):399–417.

[85] Lauga, E. and T. R. Powers

2009. The hydrodynamics of swimming microorganisms. *Reports Prog. Phys.*, 72(9):096601.

[86] Lele, S. K.

1992. Compact finite difference schemes with spectral-like resolution. *J. Comput. Phys.*, 103(1):16–42.

[87] Lensky, N. G., Y. Dvorkin, V. Lyakhovsky, I. Gertman, and I. Gavrieli

2005. Water, salt, and energy balances of the Dead Sea. *Water Resour. Res.*, 41(12).

[88] Lensky, N. G., I. M. Lensky, A. Peretz, I. Gertman, J. Tanny, and S. Assouline

2018. Diurnal Course of Evaporation From the Dead Sea in Summer: A Distinct Double Peak Induced by Solar Radiation and Night Sea Breeze. *Water Resour. Res.*, 54(1):150–160.

[89] Li, G., A. Ostace, and A. M. Ardekani

2016. Hydrodynamic interaction of swimming organisms in an inertial regime. *Phys. Rev. E*, 94(5):053104.

[90] Li, G.-J. and A. M. Ardekani

2014. Hydrodynamic interaction of microswimmers near a wall. *Phys. Rev. E*, 90(1):013010.

[91] Lighthill, M. J.

1952. On the squirming motion of nearly spherical deformable bodies through liquids at very small reynolds numbers. *Commun. Pure Appl. Math.*, 5(2):109–118.

[92] Linden, P.

1971. Salt fingers in the presence of grid-generated turbulence. *J. Fluid Mech.*, 49(03):611.

[93] Linden, P.

1973. On the structure of salt fingers. *Deep Sea Res. Oceanogr. Abstr.*, 20(4):325–340.

[94] Lions, P.

1996. *Mathematical Topics in Fluid Mechanics. Volume 1: Incompressible Models.* Oxford University Press.

[95] MacIntyre, S., K. M. Flynn, R. Jellison, and J. Romero

1999. Boundary mixing and nutrient fluxes in Mono Lake, California. *Limnol. Ocean.*, 44(3):512–529.

[96] MAGAR, V. and T. J. PEDLEY

2005. Average nutrient uptake by a self-propelled unsteady squirmer. *J. Fluid Mech.*, 539(-1):93.

[97] Marques, G. M., M. G. Wells, L. Padman, and T. M. Özgökmen

2017. Flow splitting in numerical simulations of oceanic dense-water outflows. 113:66–84.

[98] Maxworthy, T., J. Leilich, J. E. Simpson, and E. H. Meiburg

2002. The propagation of a gravity current into a linearly stratified fluid. *J. Fluid Mech.*, 453:371–394.

[99] Meiburg, E. and B. Kneller

2010. Turbidity currents and their deposits. *Annu. Rev. Fluid Mech.*, 42(1):135–156.

[100] Merryfield, W. J.

2000. Origin of Thermohaline Staircases. *J. Phys. Oceanogr.*, 30(5):1046–1068.

[101] Mittal, R. and G. Iaccarino

2005. Immersed boundary methods. *Annu. Rev. Fluid Mech.*, 37(1):239–261.

[102] Mohan Rai, M. and P. Moin

1991. Direct simulations of turbulent flow using finite-difference schemes. *J. Comput. Phys.*, 96(1):15–53.

[103] Monaghan, J. J.

2007. Gravity current interaction with interfaces. *Annu. Rev. Fluid Mech.*, 39(1):245–261.

[104] Mor, Z., S. Assouline, J. Tanny, I. M. Lensky, and N. G. Lensky

2018. Effect of Water Surface Salinity on Evaporation: The Case of a Diluted Buoyant Plume Over the Dead Sea. *Water Resour. Res.*, 54(3):1460–1475.

[105] Mortimer, C. H.

1952. Water movements in lakes during summer stratification; evidence from the distribution of temperature in Windermere. *Philos. Trans. R. Soc. B Biol. Sci.*, 236(635):355–398.

[106] Nasr-Azadani, M. and E. Meiburg

2011. TURBINS: An immersed boundary, NavierStokes code for the simulation of gravity and turbidity currents interacting with complex topographies. *Comput. Fluids*, 45(1):14–28.

[107] Nasr-Azadani, M. M., E. Meiburg, and B. Kneller

2018. Mixing dynamics of turbidity currents interacting with complex seafloor topography. *Environ. Fluid Mech.*, 18(1):201–223.

[108] Necker, F., C. Härtel, L. Kleiser, and E. Meiburg

2002. High-resolution simulations of particle-driven gravity currents. *Int. J. Multiph. Flow*, 28(2):279–300.

[109] Necker, F., C. Härtel, L. Kleiser, and E. Meiburg

2005. Mixing and dissipation in particle-driven gravity currents. *J. Fluid Mech.*, 545:339–372.

[110] Newman, F. C.

1976. Temperature Steps in Lake Kivu: A Bottom Heated Saline Lake. *J. Phys. Oceanogr.*, 6(2):157–163.

[111] O'Brien, D.

1988. Surface schooling behaviour of the coastal krill Nyctiphanes australis (Crustacea: Euphausiacea) off Tasmania, Australia . *Mar. Ecol. Prog. Ser.*, 42:219–233.

[112] Ouillon, R., N. G. Lensky, V. Lyakhovsky, A. Arnon, and E. Meiburg

2019a. Halite precipitation from double-diffusive salt fingers in the Dead Sea: Numerical simulations. *Water Resour. Res.*

[113] Ouillon, R., E. Meiburg, N. T. Ouellette, and J. R. Koseff

2019b. Interaction of a downslope gravity current with an internal wave. *J. Fluid Mech.*, 873:889–913.

[114] Ouillon, R., E. Meiburg, and B. R. Sutherland

2019c. Turbidity currents propagating down a slope into a stratified saline ambient fluid. *Environ. Fluid Mech.*

[115] Pak, O. S. and E. Lauga

2014. CHAPTER 4. Theoretical Models of Low-Reynolds-Number Locomotion. In *Fluid-Structure Interact. Low-Reynolds-Number Flows*, Pp. 100–167. Cambridge: Royal Society of Chemistry.

[116] Parsons, J. D., J. W. M. Bush, and J. P. M. Syvitski

2001. Hyperpycnal plume formation from riverine outflows with small sediment concentrations. *Sedimentology*, 48(2):465–478.

[117] Parsons, J. D., C. T. Friedrichs, P. A. Traykovski, D. Mohrig, J. Imran, J. P. M. Syvitski, G. Parker, P. Puig, J. L. Buttles, and M. H. Garca

2007. The Mechanics of Marine Sediment Gravity Flows. In *Cont. Margin Sediment.*, Pp. 275–337. Oxford, UK: Blackwell Publishing Ltd.

[118] Poisson, A. and A. Papaud

1983. Diffusion coefficients of major ions in seawater. *Mar. Chem.*, 13(4):265–280.

[119] Pond, D. W.

2012. The physical properties of lipids and their role in controlling the distribution of zooplankton in the oceans. *J. Plankton Res.*, 34(6):443–453.

[120] Pond, S. and G. L. Pickard

2013. *Introductory Dynamical Oceanography*, 2nd edition. Elsevier.

[121] Pyo, J.-H. and J. Shen

2007. GaugeUzawa methods for incompressible flows with variable density. *J. Comput. Phys.*, 221(1):181–197.

[122] Radko, T.

2003. A mechanism for layer formation in a double-diffusive fluid. *J. Fluid Mech.*, 497:S0022112003006785.

[123] Radko, T.

2013. *Double-Diffusive Convection*. Cambridge: Cambridge University Press.

[124] Radko, T. and D. P. Smith

2012. Equilibrium transport in double-diffusive convection. *J. Fluid Mech.*, 692:5–27.

[125] Reali, J. F., P. Garaud, A. Alsinan, and E. Meiburg

2017. Layer formation in sedimentary fingering convection. *J. Fluid Mech.*, 816:268–305.

[126] Rimoldi, B., J. Alexander, and S. Morris

1996. Experimental turbidity currents entering density-stratified water: analogues for turbidites in Mediterranean hypersaline basins. *Sedimentology*, 43(3):527–540.

[127] Rooij, F. D.

1999. Sedimenting particle-laden flows in confined geometries. (September).

[128] Roveri, M., R. Flecker, W. Krijgsman, J. Lofi, S. Lugli, V. Manzi, F. J. Sierro, A. Bertini, A. Camerlenghi, G. De Lange, R. Govers, F. J. Hilgen, C. Hübscher, P. T. Meijer, and M. Stoica

2014. The Messinian Salinity Crisis: Past and future of a great challenge for marine sciences. *Mar. Geol.*, 352:25–58.

[129] Samothrakis, P. and A. J. Cotel

2006. Propagation of a gravity current in a two-layer stratified environment. *J. Geophys. Res.*, 111(C1):C01012.

[130] Sánchez, X. and E. Roget

2007. Microstructure measurements and heat flux calculations of a triple-diffusive process in a lake within the diffusive layer convection regime. *J. Geophys. Res.*, 112(C2):C02012.

[131] Schmitt, R., H. Perkins, J. Boyd, and M. Stalcup

1987. C-SALT: An investigation of the thermohaline staircase in the western tropical North Atlantic. *Deep Sea Res. Part A. Oceanogr. Res. Pap.*, 34(10):1655–1665.

[132] Schmitt, R. W.

1979. The growth rate of super-critical salt fingers. *Deep Sea Res. Part A. Oceanogr. Res. Pap.*, 26(1):23–40.

[133] Schmitt, R. W.

1994. Double Diffusion in Oceanography. *Annu. Rev. Fluid Mech.*, 26(1):255–285.

[134] Segrè, P. N., F. Liu, P. Umbanhowar, and D. A. Weitz

2001. An effective gravitational temperature for sedimentation. *Nature*, 409(6820):594–597.

[135] Shen, C. Y. and R. W. Schmitt

1995. The Salt Finger Wavenumber Spectrum. Pp. 305–312.

[136] Shin, J. O., S. B. Dalziel, and P. F. Linden

2004. Gravity currents produced by lock exchange. *J. Fluid Mech.*, 521:1–34.

[137] Simpson, J. E.

1982. Gravity currents in the laboratory, atmosphere, and ocean. *Annu. Rev. Fluid Mech.*, 14(1):213–234.

[138] Sirota, I., A. Arnon, and N. G. Lensky

2016. Seasonal variations of halite saturation in the Dead Sea. *Water Resour. Res.*, 52(9):7151–7162.

[139] Sirota, I., Y. Enzel, and N. G. Lensky

2017. Temperature seasonality control on modern halite layers in the Dead Sea: In situ observations. *Geol. Soc. Am. Bull.*, 129(9-10):B31661.1.

[140] Sirota, I., Y. Enzel, and N. G. Lensky

2018. Halite focusing and amplification of salt layer thickness: From the Dead Sea to deep hypersaline basins. *Geology*.

[141] Smoot, J. P.

1983. Depositional subenvironments in an arid closed basin; the Wilkins Peak Member of the Green River Formation (Eocene), Wyoming, U.S.A. *Sedimentology*, 30(6):801–827.

[142] Snow, K. and B. R. Sutherland

2014. Particle-laden flow down a slope in uniform stratification. *J. Fluid Mech.*, 755:251–273.

[143] Spalart, P. R., R. D. Moser, and M. M. Rogers

1991. Spectral methods for the Navier-Stokes equations with one infinite and two periodic directions. *J. Comput. Phys.*, 96(2):297–324.

[144] Steinhorn, I.

1983. In situ salt precipitation at the Dead Sea. *Limnol. Oceanogr.*, 28(3):580–583.

[145] Stellmach, S., A. Traxler, P. Garaud, N. Brummell, and T. Radko

2011. Dynamics of fingering convection. Part 2 The formation of thermohaline staircases. *J. Fluid Mech.*, 677:554–571.

[146] Stern, M. E.

1960. The Salt-Fountain and Thermohaline Convection. *Tellus*, 12(2):172–175.

[147] Stern, M. E.

1969. Collective instability of salt fingers. *J. Fluid Mech.*, 35(02):209.

[148] Stern, M. E., T. Radko, and J. Simeonov

2001. Salt fingers in an unbounded thermocline. *J. Mar. Res.*, 59(3):355–390.

[149] Stern, M. E. and J. S. Turner

1969. Salt fingers and convecting layers. *Deep Sea Res. Oceanogr. Abstr.*, 16(5):497–511.

[150] Stevens, C. L. and G. A. Lawrence

1998. Stability and meromixis in a water-filled mine pit. *Limnol. Oceanogr.*, 43(5):946–954.

[151] Stiller, M., J. R. Gat, and P. Kaushansky

1997. Halite precipitation and sediemnt deposition as measured in sediment traps deployed in the Dead Sea: 19811983. In *Dead Sea lake its setting*, T. M. Niemi, Z. Ben-Avraham, and J. Gat, eds., chapter 15, Pp. 161–170. Oxford Univ. Press, Oxford.

[152] Sutherland, B. R.

2010. *Internal Gravity Waves*. Cambridge: Cambridge University Press.

[153] Tait, R. and M. Howe

1968. Some observations of thermo-haline stratification in the deep ocean. *Deep Sea Res. Oceanogr. Abstr.*, 15(3):275–280.

[154] Takiguchi, S., T. Kajishima, and Y. Miyake

1999. Numerical Scheme to Resolve the Interaction between Solid Particles and Fluid Turbulence. *JSME Int. J. Ser. B*, 42(3):411–418.

[155] Thielicke, W. and E. J. Stamhuis

2014. PIVlab Towards User-friendly, Affordable and Accurate Digital Particle Image Velocimetry in MATLAB. *J. Open Res. Softw.*, 2.

[156] Traxler, A., S. Stellmach, P. Garaud, T. Radko, and N. Brummell

2011. Dynamics of fingering convection. Part 1 Small-scale fluxes and large-scale instabilities. *J. Fluid Mech.*, 677:530–553.

[157] Tschisgale, S., T. Kempe, and J. Fröhlich

2017. A non-iterative immersed boundary method for spherical particles of arbitrary density ratio. *J. Comput. Phys.*, 339:432–452.

[158] Tseng, Y.-H. and J. H. Ferziger

2003. A ghost-cell immersed boundary method for flow in complex geometry. *J. Comput. Phys.*, 192(2):593–623.

[159] Turner, J. S.

1967. Salt fingers across a density interface. *Deep Sea Res. Oceanogr. Abstr.*, 14(5):599–611.

[160] Turner, J. S.

1974. Double-Diffusive Phenomena. *Annu. Rev. Fluid Mech.*, 6(1):37–54.

[161] Turner, J. S.

1986. Turbulent entrainment: the development of the entrainment assumption, and its application to geophysical flows. *J. Fluid Mech.*, 173:431.

[162] Uhlmann, M.

2005. An immersed boundary method with direct forcing for the simulation of particulate flows. *J. Comput. Phys.*, 209(2):448–476.

[163] Ungarish, M.

2006. On gravity currents in a linearly stratified ambient: a generalization of Benjamin's steady-state propagation results. *J. Fluid Mech.*, 548(-1):49.

[164] Ungarish, M.

2009. *An introduction to gravity currents and intrusions.* Chapman and Hall/CRC.

[165] Van Atta, C. W.

1985. Some challenges for modelling of turbulence and internal waves in stably stratified fluids. Pp. 120–133.

[166] Visser, A. W.

2007. Biomixing of the oceans? *Science (80-.).*, 316(5826):838–839.

[167] von Rohden, C., B. Boehrer, and J. Imberger

2010. Evidence for double diffusion in temperate meromictic lakes. *Hydrol. Earth Syst. Sci.*, 14(4):667–674.

[168] Vowinckel, B., J. Withers, P. Luzzatto-Fegiz, and E. Meiburg

2019. Settling of cohesive sediment: particle-resolved simulations. *J. Fluid Mech.*, 858:5–44.

[169] Walsh, D. and B. Ruddick

1995. Double-Diffusive Interleaving: The Influence of Nonconstant Diffusivities. *J. Phys. Oceanogr.*, 25(3):348–358.

[170] Wang, S. and A. Ardekani

2012. Inertial squirmer. *Phys. Fluids*, 24(10):101902.

[171] Wang, S. and A. M. Ardekani

2015. Biogenic mixing induced by intermediate Reynolds number swimming in stratified fluids. *Sci. Rep.*, 5(1):17448.

[172] Whitfield, D. W. A., G. Holloway, and J. Y. Holyer

1989. Spectral transform simulations of finite amplitude double-diffusive instabilities in two dimensions. *J. Mar. Res.*, 47(2):241–265.

[173] Wilhelmus, M. M. and J. O. Dabiri

2014. Observations of large-scale fluid transport by laser-guided plankton aggregations. *Phys. Fluids*, 26(10):101302+.

[174] Winters, K. B., P. N. Lombard, J. J. Riley, and E. a. D'Asaro

1995. Available potential energy and mixing in density-stratified fluids. *J. Fluid Mech.*, 289(-1):115.

[175] Wüest, A., W. Aeschbach-Hertig, H. Baur, M. Hofer, R. Kipfer, and M. Schurter

1992. Density structure and tritium-helium age of deep hypolimnetic water in the northern basin of Lake Lugano. *Aquat. Sci.*, 54(3-4):205–218.

[176] Yuan-Hui, L. and S. Gregory

1974. Diffusion of ions in sea water and in deep-sea sediments. *Geochim. Cosmochim. Acta*, 38(5):703–714.

[177] Zhang, X. and H. G. Dam

1997. Downward export of carbon by diel migrant mesozooplankton in the central equatorial Pacific. *Deep Sea Res. Part II Top. Stud. Oceanogr.*, 44(9-10):2191–2202.

[178] Zhou, Q., J. R. Taylor, C. P. Caulfield, and P. F. Linden

2017. Diapycnal mixing in layered stratified plane Couette flow quantified in a tracer-based coordinate. *J. Fluid Mech.*, 823:198–229.